Size, age, distribution and mass accumulation rates of seafloor hydrothermal sulfide deposits

John William Jamieson

Thesis submitted to the
Faculty of Graduate and Postdoctoral Studies
in partial fulfillment of the requirements
for a doctoral degree in Earth Sciences

Department of Earth Sciences
Faculty of Science
University of Ottawa

© John William Jamieson, Ottawa, Canada, 2013

Abstract

Hydrothermal discharge on the seafloor results in significant accumulation of base- and precious-metal-rich sulfide material. Technological advances as well as elevated metal prices have led to a growing interest in the direct mining of these deposits from the modern ocean floor. The research presented in this thesis details an investigation of the size, grades, distribution, and accumulation rates of these deposits on the seafloor. A three-part resource assessment, originally designed for land-based ore deposits, was used to generate a predictive framework for the global seafloor sulfide resource. Using detailed descriptions of sizes, grades and locations for 92 known deposits, a resource estimate was generated that predicts a total of ~1,000 deposits and a total global abundance of 600 Mt of sulfide within the neovolcanic zones of the modern ocean floor. A detailed study of the hydrothermal sulfide deposits along the Endeavour Segment of the Juan de Fuca Ridge was carried out to investigate the processes of sulfide accumulation at the ridge-segment scale. Results of ^{226}Ra/Ba dating of barite within the deposits indicate that hydrothermal activity has been ongoing for ~6,000 years and venting has been continuous at the Main Endeavour and High Rise vent fields for ~2,300 and 850 years, respectively. Abundant older sulfide samples from inactive sites outside of the main vent fields indicate a complex history of venting along the ridge segment. Analysis of high-resolution bathymetry of the Endeavour Segment, generated from eight autonomous underwater vehicle surveys, revealed the location of 581 individual hydrothermal sulfide edifices along 15 km of ridge length. Using GIS-based software, the volume of each edifice was calculated, and the total amount of sulfide at Endeavour is estimated to be 1.2 Mt. This estimate is the first comprehensive resource evaluation on the seafloor at this scale. Sulfide has been accumulating within the Endeavour axial valley at a rate of ~400 tonnes per year, which is similar to estimates for the TAG

deposit on the Mid-Atlantic Ridge. Using endmember hydrothermal fluid chemistry data and estimates of fluid discharge rates, the mass accumulation rate calculated for Endeavour corresponds to a sulfide depositional efficiency of 6%.

Résumé

Les décharges hydrothermales sur le fond marin résultent en une accumulation importante de matériel sulfurique riche en métaux de bases et précieux. Les récentes avancées technologiques et les prix augmentant des métaux ont engendré un intérêt toujours croissant pour l'extraction de ces gîtes directement du fond océanique moderne. La recherche présentée dans cette thèse présente une investigation détaillée de la taille, des concentrations, de la distribution et des vitesses d'accumulation de ses gîtes sur les fonds océaniques. Une évaluation de ressources en trois parties, originalement conçue pour des gîtes trouvés sur terre, fut utilisée pour mettre en place un model anticipé des ressources de sulfures globales sur les fonds marins. En utilisant des descriptions détaillées de tailles, de concentrations et de localités de 92 gîtes connus, un estimé des ressources fut mis en place et prédit un total de ~1000 gîtes avec une abondance globale de 600 Mt de sulfures parmi les zones de néo volcanisme des fonds marins modernes. Une étude détaillée des gîtes sulfuriques hydrothermaux trouvés le long du segment d'Endeavour, une section de la dorsale médio-océanique de Juan de Fuca, fut effectuée pour examiner les processus d'accumulation de sulfures à l'échelle du segment. Les résultats de datation au ^{226}Ra/Ba de barytine trouvé dans ces gîtes indiquent que l'activité hydrothermale est en cours depuis ~6 000 ans et que le dégazage est en continu aux évents de Main Endeavour ainsi que High Rise depuis ~2 300 et 850 ans respectivement. Des analyses à haute résolution de la bathymétrie sur la section

d’Endeavour, obtenues de huit levées à partir d’un véhicule sous-marin autonome, ont révélé l’emplacement de 581 monticules de sulfures hydrothermaux sur une longueur de 15 km de dorsale. En utilisant un logiciel à base de SIG, le volume de chaque monticule fut calculé, et une abondance de 1,2 Mt de sulfure est estimée pour Endeavour. Les sulfures s’accumulent dans la vallée d’Endeavour à une vitesse de ~400 tonnes par année. La masse calculée pour Endeavour correspond à une déposition de sulfures efficace à 6%.

Acknowledgements

This thesis is the product of a five-year journey (both physical and metaphorical) that at times I felt totally unprepared for, unqualified to be undertaking, and otherwise totally over my head. I owe a debt of gratitude to the people I met and worked with along that way who provided me with the knowledge, tools, confidence, motivation and encouragement that allowed me to complete this work while maintaining some form of sanity.

To my supervisor, Mark Hannington, whose vision and wealth of knowledge allowed me to work on a research topic that is scientifically fascinating, relevant to society, and downright sexy. Mark perfectly balanced providing a leash long enough to explore different ideas, collaborate with different researchers, and travel to weird and exotic locations, with a leash short enough to keep my ideas in check and focus on attainable goals for the project. His trust in my skills as a researcher and spokesperson for our work was instrumental to the development of my confidence as a scientist.

To my three undergraduate honours students/co-authors: Nicole Williamson, Leigh Allen and Meg Engelbert, who not only did a lot of the analytical work so I didn't have to, but, more importantly, provided unique perspectives to the project that made the results infinitely more significant, important, and scientifically interesting than had I done it alone. What they may not realize is that I learned more from them they ever would from me.

To Linda Kimpe, in the Chemical and Environmental Toxicology Laboratory at the University of Ottawa, whose unlimited knowledge of gamma spectrometry and the analysis of radionuclides made the dating of my hydrothermal samples not only possible, but relatively painless and easy to understand, and one of the standout achievements of my thesis.

To David Clague, at Monterey Bay Aquarium Research Institute (MBARI), who generously allowed me access to his high-resolution multibeam data of the Endeavour Segment. Many of the most important ideas and conclusions within this thesis are the result of the analysis of these data. Thanks also to Dave for his gracious invitation to return to Endeavour to collect further data. This cruise led to several major discoveries, including the active Marias vent and the Sweetland Mound, as well as the collection of several samples that were pivotal to the reconstruction of the hydrothermal history of the segment, and illustrated what can be accomplished when science is pursued without blinders. Thanks also to Jenny Paduan, also of MBARI, whose GIS wizardry made the sulfide volume/tonnage analysis possible.

To James Holden (U. of Massachusetts, Amherst), Dave Butterfield (PMEL/NOAA) and Deborah Kelley (U. of Washington) for providing me with two opportunities to go to sea with the *Alvin* submersible, dive to the bottom of the ocean, and see black smokers up close and personal. The experience of first hand observation of these systems, as well as the data collected on these cruises and the colleagues that I met on board and continue to work with were indispensable to the research presented in this thesis.

To Meg Tivey (Woods Hole Oceanographic Institution) who allowed me to pillage her vast sulfide collection in search of barite-rich samples.

I would like to thank my defence committee: Neil Banerjee (U. of Western Ontario), Ian Clark (U. of Ottawa), Brian Cousens (Carleton University) and Keiko Hattori (U. of Ottawa) for a) passing me, and, b) their critical dissection of this thesis. They, along with my parents, are likely the only people that have read or will read my entire thesis, and for that, I am truly sorry.

To my mental lifeline at sea: Helene Ver Eecke, Rika Anderson and Annie Bourbonnais. Having a group to share such an amazing yet sometimes inexplicably stressful experience that research cruises can be was life-changing, and I am forever grateful that I could share it with them. I hope we can do it again soon! A special thanks also to Eric Olson for his guiding and calming demeanour at sea, and for the epic ping pong battles.

Merci, Émilie Gagnon, pour la traduction de mon résumé.

To my early MRN 205 brethrens: Mark Smith, Andre Pellerin and Nicholas Utting, whose antics and otherwise questionable behaviour was balanced by their experience and knowledge of the inner workings of the department and general graduate school survival. Thank you for the loud music, the Timmy's addiction, and the endless train of co-eds wanting a little one-on-one tutelage with Prof. Pellerin.

To Greg van Hees, Julia King, John and Libby Chapman, Nathan Steeves and Ben Moulton, who understood that the best time to argue about VMS formation processes is beer'o'clock. Or a large pizza, with bacon, pineapple and green pepper.

To the faculty, fellow graduate and undergraduate students in the Dept. of Earth Sciences for their support, entertainment and friendship. I leave the department with a long list of very good friends and colleagues that I hope to work with in the future. A special thanks to David Schneider, who provided me with the unforgettable opportunity to teach several undergraduate courses during my Ph.D. tenure. A special thanks as well to Sandy Sheperd and Hélène de Gouffe, for somehow keeping organized my ridiculously complicated travel itineraries, receipts and contracts. A special shout-out to those that supported DJ^3 as he rose from obscurity in the basement afterhours clubs to headlining the now famous (infamous?) Scorpio Bash parties. "Le7els" and "Seek Bromance" will forever have special meaning as a result.

And, finally, to the girls of the class of 2010: words cannot describe. <3

Table of Contents

1. Introduction 1

2. Grade and Tonnage Models for Seafloor Sulfide Deposits On the Modern Seafloor 7

Abstract 8
1. Introduction 10
2. Sizes of Seafloor Massive Sulfide Deposits 11
2.1 Global Seafloor Massive Sulfide Tonnage Model 13
3. Global Seafloor Massive Sulfide Grade Models 17
4. Discussion 20
4.1 Three-part Resource Assessment 20
4.2 Comparison with land-based deposit models 22
5. Conclusions 25
References 27
Tables 32
Figures 36

3. Precipitation of Barite in Hydrothermal Vents Along the Endeavour Segment of the Juan de Fuca Ridge 46

Abstract 47
1. Introduction 48
2. The Endeavour Segment 50
3. Methods 52
3.1 Sampling 52
3.2 Geochemistry 53
3.3 Petrographic Analysis 53
3.4 Electron Microprobe Analysis 53
3.5 Sr-Isotope Composition of Barite 54
4. Results 54
4.1 Geochemistry 54
4.2 Petrographic Analysis 55
4.3 Sr-concentrations within Barite Crystals 56
4.4 Sr-Isotope Ratios in Barite 56

5. Discussion 56
5.1 Mineralogical Controls on Sr-Distribution 57
5.2 Hydrothermal Fluid-Seawater Mixing during Barite Precipitation 58
5.3 Temperature of Barite Crystallization 60
5.4 Barite Crystal Morphology 61
6. Conclusions 63
References 65
Tables 68
Figures 73

4. Sulfide Geochronology along the Endeavour Segment of the Juan de Fuca Ridge 81
Abstract 82
1. Introduction 83
2. Radium-226/Ba Dating of Hydrothermal Barite 85
3. Geologic Setting 86
4. Samples 89
5. Methods 89
6. Results 91
6.1 Initial ^{226}Ra/Ba ratios of 'zero-age' samples 91
6.2 ^{226}Ra/Ba ratios of inactive samples 92
7. Discussion 93
7.1 Venting History within the Endeavour Axial Valley 94
7.2 The Age of the Valley Floor and Rate of Spreading 98
7.3 Ages of Sulfides at Other Mid-Ocean Ridges 100
8. Conclusions 102
References 104
Tables 112
Figures 116

5. Volumes, Tonnages and Mass Accumulation Rates of Hydrothermal Sulfide Along the Endeavour Segment 125
Abstract 126
1. Introduction 127
2. Geologic Setting 128
3. Methods 129
4. Results 131
5. Discussion 133

5.1 Previous Mapping of Sulfides at Endeavour 133
5.2 Hydrothermal Mounds 135
5.3 Mass Accumulation Rates 137
5.4 Implications for the Global Seafloor sulfide Resource 140
6. Conclusions 143
References 145
Tables 150
Figures 153

6. Conclusions 162

Appendices 168
Appendix A – Seafloor hydrothermal deposit names 169
Appendix B – Hydrothermal sulfide deposit area estimates 170
Appendix C – Sulfide Geochemistry 207
Appendix D – Petrographic Descriptions 216
Appendix E – Volume Estimates for Endeavour Sulfides 260
Appendix F – Calculation of age uncertainties 272

CHAPTER 1

INTRODUCTION

The occurrence of active seafloor hydrothermal systems has been confirmed on the seafloor of every major ocean and in every marine tectonic setting, from mid-ocean ridges to volcanic arcs (Hannington et al., 2005). The circulation of seawater through oceanic lithosphere within the neovolcanic zones of the ocean floor, driven by the heat of shallow magmatic activity, is an important process for the transfer of heat and chemicals between the lithosphere and overlying ocean. As modern analogues for ancient volcanogenic massive sulfide (VMS) deposits, active seafloor hydrothermal systems provide a unique opportunity to directly observe and study an important ore-forming process. Recent technological advances and elevated metal prices have resulted in the metal-rich deposits being considered for direct exploitation from the seafloor for the high contents of Cu, Zn, Pb, Au and Ag.

Many questions remain regarding the accumulation of sulfide material at sites of high-temperature hydrothermal venting on the seafloor. The primary focus of the research presented in this thesis is the occurrence and genesis of these sulfide deposits. Specifically, what is the abundance and rate of accumulation of these deposits on the seafloor? This question is addressed using three different, but related approaches: 1) a global resource assessment of seafloor sulfides is established to determine the total amount of sulfide deposit along the neovolcanic zones of the modern ocean floor; 2) a geochronological method is developed to determine the ages of sulfide deposits and to calculate the rates of sulfide accumulation and efficiency of sulfide deposition; and 3) a detailed, high-resolution survey of hydrothermal sulfide deposits from a single mid-ocean ridge segment is used to document the total inventory of hydrothermal sulfide at the segment scale.

This thesis contains four main chapters (Chapters 2-5). The four chapters are presented independently, but are linked by the common themes outlined in this introduction.

In Chapter 2, results from a study of the size, grade, and spatial distribution of hydrothermal sulfide deposits on the seafloor are presented. The aim of this study was to determine the resource potential of seafloor sulfides and generate a predictive framework for the occurrence of these deposits. A three-part resource assessment, developed for land-based ore deposit models, was used as the basis for this study. This approach uses data from known deposits and well-explored regions of the seafloor in order to generate statistical estimates for the distribution, size and grades of deposits in un- or under-explored regions. Data for this study was compiled from an exhaustive survey of all documented sulfide deposits on the seafloor. The results of this study have been published in an *Society of Economic Geologists Special Publication* (Hannington et al., 2010).

Chapter 3 summarizes an investigation of the chemical and physical conditions under which barite precipitates in hydrothermal chimneys from the Endeavour Segment. The conditions under which barite precipitates are critical to the proper interpretation of ages calculated using ^{226}Ra/Ba values in barite (see Chapter 4). In particular, the relationship between barite precipitation and the mixing of hydrothermal fluid with local seawater within chimney walls was investigated by a petrographic study of barite morphology in chimney wall samples. The Sr-content and $^{87}Sr/^{86}Sr$ values within barite were also used to quantify the degree of fluid mixing that occurs during barite precipitation. Aspects of this study were completed in conjunction with three undergraduate honours thesis projects: Nicole Williamson (Williamson, 2010) investigated the mineralogical associations and crystal morphology of barite in Endeavour chimneys; Leigh Allen (Allen, 2011) investigated the whole-rock major

and trace element geochemical associations between barite and other mineralogical phases within the chimneys, as well as the Sr-content of barite crystals; Margaret Engelbert (Engelbert, 2012) investigated the $^{87}Sr/^{86}Sr$ values of barite minerals and their relationship to fluid mixing. All three are acknowledged as contributors to this chapter.

Chapter 4 presents the results of the application of the $^{226}Ra/Ba$ dating method to hydrothermal deposits from the Endeavour Segment. This is the first application of this dating method to a mid-ocean ridge tectonic environment, and one of the most spatially extensive geochronological investigations of a seafloor hydrothermal system to date. This study presents ages of 49 hydrothermal samples along ~15 km of ridge length. The results of this study provide insights into the age of hydrothermal activity along the Endeavour Segment, the longevity of individual hydrothermal systems and changes in the location of hydrothermal activity over time. The ages also provide insights into the relationship between hydrothermal activity and the tectonic/volcanic evolution of the ridge segment. The results of this study are currently in press in *G-Cubed*.

In Chapter 5, results are presented of an analysis of hydrothermal deposit occurrences from a series of high-resolution autonomous underwater vehicle (AUV) bathymetric surveys of the Endeavour Segment. One-meter resolution mapping provided the necessary detail to distinguish individual sulfide structures on the seafloor, allowing for a complete inventory of hydrothermal deposition along the ridge segment, including the discovery of several large but previously undocumented sulfide edifices in this well-explored area. Using GIS-based software, the total volume of sulfide material could also be quantified. These data, in conjunction with sulfide ages presented in Chapter 4, are used to determine the mass

accumulation rates of sulfide material and the efficiency of precipitation along the Endeavour Segment.

Previous Work

The results presented in this thesis include contributions from other authors. These contributions are listed below:

Chapter 2: The estimate of seafloor sulfide deposit density, based on the analysis of known deposit occurrences within 32 control areas on the seafloor was carried out by Mark Hannington and Thomas Monecke (2009). These data were incorporated into the global resource estimate (Hannington et al., 2010).

Chapter 3: The investigation of barite precipitation was completed in conjunction with three undergraduate honours theses (Allen, 2011; Engelbert, 2012; Williamson, 2010), for which I was the primary supervisor. Thin section descriptions and photographs presented in Chapter 3 and in the appendix were completed by Ms. Williamson. The interpretation of the results was collaborative between Ms. Williamson and me. The electron microprobe analyses and interpretation of the resulting mineral chemistry data were completed by Ms. Allen and me. Strontium isotope compositions of the sulfide samples were completed by Ms. Engelbert, under the guidance of Dr. Brian Cousens at Carleton University. The interpretation of the results was competed by Ms. Engelbert and me.

Chapter 5: The initial identification of sulfide structures along the Endeavour Segment using the high-resolution bathymetry was originally undertaken by Dr. David Clague. The refining of the criteria used to identify sulfide structures and subsequent re-evaluation of the entire dataset was completed predominantly by me, with inputs from Dr. Clague.

References:

Allen, L., 2011. Behaviour and occurrence of strontium in hydrothermal barite from the Endeavour Segment, Juan de Fuca Ridge, Department of Earth Sciences. University of Ottawa, Ottawa, Canada.

Engelbert, M., 2012. Strontium isotopic study of hydrothermal barite from the Endeavour Segment of the Juan de Fuca Ridge: Implications for seawater-hydrothermal fluid mixing, Department of Earth Sciences. Carleton University, Ottawa, Canada.

Hannington, M., De Ronde, C., Petersen, S., 2005. Sea-Floor Tectonics and Submarine Hydrothermal Systems. Economic Geology 100th Anniversary Volume, pp. 111-141.

Hannington, M., Jamieson, J., Monecke, T., Petersen, S., 2010. Modern sea-floor massive sulfides and base metal resources: towards an estimate of global sea-floor massive sulfide potential. Society of Economic Geologists Special Publication 15, 111-141.

Hannington, M., Monecke, T., 2009. Global Exploration Models for Polymetallic Sulphides in the Area: An Assessment of Lease Block Selection under the Draft Regulations on Prospecting and Exploration for Polymetallic Sulphides. Marine Georesources & Geotechnology 27, 132-159.

Williamson, N., 2010. Occurrence and genesis of hydrothermal barite along the Endeavour Segment, Juan de Fuca Ridge, Department of Earth Sciences. University of Ottawa, Ottawa, Canada.

CHAPTER 2

GRADE AND TONNAGE MODELS FOR SEAFLOOR SULFIDE DEPOSITS ON THE MODERN SEAFLOOR

Abstract

Mineral deposit resource estimates and predictive mapping are tools used to determine the probability of finding ore bodies in unexplored or under-explored regions. Predictive maps for different genetic ore-forming models are developed using a three-part resource assessment and are commonly applied to land based ore deposit types. The three part assessment consists of: 1) building deposit type-specific grade and tonnage models from known deposits; 2) determining the geologically permissive area that the deposits are likely to form in; and 3) determining the deposit distribution (density) within well-explored geologically permissive areas. Recent interest in seafloor hydrothermal sulfide deposits from mining and mineral exploration companies has highlighted the lack of knowledge regarding the size, grades or distribution of these deposits on the seafloor. In this chapter we describe the methods and results of a study to constrain the global seafloor sulfide resource, using a global database of over 300 seafloor massive sulfide occurrences. Results from this endeavour have provided insights into the size and grade distribution of seafloor sulfide deposits, as well as their global distribution. A critical component of this analysis is the construction of grade and tonnage models for seafloor sulfide deposits. Deposit size distribution was determined from detailed descriptions of the extent of sulfide deposition on the seafloor from 62 deposits for which this information is available. Reported surface areas of deposits, based on maps, visual descriptions, and in rare cases, subsurface drilling data, were converted to sulfide tonnages using the tonnage to surface area relationship of the well-constrained Solwara 1 deposit as a guide. The median deposit size is about 70,000 tonnes, and the top 10% of deposits are over 2 Mt. Multiple lines of evidence (e.g., deposit distribution in well-explored areas, incidence of hydrothermal plumes, global heat and chemical fluxes from hydrothermal systems) all point to a spacing of major hydrothermal

systems along every ~100 km of ridge length, for a total of ~1,000 active systems along the current global ridge, arc, and back-arc length of 89,000 km. By applying the seafloor sulfide tonnage curve to this estimate results in a total of 600 Mt of sulfide deposited within the neovolcanic zones of the modern seafloor. Tonnage models of land-based volcanogenic massive sulfide (VMS) deposits show a shift towards higher tonnages by at least an order of magnitude, compared to the modern seafloor tonnage model. This is likely a result of only mined or economically mineable ore deposits being included in the generation of land-based VMS deposits and the omission of smaller sulfide showings or uneconomic deposits.

Grade models for Cu, Zn, Pb, Au and Ag were constructed from over 3,800 geochemical analyses from sulfide samples collected from 95 of the deposits in the global database. The average concentrations of metals based on analyses of surface samples are 3.6 wt.% Cu, 7.9 wt.% Zn, 0.4 wt.% Pb, 1.7 g/t Au, and 115 g/t Ag, although comparisons with drill core indicate that grades can be significantly lower below the seafloor in many, but not all, deposits. Using a combined Cu+Zn+Pb grade of 5 wt.%, which may be more representative of the grades of buried sulfide, the total metal content for sulfide deposits within the neovolcanic zones would be 30Mt. These grades are consistent with the grades of land-based VSM deposits.

1. Introduction

Volcanic-associated and sedimentary-exhalative massive sulfide deposits on land account for more than one-half of the world's total past production and current reserves of zinc and lead, 7% of the copper, 18% of the silver, and a significant amount of gold and other byproduct metals (Singer, 1995). A new source of these metals is now being considered for exploitation from submarine massive sulfide deposits, the modern equivalent of ancient volcanogenic massive sulfide (VMS) deposits. Because the oceans cover more than 70% of the Earth's surface, many expect the ocean floor to host a proportionately large number of these deposits. However, there have been few attempts to estimate the global mineral potential. At present, more than 300 sites of seafloor hydrothermal activity and associated mineralization have been found at mid-ocean ridges, volcanic arcs and back-arc basin environments. About 200 of these are confirmed sites of massive sulfide occurrences (Fig. 2.1); 95 of these deposits have now been sampled and at least partly mapped (Table 2.1), providing the first indications of the likely grades, tonnages, and distribution of deposits that remain to be discovered. Comparisons between modern seafloor massive sulfide and ancient VMS deposits also have become increasingly sophisticated, highlighting important similarities and differences in their distribution, sizes, and bulk compositions (Franklin et al., 2005; Hannington et al., 2005). Using the principle that the tonnages and grades of well-explored deposits and deposit densities serve as models for the size, grade, and distribution of undiscovered deposits, the first estimates of the total amount of seafloor sulfide deposits in the volcanically active parts of the present-day oceans can be made by following the three-part mineral assessment practice employed by the USGS (Singer and Menzie, 2010).

The first step in this assessment is an estimate of the tonnages and grades of undiscovered resources using the data from well-explored deposits that are considered to be representative of the total population. The second part involves an examination of geological maps to determine the area that may be permissive for the discovery of new deposits. The third part is an estimate of the number of undiscovered deposits in that area based on an analysis of deposit densities. The essential criterion is that all deposits are represented by the same grade-tonnage model developed from a subset of well-explored examples. Below, the process of generating the grade and tonnage models for seafloor massive sulfide deposits, and the results of the application of these models to the three-part mineral assessment are described. This analysis is based on detailed information from 95 of the best studied deposits, including some data from deep-sea drilling, and analyses of more than 3,800 samples. Comparisons with grade-tonnage models for land-based mineral deposits provide a measure of confidence in the estimated numbers.

2. Sizes of Seafloor Massive Sulfide Deposits

The tectonic setting in which a sulfide deposit forms on the seafloor can have a significant control on how large deposits will typically form. On fast-spreading ridges, such as the southern East Pacific Rise (EPR), lavas are extruded onto the seafloor faster than the rate of extension, so the flows accumulate as local volcanic highs as much as 100 m above the surrounding seafloor. The eruptive fissures typically occupy a narrow axial graben (~1 km wide), and this is the most common location for hydrothermal vents. However, because the eruption rates are so high, lavas can disrupt the flow of hydrothermal fluids and bury sulfide occurrences that are localized along the fissures. Also, because the upflow zones are

relatively narrow (e.g., Coumou et al., 2008), they are subject to perturbation by intrusive activity that affects permeability within the neovolcanic zone. As a result, sulfide deposits on fast-spreading ridges tend to be abundant but small, and they are rapidly displaced from their heat source by the high spreading rates.

Slow and intermediate-rate spreading centers, such as the Mid-Atlantic Ridge and Juan de Fuca Ridge, are characterized by lower rates of magma supply and greater structural control on hydrothermal upflow than at fast-spreading ridges. Slow-spreading ridges, in particular, have wide (up to 15 km) and deep (up to 2 km), fault-bounded axial valleys. Here, eruptions occur only very rarely, typically at intervals of thousands of years; at the slowest spreading rates, the time between eruptions may be tens of thousands of years. Deeply-penetrating faults allow circulation of hydrothermal seawater to much greater depths than on fast-spreading ridges, exposing a larger volume of hot rock to the hydrothermal fluids, and this important difference in hydrology contributes to the longevity of the hydrothermal systems and the sizes of the deposits. Recent seismic data from the TAG Field suggest that hydrothermal upflow occupies a large-scale ridge detachment fault and may be sourced at considerable depth (~7 km) and tens of kilometers from the site of hydrothermal discharge (de Martin et al., 2007). Because deposits on the slow-spreading ridges are commonly located well off-axis, the substrate is stable enough (i.e. free from volcanic activity and structural perturbations common within the neovolcanic zones) to support hydrothermal upflow for many thousands of years and thus the growth of large sulfide mounds. Large off-axis volcanoes (e.g., at 13°N EPR), which may be located 5 to 10 km from the ridges, similarly host large sulfide occurrences.

Some heavily sedimented environments, including sediment-covered ridges and rifted margins, are particularly important sites of sulfide deposit formation. One of the largest occurrences, Middle Valley on the Juan de Fuca Ridge, is in an area of 100% sediment cover and was discovered in the absence of high-temperature venting. High heat flow and hydrothermal manifestations in the sediment overlying the deposit indicate that it formed mainly by near sub-seafloor mineralization (Davis et al., 1992a; Fouquet et al., 2000).

About one-third of the known high-temperature seafloor hydrothermal systems occur at submarine volcanic arcs or in back-arc basins (Hannington et al., 2005). Hydrothermal systems in subduction-related environments are broadly similar to those at the mid-ocean ridges. In contrast to the mid-ocean ridges, the convergent margin settings are characterized by a range of different crustal thicknesses, heat flow regimes, and magma compositions, depending on the nature of the converging plates (e.g., intraoceanic, continental, or transitional). The compositions of the volcanic rocks, in particular, vary from mid-ocean ridge basalt (MORB) to more felsic lavas (andesite, dacite, and rhyolite), which leads to major differences in the composition of the hydrothermal fluids and the mineralogy and bulk composition of the sulfide deposits (Hannington et al., 2005). However, the sizes of the deposits are comparable to those found on the mid-ocean ridges.

2.1 Global Seafloor Massive Sulfide Tonnage Model

The deposits listed in Table 2.1 that have associated size estimates are a test group considered to have the most reliable information about deposit size, but the true sizes are commonly incompletely known. Reported dimensions commonly include large areas of discontinuous sulfide outcrop or barren substrate between chimneys and mounds, thereby

over-estimating the sizes of the deposits. Because of the widespread dusting of metalliferous sediment and debris from collapsed chimneys, the continuity of sulfide bodies is difficult to assess, even with the most detailed surveys. A number of examples illustrate the challenges of reliably determining deposit sizes. When polymetallic sulfides were first discovered at Southern Explorer Ridge, the largest mound was estimated to be 250 m x 200 m in area, based on submersible observations of the time (Goodfellow et al., 1988). However, recent high-resolution surveys have shown that the mound comprises mainly lava covered by Fe-stained sediment, with only four clusters of chimneys covering a fraction of the area originally considered to be massive sulfide (Embley et al., 2002). In a submersible survey of the Sunrise occurrence, on the Myojin Knoll submarine volcano, an area of sulfide mineralization measuring 400 m x 400 m was reported (Iizasa et al., 1999). Based on a relief of 30 m and a bulk density of 1.9 gm/cm^3, a total accumulation of 9 Mt of massive sulfide was calculated. Three important assumptions were implicit in this calculation: (i) the sulfide outcrop was considered to cover 100% of the outlined area, including areas between sulfide ridges and mounds that are concealed by sediment; (ii) the observed relief is due entirely to the accumulation of massive sulfide on a flat seafloor and not due to faults or buried volcanic features (e.g., lava domes); (iii) the bulk density is uniform and represents the entire volume used in the calculation. However, dive tracks indicate that submersible surveys cover only about 25% of the total area, and the visually identifiable sulfide outcrop cannot be reliably extrapolated to the limits of the mapped area (see Appendix A). Thus, the estimate of 9 Mt is considered to be a maximum and possibly overestimated by a considerable margin.

In many cases, the confidence in a deposit's size estimate is related to the number of different mapping techniques used to make the estimate (e.g., drilling, high-resolution

bathymetry, surface sampling and geophysics for the Solwara 1 deposit; Lipton, 2012) and to how detailed the geological descriptions are. The geological map of the Brothers hydrothermal systems, on the Kermadec Arc includes legend symbols for Fe-stained sediments, sulfide outcrop, subcropping sulfides, sulfide talus, black smoker, sulfide chimneys and buried sulfide zone/exposed sulfide field (Appendix A). This level of description is in sharp contrast to descriptions of less well-explored vent fields that include only the aerial extent of hydrothermal activity, and perhaps the number of vent chimneys observed, but no information on vent edifice size or the nature of the substrate within the vent field (e.g. 12º50N; Appendix A).

Recent developments in marine geophysical methods, such as deep-towed magnetics and electromagnetic (EM) surveys, are providing tools for reliably determining the surface extent and continuity of massive sulfides on the seafloor (Tivey and Johnson, 2002; Kowalczyk and Jackson, 2007; Kinsey et al., 2008). Deep-towed EM was successfully employed in surveys of the Solwara 1 deposit in the Eastern Manus Basin to delineate areas of near-surface massive sulfides (Lipton, 2008). However, drilling is required to judge the continuity and thickness of sulfide outcrops in most cases and sometimes just to identify the deposits. For example, at Middle Valley on the Juan de Fuca Ridge, the seafloor is punctuated by numerous large mounds as much as several hundred meters in diameter and 50 m high. Drilling and other detailed surveys showed that most of these mounds are only uplifted blocks of sediment above buried volcanic sills. However, in one of the mounds, Bent Hill, 95 m of massive sulfide was intersected below the seafloor (Davis et al., 1992b). A second smaller mound 300 m away (ODP mound) also was shown to be mostly massive sulfide (Zierenberg and Miller, 2000).

Reliable estimates of the total sulfide accumulation have been possible in only a few cases where drilling information is available. The four deep drill holes that penetrated the Bent Hill and ODP mounds at Middle Valley (ODP Legs 139 and 169) indicate a combined tonnage of between 10 and 15 Mt (Fouquet et al., 1998; Zierenberg et al., 1998). Seventeen holes drilled to a maximum depth of 125 m in the large TAG mound on the Mid-Atlantic Ridge, indicated 2.7 Mt of massive sulfide averaging 2 wt.% Cu and 1.2 Mt of stockwork mineralization at 1 wt.% Cu (ODP Leg 158: Hannington et al., 1998). Data from extensive drilling of the Solwara 1 deposit in the Eastern Manus Basin (146 holes to a maximum depth of 20 m) have been used to estimate the first NI 43-101 compliant resource for a seafloor sulfide deposit of 2.1 Mt (Lipton, 2008).

From the size estimates of 62 deposits (Table 2.1) and from drilling information at deposits such as Solwara 1 (i.e., 2.1 Mt in a chimney zone covering 90,000 m^2: Lipton, 2008), a global tonnage model for seafloor sulfide deposits can be constructed. Due to the uncertainties associated with the size estimates, each deposit in the test group has been classified into size bins that range from <3,000 t to >1 Mt (Fig. 2.2), using the area versus tonnage relationship for Solwara 1 as a guide. About 33% of the deposits are considered to be smaller than 3,000 t and are not included in the plot.

The binned data can also be plotted as a cumulative frequency "curve", similar to that used in land-based resource assessments (Fig. 2.3). In this plot, the median size of the deposits is seen to be less than 100,000 t and closer to 50,000 t. No distinction is made between deposits on the mid-ocean ridges and deposits in arc and back-arc settings. So far, no deposits have

been found in back-arc basins or on active volcanic arcs that are significantly larger than those on mid-ocean ridges, although the grades are different. Therefore, with the limited data available, a separate tonnage model for deposits in subduction-related environments is probably not justified at this time. If we assume that these size classes are representative of deposits that remain to be discovered on the seafloor, then only 1 in 10 new deposits would be expected to contain more than 2 Mt. New information about the sizes of the known deposits is unlikely to change the median tonnage of the population; certain deposits may be moved from one size class to another, but the general features of the tonnage curve will remain the same. The discovery of one or more large deposits would change the proportion of massive sulfide in the 10th percentile, but not the expected median size.

3. Global Seafloor Massive Sulfide Grade Models

Samples collected from hydrothermal deposits worldwide have economically significant concentrations of Cu, Zn, Pb, Au, and Ag. Geochemical data compiled for the International Seabed Authority (Hannington et al., 2004), have recently been updated and now include analyses of more than 3,800 samples from 95 deposits (Table 2.1). Summary data listed in Table 2.2 reveal systematic differences in the bulk compositions of the deposits in different volcanic and tectonic settings. This reflects the different substrates, including mid-ocean ridge basalt, ultramafic intrusive rocks, more evolved lavas associated with volcanic arcs, and sediments, in both oceanic and continental crust. Superimposed on this source-rock control is a strong temperature dependence of metal concentrations in the vent fluids, as well as contributions of metals directly from the magma.

Mid-ocean ridge deposits for which there are representative suites of 50 samples or more have average metal concentrations of 5.9 wt.% Cu, 6.1 wt.% Zn, <0.1 wt.% Pb, 1.6 ppm Au, and 89 ppm Ag (Table 2.2). Calcium, Ba, and SiO_2 (in anhydrite, barite, and amorphous silica, respectively) are major constituents of the deposits, but on average account for <20 wt.% of most samples. Sulfide deposits on sedimented ridges have average metal concentrations of 1.1 wt.% Cu, 3.6 wt.% Zn, 0.5 wt.% Pb, 0.5 ppm Au, and 84 ppm Ag (n = 173). These data reflect the influence of hydrothermal fluids ascending through thick sequences of turbidites, as well as the tendency for precipitation of metals beneath the sediment-seawater interface (Hannington et al., 2005). Calcite, anhydrite, barite, and amorphous silica are major components of the sediment-hosted deposits and commonly dilute the base metals. Unusually high metal concentrations have been encountered in deposits hosted by ultramafic rocks at several locations on the slow-spreading Mid-Atlantic Ridge (Hannington et al., 2005). Reported metal concentrations in samples collected from these deposits average 14.0 wt.% Cu, 12.8 wt.% Zn, <0.1 wt.% Pb, 9.3 ppm Au, and 83 ppm Ag, although in some cases this may reflect seafloor weathering and secondary enrichment.

Seafloor sulfide deposits hosted by more evolved volcanic suites, typical of subduction-related arc- and back-arc settings, have much higher concentrations of Zn, Pb, Au, and Ag compared to typical mid-ocean ridge deposits (Hannington et al., 2005). Samples from deposits at intraoceanic back-arc spreading centers have average metal concentrations of 3.9 wt.% Cu, 16.4 wt.% Zn, 0.9 wt.% Pb, 6.6 ppm Au, and 210 ppm Ag. Samples from deposits in the summit calderas of arc volcanoes have average concentrations of 5.3 wt.% Cu, 17.7 wt.% Zn, 2.4 wt.% Pb, 9.6 ppm Au, and 407 ppm Ag. At arc-continent transitions and in intracontinental back-arc rifts, average metal concentrations are 6.4 wt.% Cu, 14.8 wt.% Zn,

2.0 wt.% Pb, 12.2 ppm Au, and 692 ppm Ag, and 3.1 wt.% Cu, 20.3 wt.% Zn, 10.0 wt.% Pb, 2.3 ppm Au, and 953 ppm Ag, respectively. The average metal contents of surface samples collected from all 95 sulfide deposits listed in Table 2.1 are summarized in cumulative frequency plots in Figure 2.4. The data define general grade curves for Cu, Zn, Pb, Ag, and Au and can be approximated by typical log-normal distributions.

In almost all cases, the average metal concentrations of surface samples from seafloor deposits are higher than reported grades of VMS deposits on land. This is because of a strong bias in sampling towards high-temperature sulfide chimneys, which are easiest to recover and are commonly the focus of detailed studies. Much less is known about the interiors of larger sulfide mounds, but it is clear that sulfide chimneys alone are not representative of the bulk compositions of the deposits as a whole. Evidence from a few well-documented examples indicates that most deposits are compositionally zoned; Cu- and Fe-rich sulfide minerals formed at higher-temperatures (300-350°C) are most abundant in the interiors of the mounds, whereas Zn-sulfide minerals formed at lower-temperatures (250-300°C) are deposited on the surfaces of the mounds (e.g., Hannington et al., 1995, 1998). Systematic sampling of both high- and low-temperature assemblages across the surfaces of large deposits can provide a more representative picture of their bulk compositions. However, accurate information about the continuity of base and precious metal grades in the interiors of the deposits can only be obtained by drilling. A comparison of data from surface samples and drill core in deposits that have been drilled shows that the grades can be significantly lower below the seafloor in many, but not all, cases (Table 2.3).

4. Discussion

4.1 Three-Part Resource Assessment

The grade and tonnage models presented here provide the basis for a first estimate of the global abundance of seafloor massive sulfide deposits and their contained metal. This information is used in conjunction with analysis of the geologically permissive area and distribution of hydrothermal sulfide deposits on the seafloor in order to estimate a global seafloor sulfide resource (Hannington et al., 2011).

To estimate the global abundance of deposits, the simplest definition of the permissive "area" is the cumulative strike length of the oceanic plate boundaries of 89,000 km (Bird, 2003). Exploration (commercial and scientific) for seafloor sulfide deposits currently focuses on the neovolcanic zones of the oceans, where hydrothermal systems are most likely to be detected. Since all oceanic crust formed at mid-ocean ridges, the entire seafloor will have, at some point, been exposed to conditions favorable for hydrothermal sulfide deposition within the neovolcanic zones. However, as ocean crust migrates away from spreading ridges and active high-temperature hydrothermal circulation, oceanic sedimentation will bury the deposits (Fig. 2.5). Current methods of exploration for seafloor sulfide deposits focus on locating surface exposures or active plumes. Even sediment thicknesses of only a few meters may be enough to make underlying sulfide deposits undetectable using current exploration methods. For this reason, only oceanic crust within 5-10 km of ridge axes is considered geologically permissive for the resource calculation (Hannington et al., 2010).

Deposit densities were determined by Hannington and Monecke (2009) by determining the number of deposits within the permissive areas of 32 well-explored control areas of 5 degrees latitude by 5 degrees longitude. Results of the analysis of deposit densities in these control areas indicate an average spacing of 98 km along ridge axes or volcanic front between sulfide deposits. Using this spacing estimate over a total ridge, arc and back-arc spreading length of 89,000 km, the total number of deposits expected for the volcanically active parts of the oceans is ~900. Several independent estimates of the spacing of hydrothermal vents, at least on the mid-ocean ridges, confirm that the distance between sulfide occurrences is likely quite regular at the regional scale and closely approximates the ~100 km average spacing determined by Hannington and Monecke (2009). Estimates of global fluid, heat and geochemical fluxes from seafloor hydrothermal systems both point to a similar number of ~1000 active vent fields along the global neovolcanic zones (Hannington et al., 2010 and references therein). Similarly, the incidence and spacing of hydrothermal plumes in the water column along the mid-ocean ridges (Baker and German, 2004; Baker, 2007) also point to the occurrence of hydrothermal systems at a spacing of ~100 km along the ridge length, again for a total of ~1,000 active hydrothermal systems.

Once an estimate has been made of the number of deposits, it is possible to place some constraints on the total amount of massive sulfide present by assuming a size distribution similar to that represented in Figure 2.3. Assuming ~1,000 deposits with a minimum size of 100 t, a maximum size of 10 Mt, the total amount of massive sulfide within the neovolcanic zones is on the order of 600 Mt (Hannington et al., 2011). The top 10% of deposits would contain ~400 Mt. Importantly, these estimates do not include extinct deposits that may be buried beneath sediments flanking the mid-ocean ridges and back-arc spreading centers.

Furthermore, this global tonnage estimate is based largely on a database of active hydrothermal systems, due to the difficulties in detecting inactive sulfide deposits. Recent mapping of the Endeavour Segment on the Juan de Fuca Ridge that detected large numbers of inactive sulfide edifices suggests that up to four times as much sulfide as that predicted using the method outlined above may occur within the neovolcanic zones. See chapter 5 for further discussion.

The total contained metal is more difficult to assess, owing to the large bias in sampling of seafloor deposits and the very high grades illustrated in Figure 2.4. Figure 2.6 compares the bulk compositions of modern seafloor deposits at mid-ocean ridges and in arc-related settings to grades of land-based VMS deposits. Metal concentrations similar to those of samples collected from seafloor deposits are found in only the highest-grade VMS deposits on land. Grades of more than 10 wt.% combined Zn+Cu+Pb, such as those reported for many seafloor deposits, occur in only 10% of deposits in the bimodal-mafic class on land (Mosier et al., 2009). As discussed above, the bulk metal concentrations of seafloor deposits are probably much lower than suggested by the surface samples. Therefore, to estimate the total contained metal, a median grade of no more than 5 wt.% combined Zn+Cu+Pb was chosen, which more closely matches that of VMS deposits on land (Table 2.4). Applied to the modern seafloor deposit tonnage model, the total contained metal of the deposits in the neovolcanic zones is about 30 Mt. The top 10% of deposits would contain about 20 Mt of Zn+Cu+Pb.

4.2 Comparison with land-based deposit models

The grade and tonnage models for land-based VMS deposits (e.g., Mosier et al., 2007, 2009) show expected trends; deposits associated with mafic volcanic rocks tend to be more copper-rich and those associated with felsic rocks tend to have higher grades of zinc, lead, silver, and gold (Table 2.4) . The metal contents and deposit sizes can be approximated by log-normal distributions. The largest deposits are on the order of several hundreds of millions of tonnes in size, but they are rare. Only about 10% of VMS deposits contain between 25 and 50 Mt of ore, fewer than 5% contain between 50 and 100 Mt, and only 3% are giant deposits of more than 100 Mt. The median sizes are 0.7, 1.9, and 3 Mt, respectively, in mafic-dominated, bimodal-mafic, and felsic-dominated successions (Mosier et al., 2009). Almost all of the metal is contained in the largest size classes and, in a typical VMS district, the single largest deposit commonly accounts for 60-70% of the total metal; the second largest deposit may contain only 10-20% of the metal (Sangster, 1980).

Comparisons with land-based VMS deposits provide a number of additional clues to the likely abundance and distribution of modern seafloor deposits. Based on the current lithostratigraphic classification of VMS deposits, it is possible to identify close analogs of many ancient deposits on the present-day seafloor (e.g., Franklin et al., 2005). The two most relevant models are those for so-called "Cyprus-type" deposits and the Kuroko deposits of Japan. Cyprus-type massive sulfide deposits have long been considered to be the best ancient examples of sulfide deposits on the mid-ocean ridges and in mature back-arc basin environments (e.g., Hannington et al., 1998). The Kuroko deposits are analogs of deposits that occur in volcanic arc environments (Ishibashi and Urabe, 1995; Glasby et al., 2008).

The data for VMS deposits in Cyprus (Mosier et al., 1983; Singer and Mosier, 1986) indicate a median size of about 2 Mt (Fig. 2.7). This is significantly larger than the estimated median size of seafloor sulfide deposits, mainly because the data for deposits on land include only those deposits that were of sufficient size to be mined or large enough to have justified drilling. In reality, large numbers of sulfide occurrences are either too small or of too low grade to have been mined and, therefore, are not considered in the total past production and current reserves. Among the Cyprus deposits, this is estimated to include more than 90 undeveloped prospects containing <100,000 t each, and probably many more much smaller occurrences that were never even considered to be prospects (Hannington et al., 1998, and references therein). These are probably analogous to the many small isolated chimneys and mounds that are found along the mid-ocean ridges and back-arc spreading centers. If all of these smaller undeveloped prospects were included, then the median size of Cyprus-type massive sulfides would shift toward significantly lower tonnage, similar to that estimated for modern seafloor deposits. A revised model for all mafic-hosted VMS deposits (n=174; Mosier et al., 2009) more closely matches that estimated for modern deposits, but the median size of 0.74 Mt is still an order of magnitude larger (Table 2.4 and Fig. 2.7). The size distribution of the Kuroko deposits is also shown in Figure 2.7. During mining of the Kuroko deposits, careful records were kept of the physical dimensions of the orebodies, which are minimally deformed (Tanimura et al., 1983). The average surface area of the 44 mined deposits in the Hokuroku basin was about 200 m x 200 m, which is similar to that of the largest seafloor sulfide deposits.

The total tonnage of modern sulfide deposits estimated here for seafloor neovolcanic zones (~600 Mt) is small compared to the total past production and current reserves of VMS on

land. The most recent databases of Franklin et al. (2005) and Mosier et al. (2009) indicate past and current geological resources of ~14,000 Mt in global VMS. The cumulative tonnage of mafic rock-hosted VMS deposits, which are considered to be the closest analogs of presently known deposits on the seafloor, is 831 Mt, but this includes deposits that are as old as 600 Ma.

5. Conclusions

The grade and tonnage models presented here provide the first indications of the expected sizes and metal endowment of deposits on the seafloor. With a median deposit size of ~70,000 tonnes, seafloor deposits are significantly smaller than the land-based VMS deposit. This may be a result of inclusion of sub-economic deposits in the seafloor tonnage model. However, the largest deposits so far discovered on the seafloor (e.g. Middle Valley, ~10 Mt; Semyenov, ~9 Mt) pale in comparison to the largest VMS deposits on land, which can be over 100 Mt (e.g. Neves Corvo in Spain, and Windy Craggy, Brunswick #12, Kidd Creek in Canada, for example; Galley et al., 2007), suggesting a potential for the discovery of larger deposits on the seafloor.

Grade models for seafloor sulfide deposits indicate potentially economic grades for Cu, Zn, Pb, Au and Ag. Higher grades for these metals, relative to the grades of land-based VMS deposits, are likely a result of preferential sampling of high-grade surface samples. Grades from subsurface samples collected by drilling are generally more consistent with typical grades from VMS deposits.

The total estimated tonnage for seafloor sulfide deposits of 600 Mt is based largely on the occurrence and distribution of active hydrothermal systems within the global neovolcanic zones. Improvements in high-resolution mapping techniques of the seafloor are now starting to provide insights into the amount of inactive sulfide deposits within the neovolcanic zones that are not accounted for when active hydrothermalism is the basis for exploration (see Chapter 5 for further discussion on inactive sulfide deposits). As a result, the 600 Mt resource should be taken as a minimum estimate for the neovolcanic zones. Significant sulfide deposits also likely occur off-axis, on older oceanic crust. However, these deposits are likely buried under sediment. Current exploration techniques, which rely on discovery of active hydrothermal plumes or the surface morphology of sulfide deposits, are not practical for locating buried deposits, and the inclusion of these buried deposits in a resource assessment would be premature.

References

Baker, E.T., 2007, Hydrothermal cooling of midocean ridge axes: Do measured and modeled heat fluxes agree?: Earth and Planetary Science Letters, v. 263, p. 140-150.

Baker, E.T., and German, C.R., 2004, On the global distribution of mid-ocean ridge hydrothermal vent-fields, *in* German, C.R., Lin, J., and Parson, L.M., eds., Mid-Ocean Ridges: Hydrothermal Interactions Between the Lithosphere and Oceans: Geophysical Monograph 148, p. 245-266.

Bird, P., 2003, An updated digital model of plate boundaries: Geochemistry, Geophysics, Geosystems, v. 4, no. 3, doi: 10.1029/2001GC000252.

Coumou, D., Driesner, T., and Heinrich, C.A., 2008, The structure and dynamics of mid-ocean ridge hydrothermal systems: Science, v. 321, p. 1825-1828

Davis, E.E., and Villinger, H., 1992a, Tectonic and thermal structure of the Middle Valley sedimented rift, northern Juan de Fuca Ridge, in Davis, E.E., Mottl, M.J., and Fisher, A.T., eds., Proceedings of the Ocean Drilling Program, Initial Reports, v. 139: College Station, Texas, Ocean Drilling Program, p. 9-41.

Davis, E.E., Mottl, M.J., and Fisher, A.T., 1992b, Proceedings of the Ocean Drilling Program, Initial Reports, v. 139: College Station, Texas, Ocean Drilling Program, 459 p.

de Martin, B.J., Sohn, R.A., Canales, J.P., and Humphris, S.E., 2007, Kinematics and geometry of active detachment faulting beneath the Trans-Atlantic Geotraverse (TAG) hydrothermal field on the Mid-Atlantic Ridge: Geology, v. 35, p. 711-714.

Embley, R., E, B., Baross, J., Bates, A., 2002. Rediscovery and Exploration of Magic Mountain, Explorer Ridge, NE Pacific. EOS Transactions AGU 83, TIIC-1264 (Fall Meeting).

Fouquet, Y., 1997, Where are the large hydrothermal sulphide deposits in the oceans?: Philosophical Transaction of the Royal Society of London, v. A355, p. 427-441.

Fouquet, Y., Zierenberg, R.A., Miller, D.J., Bahr, J.M., Baker, P.A., Bjerkgård, T.,Brunner, C.A., Duckworth, R.C., Gable, R., Gieskes, J., Goodfellow, W.D., Gröschel-Becker, H.M., Guèrin, G., Ishibashi, J., Iturrino, G., James, R.H., Lackschewitz, K.S., Marquez, L.L., Nehlig, P., Peter, J.M., Rigsby, C.A., Schultheiss, P., Shanks, W.C., III, Simoneit, B.R.T., Summit, M., Teagle, D.A.H., Urbat, M., Zuffa, G.G., 1998, Investigation of hydrothermal circulation and genesis of massive sulfide deposits at sediment-covered

spreading centers at Middle Valley and Escanaba Trough, *in* Zierenberg, R.A., Fouquet, Y., and Miller, D.J., eds., Proceedings of the Ocean Drilling Program, Initial Reports, v. 169: College Station, Texas, Ocean Drilling Program,p. 7-16.

Franklin, J.M., Gibson, H.L., Jonasson, I.R., and Galley, A.G., 2005, Volcanogenic massive sulfide deposits, *in* Hedenquist, J.W., Thompson, J.F.H., Goldfarb, R.J., Richards, J.P., eds., Economic Geology One Hundredth Anniversary Volume, p. 523-560.

Fouquet, Y., Zierenberg, R., Miller, D., Normark, W., 2000. Proceedings of the Ocean Drilling Program, 169, Scientific Results.

Galley, A. G., M. D. Hannington, and I. R. Jonasson. "Volcanogenic massive sulphide deposits." *Mineral Deposits of Canada: A Synthesis of Major Deposit-Types, District Metallogeny, the Evolution of Geological Provinces, and Exploration Methods: Geological Association of Canada, Mineral Deposits Division, Special Publication 5* (2007): p. 141-161.

Glasby, G.P., Iizasa, K., Hannington, M., Kubota, H., and Notsu, K., 2008, Mineralogy and composition of Kuroko deposits from northeastern Honshu and their possible modern analogues from the Izu-Ogasawara (Bonin) Arc south of Japan: Implications for mode of formation: Ore Geology Reviews, v. 34, p. 547-560.

Goodfellow, W., and Blaise, B., 1988, Sulfide formation and hydrothermal alteration of hemipelagic sediment in Middle Valley, Northern Juan de Fuca Ridge. Canadian Mineralogist, v. 26, 675-696.

Hannington, M., Jamieson, J., Monecke, T., Petersen, S., 2010. Modern sea-floor massive sulfides and base metal resources: towards an estimate of global sea-floor massive sulfide potential. Society of Economic Geologists Special Publication 15, 111-141.

Hannington, M., Jamieson, J., Monecke, T., Petersen, S., Beaulieu, S., 2011. The abundance of seafloor massive sulfide deposits. Geology 39, 1155-1158.

Hannington, M., and Monecke, T., 2009, Global exploration models for polymetallic sulphides in the Area: An assessment of lease block selection under the Draft Regulations on Prospecting and Exploration for Polymetallic Sulphides: Marine Georesources and Geotechnology, v. 27, p. 132-159.

Hannington, M.D., Jonasson, I.R., Herzig, P.M., and Petersen, S., 1995, Physical and chemical processes of seafloor mineralization at mid-ocean ridges, *in* Humphris, S.E.,

Zierenberg, R.A., Mullineaux, L.S., Thomson, R.E., eds., Seafloor Hydrothermal Systems: Physical, Chemical, Biological and Geological Interactions: Geophysical Monograph 91, p. 115-157.

Hannington, M.D., Galley, A.G., Herzig, P.M., and Petersen, S., 1998, Comparison of the TAG Mound and stockwork complex with Cyprus-type massive sulfide deposits, *in* Herzig, P.M., Humphris, S.E., Miller, D.J., Zierenberg, R.A., eds., Proceedings of the Ocean Drilling Program, Scientific Results, v. 158: College Station, Texas, Ocean Drilling Program, p. 389-415.

Hannington, M.D., Petersen, S., Herzig, P.M., and Jonasson, I.R., 2004, A global database of seafloor hydrothermal systems, including a digital database of geochemical analyses of seafloor polymetallic sulfides: Geological Survey of Canada Open File 4598, 1 CD-ROM.

Hannington, M.D., de Ronde, C.E.J., and Petersen, S., 2005, Sea-floor tectonics and submarine hydrothermal systems, *in* Hedenquist, J.W., Thompson, J.F.H., Goldfarb, R.J., Richards, J.P., eds., Economic Geology One Hundredth Anniversary Volume, , p. 111-141.

Iizasa, K., Fiske, R.S., Ishizuka, O., Yuasa, M., Hashimoto, J., Ishibashi, J., Naka, J., Horii, Y., Fujiwara, Y., Imai, A., and Koyama, S., 1999, A Kuroko-type polymetallic sulfide deposit in a submarine silicic caldera: Science, v. 283, p. 975-977.

Ishibashi, J., and Urabe, T., 1995, Hydrothermal activity related to arc-backarc magmatism in the Western Pacific: in Taylor, B., ed., Backarc Basins: Tectonics and Magmatism: New York, Plenum Press, p. 451-495.

Kinsey, J.C., Tivey, M.A., and Yoerger, D.R., 2008, Toward high-spatial resolution gravity surveying of the mid-ocean ridges with autonomous underwater vehicles: Oceans 2008 Marine Technology Society/ Institute of Electrical and Electronics Engineers Conference, Quebec City, Canada, 15-18 September 2008, Proceedings, 10 p.

Kowalczyk, P., and Jackson, E., 2007, The role of subsea geophysical exploration for SMS deposits: Oceans 2007 Marine Technology Society/ Institute of Electrical and Electronics Engineers Conference, Vancouver, Canada, 29 September – 4 October 2007, ProceedingsVancouver, 4 p.

Lipton, I., 2008, Mineral resource estimate, Solwara 1 project, Bismarck Sea, Papua New Guinea: Canadian NI 43-101 Technical Report for Nautilus Minerals Inc., 277 p.

Lipton, I., 2012. Mineral Resource Estimate - Solwara Project, Bismarck Sea, PNG: Canadian NI 43-101 Technical Report for Nautilus Minerals Inc., 240 p.

Mosier, D.L., Singer, D.A., and Salem, B.B., 1983, Geologic and grade-tonnage information on volcanic-hosted copper-zinc-lead massive sulfide deposits: U.S. Geological Survey Open-File Report 83-89, 78 p.

Mosier, D.L., Singer, D.A., and Berger, V.I., 2007, Volcanogenic Massive Sulfide Deposit Density: U.S. Geological Survey Scientific Investigations Report 2007-5082, 15 p.

Mosier, D.L., Berger, V.I., and Singer, D.A., 2009, Volcanogenic Massive Sulfide Deposits of the World – Database and Grade and Tonnage Models: U.S. Geological Survey Open-File Report 2009-1034, 46 p.

Sangster, D.F., 1980, Quantitative characteristics of volcanogenic massive sulphide deposits: Metal content and size distribution of massive sulphide deposits in volcanic centres: Canadian Institute of Mining and Metallurgy Bulletin, v. 73, p. 74-81.

Singer, D.A., 1986, Descriptive model of Cyprus massive sulfide, *in* Cox, D.P., and Singer, D.A., eds., Mineral Deposit Models: U.S. Geological Survey Bulletin 1693, p. 131.

Singer, D.A., and Menzie, W.D., 2010, Quantitative Mineral Resource Assessments – An Integrated Approach: Oxford, Oxford University Press, , 232 p.

Tanimura, S., Date, J., Takahashi, T., and Ohmoto, H., 1983, Stratigraphy and structure of the Hokuroku district, *in* Ohmoto, H., and Skinner, B.J., eds., The Kuroko and Related Volcanogenic Massive Sulfide Deposits: Economic Geology Monograph 5, p. 24-39.

Tivey, M.A., and Johnson, H.P., 2002, Crustal magnetization reveals subsurface structure of Juan de Fuca Ridge hydrothermal vent fields: Geology, v. 30, p. 979-982.

Zierenberg, R.A., and Miller, D.J., 2000, Overview of Ocean Drilling Program Leg 169: Sedimented ridges II, *in* Zierenberg, R.A., Fouquet, Y., Miller, D.J., and Normark, W.R., eds., Proceedings of the Ocean Drilling Program, Scientific Results, v. 169: College Station, Texas, Ocean Drilling Program, p. 1-39.

Zierenberg, R.A., Fouquet, Y., Miller, D.J., Bahr, J.M., Baker, P.A., Bjerkgård, T.,Brunner, C.A., Duckworth, R.C., Gable, R., Gieskes, J., Goodfellow, W.D., Gröschel-Becker, H.M., Guèrin, G., Ishibashi, J., Iturrino, G., James, R.H., Lackschewitz, K.S., Marquez,

L.L., Nehlig, P., Peter, J.M., Rigsby, C.A., Schultheiss, P., Shanks, W.C., III, Simoneit, B.R.T., Summit, M., Teagle, D.A.H., Urbat, M., Zuffa, G.G., 1998, The deep structure of a sea-floor hydrothermal deposit: Nature, v. 392, p. 485-488.

Table 2.1: Estimated sizes (area) and average bulk chemical compositions of 95 seafloor sulfide deposits.

Location	Estimated Area (m^2)	(n)	Cu	Zn	Pb	Au	Ag
			wt.%			ppm	
Mid-Ocean Ridges:							
Juan de Fuca and Explorer							
S. Explorer Ridge	5,000	51	3.2	5.4	0.1	0.72	125
Endeavour Segment							
High Rise	3,000	49	1.9	9.6	0.2	0.28	63
Main Field	5,000	97	2.6	6.7	0.5	0.14	260
Clam Bed	<100	5	0.3	2.8	1.1	0.12	145
Mothra	5,000	20	3.3	14.9	0.5	0.05	105
Co-Axial	<100	6	-	23.2	-	0.98	59
Northern Cleft	<100	26	1.7	26.6	0.5	0.25	225
Southern Cleft	<100	16	1.1	30.9	0.1	0.11	230
East Pacific Rise							
21°N, EPR	<100	46	5.4	12.2	0.1	0.12	83
21°N, Green Seamount	300	6	2.6	0.2	<0.1	0.16	<1
14°N, EPR	<100	5	2.8	4.7	<0.1	0.51	48
13°N, EPR	5,000	71	6.4	11.1	0.1	0.45	61
13°N Seamount	30,000	13	2.4	4.3	0.03	0.80	32
11°30'N, EPR	<100	23	3.2	1.8	<0.1	0.25	23
11°32'N, EPR	<100	32	3.4	0.1	<0.1	0.13	4
11°N, EPR	<100	18	1.6	26.6	0.1	0.15	37
09°50'N, EPR	<100	29	7.9	6.3	<0.1	-	-
07°24'S, EPR	<100	14	11.1	2.1	<0.1	0.05	23
16°43'S, EPR	<100	19	10.2	8.5	<0.1	0.32	55
17°26'S, EPR	<100	-	1.3	5.6	<0.1	0.10	31
18°25'S, EPR	<100	35	4.7	18.6	0.1	0.58	170
21°30'S, EPR	<100	28	9.8	4.3	0.1	0.41	62
21°50'S, EPR	<100	-	2.4	21.7	0.1	0.36	120
37°40'S, SEPR	<100	24	3.8	3.1	<0.1	0.82	40
Galapagos Rift, 86°W	30,000	128	4.5	3.5	<0.1	0.29	35
Indian Ocean							
Sonne Field, CIR	50,000	35	13.1	3.0	<0.1	1.02	46
Kairei Field, CIR	3,000	8	20.4	10.3	<0.1	7.99	101
Edmond Field, CIR	3,000	17	6.5	10.7	<0.1	4.01	188
Mt. Jourdanne, SWIR	<100	9	1.9	16.7	1.2	4.29	630
Mid-Atlantic Ridge							
Broken Spur	5,000	76	4.9	3.7	<0.1	1.64	30
24°30'N, MAR		-	16.2	4.1	<0.1	5.30	-
TAG, surface and core	30,000	310	4.9	6.5	<0.1	1.80	92
Mir Zone	50,000	137	5.0	8.7	<0.1	4.20	115
Alvin Zone	100,000	7	2.0	0.3	<0.1	0.85	17
Snakepit	15,000	93	6.5	4.6	0.1	1.66	70
Krasnov Field	150,000	137	5.6	0.4	<0.1	1.11	22
Semyenov, 13°30'N	300,000	-	-	-	-	-	-
Turtle Pits, 5°S	5,000	43	7.0	2.3	<0.1	0.26	17

Nibelungen, 8°S	<100	9	17.3	16.2	0.1	8.95	37
Ridge-Hotspot Intersections:							
Lucky Strike	3,000	36	4.5	2.0	<0.1	0.08	35
Axial Volcano, CASM	<100	31	0.3	16.3	0.4	4.12	250
Axial Volcano, ASHES	<100	90	2.3	17.3	0.2	1.56	295
Uultramafic-hosted:							
Mid-Atlantic Ridge							
Rainbow	30,000	62	11.0	18.0	<0.1	2.53	189
Ashadze-1	50,000	104	10.5	16.3	<0.1	2.60	90
Ashadze-2	50,000	23	10.4	0.5	<0.1	8.50	6
Logatchev-1	5,000	78	23.4	3.9	<0.1	8.95	37
Logatchev-2	1,000	5	14.7	25.4	<0.1	23.80	92
Sedimented Ridges and Rifts:							
Middle Valley	50,000	100	1.1	2.8	0.03	0.16	7
Escanaba Trough	1,000	51	1.8	5.6	1.2	1.29	163
Guaymas Basin	15,000	22	0.4	2.2	0.4	0.15	82
Intraoceanic Back-Arc Basins:							
Mariana Trough							
Alice Springs, 18°N	1,000	16	1.2	10.0	7.4	0.78	185
Forecast, 13°N	300	13	0.8	6.7	0.5	22.90	355
Manus Basin							
Western Manus, Solwara 11		17	1.8	9.4	1.3	1.07	213
Central Manus, Solwara 3		31	1.1	21.3	1.4	15.15	642
Central Manus, Solwara 2		44	1.2	22.9	0.2	6.73	234
Central Manus, Solwara 10		13	7.1	7.5	0.1	2.31	152
North Fiji Basin	5,000	93	7.8	9.8	0.1	2.55	200
Lau Basin							
Northeast Lau, NELSC		17	4.5	4.1	<0.1	4.64	62
Fonualei Rift		29	2.1	14.5	0.3	-	-
MTJ Caldera		29	6.7	9.2	<0.1	20.47	183
Kings Triple Junction		78	5.6	28.2	0.1	-	17
Kilo Moana, ELSC		16	3.7	22.9	<0.1	4.16	68
Towcam, ELSC		9	4.9	35.4	0.3	4.44	121
ABE, ELSC		23	3.1	29.3	0.3	2.85	107
White Church, NVFR		66	3.6	12.0	0.4	2.60	86
Tui Malila, NVFR		22	1.4	18.7	0.6	4.87	94
Vai Lili, CVFR		96	5.4	26.6	0.2	3.02	113
Mariner, CVFR		14	10.8	17.8	0.2	3.11	172
Misiteli, SVFR		5	0.4	8.0	1.9	13.44	656
Hine Hina, SVFR		37	4.5	13.8	0.5	3.22	337
Volcanic Arcs:							
Izu-Bonin Arc							
Sunrise, Myojin Knoll	150,000	69	6.0	16.8	3.7	16.17	814
Kita Bayonnaise		3	4.7	17.3	0.4	9.13	162
Hakurei		24	1.0	37.2	3.1	6.00	692
Myojinsho Caldera		3	1.5	25.5	4.6	1.71	205
Suiyo Seamount	3,000	32	13.0	13.5	0.5	24.28	229
Kermadec Arc							
Brothers Seamount	5,000	37	0.9	13.2	1.9	0.5	340
Rumble II		1	9.8	0.1	<0.1	-	-
Transitional Arcs and Back-arc Basins:							
Manus Basin							
Solwara 1 (Surface only)	90,000	250	9.7	5.4	1.1	14.96	174
Solwara 4 (Pacmanus)	15,000	257	7.3	22.6	1.2	13.38	257

Solwara 5	30,000	30	5.4	8.3	1.6	16.06	277
Solwara 6	15,000	14	14.0	13.9	0.6	18.84	5702
Solwara 7	15,000	27	4.3	19.4	1.3	13.35	317
Solwara 8		43	9.0	23.3	1.6	14.37	240
Solwara 9		17	6.3	10.6	1.5	19.91	296
Solwara 12		10	7.0	22.6	3.5	13.69	425
Solwara 13		7	9.1	30.7	3.3	4.72	546
Franklin Seamount		34	<0.1	0.4	0.2	13.12	294
Tyrrhenian Sea							
Panarea Seamount		5	<0.1	6.2	2.8	-	11
Palinuro Seamount	3,000	15	0.4	17.9	8.6	3.40	270
Bransfield, Hook Ridge		9	2.6	11.8	1.3	0.35	191
Piip Volcano, Aleutians		10	1.2	-	0.1	-	-
Intracontinental Back-arc Rift:							
Okinawa Trough							
Izena Cauldron	5,000	40	3.3	20.2	11.8	3.13	2305
North Iheya Ridge		6	3.0	31.4	13.5	1.20	465
Minami Ensei Knolls		6	1.5	12.8	5.0	2.43	90
Yonaguni Knoll		8	4.7	17.0	9.8	-	-

Sources: Data compiled from Hannington et al. (2004 and 2005) and references therein. Area estimates are indicated only for those deposits for which published maps or other detailed descriptions are available in the literature (see Appendix A). Numbers represent cumulative area of exposed sulfide where multiple vent complexes or mounds are included as part of one deposit. All values are approximate only. Bulk compositions are for data reported in the literature (averages of n samples) and represent surface material only, except for the TAG mound.

Table 2.2. Grade and tonnage data for VMS and modern seafloor deposits based on reported non-zero grades (data are from Mosier et al., 2009, and this study).

VMS Classification (host rock)	(n)	75th Percentile	50th Percentile	25th Percentile
			Felsic-dominated	
Million Tonnes	421	0.7	3.0	11
ΣZn+Cu+Pb			6.3 wt.%	
Cu (wt.%)	412	0.7	1.3	2.2
Zn (wt.%)	350	2.1	4.0	6.6
Pb (wt.%)	273	0.5	1.0	2.2
Au (ppm)	280	0.4	1.0	2.0
Ag (ppm)	301	22	42	94
			Bimodal-Mafic	
Million Tonnes	272	0.5	1.9	7
ΣZn+Cu+Pb			4.0 wt.%	
Cu (wt.%)	267	0.9	1.4	2.1
Zn (wt.%)	217	1.2	2.3	4.6
Pb (wt.%)	77	0.1	0.3	1.0
Au (ppm)	158	0.4	1.0	2.0
Ag (ppm)	172	10	22	49
			Mafic-dominated	
Million Tonnes	174	0.1	0.7	5
ΣZn+Cu+Pb			2.8 wt.%	
Cu (wt.%)	174	1.1	1.7	2.8
Zn (wt.%)	58	0.4	1.1	2.5
Pb (wt.%)	13	<0.1	0.1	1.4
Au (ppm)	72	0.3	0.7	1.8
Ag (ppm)	70	7	12	31
			Seafloor massive sulfide†	
Million Tonnes	62	<0.01	0.07	0.7
ΣZn+Cu+Pb			15.0 wt.%	
Cu (wt.%)	93	1.7	4.3	7.0
Zn (wt.%)	93	4.3	10.6	18.6
Pb (wt.%)	63	<0.1	0.1	1.2
Au (ppm)	87	0.3	1.7	5.3
Ag (ppm)	88	37	107	234

†Estimates from this study. Tonnages are based on 62 deposits listed in Table 2.1. Median grades are based on surface samples from 95 deposits listed in Table 2.1.

Figure 2 . 1

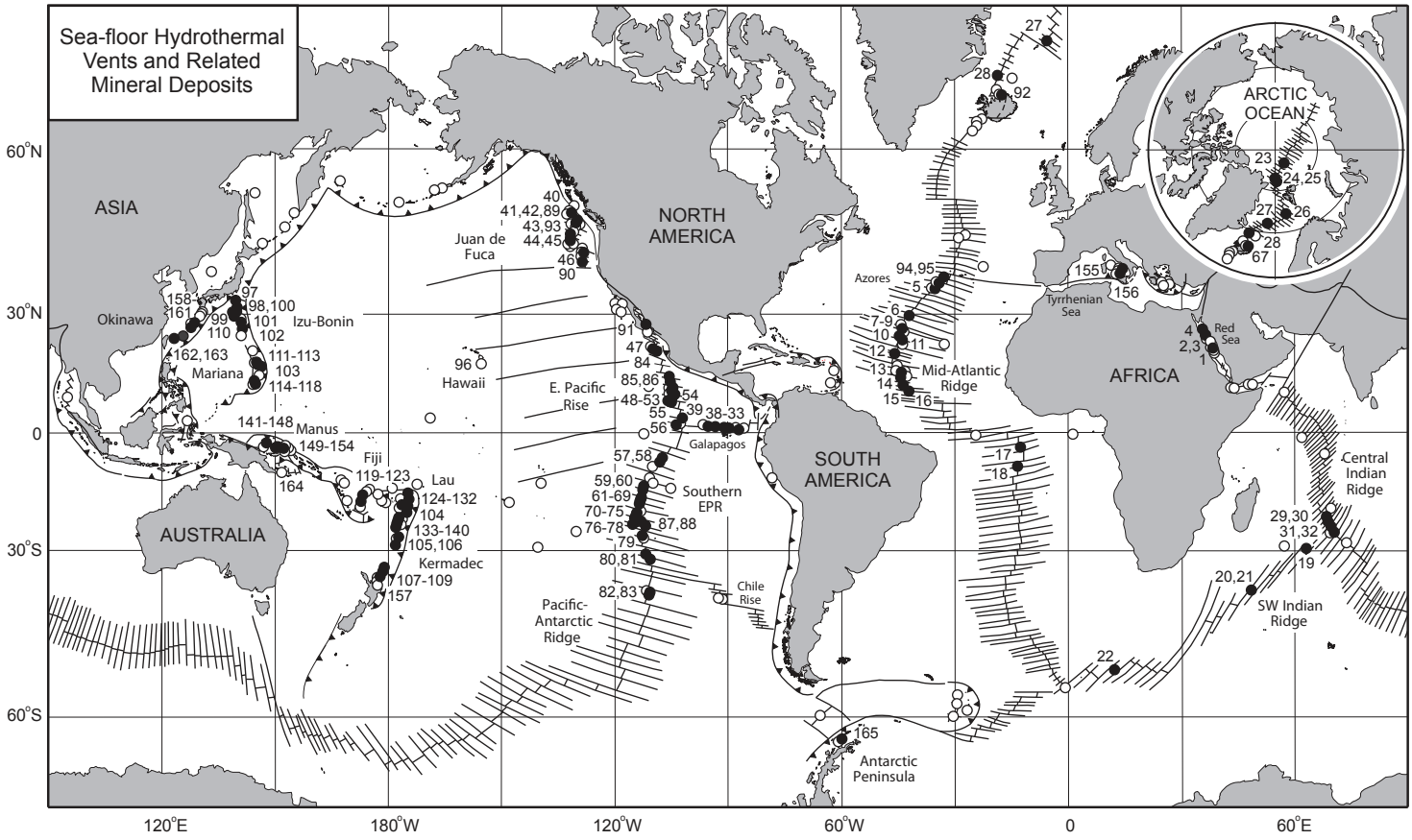

Figure 2.1: Locations of seafloor massive sulfide deposits and related hydrothermal vents (modified from Hannington et al., 2005). Numbers refer to high-temperature hydrothermal vents and related sulfide deposits (filled circles). Other low-temperature hydrothermal vents and related mineralization are indicated by open circles. Major spreading ridges and subduction zones are indicated. Note that the current database contains more than 200 discrete deposits; a number of clusters of deposits are indicated here by just one symbol (e.g., Bent Hill, ODP Mound, Area of Active Venting at Middle Valley, no. 89). See Appendix A for corresponding deposit names.

Figure 2 . 2

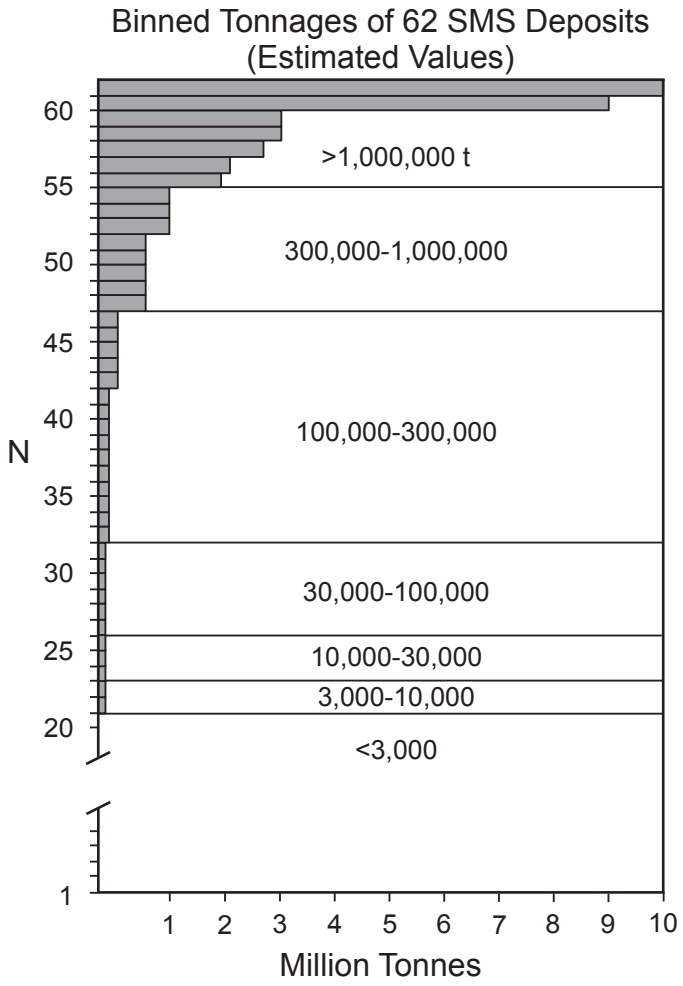

Figure 2.2: Binned tonnages for 62 seafloor sulfide deposits listed in Table 2.1. The size classes are estimated using the area versus tonnage relationship for the Solwara 1 deposit as a guide. Only those deposits having surface areas larger than 100 m^2 (~3,000 t) are included on the plot.

Figure 2.3

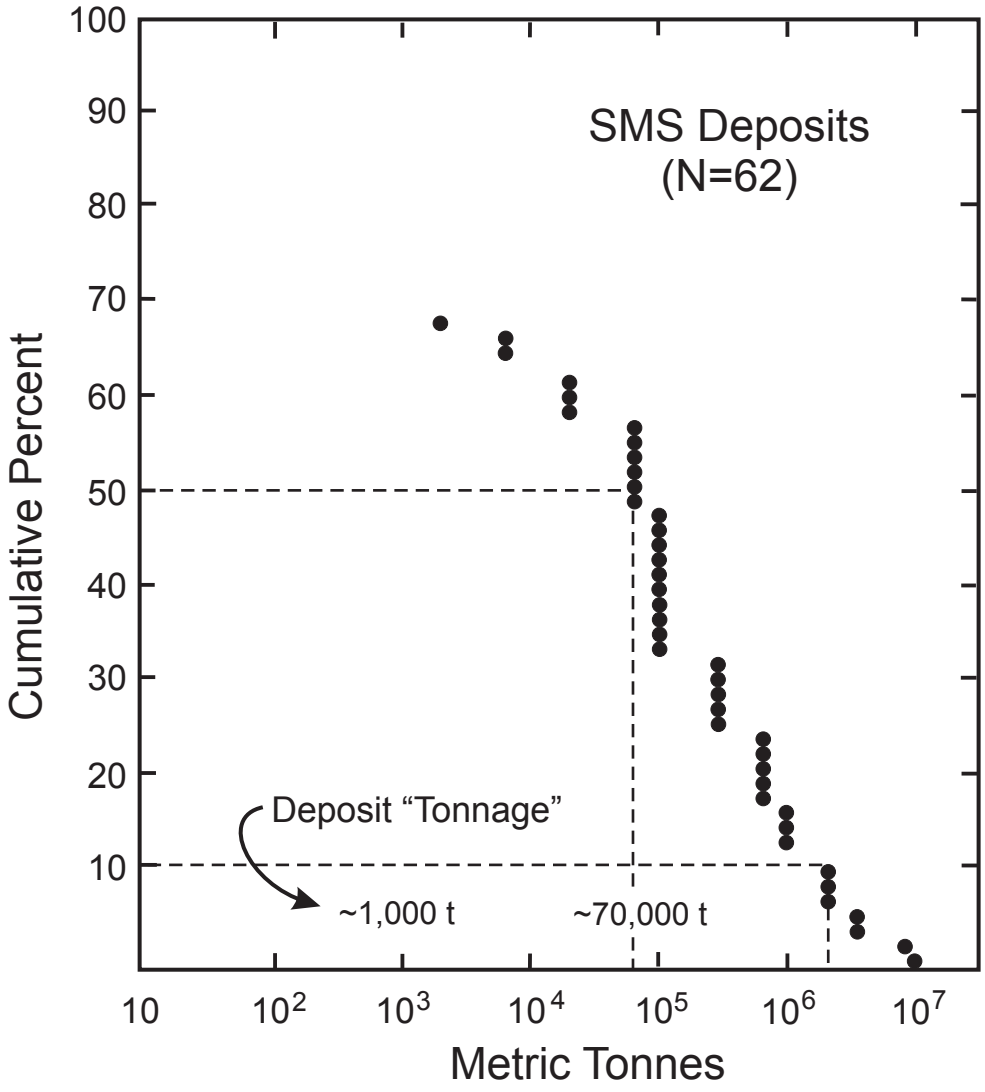

Figure 2.3: Cumulative frequency plot of binned tonnages for 62 seafloor sulfide deposits based on data listed in Table 2.1 and shown in Figure 2.2. The size classes are estimated using the area versus tonnage relationship for the Solwara 1 deposit as a guide and plotted at the endpoints of each bin. Only the first 42 deposits are shown, accounting for 67% of the population. All other deposits are estimated to be smaller than 100 m^2 in size (~3,000 t; Table 2.1). The plotted points define a general tonnage curve (log-normal distribution), and approximate intercepts for the 50th and 10th percentiles of the log-normal distribution are indicated. Based on this model, the median size of the sulfide deposits is ~70,000t. With additional exploration or more accurate data from drilling, certain deposits may move from one size class to another, but the general features of the tonnage curve are unlikely to change significantly.

Figure 2 . 4 (part 1)

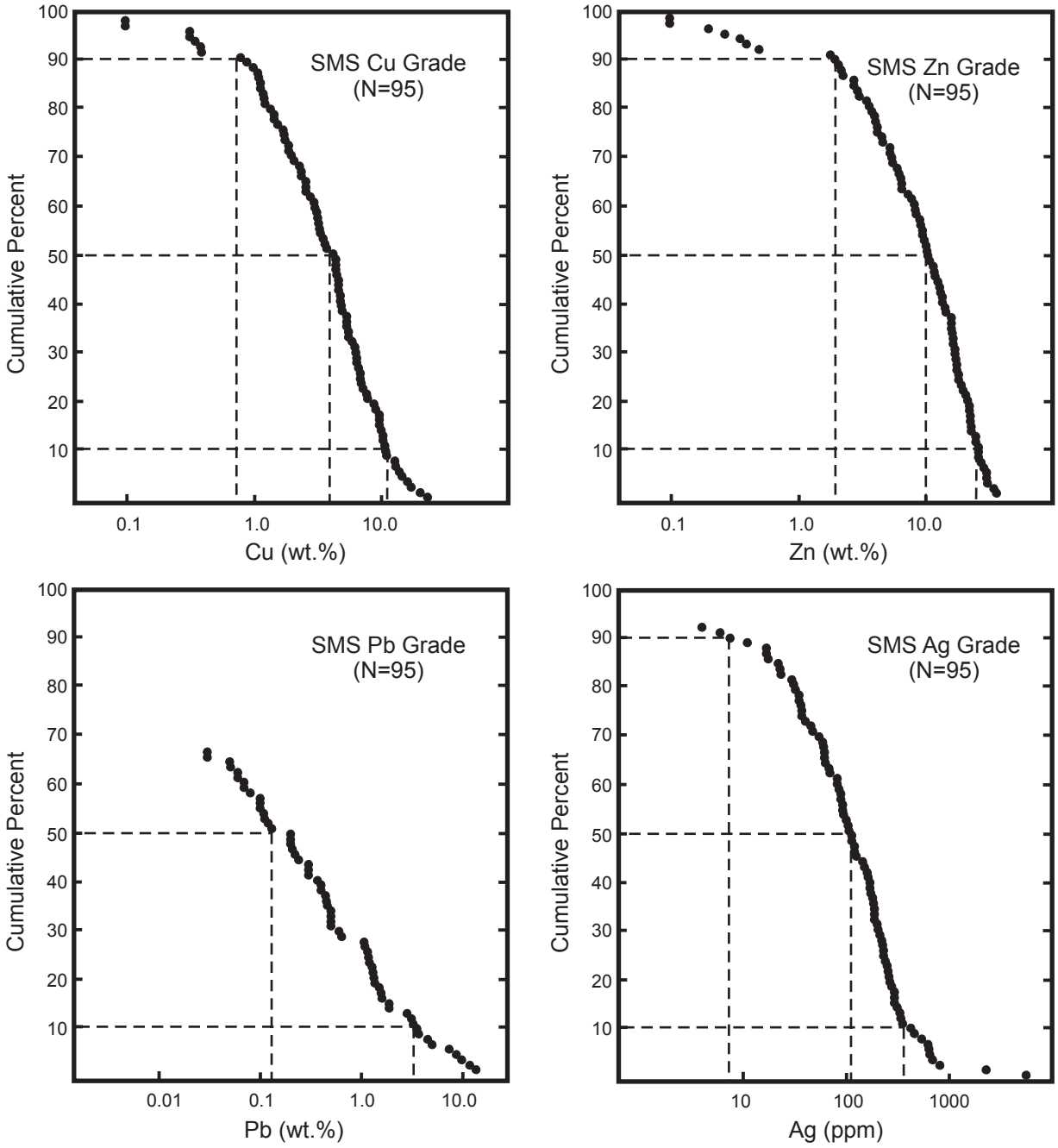

Figure 2.4: Cumulative frequency plots of Cu, Zn, Pb, Ag, and Au grades for seafloor sulfide deposits. The plotted data are based on averages of surface samples collected from 95 deposits listed in Table 2.1. The data define general grade curves (log-normal distribution), and intercepts for the 90th, 50th, and 10th percentiles of the log-normal distribution are indicated. The summary data are also listed in Table 2.2.

Figure 2 . 4 (part 2)

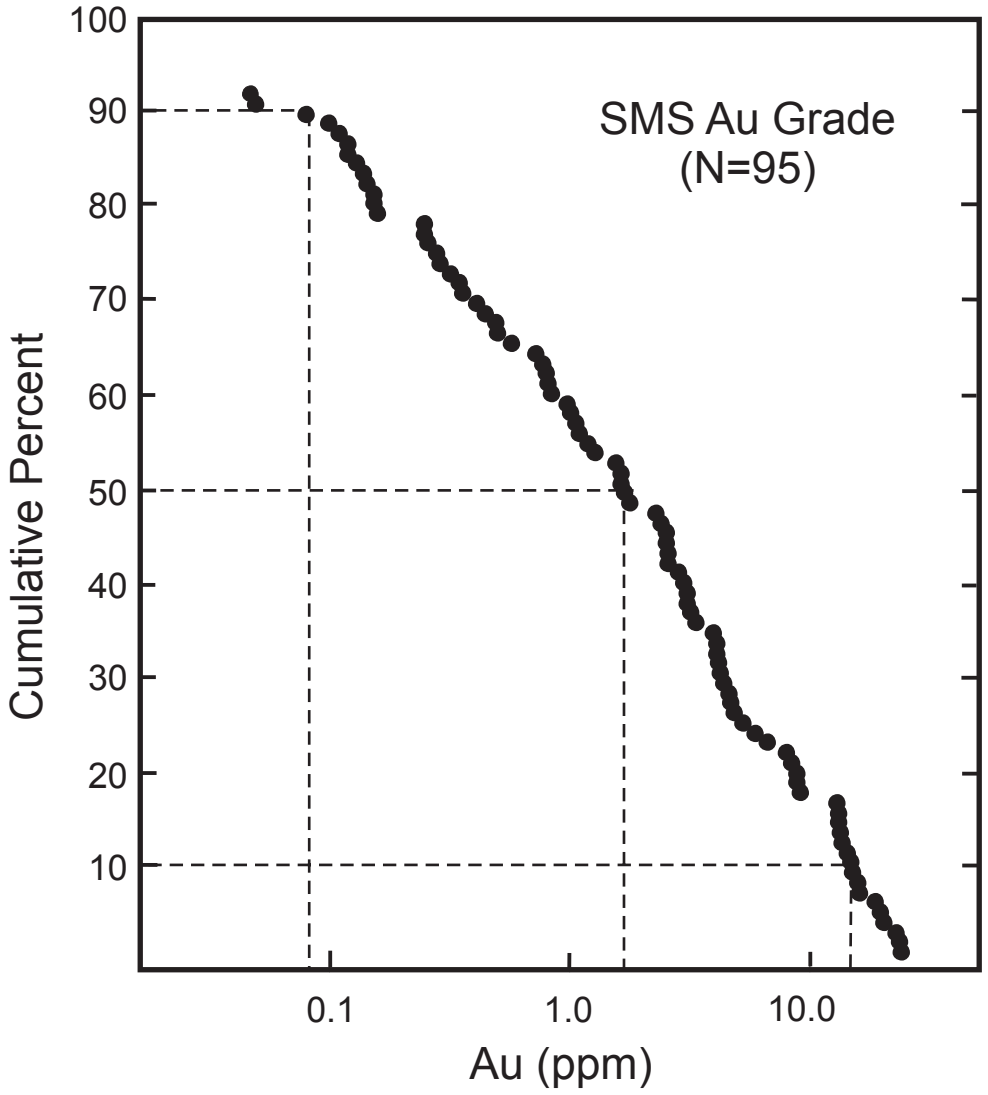

Figure 2 . 5

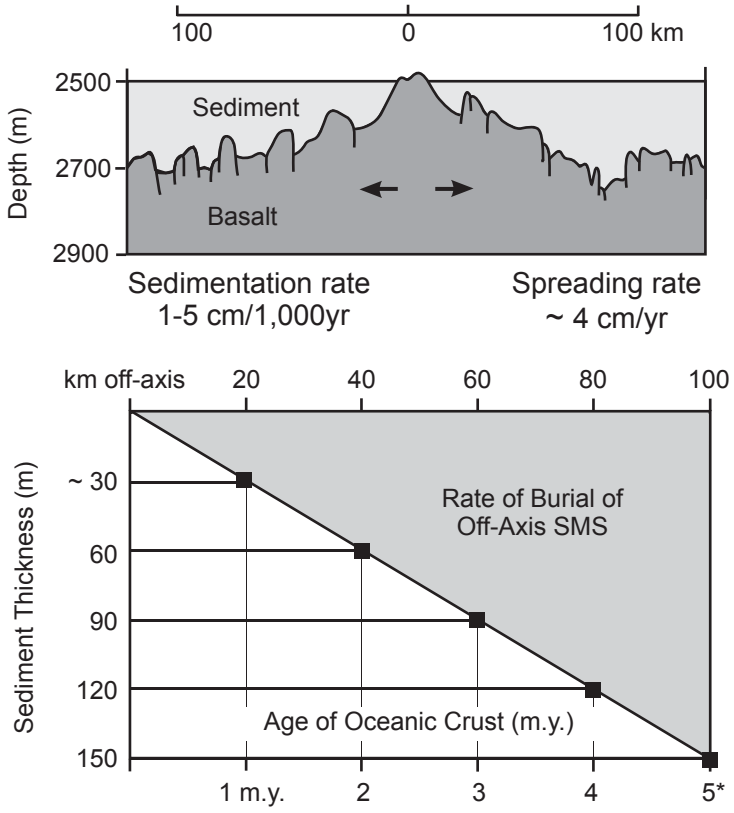

Figure 2.5: Seafloor sediment thickness as a function of distance from spreading axis (or age of crust). As oceanic crust migrates away from the spreading axis, sulfide deposits will be buried beneath 10m of sediment after ~ 1 million years, or within 40 km of the spreading axis.

Figure 2 . 6 (part 1)

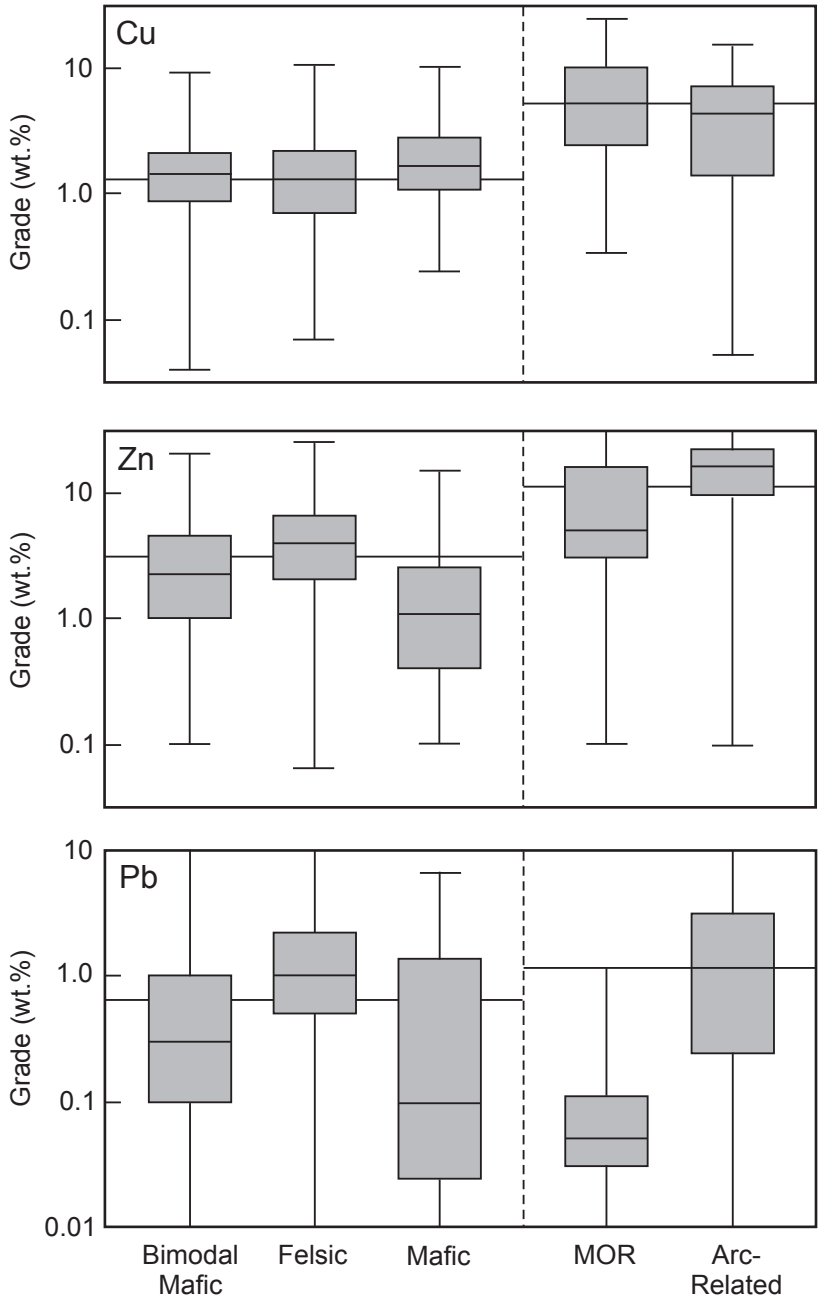

Figure 2.6: Base metal grades of land-based VMS deposits and seafloor sulfide deposits in mid-ocean ridge and supra-subduction settings. Grades are indicated for bimodal-mafic (n = 272), felsic-dominated (n = 421), and mafic-dominated (n = 174) VMS deposits from Mosier et al. (2009) (Table 2.2). Data for the mid-ocean ridge and supra-subduction deposits (n = 95) are listed in Table 1. Boxes are define the 25th and 75th quartiles and the median (center line). The horizontal line indicates the average values for all VMS and all modern seafloor deposits.

Figure 2 . 6 (part 2)

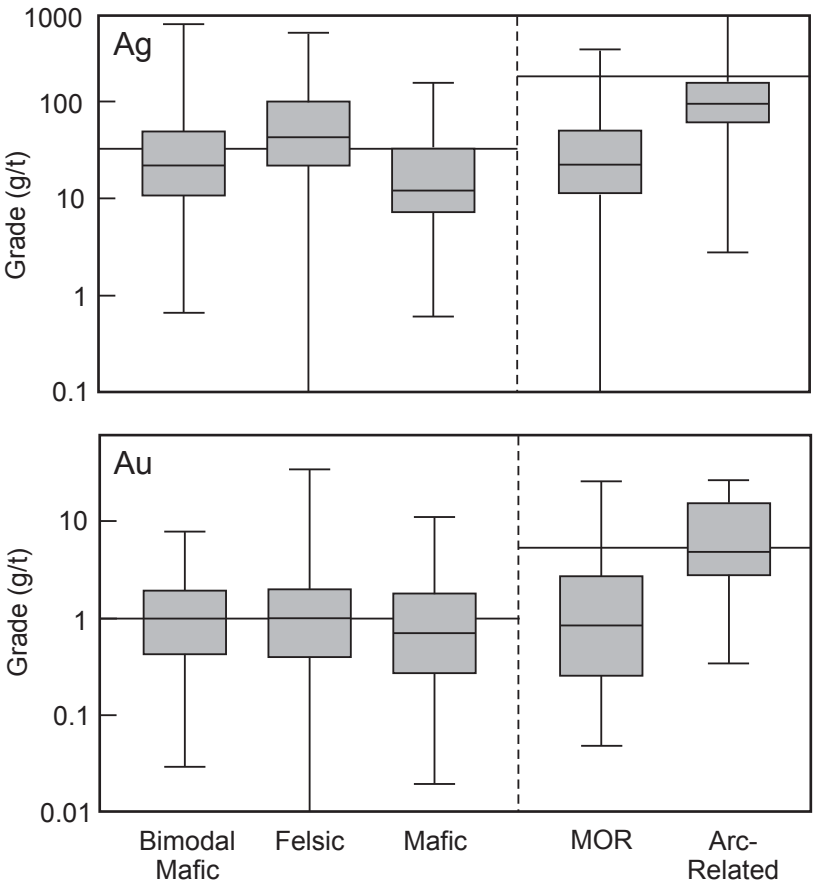

Figure 2 . 7 (part 1)

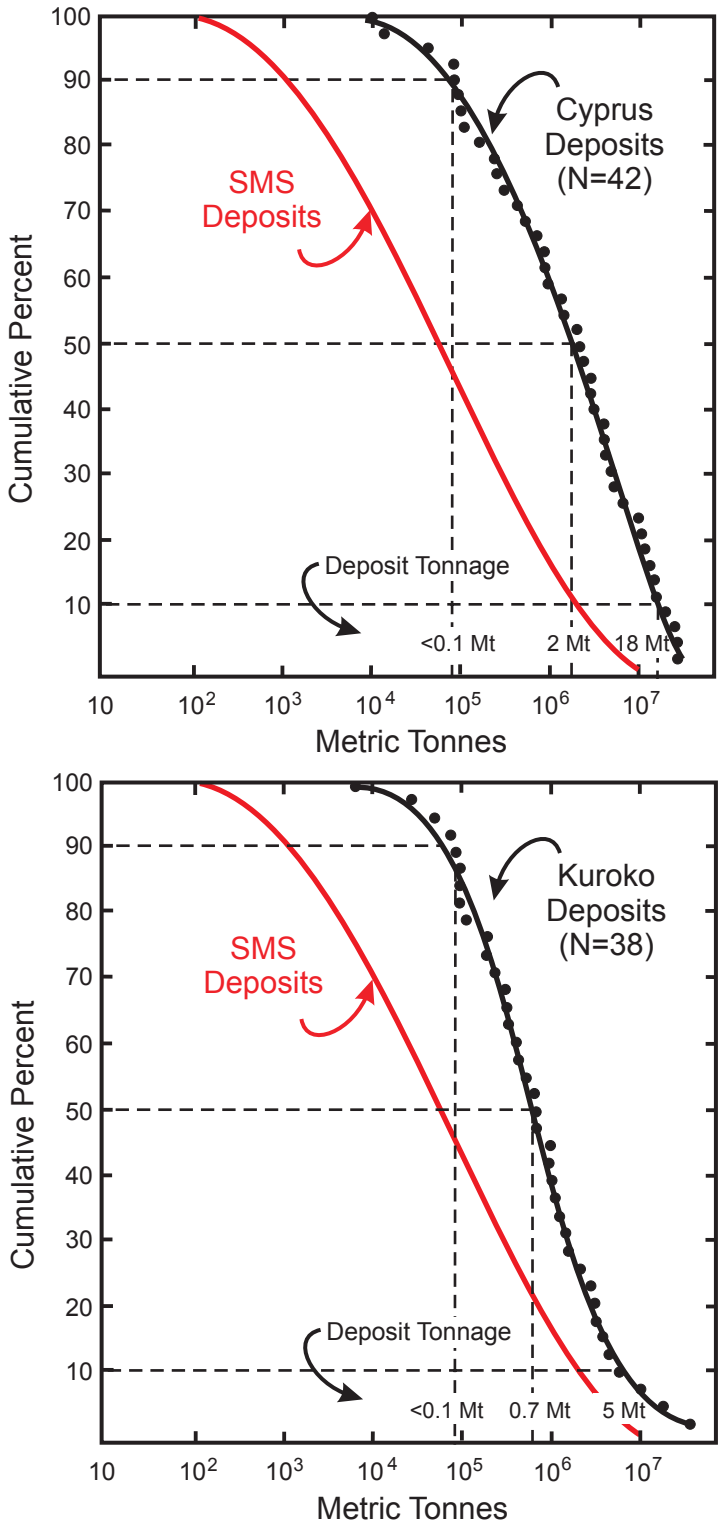

Figure 2.7: Comparison of the estimated tonnage curve for seafloor sulfide deposits with tonnages curves for selected VMS deposit types on land. The modern seafloor curve is based on binned data shown in Figure 2.3. The curve for VMS deposits in the Troodos ophiolite of Cyprus (n=42) is from data in Mosier et al. (1983) and Singer and Mosier (1986a). The curve for Kuroko deposits in the Hokuroku district of Japan is from data in Tanimura et al. (1983). The more recent compilation for mafic-hosted VMS deposits (n=174) from Mosier et al. (2009) is also shown. Intercepts for the 90th, 50th, and 10th percentiles of the log-normal distribution are indicated for the VMS deposits. The plotted data for VMS include only those deposits of sufficient size to have been mined economically. If undeveloped prospects are included, the curves for VMS deposits would shift toward significantly lower tonnages.

Figure 2 . 7 (part 2)

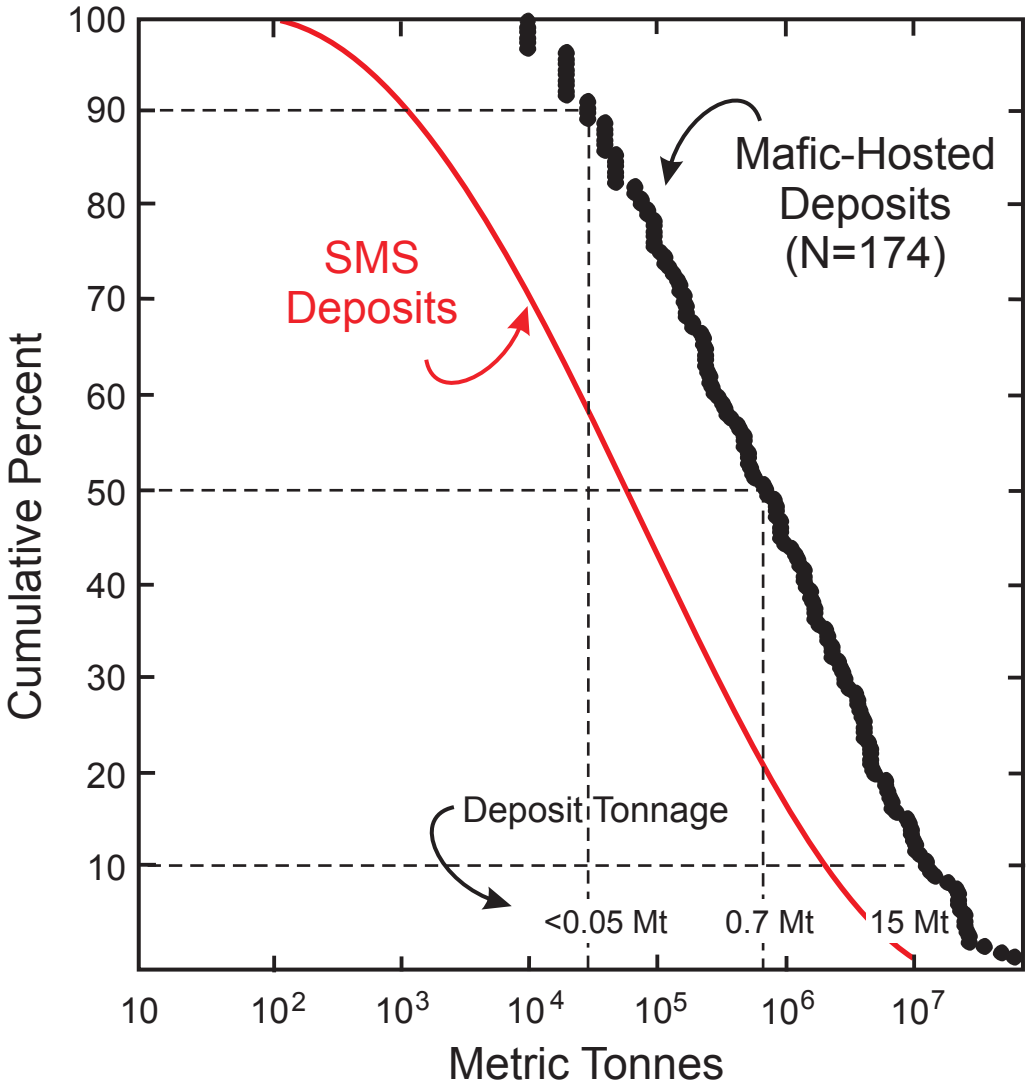

CHAPTER 3

PRECIPITATION OF BARITE IN HYDROTHERMAL VENTS ALONG THE ENDEAVOUR SEGMENT OF THE JUAN DE FUCA RIDGE

Abstract

Barite is a common mineral phase in hydrothermal vents along the Endeavour Segment of the Juan de Fuca Ridge. The precipitation of barite occurs when hot hydrothermal fluid, rich in dissolved Ba, mixes with cold, sulfate-rich seawater in the pore spaces within the walls of hydrothermal vent chimneys. However, the physical and chemical conditions under which barite precipitates in this region of fluid mixing remain poorly constrained. In this chapter, results of a study of the physical and chemical properties of barite crystals within vent chimneys from Endeavour are presented. Petrographic analyses of 22 barite-rich samples show a range of barite crystal morphologies, from dendritic and acicular, to blocky and euhedral. $^{87}Sr/^{86}Sr$ values of the barites indicate a clear mixing relationship between hydrothermal fluid and seawater during barite precipitation. Samples with dendritic or tapered acicular crystals tend to contain higher $^{87}Sr/^{86}Sr$ ratios, resulting from a greater component of seawater relative to hydrothermal fluid in the mineralizing fluid. A greater seawater component results in lower temperatures, and less Ba^{2+} availability during precipitation. Blocky and well-formed crystals formed from hotter fluid mixtures dominated by hydrothermal fluid resulting in a higher availability of Ba^{2+} ions. In all cases, the thermal conditions and Ba^{2+} ions supplied by the hydrothermal fluid indicate that barite precipitation in the chimney walls occurs only when the chimney is actively venting a high-temperature vent fluid.

1. Introduction

The formation of hydrothermal sulfide-sulfate-silica chimneys and mounds on the seafloor is the result of physical and chemical interactions between hot, discharging hydrothermal fluid and cold ambient seawater (Hannington et al., 1995). The chemical constituents that form the precipitating minerals are derived from either the hydrothermal fluid (e.g., base metals, S^{2-}, Ba^{2+}, SiO_2) or the local seawater (SO_4^{2-}, Ca^{2+}, Mg^{2+}) (Hannington et al., 2005; Tivey et al., 1999; Von Damm, 1990). The dissolved constituents in hydrothermal fluid are mostly leached from the underlying oceanic crust and thus the composition of the underlying crust is a primary control on hydrothermal fluid composition and the composition of hydrothermal deposits on the seafloor. Variations in mineralogy and chemistry between vents within a single vent field can result from differing degrees of cooling and mixing below the seafloor and within the chimneys/mounds due to the complex plumbing systems associated with fluid flow in hydrothermal systems (Hannington and Scott, 1988).

With the exception of anhydrite, which has retrograde solubility, the precipitation of minerals occurs primarily as a result of the decrease in fluid temperature upon the mixing of hot (350 to 400°C) ascending hydrothermal fluid with cold (~2°C) seawater. The temperature-dependence of solubility for different minerals results in hydrothermal chimneys that commonly have a distinct mineral zonation with high-temperature minerals (e.g., chalcopyrite, pyrite, wurtzite) precipitating primarily along inner fluid conduits. The porous outer chimney walls contain lower-temperature minerals (e.g., sphalerite, barite, amorphous silica) that precipitate as a result of a higher degree of mixing with cold seawater, and/or conductive cooling of the hydrothermal fluid (Tivey et al., 1999). The lower temperature at which barite precipitates, relative to most other mineral phases within the chimneys (with the

exception of amorphous silica), results in barite generally forming early and late in the evolution of a chimney, when fluid temperatures are generally lower (Hannington et al., 2005). At the peak venting temperatures (e.g. >300ºC), barite precipitation is restricted to the outer walls of the chimneys, where temperatures are lower from the greater influence of cold seawater.

For some minerals (e.g., pyrite), their respective chemical components (Fe^{2+} and S^{2-}) are derived primarily from the hydrothermal fluid. Anhydrite, on the other hand, forms largely from the heating of local seawater at the hydrothermal discharge site, and its respective chemical components (Ca^{2+} and SO_4^{2-}) are sourced directly from seawater, not the hydrothermal fluid. Barite, a common hydrothermal sulfate mineral in many seafloor tectonic settings, precipitates when Ba^{2+}-rich hydrothermal fluid mixes with SO_4^{2-}-rich seawater at temperatures of between 100 and 300°C (Hannington et al., 1991). The requirement for interaction between hydrothermal fluid and seawater in order for barite to precipitate can therefore provide a record of fluid mixing within a hydrothermal chimney.

Strontium is a common trace-element substitution in hydrothermal barite. Both seawater and hydrothermal fluid at Endeavour have very different, yet distinct Sr-isotope ($^{87}Sr/^{86}Sr$) ratios. These ratios can be compared to the ratios measured in barite crystals, in order to determine the relative proportion of seawater- and hydrothermally-derived Sr in the barite, and by extension, the relative amounts of seawater and hydrothermal fluid that make up the fluid mixture from which barite precipitated. The Sr-isotope composition of anhydrite precipitated at hydrothermal vents has been extensively investigated (e.g. Mills et al., 1998; Teagle et al., 1998), however there are few reports of similar studies for hydrothermal barite

(Hannington and Scott, 1988). Barite is also the primary host in hydrothermal deposits for Ra, a common trace element in seafloor hydrothermal systems. Like Sr, Ra has similar geochemical properties (ionic radius and charge) to Ba and commonly substitutes for Ba in the barite lattice. The decay of Ra-266 (half-life of 1,600 years) substituted in barite can be used to determine the age of crystallization of barite within a hydrothermal deposit (see Chapter 4).

The primary objective of this study is to investigate the physical and chemical conditions under which barite precipitates within walls of hydrothermal vents from the Endeavour Segment of the Juan de Fuca Ridge. In particular, this study focuses on what can be inferred about chimney growth based on the morphology of barite crystals, as well as the relationship between barite crystallization and fluid mixing. These questions are addressed by: 1) a detailed investigation of the morphology of barite crystals within chimney samples, and the petrogenetic relationships between barite and other mineral phases within the chimneys; 2) an investigation of the geochemical controls on Sr distribution in the Endeavour chimneys; and 3) the use of $^{87}Sr/^{86}Sr$ isotope ratios within barite to determine the amount of fluid mixing that occurs at the sites of barite precipitation, and how this relates to barite crystal morphology.

2. The Endeavour Segment

The Endeavour Segment is the second northernmost spreading segment of the Juan de Fuca Ridge, located approximately 300 km off the coast of Vancouver Island (Fig. 3.1). The segment is bound to the south by the Cobb Offset and the Cobb overlapping spreading center

(OSC) and to the north by the Endeavour Offset and the Endeavour OSC. The Cobb Offset represents a major geochemical division in the Juan de Fuca Ridge, with normal mid-ocean ridge basalt (N-MORB) dominating the oceanic crust south of the offset and enriched-MORB (E-MORB) dominating oceanic crust north of the offset (Karsten et al., 1990). The occurrence of E-MORB at Endeavour has been attributed to a heterogeneous mantle source of both enriched and depleted upper mantle with the enriched component of the mantle source exhibits enhanced melting relative to the depleted mantle source (Cousens et al., 1995).

The Endeavour Segment is 90 km long, ranging in depth from 2050 meters below sea level (mbsl) at a central bathymetric high to >2700 mbsl towards the south (Fig. 3.2) (Delaney et al., 1992). Active hydrothermal venting is focused within a 15 km-long central axial valley (Kelley et al., 2012). This central valley widens to several kilometers in the south from ~500 m at its narrowest in the central portion of the segment. Within the axial valley are five major hydrothermal vent fields (Sasquatch, Salty Dawg, High Rise, Main Endeavour Field, Mothra), two smaller vent fields (Raven, Stockwork), and four diffusely venting areas (Cirque, Dune, Clam Bed, Quebec), making the Endeavour Segment one of the most active hydrothermal areas on the mid-ocean ridge system (Kelley et al., 2012). The five main vent fields are approximately 2 km apart and host multiple sulfide edifices. Hydrothermal fluids reaching temperatures of up to 400°C circulate through 100 to 150 black smokers in the main vent fields (Hannington et al., 2005). The sulfide edifices at Endeavour are typically steep-sided, commonly reaching heights of greater than 20 metres above the seafloor (Delaney et al., 1992; Glickson et al., 2006; Kelley et al., 2012; Robigou et al., 1993).

Both focused and diffuse venting occur within the active vent fields, resulting in a range of measured venting temperatures between from <10°C up to ~400°C (Butterfield et al., 1994). The hydrothermal fluids circulating at Endeavour are enriched in ammonia and have higher pH values (~4.4) than a typical sediment-free mid-ocean ridge (Kristall et al., 2006). The hydrothermal edifices also contain a relatively high abundance of barite, compared to other mid-ocean ridge hydrothermal deposits (Hannington et al., 1995). The presence of E-MORB and/or buried sediments have been suggested as possible sources for the high barium content (Hannington et al., 1995; Proskurowski et al., 2004).

3. Methods

3.1 Sampling

Exploration of the Endeavour Segment is carried out from research vessels operating out of the northwest United States or Canada. The manned submersible *ALVIN* and remote-operated vehicles (ROVs) *JASON* and *ROPOS* were used for observing the vent fields and collecting fluid, biological and rock samples (Delaney et al., 1992; Glickson et al., 2006; Glickson et al., 2007; Kelley et al., 2001; Kristall et al., 2006; Robigou et al., 1993). Dredging was also used to collect some rock samples (Tivey and Delaney, 1986). Once brought to the surface, rock samples were rinsed in fresh water and left to dry. In some cases, samples were further dried in a 40°C oven for several days, due to their very high porosity (up to 70%). A dedicated sampling program in 2008/2009 (with *ALVIN*) and in 2011 (with the ROV *Doc Ricketts*) focused on the collection of barite-rich samples from inactive sulfide edifices within the active vent fields as well as extinct sites outside of the active vent fields.

3.2 Geochemistry

Whole rock, multi-element geochemical data was comes from Hannington (2004). These data include major and trace elements. Elemental abundances were determined using Inductively Coupled Plasma Emission Spectroscopy (ICP-ES), Inductively Coupled Plasma Mass Spectroscopy (ICP-MS), and Instrumental Neutron Activation Analysis (INAA).

3.3 Petrographic Analysis

Twenty-two samples were selected for thin section examination based on high barite abundance (Williamson, 2010). Barite content was estimated from the concentration of Ba in the collected samples, which ranged from trace up to 33 wt.% Ba. Thin sections were prepared at the University of Ottawa by first impregnating them in epoxy, due to their fragile nature, before cutting and polishing each sample. The sections were examined using an Olympus BX 51 polarizing microscope with an attached Olympus DP71 digital camera. Sections were observed under both transmitted and reflected light modes, in order to observe both the mineral phases that transmit light (sulfates and amorphous silica) and the opaque minerals (sulfides). Both modes were sometimes used synchronously, in order to observe the relationships between all phases in a section.

3.4 Electron Microprobe Analysis

Concentrations of Sr, Ba, Ca and SO_4 within individual barite crystals were determined by electron microprobe analysis (Allen, 2011). Barites from seven carbon-coated thin-sections were analyzed using the automated Cameca Camebax MBX electron microprobe at Carleton University, equipped with 4 WDX X-ray spectrometers. Samples were analyzed using both

energy-dispersive and wavelength-dispersive analytical modes, with an accelerating voltage of 15 keV and a 20nA beam current. Samples were selected in order to maximize the variability in sample bulk Sr/Ba ratios and barite crystal morphology.

3.5 Sr-Isotope Composition of Barite

The strontium isotope ($^{87}Sr/^{86}Sr$) composition of 16 samples was determined using thermal ionization mass spectrometry (TIMS) at Carleton University, Ottawa (Engelbert, 2012). For each analysis, approximately 50 mg of crushed sample was leached in ~2 mL of 7M HNO_3 on a 100°C hot plate in order to dissolve the sulfide minerals. This process was repeated three times in order to ensure complete dissolution of sulfides. The remaining barite crystals were immersed in 6M HCl and left covered on a 100°C hot plate for three days. The solution was then removed by pipette and the samples were left to dry down overnight. Finally, approximately 1.5 mL of 2.5M HCl was added to each beaker and the samples were left covered for two days. The solutions containing the dissolved barite were run through Sr resin columns to isolate the Sr. The resulting samples were analyzed using a ThermoFinnigan TRITON thermal ionization multicollector mass spectrometer. Samples underwent ~100 analyses at 1200-1406°C with a baseline measurement taken after every 10 analyses.

4. Results

4.1 Geochemistry

Select major and trace element concentrations for hydrothermal sulfide samples from Endeavour were determined in order to investigate the mineralogical and geochemical

relationships between barite and the other primary mineral phases in the samples (pyrite/marcasite, chalcopyrite, sphalerite/wurtzite, anhydrite and amorphous silica). Full results are listed in Appendix B. Elemental abundances are directly linked to the mineralogy of each sample (e.g., sphalerite-rich samples have a high concentration of Zn). Barite content ranges from below detection to 39.0 wt.%. Ba content correlates strongly with Sr and, to a lesser extent, SiO_2 (Fig. 3.3). There is a strong negative correlation between Ba and both Fe and reduced-S.

Strontium content ranges from below detection (10 ppm) to 1.3 wt.% in a sample ALV2116-R3-H1, which also contains 24.5 wt.% SiO_2. Besides the strong correlation with Ba, Sr also correlates with SiO_2 and CaO content, although to a much lesser degree (Fig. 3.3). Strontium also has a negative correlation with Fe and S.

4.2 Petrographic Analysis

A summary of the main petrographic features for 22 thin sections from hydrothermal samples from the Endeavour Segment is provided in Table 3.1. Full descriptions for each section can be found in Appendix D.

Barite typically grows into open pore spaces, precipitating on pre-existing sulfide minerals. Amorphous silica is the only phase that typically precipitates on pre-existing barite crystals although sulfide overgrowth of relict barite crystals can occur. The barite crystals exhibit a wide range of morphologies that vary from blocky to acicular to dendritic. The majority of thin sections contained two or more morphologies. However, samples can be grouped into four broad morphological categories defined by the dominant morphologies present: 1) well-

formed, blocky crystals; 2) acicular and/or radiating blocky crystals; 3) acicular and/or radiating tapered crystals; and 4) dendritic crystals (Fig. 3.4) (Williamson, 2010). Barite crystal vary in size from <0.1mm up to 2mm. The larger crystals tend to have a blocky or transitional blocky-acicular morphology, but large dendritic fans can also occur, although they are less common.

4.3 Sr-Concentrations within Barite Crystals

Results of exploratory electron microprobe analysis of barite crystals from Endeavour hydrothermal vents indicated that Sr and Ca were the major trace elements within barite (Allen, 2011). Results from spot analyses of barite crystals were thus normalized to total Ba + Sr + Ca content (Table 3.2; full results summarized in Appendix 3C). Strontium contents within barite crystals range from 3.1 to 10 wt.% Sr. Many barite crystals showed distinct zonation in the backscatter images with darker zones having a lower Sr-content than the brighter zones (Fig. 3.5). Sr-content within a single crystal can vary by up to 15 wt. % (c.f. ALV-2068-1, Appendix 3C). Calcium content can range up to 11 wt.% but are generally very low.

4.4 Sr-Isotope Ratios in Barite

Strontium-isotope ($^{87}Sr/^{86}Sr$) ratios for 16 hydrothermal samples are reported in Table 3.3 with ratios ranging from 0.703798 to 0.707581 (Fig. 3.6) (Engelbert, 2012). All ratios fall between and that of the average ratio for Endeavour vent fluids (0.7033) and seawater (0.709183) (Butterfield et al., 2001).

5. Discussion

5.1 Mineralogical controls on Sr distribution

A correlation plot illustrates the main relationships between the major elements and select trace elements in Endeavour vent chimneys (Fig. 3.3). These elements can be divided into those that are associated with high-temperature and low-temperature minerals. The high-temperature mineral assemblage is dominated by chalcopyrite, pyrite and pyrrhotite, resulting in positive correlations between Cu, Fe and S. Lower-temperature minerals (sphalerite, barite and amorphous silica) result in positive correlations between elements such as Ba and SiO_2. The high- and low-temperature mineral assemblages also result in negative correlations between elements such as Ba with Fe or SiO_2 with S.

With Sr concentrations in barite ranging from 3.1 to 10 wt.%, and a strong correlation between Sr and Ba of 0.80, barite is likely the primary host for Sr in the chimneys at Endeavour. Positive correlations between Sr with SiO_2 (0.284) and Ca (0.216) indicate that amorphous silica and anhydrite may also contain significant amounts of Sr. However, a strong correlation between Ba and SiO_2 suggests that the positive correlation between Sr and SiO_2 is more likely a result of a close mineralogical association between barite and silica. A scatterplot of Ba vs. Sr indicates two trends: a positive linear trend, and a grouping of samples with almost no Ba that sit on the x-axis (Fig. 3.7A). The linear trend showing the strong correlation between Ba and Sr is interpreted to represent Sr substitution in barite. A similar plot of CaO versus Sr shows a similar trend (Fig. 3.7B). However, in this plot the samples that plotted along the x-axis in (A) now form a positive linear trend, and the samples that formed the linear trend in (A) now plot along the x-axis. The Ca-rich samples in (B) represent anhydrite which is also a host for Sr. The much higher concentrations of Sr in the

Ba-rich samples, relative to the Ca-rich samples, as well as the high correlation coefficient for Sr-Ba indicate that anhydrite is a secondary host of Sr in the hydrothermal vents, and the occurrence of barite is the dominant control on Sr distribution. Because of the strong association of Sr with barite, whole-rock Sr concentrations and $^{87}Sr/^{86}Sr$ values can be used to provide insights into the conditions under which barite precipitates in hydrothermal vents at Endeavour.

5.2 Hydrothermal Fluid – Seawater Mixing during Barite Precipitation

Barite precipitation requires the mixing of hydrothermal fluid (primary source of Ba^{2+}) and seawater (source of SO_4^{2-}). The mixing of cold (~2°C) seawater with hot (~350°C) hydrothermal fluid also reduces the temperature of the mineralizing fluid to a level at which barite will be saturated in the fluid and precipitate (100 – 300°C) (Blount, 1977; Hannington et al., 1991).

Using a two component mixing model (equation 1) with endmember $^{87}Sr/^{86}Sr$ values for seawater and Endeavour hydrothermal fluid (Table 3.4), the $^{87}Sr/^{86}Sr$ values of barites from hydrothermal vents can be used to determine the amount of mixing that occurred during barite precipitation (Table 3.3 and Fig. 3.8) (Mills et al., 1998). Average endmember $^{87}Sr/^{86}Sr$ values for Endeavour are 0.7033 (Butterfield, pers. comm). Reported $^{87}Sr/^{86}Sr$ values for hydrothermal fluids from the eastern and western Pacific, as well as the Mid-Atlantic Ridge range from 0.7028 to 0.7047 (Bach and Humphris, 1999). This mixing model accounts for the different concentrations of Sr in the two endmember fluids (Table 3.4). The results indicate that barite at Endeavour precipitates under a range of degrees of mixing, from a minimum of 19% hydrothermal fluid to a maximum of 87% hydrothermal fluid.

$$\%\,HF = 100 \times \frac{[Sr]_{SW}\left[\left({}^{87}Sr/{}^{86}Sr\right)_{SW} - \left({}^{87}Sr/{}^{86}Sr\right)_{BA}\right]}{[Sr]_{SW}\left[\left({}^{87}Sr/{}^{86}Sr\right)_{SW} - \left({}^{87}Sr/{}^{86}Sr\right)_{BA}\right] + [Sr]_{HF}\left[\left({}^{87}Sr/{}^{86}Sr\right)_{BA} - \left({}^{87}Sr/{}^{86}Sr\right)_{HF}\right]} \quad (1)$$

Where:

SW = Seawater

HF = Hydrothermal Fluid

BA = barite

The stoichiometric relationship between Ba^{2+} and SO_4^{2-} in barite is such that, ignoring trace substitutions, equal molar amounts of each constituent are consumed from the mineralizing fluid during crystallization. Using the fluid parameters outlined in Table 3.4 and the mixing model defined by equation 1, equal moles of Ba^{2+} and SO_4^{2-} in a mineralizing fluid would require a 98.9% hydrothermal fluid component and 1.1% seawater, due to the much higher sulfate concentrations in seawater, relative to the hydrothermal fluids at Endeavour. The $^{87}Sr/^{86}Sr$ values of all analyzed barites indicate that a much smaller component of hydrothermal fluid was present during crystallization. This would result in an excess of sulfate present during crystallization, and Ba^{2+} would be the limiting reactant.

The source of the strong Sr/Ba zonations within individual barite crystals remains unclear. The nearly identical concentrations of Sr in seawater and average Endeavour vent fluids (Table 3.4) make it difficult to determine if the variations in Sr content are a result of

changing degrees of fluid mixing as the crystals grow, or if there is a temperature control on Sr partitioning during crystal growth.

5.3 Temperature of Barite Crystallization

A linear relationship between mixing and endmember fluid temperatures is used to estimate the temperature at which barite precipitated (Table 3.3 and Fig. 3.8). From this relationship, the analyzed barites precipitated at temperatures that range between 70 and 306°C. With the exception of the lowest and two highest recorded temperatures, all of the analyzed barites precipitated within the 100 to 300 °C temperature range that barite is predicted to precipitate at under seafloor hydrothermal venting conditions (Blount, 1977; Hannington et al., 1995).

While seawater-hydrothermal fluid mixing accounts for a significant amount of heat exchange in hydrothermal vent systems, conductive heating and cooling is also an important mechanism for changing the temperature of fluids. Conductive heating and cooling commonly occur in the porous walls of a hydrothermal vent due to high thermal gradients. These gradients can result in mineral precipitation of phases such as amorphous silica, a common late stage phase in chimney walls, that would otherwise not precipitate from mixing-induced cooling because seawater would dilute the SiO_2 content of the hydrothermal fluid to the point where saturation would not be reached (Tivey and Delaney, 1986). The common association of amorphous silica coating barite in the walls of vent chimneys along the Endeavour Segment suggests that conductive cooling occurs during the lower temperature, waning stages of a chimney's growth (Hannington et al., 1995). The two samples with the highest calculated component of hydrothermal fluid, ALV2467-R2 and -R9, both contain very high concentrations of SiO_2 (25.24 and 30.59 wt.%, respectively). The

estimated temperatures of barite precipitation for these samples (306 and 301°C, respectively) are slightly above the upper limit of 300°C for barite precipitation (Hannington and Scott, 1988), suggesting that some conductive cooling of the fluids from which the barites precipitated occurred, and the calculated temperature based on $^{87}Sr/^{86}Sr$ values is artificially high. The temperatures estimated for barite precipitation in the other samples may also be similarly artificially high as a result of conductive cooling, especially if evidence of conductive cooling from the presence of significant amounts of amorphous silica is present.

While conductive cooling may cause barite to precipitate from a fluid mixture with a large hydrothermal fluid component, conductive heating may similarly cause barite to form from a fluid mixture with a large seawater component. Most of the barite was determined to have precipitated from fluid mixtures above the threshold temperature for barite precipitation; however, the $^{87}Sr/^{86}Sr$ ratio of ALV1452-1A suggests that it precipitated from a fluid mixture at only ~70°C, significantly lower than the lower limit estimate of 100°C (Hannington and Scott, 1988). This fluid may have been conductively heated after mixing with a large component of seawater.

5.4 Barite Crystal Morphology

Laboratory experiments have linked the crystal morphology of barite to the degree of under- or supersaturation of Ba^{2+} or SO_4^{2-} in the fluid from which the crystals are precipitating (Judat and Kind, 2004; Li et al., 2007; Shikazono, 1994). Dendritic crystal morphologies tend to occur at higher degrees of supersaturation as a result of diffusion-limited aggregation of solute atoms, where ions are more likely to accrete near the tip of a branching cluster

rather than near the nucleation core (Turcotte, 1997). More euhedral, rhombohedral, or polyhedral crystals tend to occur at lower degrees of supersaturation, predominantly from a surface reaction precipitation mechanisms (Shikazono, 1994). The $^{87}Sr/^{86}Sr$ values of the analyzed barites indicate that, in all cases, precipitation occurred from a fluid that contained an excess of sulfate relative to Ba^{2+}.

A comparison of barite crystal morphologies to degree of fluid mixing and temperature indicate a progression from dendritic to acicular/radiating to blocky/euhedral crystals with increased hydrothermal fluid contribution and temperature (Fig. 3.8). The increased hydrothermal fluid contribution results in an increase in Ba^{2+} availability. The barite crystal morphology may thus be a function of Ba^{2+} availability, with reduced availability resulting in diffusion-limited crystal growth along branching edges. Increased Ba^{2+} availability would allow for crystal growth to occur along crystal surfaces, instead of being limited to the more energetically-favorable corner sites of the crystal lattice.

Alternately, differing crystal morphologies may be a result of differing temperatures of precipitation. The dendritic crystals precipitated at lower temperatures than the more euhedral crystals. A larger decrease in temperature with increased mixing of the hydrothermal fluid with seawater would result in a greater degree of barite supersaturation in the mixed fluid. The dendritic morphology may be a result of more rapid crystallization associated with quenching of the hydrothermal fluid by cold seawater during mixing. A lesser degree of mixing would result in higher temperatures, a lower degree of supersaturation, and more time for crystals to grow, resulting in more euhedral crystals.

6. Conclusions

Barite within hydrothermal chimneys along the Endeavour Segment records a complex interaction between hydrothermal fluids and seawater within the porous chimney walls. The partitioning of Sr primarily into barite within chimneys allows for the use of whole-rock Sr concentrations and $^{87}Sr/^{86}Sr$ values to be used to investigate the physical and chemical properties of the hybrid hydrothermal-seawater fluid mixture from which barite precipitates. All $^{87}Sr/^{86}Sr$ values for the analyzed barites fall between the endmember values for seawater and average Endeavour hydrothermal fluid. The resulting calculated degree of fluid mixing ranges between 19 and 87% hydrothermal fluid component. In most cases, the predicted temperatures of barite crystallization, based on degree of fluid mixing, are in agreement with typical precipitation temperatures of barite in hydrothermal systems (~100 to 300°C) based on thermodynamic data and mineral associations. Estimated precipitation temperatures that fall outside of the predicted precipitation temperature window are likely a result of conductive heating or cooling of the fluid through the chimney walls, or the result of venting temperatures that were higher or lower than 350°C.

Insight into the conditions under which barite form may also be imparted by the diverse crystal morphologies that are exhibited in the hydrothermal chimneys. The $^{87}Sr/^{86}Sr$ values indicate that, as a result of the very high sulfate concentrations in seawater relative to Ba^{2+} concentrations in the hydrothermal fluid, barite precipitates from a fluid with a stoichiometric excess of SO_4^{2-}. A relationship between the progression of increasingly well-formed crystals, from dendritic to acicular to blocky, to the degree of mixing and, by extension, temperature, suggests that either the availability of Ba^{2+} and/or crystallization

temperature (or a combination of both) may be an important controlling factor on barite morphology.

Although the range in $^{87}Sr/^{86}Sr$ values and crystal morphologies indicate that barite precipitates under a variety of conditions, in all cases a component of endmember hydrothermal fluid is required as the primary source for Ba^{2+} as well as providing the thermal conditions necessary for barite precipitation. Barite precipitation therefore occurs during periods when the chimney is actively venting a focused, high-temperature hydrothermal fluid, as opposed to much lower temperature diffuse fluid. The age of most recent high-temperature venting, determined from the ^{226}Ra-content within barite crystals, can thus be used to record the most recent high-temperature venting episode of the chimney (see Chapter 4).

References

Allen, L., 2011. Behaviour and occurrence of strontium in hydrothermal barite from the Endeavour Segment, Juan de Fuca Ridge, Department of Earth Sciences. University of Ottawa, Ottawa, Canada.

Bach, W., Humphris, S.E., 1999. Relationship between the Sr and O isotope compositions of hydrothermal fluids and the spreading and magma-supply rates at oceanic spreading centers. Geology 27, 1067-1070.

Blount, C.W., 1977. Barite solubilities and thermodynamic quantities up to 300-degrees-C and 1400 bars. American Mineralogist 62, 942-957.

Butterfield, D.A., McDuff, R.E., Mottl, M.J., Lilley, M.D., Lupton, J.E., Massoth, G.J., 1994. Gradients in the composition of hydrothermal fluids from the Endeavour Segment vent field - Phase-separation and brine loss. Journal of Geophysical Research-Solid Earth 99, 9561-9583.

Butterfield, D.A., Nelson, B.K., Wheat, C.G., Mottl, M.J., Roe, K.K., 2001. Evidence for basaltic Sr in midocean ridge-flank hydrothermal systems and implications for the global oceanic Sr isotope balance. Geochimica Et Cosmochimica Acta 65, 4141-4153.

Cousens, B.L., Allan, J.F., Leybourne, M.I., Chase, R.L., Vanwagoner, N., 1995. Mixing of magmas from enriched and depleted mantle sources: The Northeast Pacific - West-Valley Segment, Juan-de-Fuca Ridge. Contributions to Mineralogy and Petrology 120, 337-357.

Delaney, J.R., Robigou, V., McDuff, R.E., Tivey, M.K., 1992. Geology of a vigorous hydrothermal system on the Endeavour Segment, Juan de Fuca Ridge. Journal of Geophysical Research-Solid Earth 97, 19663-19682.

Engelbert, M., 2012. Strontium isotopic study of hydrothermal barite from the Endeavour Segment of the Juan de Fuca Ridge: Implications for seawater-hydrothermal fluid mixing, Department of Earth Sciences. Carleton University, Ottawa, Canada.

Glickson, D.A., Kelley, D.S., Delaney, J.R., 2006. The Sasquatch Hydrothermal Field: Linkages Between Seismic Activity, Hydrothermal Flow, and Geology. American Geophysical Union, Fall Meeting 2006 Abstract #V23B-0614.

Glickson, D.A., Kelley, D.S., Delaney, J.R., 2007. Geology and hydrothermal evolution of the Mothra Hydrothermal Field, Endeavour Segment, Juan de Fuca Ridge. Geochemistry Geophysics Geosystems 8.

Hannington, M., De Ronde, C., Petersen, S., 2005. Sea-Floor Tectonics and Submarine Hydrothermal Systems. Economic Geology 100th Anniversary Volume, pp. 111-141.

Hannington, M., Herzig, P., Scott, S., Thompson, G., Rona, P., 1991. Comparative mineralogy and geochemistry of gold-bearing sulfide deposits on the midocean ridges. Marine Geology 101, 217-248.

Hannington, M., Jonasson, I., Herzig, P., Petersen, S., 1995. Physical and chemical processes of seafloor mineralization at mid-ocean ridges. Geophysical Monograph 11, 115-157.

Hannington, M.D., 2004. A global database of seafloor hydrothermal systems, including a digital database of geochemical analyses of seafloor polymetallic sulfides. Geological Survey of Canada Open File 4598.

Hannington, M.D., Scott, S.D., 1988. Mineralogy and geochemistry of a hydrothermal silica sulfide sulfate spire in the caldera of Axial Seamount, Juan-de-Fuca Ridge. Canadian Mineralogist 26, 603-625.

Judat, B., Kind, M., 2004. Morphology and internal structure of barium sulfate - derivation of a new growth mechanism. Journal of Colloid and Interface Science 269, 341-353.

Karsten, J.L., Delaney, J.R., Rhodes, J.M., Liias, R.A., 1990. Spatial and temporal evolution of magmatic systems beneath the Endeavour Segment, Juan de Fuca Ridge - Tectonic and petrologic constraints. Journal of Geophysical Research-Solid Earth and Planets 95, 19235-19256.

Kelley, D.S., Carbotte, S.M., Caress, D.W., Clague, D.A., Delaney, J.R., Gill, J.B., Hadaway, H., Holden, J.F., Hooft, E.E.E., Kellogg, J.P., Lilley, M.D., Stoermer, M., Toomey, D., Weekly, R., Wilcock, W.S.D., 2012. Endeavour Segment of the Juan de Fuca Ridge One of the most remarkable places on Earth. Oceanography 25, 44-61.

Kelley, D.S., Delaney, J.R., Yoerger, D.R., 2001. Geology and venting characteristics of the Mothra hydrothermal field, Endeavour segment, Juan de Fuca Ridge. Geology 29, 959-962.

Kristall, B., Kelley, D.S., Hannington, M.D., Delaney, J.R., 2006. Growth history of a diffusely venting sulfide structure from the Juan de Fuca Ridge: A petrological and geochemical study. Geochemistry Geophysics Geosystems 7.

Li, S.W., Xu, J.H., Luo, G.S., 2007. Control of crystal morphology through supersaturation ratio and mixing conditions. Journal of Crystal Growth 304, 219-224.

Mills, R., Teagle, D., Tivey, M., 1998. Fluid mixing and anhydrite precipitation within the TAG mound.

Proskurowski, G., Lilley, M.D., Brown, T.A., 2004. Isotopic evidence of magmatism and seawater bicarbonate removal at the endeavour hydrothermal system. Earth and Planetary Science Letters 225, 53-61.

Robigou, V., Delaney, J.R., Stakes, D.S., 1993. Large massive sulfide deposits in a newly discovered active hydrothermal system, the Highrise Field, Endeavour Segment, Juan-de-Fuca Ridge. Geophysical Research Letters 20, 1887-1890.

Shikazono, N., 1994. Precipitation mechanisms of barite in sulfate-sulfide deposits in back-arc basins. Geochimica et Cosmochimica Acta 58, 2203-2213.

Tivey, M.K., Delaney, J.R., 1986. Growth of large sulfide structures on the Endeavour Segment of the Juan-de-Fuca Ridge. Earth and Planetary Science Letters 77, 303-317.

Tivey, M.K., Stakes, D.S., Cook, T.L., Hannington, M.D., Petersen, S., 1999. A model for growth of steep-sided vent structures on the Endeavour Segment of the Juan de Fuca Ridge: Results of a petrologic and geochemical study. Journal of Geophysical Research-Solid Earth 104, 22859-22883.

Turcotte, D., 1997. Fractals and Chaos in Geology and Geophysics, Cornell University, New York.

Von Damm, K.L., 1990. Seafloor hydrothermal activity - black smoker chemistry and chimneys. Annual Review of Earth and Planetary Sciences 18, 173-204.

Williamson, N., 2010. Occurrence and genesis of hydrothermal barite along the Endeavour Segment, Juan de Fuca Ridge, Department of Earth Sciences. University of Ottawa, Ottawa, Canada.

Table 3.1: Summary of petrographic features for Endeavour chimney thin-sections

	wt% Ba	Main mineral assemblage	Petrographic summary
TIVEY MISC-2	33	Pyrite Marcasite Minor chalcopyrite Minor sphalerite Barite	Two distinct sections; the denser, sulphide-rich section contains well formed intergrowing pyrite and marcasite with minor barite occurring as small tabular crystals or circular arrangements of acicular crystals stained orange, and the porous section contains minor marcasite and pyrite occurring in the same way, with barite also present in the same way, in addition to blocky elongate crystals and acicular crystals of varying lengths organised in a radial pattern.
ALV2467-R3_section 1	26.5	Barite Marcasite Fossil worm tubes	Section of fossil worm tubes with marcasite crusts as the main sulfide. Barite occurs mainly as acicular crystals of varying sizes, as well as small blocky ones, growing in association with the fossil worm tubes, towards the inside or outside.
ALV2467-R3_section 2	26.5	Barite Marcasite Fossil worm tubes Minor pyrite	Section of fossil worm tubes with minor marcasite occurring as colloform crusts. Barite occurs as small blocky elongate crystals mainly growing into the fossil worm tube cavities and radial arrangements of these blocky crystals as well as acicular ones.
ALV2463-R4-pc	26	Barite $AmSiO_2$ Minor pyrite, marcasite, & sphalerite	The main feature of this section are the large, 1.5 to 2 mm, euhedral blocky elongate barite crystals that occur throughout, individually as well as in groups arranged radially.
ALV2068-1	23	Barite $AmSiO_2$ Marcasite Pyriterite Minor sphalerite	Porous section of fine sulfides and abundant $AmSiO_2$ as well as many varieties of barite growth; small and large acicular crystals, blocky and tabular crystals, branching dendritic growth, as well as "spherulite-like" barite. Needle-like acicular barite grows in association with marcasite.
ALV1452-1A	12	Barite Sphalerite Marcasite Pyrite $AmSiO_2$	Section of sulphides and barite arranged in a zoned pattern. Barite occurs mainly as a feathery dendritic crust as well as small acicular crystals. $AmSiO_2$ coats almost all material. Sphalerite is present as large euhedral and subhedral crystals, and marcasite occurs colloform, botryoidally, as well as dendritically. Pyrite framboids are present.
ALV3589-R2	11	Barite Marcasite Pyrite ZnS	Pyrite and marcasite difficult to distinguish in this section, but both are believed to be present. Barite occurs as small blocky elongate crystals as well as fine "disseminated-like" barite distributed among sulphides. Pyrite occurs here in association with acicular barite, and sphalerite as colloform crusts.
ALV1452-2	8.5	Wurtzite (+sphalerite?) Pyrite Marcasite Barite Chalcopyrite disease Minor $AmSiO_2$	Barite occurs as acicular crystals growing radially as well as fine crystals, "disseminated" among sulfides and amorphous oxides. Blocky elongate barite is present, although very small. Wurzite is present euhedrally, and marcasite forms a crust around crystals of pyrite that appear zoned.
ALV2072-1B	7.5	Marcasite Pyrite Barite Minor $AmSiO_2$	Marcasite and pyrite occur together in this section as a crust with pyrite generally occurring first. Barite occurs minimally and as accretions of small acicular radial crystals as well as "disseminated-like". Some tabular barite crystals are present.
ALV3587-R-1	6.1	Sphalerite Barite Minor galena Very minor covellite	Section mainly of dendritic sphalerite, at times with inclusions of galena. Barite occurs as blocky and acicular crystals, as well as a crust of small blocky to blocky-acicular crystals, often growing off sphalerite. As the presence of barite increases from left to right, sphalerite becomes more and more anhedral.
ALV3622-01A	5.4	ZnS Pyrite Marcasite Barite Minor covellite Abundant chp disease	Barite occurs mainly as dendrites lining and facing the inside of a central conduit in the section. Barite also occurs as small blocky elongate as well as acicular crystals. Dirty ZnS occurs abundantly here, contains chalcopyrite disease, and in some places is being replaced by covellite. Pyrite and marcasite occur mostly together, as intergrowing fairly euhedral crystals, and in association with barite. $AmSiO_2$ is abundant and coats all material.
ALV2072-7	5	Sphalerite/wurtzite Marcasite Pyrite Barite Chp disease $AmSiO_2$	Barite occurs as acicular fans with colloform marcasite growth that occurs mostly near the tips of the fans in between needles. One barite "spherulite-like" crystal noted. ZnS occurs as small crystals triangular to hexagonal in shape with chalcopyrite disease.
ALV3616-B	4.1	ZnS Pyrrhotite Pyrite Chalcopyrite Barite/Anhydrite/Gordaite?	Confusing section consisting of a mineral greatly resembling anhydrite, though the CaO content is very low. ZnS occurs in minor amounts, sub to anhedral, and contains chp disease, as well as dissolving and fractured crystals. Pyrrhotite occurs as needles, mainly associated with fine sub to euhhedral pyrite.
ALV2415-1D(3)	2.7	Marcasite Pyrite ZnS Barite	Marcasite and pyrite occur together as layers and crusts, with fine barite needles present between these crusts – some barite needles occur as small circular radiations where space permits. Also here is the acicular bar-colloform marcasite occurrence seen in many other samples. ZnS appears as semi-circular layers and as round aggregations around pyrite-marcasite.
ALV2460-R2-14a	2.6	Marcasite Pyrite Barite Abundant $AmSiO_2$ Chalcopyrite Minor ZnS	This section contains high AmSiO2, which coats everything. Barite occurs mainly as thin elongate, crystals and needles. Marcasite occurs with pyrite as fine and encrusting crystals, and chp is present in a disseminated manor and as subhedral crystals.

Table 3.1 (cont.):

	wt% Ba	Main mineral assemblage	Petrographic summary
ALV3000C	1.7	Sphalerite Pyrite Marcasite Barite Pyrrhotite Minor $AmSiO_2$	In this section, ZnS is growing around pyrite and/or marcasite, which forms a crust around marcasite. Some places where pyrite and marcasite occur together contain relict needles in their centre. Minimal barite occurs almost exclusively in association with the ma crust, as well as small crystals, needle-like, growing in between the marcasite dendrites. Pyrrhotite occurs as needles.
ALV2408-1A	1.65	Pyrite Marcasite ZnS Barite Minor $AmSiO_2$	Pyrite and marcasite occur as intergrowths, colloform and dendritic. In this section, barite occurs as needles between the marcasite-pyrite layers and as fine crystals growing near sulfides on the edge of the crust. ZnS grew after the pyrite-marcasite as semi-circular layers and as round aggregations.
ALV2452-2	1.65	ZnS Pyrite Marcasite Chp disease Barite	Barite occurs “disseminated-like” around or under the sulfides, as well as small, tabular crystals. Barite is also present with large subhedral ZnS as circular arrangements of needles. A layer of ZnS and fine pyrite-marcasite transitions into a crust of large Zns crystals. ZnS crystals demonstrate chalcopyrite disease and when better formed take on a hexagonal shape.
ALV2449-1	1.6	Marcasite Pyrite Chalcopyrite ZnS Pyrrhotite? Minor barite/anhydrite	Section containing almost no barite; if present, occurs fine crystals possibly overprinted by sulphides, which are mainly alternating layers of large pyrite-marcasite dendrites and finer pyrite-marcasite. ZnS occurs mainly as wurtzite and contains chalcopyrite disease. Some anhedral ZnS also surrounds relict needles and pyrite-marcasite.
ALV2461-R6-4 (EN52)	1.5	Marcasite Pyrite ZnS Minor barite	Section consisting mainly of abundant sub to euhedral ZnS containing holes from plucked material. Barite needles grow radially off sulfides. Some of the ZnS appears skeletal, and is associated with small pyrite crystals. Marcasite is bortyoidal and associated with pyrite as well as a pinkish-beige opaque in some places. Chalcopyrite disease is present within ZnS.
ALV2464-R4	N/A	Barite Pyrite Sphalerite $AmSiO_2$	Barite crystals are large and small (1 to 1.5mm), blocky and elongate, and large tabular (most of which look zoned), occurring alone or radially. Pyrite occurs as framboids, and any other sulfides in this section are very small crystals of anhedral pyrite, and subhedral sphalerite. Structure of the sample is quite obviously kept by a mix of AmSiO2 and gangue.
ALV 4446 (1735)	1.19	Barite Sphalerite Marcasite Pyrite $AmSiO_2$	Barite occurs as “disseminated-like” among sulphides, as small needles fuzzy and grey from sulphide inclusions, and as small tabular crystals. Fine intergrowing sphalerite, marcasite and pyrite, with chalcopyrite occurring within the ZnS, as well as dendritic sphalerite and fine dendritic pyrite is present. Sphalerite is often green translucent in TL, and small $AmSiO_2$ spheres abundantly occurring over all material.

$AmSiO_2$ = Amorphous Silica

Table 3.2: Summary of Sr-concentrations within barite crystals

Sample Analyzed	**Morphology**	**Average Sr Concentration (wt.%) (normalized to total Ba + Sr + Ca)**	**Sr/Ba Mass ratio**
ALV 2072-7	Small & Large Acicular	7.3	0.09
ALV 2068-1	Fine Acicular	10.0	0.12
ALV 3589-R2	Dendritic	5.8	0.04
ALV 3589-R2	Tabular	3.6	0.04
TIVEY-MISC-2	Small Tabular	3.1	0.03
EN 16	Radiating Blocky	4.0	0.04
ALV 2464-R4	Zoned Blocky	6.1	0.07
ALV 2467-R2	Blocky	4.8	0.05

Table 3.3: Summary of $^{87}Sr/^{86}Sr$ ratios, fluid mixing data and inferred temperatures for barite samples.

Sample	$^{87}Sr/^{86}Sr \pm 2\sigma$	% Hydrothermal fluid[1]	% Seawater[1]	Temperature of fluid mixture (°C)[2]
ALV1452-1A	0.707581 ± 0.000011	19.4	80.6	70
ALV1452-2	0.704496 ± 0.000007	71.6	28.4	251
ALV2068-1	0.704779 ± 0.000010	65.8	34.3	231
ALV2072-7	0.705116 ± 0.000010	59.1	40.9	208
ALV2415-1D(3)	0.704525 ± 0.000010	71.0	29.0	249
ALV2449-1 (EN-8)	0.704380 ± 0.000010	74.1	25.9	260
ALV2461-R6-4 (EN-52)	0.704630 ± 0.000010	68.8	31.2	241
ALV2464-R4	0.704584 ± 0.000009	69.8	30.2	245
ALV2467-R2	0.703798 ± 0.000009	87.5	12.6	306
ALV2467-R3 (EN-16)	0.704816 ± 0.000011	65.0	35.0	228
ALV2467-R9	0.703862 ± 0.000011	85.9	14.1	301
ALV3000C	0.704545 ± 0.000009	70.6	29.4	248
ALV3589-R2	0.705635 ± 0.000010	49.5	50.5	174
ALV4446-1628	0.706058 ± 0.000009	42.2	57.8	149
ALV4450-1829	0.705461 ± 0.000009	52.6	47.4	185
TIVEYMISC2	0.704198 ± 0.000012	78.2	21.8	274

[1] % relative fluid contribution calculated using (Mills et al., 1998):

$$\%\ \text{hydrothermal component} = 100 \times \frac{[Sr]_{SW}\left[\left(^{87}Sr/_{86}Sr\right)_{SW} - \left(^{87}Sr/_{86}Sr\right)_{BA}\right]}{[Sr]_{SW}\left[\left(^{87}Sr/_{86}Sr\right)_{SW} - \left(^{87}Sr/_{86}Sr\right)_{BA}\right] + [Sr]_{HF}\left[\left(^{87}Sr/_{86}Sr\right)_{BA} - \left(^{87}Sr/_{86}Sr\right)_{HF}\right]}$$

where [Sr] represents the concentration of Sr, and SW, BA, and HF represent seawater, barite and hydrothermal fluid, respectively, and assuming an $^{87}Sr/^{86}Sr$ ratio of 0.7033 and 0.709183 for endmember hydrothermal fluid and seawater, respectively (Butterfield et al., 2011).

[2] Temperatures are estimated from mixing data, assuming temperatures for hydrothermal fluid and seawater as 350 and 2 degrees Celsius, respectively.

Table 3.4: Summary of physical and chemical properties of seawater and hydrothermal fluid at Endeavour.

	Seawater[1]	**Endeavour hydrothermal fluids**[2]
Ba	0.1 µmol/kg 0.01 ppm	31 µmol/kg 4 ppm
SO_4	27900 µmol/kg 2680 ppm	0.8 µmol/kg 0.08 ppm
Sr	87 µmol/kg 8 ppm	135 µmol/kg 12 ppm
$^{87}Sr/^{86}Sr$	0.709183[3]	0.7033[4]
Temperature[3]	2°C	350°C

1 Broecker and Peng, 1982
2 Seyfried et al., 2003
3 Butterfield et al., 2001
4 Butterfield, 2011, personal communication

Figure 3.1

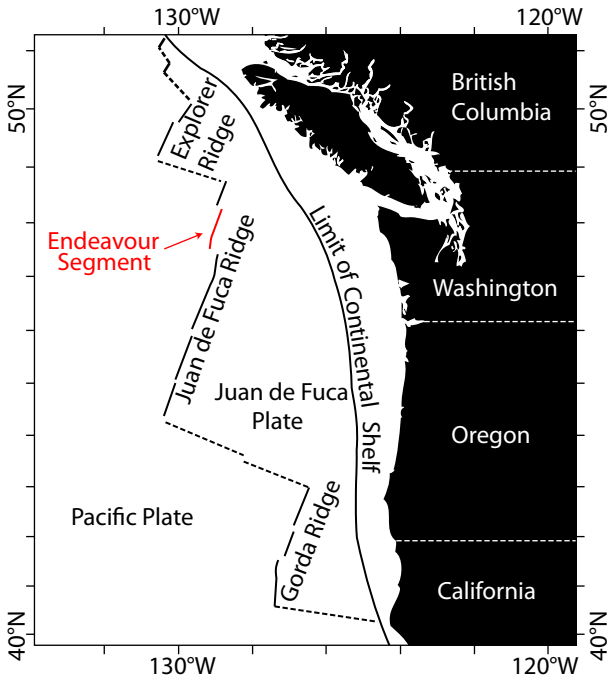

Figure 3.1: Map of the Juan de Fuca Plate showing the location of the Endeavour Segment.

Figure 3.2

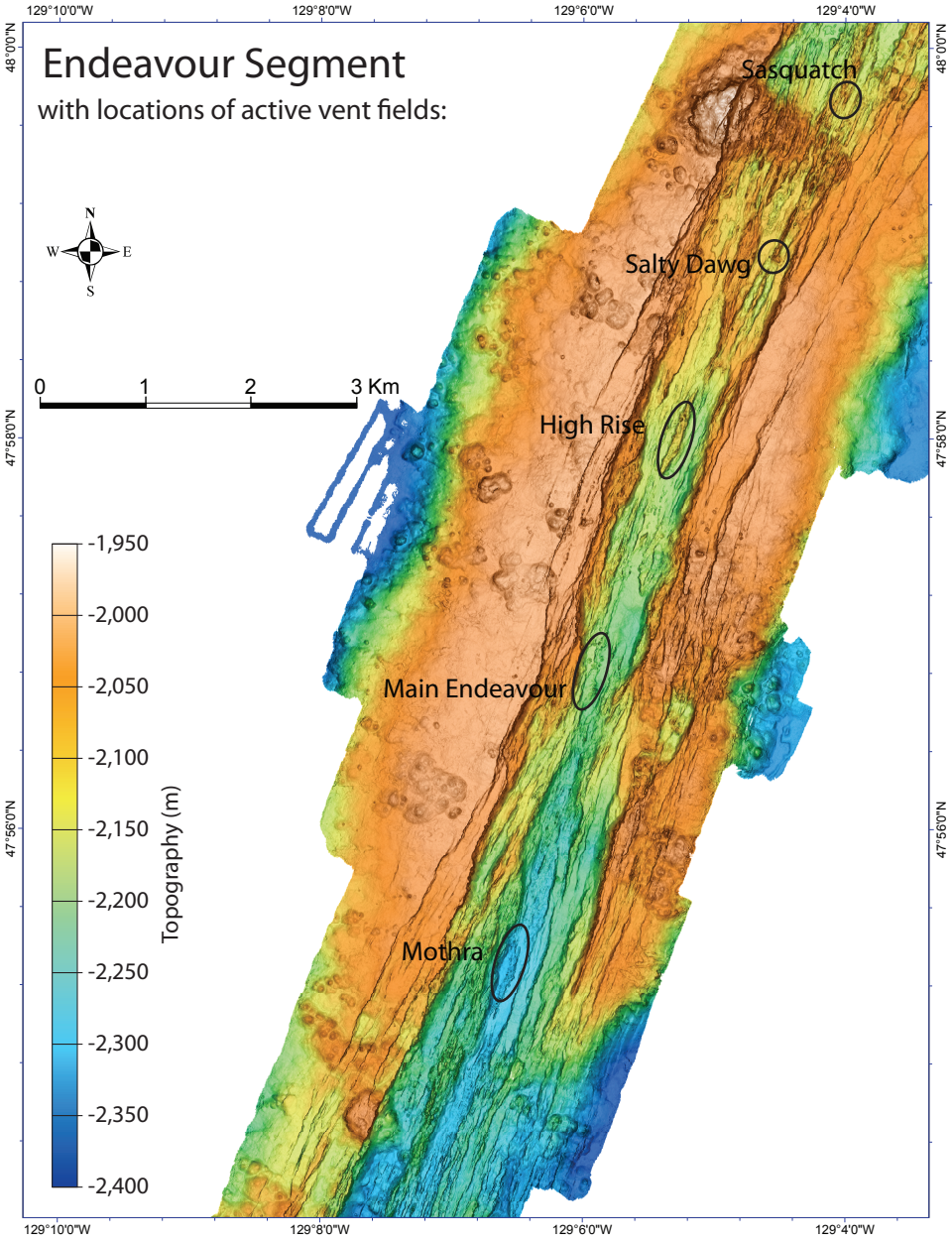

Figure 3.2: Bathymetric map of the Eneavour Segment, showing the locations of the five main active hydrothermal vent fields, from which samples for this study were collected. Bathymetry is 1-meter resolution, collected between 2008 and 2011 using the Monterey Bay Aquarium Research Institute (MBARI) autonomous underwater vehicle (AUV) D. Allan B.

Figure 3.3

	Cu	*Fe*	*Zn*	*Pb*	*S*	*SiO2*	*Ba*	*MgO*	*CaO*	*Cd*	*Sr*
Cu	1										
Fe	0.127	1									
Zn	-0.123	-0.242	1								
Pb	-0.058	-0.159	0.164	1							
S	0.105	**0.825**	-0.039	-0.062	1						
SiO2	*-0.243*	*-0.367*	-0.015	0.0689	*-0.581*	1					
Ba	-0.159	*-0.404*	-0.115	-0.023	*-0.510*	**0.398**	1				
MgO	0.001	-0.196	-0.107	-0.025	*-0.285*	**0.222**	-0.067	1			
CaO	-0.021	*-0.531*	*-0.254*	-0.035	*-0.361*	*-0.256*	-0.135	0.113	1		
Cd	-0.035	-0.259	**0.907**	**0.292**	-0.004	-0.094	-0.120	-0.098	-0.199	1	
Sr	-0.167	*-0.545*	*-0.202*	-0.015	*-0.586*	**0.284**	**0.804**	0.063	**0.216**	-0.189	1

Figure 3.3: Correlation plot for selected major and trace elements from 336 hydrothermal samples from the Endeavour Segment. Corelation coefficients highlighted in **bold red** and *italic green* show elevated positive and negative correlations, respectively.

Figure 3.4:

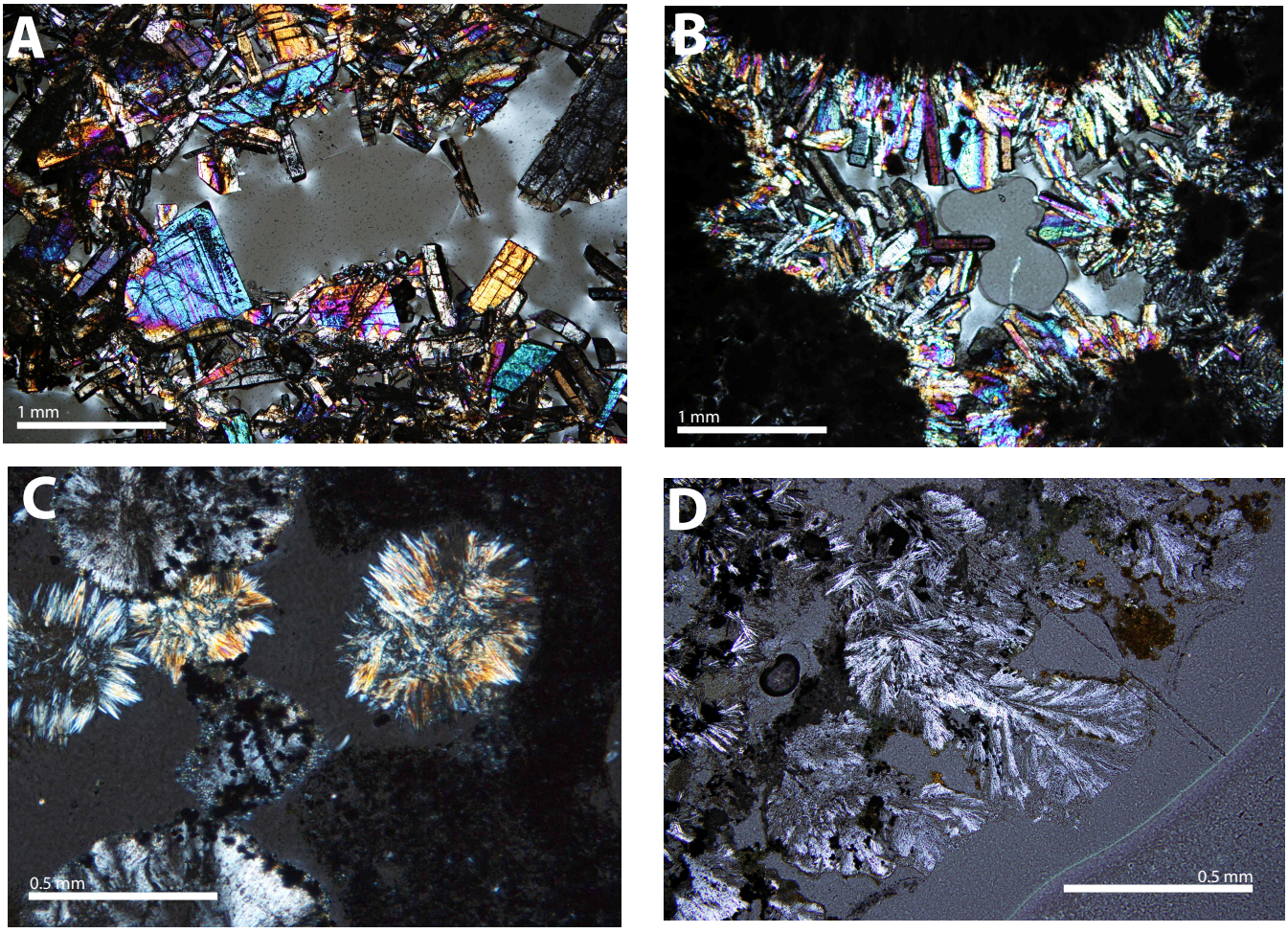

Figure 3.4: Transmitted light (cross-polarized) photomicrographs of dominant barite crystal morphologies from hydrothermal chimneys at the Endeavour Segment: A) Well-formed, blocky crystals; B) Acicular and/or radiating tabular crystals; C) Acicular and/or radiating needle-like crystals; D) Dendritic crystals.

Figure 3.5

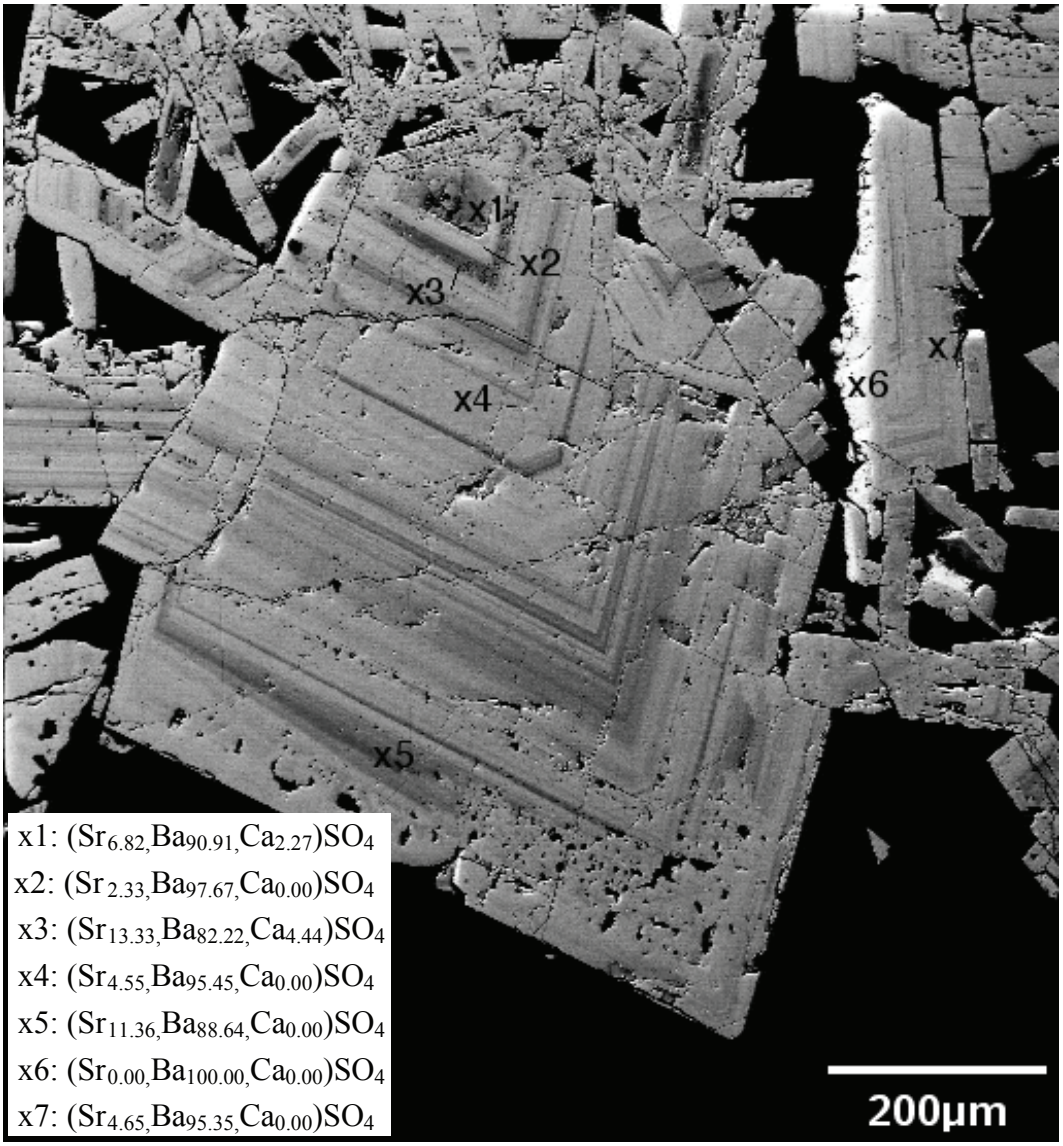

Figure 3.5: Backscatter electron microprobe image of a zoned, blocky barite crystal from ALV2464-R4. Spot chemical analyses are marked by an "X". Brightness variations within the crystal are a result of varying Sr-content.

Figure 3.6:

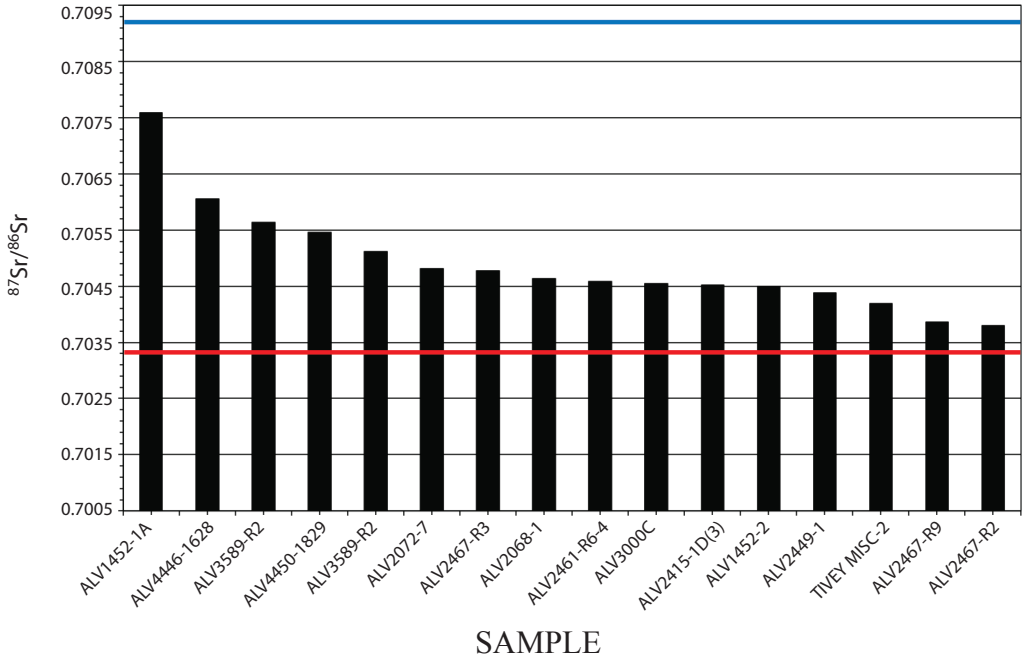

Figure 3.6: $^{87}Sr/^{86}Sr$ results for hydrothermal barite at Endeavour. The red line represents the $^{87}Sr/^{86}Sr$ ratio of end-member hydrothermal fluid (Butterfield, 2011; pers. comm) while the blue line represents the $^{87}Sr/^{86}Sr$ ratio of seawater (Butterfield et al., 2001). All of the $^{87}Sr/^{86}Sr$ ratios of barite plot between the ratios of hydrothermal fluid and seawater.

Figure 3.7:

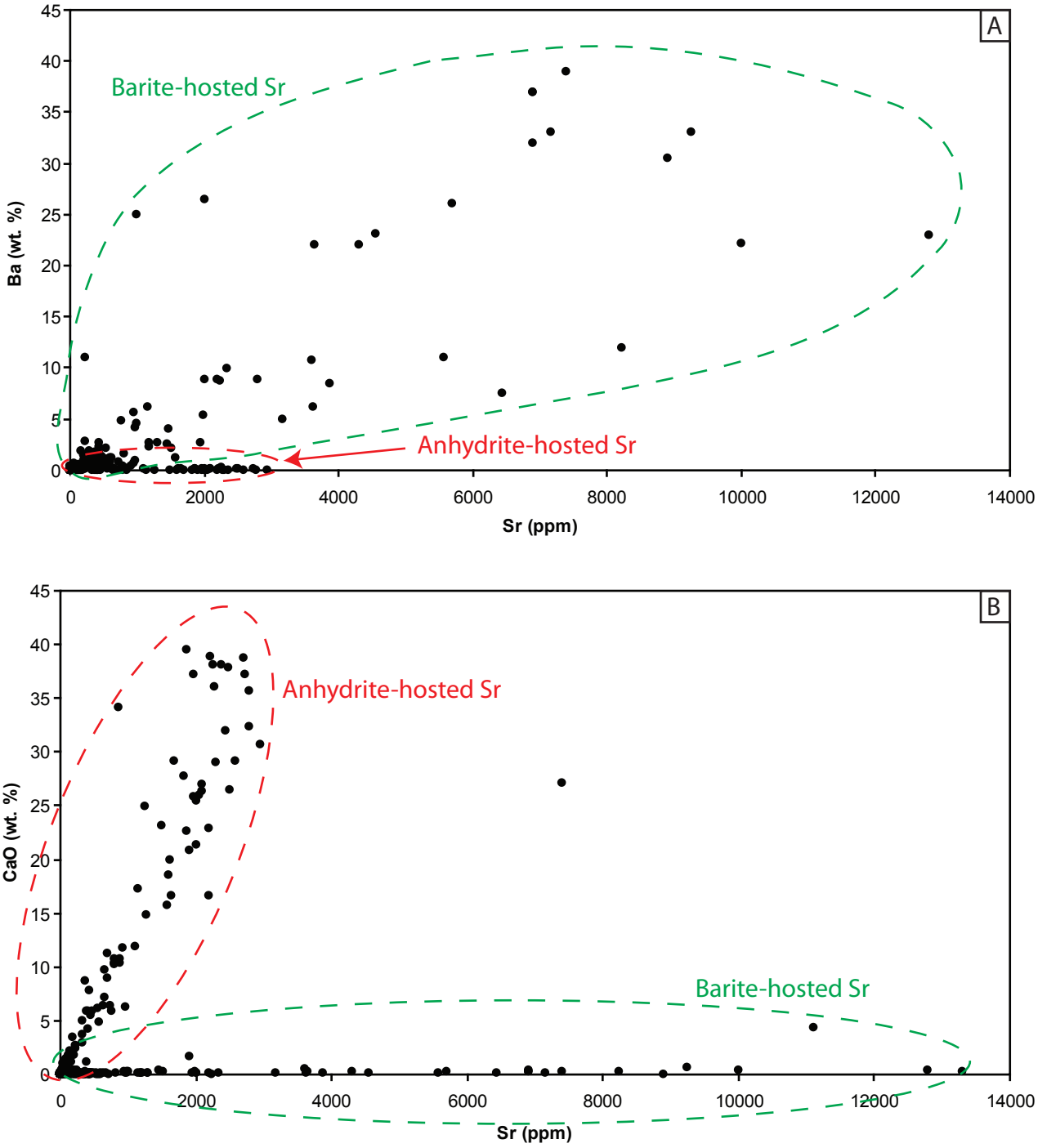

Figure 3.7: Plots of Ba and CaO versus Sr concentrations for hydrothermal chimney samples from the Endeavour Segment. The grouping of data into either a positive linear trend or plotting along the x-axis indicates that barite and anhydrite are the primary hosts of Sr in the chimneys, with barite containing the highest concentrations of Sr.

Figure 3.8:

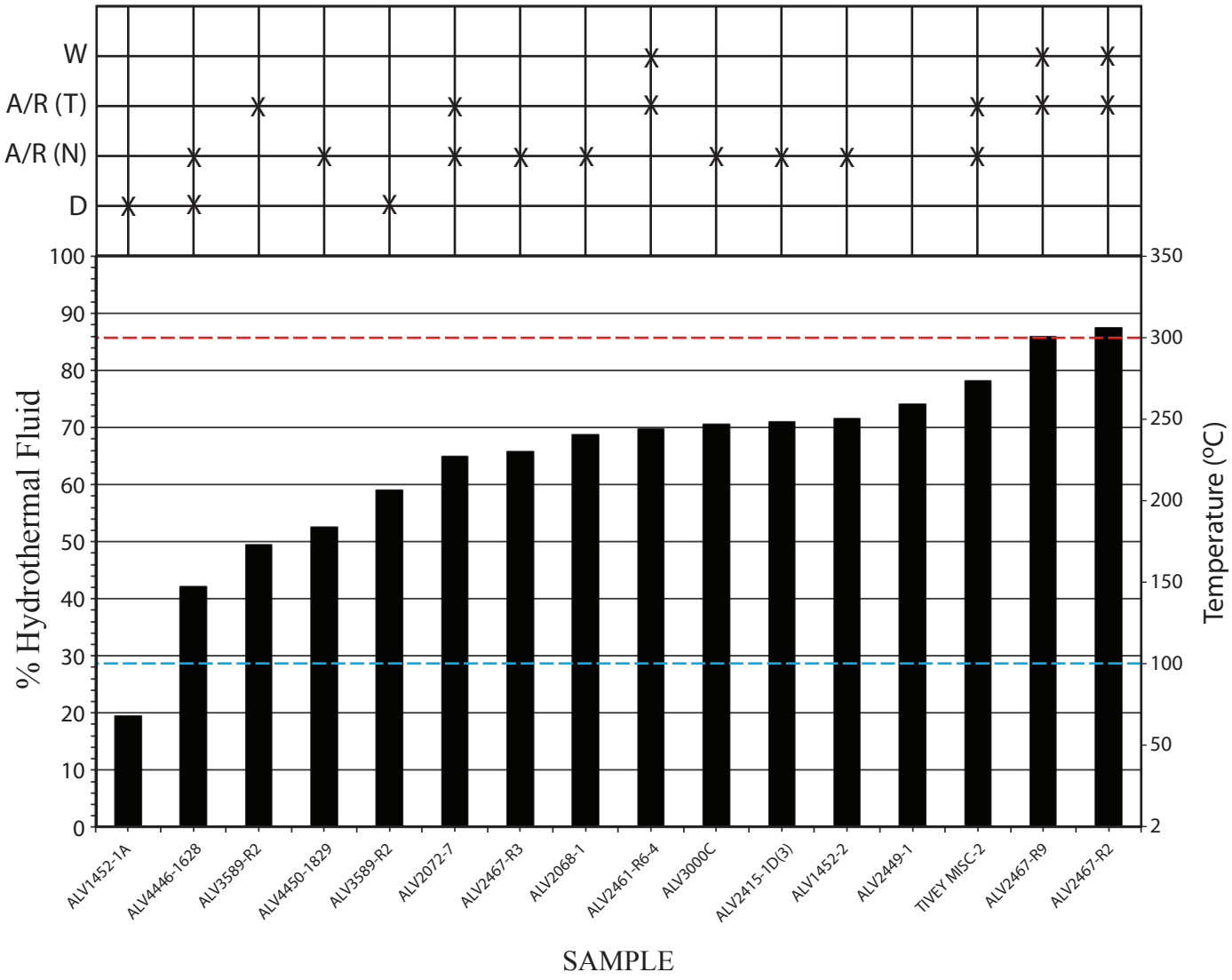

Figure 3.8: Degrees of mixing and temperatures of precipitation for barites within hydrothermal chimneys from Endeavour (from data reported in Table 3.3). Red and blue dashed lines represent estimated upper and lower temperature limits, respectively, for barite precipitation in hydrothermal chimneys. Correlation between the % hydrothermal fluid component and barite crystal morphology, showing a trend from dendritic (D) to acicular/radiating (A/R) (tapered (T) and blocky (B)) to well-formed blocky crystals (W) with an increase in relative proportion of hydrothermal fluid present during crystallization.

CHAPTER 4

SULFIDE GEOCHRONOLOGY ALONG THE ENDEAVOUR SEGMENT OF THE JUAN DE FUCA RIDGE

Abstract

Forty-nine hydrothermal sulfide-sulfate rock samples from the Endeavour Segment of the Juan de Fuca Ridge in the northeastern Pacific Ocean were dated by measuring the decay of ^{226}Ra (half-life of 1,600 years) in hydrothermal barite to provide a history of hydrothermal venting at the site over the past 6,000 years. This dating method is effective for samples ranging in age from ~200 to 20,000 years old and effectively bridges an age gap between shorter- and longer-lived U-series dating techniques for hydrothermal deposits. Results show that hydrothermal venting at the Main Endeavour, High Rise and Sasquatch vent fields began at least 2,300, 850 and 1,450 years ago, respectively. Barite ages of inactive deposits on the axial valley floor are between 1,200 and 2,200 years old, indicating past widespread hydrothermal venting outside of the currently active vent fields. Samples from the half-graben on the eastern slope of the axial valley range in age from ~1,700 to 2,930 years, and a single sample from outside the axial valley, near the westernmost valley fault scarp is 5,850 years old. The spatial relationship between hydrothermal venting and normal faulting suggests a temporal relationship, with progressive younging of sulfide deposits from the edges of the axial valley towards the center of the rift. These relationships are consistent with the possible inward migration of normal faulting towards the center of the valley over time and a minimum age of hydrothermal activity of ~6,000 years.

1. Introduction

The circulation of hydrothermal fluids through the oceanic crust at mid-ocean ridges results in significant transfer of mass and energy between the oceans and underlying lithosphere. The rate and intensity of hydrothermal circulation has been investigated at scales ranging from the global ridge system [*Baker and German*, 2004; *Davis and Elderfield*, 2004; *M. Hannington et al.*, 2011] down to the scale of individual discharging vents [*Converse et al.*, 1984; *Lowell et al.*, 1995; *Von Damm*, 1990]. Direct measurements of flow rate, fluid composition, and temperature provide only a snapshot of the physical and chemical attributes of a hydrothermal vent or vent field. Studies of vent fields along the intermediate-spreading rate Juan de Fuca Ridge in the northeastern Pacific Ocean show that these attributes can vary significantly over time scales as short as days to weeks in response to tectonic and volcanic events [*Butterfield et al.*, 1997; *Embley et al.*, 1995; *Hooft et al.*, 2010; *Johnson et al.*, 2000; *Kelley et al.*, 2012; *Lilley et al.*, 2003; *Seyfried et al.*, 2003]. In one instance, a chimney was observed to grow 1.2 m in a day after a microseismic event [*J Delaney et al.*, 1990], and the massive 45 m tall sulfide edifice 'Godzilla', within the Endeavour system, completely collapsed in 1996, with new growth of 10 m one year later [*Kelley et al.*, 2012]. Studies of the short-term (<150 years) growth rates of individual vent chimneys along Juan de Fuca Ridge using short-lived uranium-series disequilibrium techniques such as ^{210}Pb/Pb and ^{228}Th/^{228}Ra indicate highly variable growth rates that range from 1 to 6 cm/yr [*Grasty et al.*, 1988; *Kadko et al.*, 1985; *Kim and McMurtry*, 1991; *Reyes et al.*, 1995; *Stakes and Moore*, 1991]. Because of this variability, meaningful rates of deposit growth over the lifespan of a hydrothermal system cannot be extrapolated from limited duration time-series observations or short-lived radioisotope studies.

Longer-lived U-series isotope systems, such as $^{230}Th/^{234}U$, have been used to date active and inactive sulfide deposits on the East-Pacific Rise [*Alt et al.*, 1987; *Lalou et al.*, 1985], Mid-Atlantic [*Y Kuznetsov et al.*, 2007; *Lalou et al.*, 1995; *Shilov et al.*, 2012] and Central Indian Ridges [*Lalou et al.*, 1998]. Data from an intensive geochronological study of the TAG hydrothermal mound on the Mid-Atlantic Ridge are consistent with venting occurring in long-lived pulses (up to 50,000 years), punctuated by periods of little to no deposition [*Lalou et al.*, 1995]. Lalou *et al.*[1993] suggested that the lifespan of a hydrothermal system may be largely dependent on the local tectonic environment and may be inversely correlated with spreading rate, with hydrothermal systems on intermediate-rate spreading ridges (4-6 cm/yr) being active on the order of 1,000s of years.

Unfortunately, there is a large gap in the applicable range between short-lived isotope systems (<150 years; e.g. ^{210}Pb, $^{228}Th/^{228}Ra$) and longer-lived systems (>5,000; e.g. $^{230}Th/^{234}U$) that are most commonly used to date seafloor hydrothermal systems. Radium-226, which has a half-life of 1,600 years, can be used to determine the age of vent deposits between ~150 to 20,000 years old [*de Ronde et al.*, 2005], effectively bridging the age gap between shorter- and longer-lived systems.

In this study, ages of a regionally extensive suite of sulfide-sulfate samples from hydrothermally active and inactive sites along the Endeavour Segment of the Juan de Fuca Ridge (Fig. 4.1) were determined, using the decay of ^{226}Ra in barite. The Endeavour Segment is spreading at a full rate of 6 cm/yr [*Goldstein et al.*, 1991; *Riddihough*, 1984], and contains five known active vent fields spanning hundreds of meters in length, a few

small isolated areas of black smoker discharge, and several smaller areas of diffuse venting [*Kelley et al.*, 2012]. There is also an abundance of inactive sulfide deposits both within and between the active fields [*Clague et al.*, 2008; *J R Delaney et al.*, 1992; *Deborah A Glickson et al.*, 2006; *Kelley et al.*, 2002; *Kelley et al.*, 2012]. Hydrothermal deposits at Endeavour are enriched in barite, relative to other mid-ocean ridge deposits [*Kristall et al.*, 2006; *Stakes and Moore*, 1991; *Tivey et al.*, 1999]. The barite is the primary host for the radiogenic isotope ^{226}Ra, which is used to date these deposits. In this paper, we present age constraints on hydrothermal activity and the spatial and temporal history of hydrothermal venting along the Endeavour Segment.

2. Radium-226/Ba dating of hydrothermal barite

Samples were dated by measuring the decay of ^{226}Ra within barite, largely following the methods of *de Ronde et al.* [2005] and *Ditchburn et al.* [2012]. Radium-226 accumulates in basaltic oceanic crust from the decay of ^{238}U and its intermediate daughter products. During hydrothermal alteration of the crust, both Ra and Ba are leached from basalt and transported to the seafloor by upwelling fluids. Radium has similar geochemical properties to Ba (e.g., ionic charge and radius) and substitutes readily for Ba within the barite lattice. Thorium-230, the immediate parent isotope of ^{226}Ra, has very low solubility and is not leached from basalt during hydrothermal alteration, resulting in ^{226}Ra in hydrothermal barite being unsupported by its parent isotope. Sample ages (t, in years) were calculated using the following formula:

$$t = \frac{\ln {}^{N_0}\!/_{N} \times 1600\,yrs}{\ln 2}$$

Where:

N = ^{226}Ra/Ba of the sample, at the time collected

N_0 = initial ^{226}Ra/Ba of the sample at time of crystallization

1,600 yrs = Half-life of ^{226}Ra

The age of the sample is dependent on the amount of ^{226}Ra that has decayed, relative to the original ^{226}Ra content for each sample, which cannot be determined directly. However, ^{226}Ra/Ba of active, 'zero-age' vents can be used as a proxy for initial ratios along the entire ridge, if it is shown that the ^{226}Ra/Ba in the hydrothermal fluids does not vary spatially along the ridge segment or temporally over timescales of 1,000s of years. The spatial variability of ^{226}Ra/Ba can be established by measuring the ratios in active deposits from various locations along the ridge segment. Temporal variability is much more difficult to ascertain directly. However, the ^{226}Ra/Ba of the source basalt for a ridge segment is unlikely to have changed significantly on a timescale of 1,000s of years [*Butterfield et al.*, 1994; *Von Damm*, 1990].

3. Geologic Setting

The Endeavour Segment forms a 90 km-long section of the Juan de Fuca Ridge in the northeastern Pacific Ocean (Fig. 4.1). The segment rises to a minimum depth of 2,050 meters below sea level (mbsl) along a central broad bathymetric high ~15 km in length

(Fig. 4.2). The depth of the segment gradually increases to the north and south, away from the central high, to a maximum depth of >2700 m [*J R Delaney et al.*, 1992]. A well-developed axial rift valley runs the center of the bathymetric high with a variable width of 500 to 1000 m [*J R Delaney et al.*, 1992; *D. A. Glickson et al.*, 2007; *Kelley et al.*, 2002]. The valley walls are up to 200 m high and consist of a series of faulted half-grabens that form a step pattern rising from the valley floor, with steep walls that represent the topographic expressions of steep, inward-dipping normal faults [*J R Delaney et al.*, 1992; *Kappel and Ryan*, 1986; *Wilcock et al.*, 2009]. The ~200 m wide valley floor consists of basaltic flows, collapsed lava lakes and fissures. With a lack of historic lava flows (i.e., <30 years old) within the axial valley, it has been suggested that the segment is currently volcanically inactive and is undergoing a period of fault-controlled extension, with the axial valley forming within the past 10,000 years based on spreading rate [*Goldstein et al.*, 1991; *Johnson et al.*, 2000; *Proskurowski et al.*, 2004; *Riddihough*, 1984; *Volpe and Goldstein*, 1993]. However, the segment is seismically active with recent seismic swarms in 1999, 2003-2004 and 2005 that have been attributed to shallow diking events and which resulted in changes in hydrothermal vent fluid temperatures, fluxes and chemistry [*Barclay and Wilcock*, 2004; *Bohnenstiehl et al.*, 2004; *Hooft et al.*, 2010; *Kelley et al.*, 2002; *Lilley et al.*, 2003; *Seyfried et al.*, 2003; *Wilcock et al.*, 2002; *Wilcock et al.*, 2009]. Recent seismic imaging reveals a discontinuous series of strong reflectors at 1.9 to 4.0 km beneath the seafloor [*Carbotte et al.*, 2012; *Van Ark et al.*, 2007]. They are interpreted to represent the top of a series of axial magma chambers that extend for 24 km along the Endeavour Segment [*Van Ark et al.*, 2007], indicating the potential for renewed volcanic activity. The inverse relationship between depth of magma chamber and depth of axial valley suggests

that the axial valley formed due to collapse related to magma withdrawal [*Carbotte et al.*, 2012; *Carbotte et al.*, 2006].

The Endeavour Segment hosts five discrete, areally extensive active hydrothermal vent fields with an average spacing of 2 to 3 km between fields (Fig. 4.2). The fields host numerous large active and inactive sulfide edifices [*J R Delaney et al.*, 1992; *Deborah A Glickson et al.*, 2006; *Kelley et al.*, 2002; *Kelley et al.*, 2012; *Robigou et al.*, 1993]. At Mothra and the Main Endeavour (MEF) fields, hydrothermal activity occurs predominantly near the western edge of the axial valley, suggesting that the western bounding fault is a major conduit for ascending hydrothermal fluids [*J R Delaney et al.*, 1992; *Kelley et al.*, 2001; *Tivey and Delaney*, 1986]. Northward from these two fields, hydrothermal activity progressively moves towards the eastern valley walls (i.e., High Rise, Salty Dawg and Sasquatch). Lower-temperature, diffuse venting sites and abundant inactive hydrothermal chimneys and debris occur between the active vent fields [*Clague et al.*, 2008; *Kelley et al.*, 2002; *Kelley et al.*, 2012]. The active vent fields are characterized by steep-sided sulfide edifices that commonly rise several tens of meters above the seafloor [*J R Delaney et al.*, 1992; *D. A. Glickson et al.*, 2007; *Kelley et al.*, 2001; *Kristall et al.*, 2006; *Kristall et al.*, 2011; *Robigou et al.*, 1993; *Tivey et al.*, 1999]. These structures are dominated by sulfide (principally pyrite, sphalerite, wurtzite, pyrrhotite, marcasite, and chalcopyrite) and sulfate (anhydrite and barite) minerals, with abundant amorphous silica [*J R Delaney et al.*, 1992; *Kristall et al.*, 2006; *Robigou et al.*, 1993; *Tivey and Delaney*, 1986]. Barite abundance is particularly high relative to typical mid-ocean ridge hydrothermal deposits [*Mark Hannington et al.*, 2005; *Sours-Page et al.*, 1999]. This is interpreted to reflect deposition from vent fluids formed by interaction with basalt enriched in incompatible elements

relative to normal mid-ocean ridge basalt [*Karsten et al.*, 1990; *Langmuir et al.*, 1997; *Moore and Stakes*, 1990].

4. Samples

The majority of the >300 hydrothermal sulfide samples collected from the Endeavour Segment over the past 30 years were from active vents, biasing the current sample suite towards young deposits and the most recent hydrothermal activity. One notable exception was a study by *Tivey et al.* [1999] that included samples from inactive sites between MEF and High Rise fields. In the present study, a dedicated sulfide sampling program between 2008 and 2011, using the deep-sea submersible *Alvin* and the remotely-operated vehicles (ROVs) *Doc Ricketts* (MBARI) and ROPOS (courtesy of Neptune Canada), focused on collection of samples from actively venting sites and from inactive deposits within and away from the active vent fields, always targeting the visibly oldest and oxidized sulfides. These latter samples were commonly collected from partly eroded or collapsed chimney structures or talus on the basalt substrate. Nineteen samples from this suite, and a further 42 samples from the archive of more than 300 sulfide samples at the University of Washington were selected for analysis.

5. Methods

The ^{226}Ra activity of each powdered sample was measured by a XLB-GWL-SV digital gamma spectrometry (DSPec, Ortec®) at the University of Ottawa. The gamma spectrometer contains a high purity germanium crystal, 54.7mm × 66.2mm, and an active

well depth of 40mm. The spectral signature was calibrated using IAEA-312 reference material. The single ^{226}Ra energy peak at 186 KeV is subject to interference from the decay of ^{235}U at the same energy level. Therefore, the activity of ^{214}Pb (half-life of 20 minutes), a significant gamma-emitting daughter isotope of ^{226}Ra via the intermediate isotopes ^{222}Rn (half-life of 3.8 days) and ^{218}Po (half-life of 3.1 minutes), was used as a proxy for ^{226}Ra activity. Lead-214 was chosen over ^{214}Bi (half-life of 20 minutes), its daughter product, due to the higher efficiency of the detector at the primary ^{214}Pb energy peaks at 352 and 295 KeV, relative to the primary ^{214}Bi peak at 609 KeV, and because of coincidence summing at the 609 KeV peak. Prior to counting, sample tubes were sealed with epoxy in sample tubes for 21 days to prevent the escape of ^{222}Rn gas and thereby attain secular equilibrium between ^{226}Ra and ^{214}Pb. Counting time for each sample varied between 2 and 23 hours, depending on the amount of ^{226}Ra in the sample. To ensure sufficient ^{226}Ra (and ^{214}Pb) activity for gamma-counting, samples with Ba concentrations of greater than ~0.5 wt. % were chosen for analysis. These samples required shorter counting times and gave higher precision results. The resulting gamma spectra were analyzed using a DOS-based software program developed and provided by Dr. Peter Appleby (University of Liverpool, U.K.), which corrects for background, detector efficiency, sample volume and matrix effects. This method differs from that of *Ditchburn et al.* [2012] in that measurements are made from whole rock samples, as opposed to chemical separation of barite. Repeat analyses of IAEA standard soil #375 result in a coefficient of variability of 8% for ^{226}Ra measurements.

Of the 61 samples analyzed, 12 were considered to be zero-age samples (Table 1) and were used to determine the initial ^{226}Ra/Ba ratio (N_0 in equation 1), defined by the slope of a

regression curve through these samples on a ^{226}Ra-activity versus Ba concentration plot (Fig. 4.3A). From this plot, an N_0-value of 1,280 ± 70 (1σ) Bq/kg·wt.% Ba was used as the initial value for all Endeavour samples. The 12 samples used to define this value were collected from sites of active venting on hydrothermal edifices within MEF (9) and High Rise (2) Fields and an actively venting edifice (named Marias) discovered in 2011 within the newly identified Vesta vent field, between High Rise and Salty Dawg [*Kelley et al.*, 2012]. The two samples from the High Rise field (ALV2461-R13TIP and ALV2463-R5c3) were documented as 'inactive' when collected near active venting at High Rise, but have ^{226}Ra/Ba ratios that are consistent with the ratios of active samples from MEF. The ^{226}Ra/Ba ratios of these samples are also the highest ratios recorded at High Rise, indicating that these samples are young, relative to the other samples from High Rise. The ^{226}Ra/Ba ratio of the sample from Marias is slightly higher than the maximum values from MEF and High Rise, likely a result of minor variability in ^{226}Ra/Ba ratios along the ridge segment. The high R^2-value for the regression line is 0.971, indicating a strong agreement in maximum, 'zero age' ^{226}Ra/Ba ratios at MEF, High Rise and Marias. The age determinations rely only on the slope of the regression line defined in Fig. 4.3, not the absolute position of the line. The line can thus be applied to samples that have Ba concentrations that fall outside the range of Ba concentrations for active samples that were used to define the line.

6. Results

6.1 Initial ^{226}Ra/Ba ratios of 'zero-age' samples

The small variation in ^{226}Ra/Ba ratios between samples from active vents at MEF, inactive but young vents at High Rise, and the isolated active chimney "Marias" is consistent with a single initial ratio (N_o, Fig. 4.3A) for the entire ridge segment. A larger initial ^{226}Ra/Ba ratio (upward shift of the regression line in Figure 4.3) would result in all calculated ages shifting towards older dates, and known 'zero-age' samples collected from active vent orifices would have calculated ages that would be inconsistent with their recent precipitation.

6.2 ^{226}Ra/Ba ratios of inactive samples

None of the ^{226}Ra/Ba values from 49 'old' samples plot above the regression line that is defined by the active samples (Figure 4.3B, Table 4.2). This relationship is a necessary condition if the ^{226}Ra/Ba defined by the 'zero-age' samples is representative of the initial ratio for all ancient samples. Age uncertainties range from 130 to 210 years, and average 140 years.

Inactive samples range in age from zero to 5,850 ± 210 years, with all but one sample having ages of less than 3,000 years (Fig. 4.4). The oldest sample is twice as old as the next oldest sample and was collected from outside the axial valley (Fig. 4.2). All samples younger than 1,300 years (n = 34) are from the active vent fields. Samples older than 1,300 years (n = 15) are from deposits both within and outside of the active fields (Fig. 4.4).

Of the 10 samples from inactive sulfide structures outside of the major vent fields, 6 were collected from the axial valley floor, 3 from the eastern half-graben on the slope of the valley, and 1 from outside the axial valley, west of the westernmost normal fault on the

volcanic ridge (Fig. 4.2). The samples on the axial valley floor range from 1,230 to 2,170 ± 130 years old (Fig. 4.4). These ages are generally older than those from the active fields though there is some overlap in ages. Three samples from the eastern half-graben range in age from 1,710 to 2,930 ± 210 years old. These samples are much older than most samples from the axial valley floor. The single sulfide sample from outside the axial valley is 5,850 ± 210 years old, almost 2,000 years older than the oldest sample from within the axial valley.

Twenty-one samples from MEF show a wide age spectrum from the present to 2,270 years, with over 75% of the samples having ages between 500 and 1,500 years (Fig. 4.5). Ten samples from the High Rise Field have a younger age range, with a maximum age of 840 years (Fig. 4.5), 90% older than 500 years. Five sub-samples were taken from a chimney on the 'Baltic' edifice (ALV2461-R13). Four of the 5 sub-samples from different parts of this sample returned ages from 300 to 400 years, all within analytical uncertainty of each other (Table 4.2). The average age for these four subsamples is 350 years. The fifth sub-sample (R13TIP), taken from the top of the chimney, is a zero-age sample (Table 4.1). Two samples from Mothra are relatively young, at 20 to 160 years old. The 20-year old sample (ALV4450-2829) was collected from a dead, toppled but still relatively intact, chimney at the base of the active Faulty Towers Complex. Only one dateable sample was collected from the Salty Dawg field, with an age of 460 years. Two samples from the Sasquatch field yielded ages of 720 and 1,470 years old (Fig. 4.5).

7. Discussion

7.1 Venting history within the Endeavour axial valley

The 49 non-zero age determinations of hydrothermal sulfide samples from the Endeavour segment provide the first quantitative characterization of the spatial and temporal history of venting along the segment. The active vent fields represent discrete hydrothermal systems controlled by extensional faulting along the axis of the valley [*J R Delaney et al.*, 1992; *Kelley et al.*, 2012; *Robigou et al.*, 1993]. Data from MEF and High Rise provide the most information on the chronology of venting within the currently active fields with 21 and 13 dates, respectively.

The spectrum of ages from the MEF (Fig. 4.6) suggests that it has been hydrothermally active for at least 2,270 years. More samples would be required to determine whether venting was truly continuous, as hiatuses of ~500 years cannot be resolved with these data. Direct observations of vent activity at MEF since 1984 show that the intensity of venting had been relatively stable from the early 1980's until 1999-2000, when major shifts in temperature, fluid chemistry and fluid flux occurred and nascent chimneys formed resulting from a diking event [*Butterfield et al.*, 1994; *Kelley et al.*, 2012; *Larson et al.*, 2009; *Lilley et al.*, 2003; *Seyfried et al.*, 2003; *Wilcock et al.*, 2009]. Although a sampling bias cannot be ruled out, the large number of samples with ages between ~500 and 1,250 years (Fig. 4.5) may indicate increased venting intensity during this time period, perhaps as a result of multiple faulting or diking events.

The High Rise field has been active for at least 840 years (Fig. 4.6). Similar to MEF, the sample age distribution shows no prolonged venting hiatuses (i.e., >500 years) during this time period (Fig. 4.5). The number of ages between 500 and 750 years ago may indicate a

period of enhanced venting and sulfide deposition. However, more samples would be needed to further explore this possibility. The two dated samples from the Mothra Field were collected from the actively-venting Faulty Towers Complex. Their young ages are unlikely to reflect the age of the entire complex, which consists of numerous vents and inactive structures that have yet to be sampled for age determination.

Although hydrothermal activity is currently focused at the five major active vent fields with minor venting associated with smaller vent fields and diffuse discharge areas [*Kelley et al.*, 2012], the abundance of sulfide debris on the axial valley floor outside of these areas (Fig. 4.2) indicates that past hydrothermal venting along the Endeavour Segment has not been restricted to these areas. The range of sulfide ages from the inactive areas points to more aerially extensive hydrothermal venting between ~1,300 and 2,200 years ago (Figs. 4.4 and 4.6). Sample ages older than 1,300 years from both MEF and Sasquatch, as well as from other areas in the axial valley indicate that these two fields were active concurrently and that venting was also occurring elsewhere in the rift valley at this time. There is a notable lack of sulfide samples from outside of the active vent fields with ages of less than ~1,200 years. The myriad of venting sites along the axial valley floor prior to ~1,300 years ago may be the product of major faulting or diking events along the ridge segment, similar to current hydrothermal activity. However, evidence of venting for the last ~2,300 years at MEF, 850 years at High Rise, 1,500 years at Sasquatch, indicates major, long-lived hydrothermal conduits controlling fluid flow at these locations (Fig. 4.6). The timing of sulfide deposition outside the currently active fields does not coincide with the pulses of increased venting at MEF (500 to 1,250 years ago) or High Rise (500 to 750 years ago) indicating distinctly separate upflow histories in these areas.

Hydrothermal venting is commonly focused within the axial valley of intermediate-rate mid-ocean ridges, due to local shallow heat sources and enhanced permeability from normal faulting [*Hannington et al.*, 2005]. With spreading, sulfide deposits become progressively older away from the ridge axis, although this relationship may be complicated by local effects such as faulting, shallow diking events, and heterogeneous permeability [*Kappel and Ryan*, 1986; *Lalou et al.*, 1985; *Petersen et al.*, 2009].

Results from this study support the general observation that the age of inactive vent sites becomes progressively older away from the ridge axis (Fig. 4.6), with active hydrothermal venting largely restricted to the present valley floor, and only minor, diffuse venting occurring on the valley walls and half-grabens [*Hannington et al.*, 2005]. The axial valley-bounding normal faults can be traced over several kilometers of ridge length and are spatially associated with older sulfide deposits [*J R Delaney et al.*, 1992; *Kadko and Butterfield*, 1998]. Whereas dated sulfides on the valley floor are mostly younger than 2,000 years, three samples from a bench on the eastern half graben are as much as 1,000 years older (Fig. 4.6). The oldest dated sulfide (5,850 years) is furthest from the ridge axis, situated outside the axial valley on the western volcanic ridge, and ~200 m west of the outermost valley fault scarp.

Because of the link between seismicity and hydrothermal discharge at Endeavour [*Wilcock et al.*, 2009], the dating of the sulfide deposits sheds new light on the history of axial valley formation. The pattern of progressively younger hydrothermal venting, from outside the axial valley towards the central valley floor suggests that faulting has migrated inwards

towards the center of the valley (Fig. 4.6), similar to the inward migration of axial valley-bounding faults on slow-spreading ridges [*Macdonald,* 1982; *Solomon et al.,* 1988]. In the southern half (Mothra to MEF) of the Endeavour Segment, active venting occurs along the innermost western fault scarp, which acts as the primary conduit for hydrothermal upflow [*J R Delaney et al.*, 1992; *D. A. Glickson et al.,* 2007; *Kelley et al.*, 2001]. Heat flow measurements by *Johnson et al.* [2010] for the MEF area are consistent with upflow occurring along the western edge of the axial valley, and recharge occurring at the eastern valley wall and half-grabens.

On fast-spreading ridges, deposits outside the axial valley are generally inactive because they are spread rapidly away from the shallow, focused axial heat source. At Endeavour, ridge flank sulfide deposits outside of the axial valley may have formed on the ridge crest, before axial valley formation. Alternately, off-axis sulfide deposition may have resulted from hydrothermal pulses associated with volcanic eruptions or dike emplacement on the ridge flanks that occurred after initial axial valley formation. If the hydrothermal deposit on the western ridge flank, from which sample D264-R22 was taken, formed prior to the current axial valley, the age of the sample can be used to constrain the maximum age of the valley to ~5,850 years. Sulfide precipitation on the eastern half-graben at 2,930 years suggests that, by this time, the valley floor was at the level of this bench, which formed the eastern edge of the axial valley floor. Hydrothermal venting occurred both on the eastern half-graben and the valley floor between ~2,270 and 1,710 years ago. As the axial rift deepened, a configuration similar to what exists today was developed. The lack of sulfides from the eastern half-graben with ages of <1,700 years suggests that hydrothermal activity on the eastern half-graben may have ceased at this time, and further venting was

constrained to the new axial valley that exists today. However, further sampling is required to fully test this interpretation. The sulfide ages suggest that hydrothermal venting was widespread over the valley floor until ~1,230 years ago, after which time venting appears to have contracted into the current vent fields.

7.2 The age of the valley floor and rate of spreading

Sulfide ages define the minimum ages for the substrate on which they are deposited. Portions of the current axial valley floor at Endeavour are thus older than ~2,300 years. The single sample from the top of the western volcanic ridge constrains the lava flow in that immediate area to >5,850 years. These ages are consistent with magma supply and tectonic extension of intermediate-rate spreading centers being periodic over time scales of 1,000 to 100,000 years [*Kappel and Ryan*, 1986; *Karsten et al.*, 1990]. However, at this point, limited spatial resolution of sulfide ages along the ridge segment prevents a reconstruction of the eruptive history at Endeavour, as the dated sulfides are more widely spaced than individual lava flows.

The axial valley floor is composed of a combination of collapsed pre-existing crust forming a graben system, and basalt flows that post-date axial-valley formation. Although no volcanic activity has been recognized at Endeavour over the past 30 years, evidence of diking events along the Endeavour Segment is well documented [*Bohnenstiehl et al.*, 2004; *Carbotte et al.*, 2012; *Hooft et al.*, 2010; *Kelley et al.*, 2012; *Wilcock et al.*, 2009]. Extension along the ridge segment in the recent past has likely been accommodated by both diking and the normal faulting, and thus the age of the valley cannot be simply related to the valley width and spreading rate. The cumulative horizontal displacement of the normal

faults at the seafloor (Table 3) combined with the age of the axial valley, can be used to determine the rate of fault-accommodated spreading along the segment. Horizontal displacements were measured from three cross-sectional profiles of the axial valley, oriented perpendicular to the ridge axis (Fig. 4.7). Most faults are roughly parallel to the length of the axial valley, continuous over several kilometers, and have exposed scarps that dip towards the center of the valley (with the exception of a few minor antithetic faults) (Fig. 4.7). Faults are divided into east-dipping and west-dipping faults on the western and eastern flanks of the valley, respectively. Fault throws were measured along three cross sections that strike perpendicular to the ridge axis (Fig. 4.7). Faults that bound the central horst hosting the High Rise field in section C-C' are included, although their spatial relationship to the locus of spreading is uncertain (Fig. 4.7).

The results show that fault-accommodated extension on either side of the valley is essentially symmetrical, with the average total measured extension across the western valley wall within 3% of extension along the eastern wall. Between sections A-A' and C-C', the total horizontal extension across the valley is also relatively constant along its length, ranging from 425 to 435 m (±5 m) for the three cross sections, and averaging 430 m.

Using the maximum valley age of 5,850 ± 210 years, as defined by the age of the single sulfide from the top of the western volcanic ridge, extension accommodated by normal faults (i.e. not including extension due to dike emplacement and volcanic eruptions) has been occurring at a full rate of at least 7.3 cm/yr. The currently accepted full spreading rate of ~6 cm/yr for the Juan de Fuca Ridge, defined using magnetic anomaly analysis

[*Riddihough*, 1984] and U-Th ages of basalts [*Goldstein et al.*, 1991], is an average over the length of the entire ridge and integrates tens of thousands to several million years of extension. This spreading rate could vary over shorter timescales and along different segments of the ridge [*Riddihough*, 1984]. Based on movement vectors calculated for either side of the axial valley of the Endeavour Segment, relative to the North American Plate, using the GPS velocity-generated Global Strain Rate Map (GSRM 1.2) [*Kreemer et al.*, 2003], the ridge segment is currently spreading at a rate of 4.9 ± 0.2 cm/yr. The fast rate calculated using fault-related extension and the suggested age of the axial valley may be an indication that the axial valley is in fact older than the oldest dated sulfide (~5,850 years old). Further work will be necessary to constrain the age of the axial valley, to better understand the relationship between normal faulting, diking events and spreading rate.

7.3 Ages of sulfides at other mid-ocean ridges

A compilation of seafloor sulfide ages from mid-ocean ridges (n = 249) reveals deposit ages that range from <10 years to >100,000 years (Fig. 4.8). With the exception of data from this study, the majority of ages were determined using shorter-lived U-series isotope systems such as ^{210}Pb/Pb (<150 years) or longer-lived systems such as ^{230}Th/^{234}U (> ~2,000 years). This results in a significant gap in recorded sulfide ages between ~200 to 2,000 years, because neither the short- nor long-lived isotope systems can resolve ages within this time interval (highlighted by the black hatched pattern in Fig. 4.8). The ^{226}Ra/Ba dating technique, with an effective range of ~150 to 20,000 years (highlighted in blue) fills this important gap. Besides this study, the only other sulfides with ages that fall within this time gap are from the Brothers Volcano, on the southern Kermadec Arc and other locations in the western Pacific [*de Ronde et al.*, 2005; *Ditchburn et al.*, 2012]: the only other studies

with ages reported using this technique. The majority of older ages (>~10,000 years) are from deposits on the intermediate-rate Central Indian Ridge, the slow-spreading Mid-Atlantic Ridge, and the ultra-slow Southwest Indian Ridge [*Cherkashov et al.*, 2010; *Kuznetsov et al.*, 2011; *Lalou et al.*, 1998; *Munch et al.*, 2001; *Shilov et al.*, 2012]. The oldest documented seafloor sulfide sample was dated at 176,200 ± 59,000 years from the Petersburg site (19°52′ N), on the Mid-Atlantic Ridge [*Shilov et al.*, 2012]. In most cases, only the most recent deposits near the spreading axes have been dated; deposits that are more than 5 km off-axis would have formed on crust that is at least ~250,000 years old. The paucity of information on older deposits is a reflection of the difficulty in locating inactive, off-axis deposits and the focus by researchers on active systems. The fate of these inactive sulfide deposits over time remains unclear, with preservation on the seafloor affected by sulfide oxidation, burial by sediment, and microbial activity.

Compared to the ages of sulfides from intermediate-, slow-, and ultra-slow-spreading ridges, the maximum age from the axial summit trough of the fast spreading East Pacific Rise (13°N) is only 170 years [*Lalou et al.*, 1985]. The negative correlation between deposit age and spreading rate (Fig. 4.9) is likely a reflection of the amount of time a section of oceanic crust resides within the hydrothermally active neovolcanic zone of a spreading center, the propensity for lava flows to cover the hydrothermal sites more often, and the reorganization of hydrothermal upflow zones associated with diking eruptive events. Because the age range provided by the ^{226}Ra/Ba technique overlaps with typical ages of deposits from fast-, intermediate- and slow-spreading ridges, this dating technique should be applicable to barite-hosting seafloor sulfide deposits from a range of tectonic environments.

8. Conclusions

Radium-226 dating of hydrothermal barite provides an important chronometer for investigating the temporal evolution of hydrothermal vents at mid-ocean ridges. Barite is a common mineral in many hydrothermal settings and is resistant to seafloor weathering processes. The ^{226}Ra/Ba technique provides an important bridge between shorter- and longer-lived isotope systems for dating seafloor hydrothermal deposits. With this technique 61 samples were analyzed from the Endeavour Segment, 12 samples of zero-age, and 49 samples with ages that range from 20 to 5,850 years old. Current hydrothermal activity at MEF, High Rise and Sasquatch fields has been ongoing for the past ~2,270, 850 and 1,470 years, respectively. At MEF and High Rise, the majority of samples have ages between 500 and 1,500 years old and the data show no significant hiatuses in venting throughout their histories. This information could provide insights into the timing and mechanisms of vent field faunal colonization and community evolution.

Hydrothermal venting at the Endeavour Segment is intimately linked to diking events, associated faulting, and magma chambers that extend beneath all known currently active vent sites. The temporal and spatial history of venting appears to have been closely related to formation of the axial valley. The link between hydrothermal activity and axial valley evolution can be broken down into 3 stages: 1) initial volcanic ridge collapse after ~5,850 years ago, and formation of a shallow, broad axial valley; 2) further faulting that resulted in a more narrow, deeper axial valley floor, with extensive hydrothermal activity on the valley floor and half-grabens at ~2,200 years ago; 3) waning hydrothermal activity along the ridge

segment, with venting restricted to the sites of current active vent fields. The age of the axial valley and the horizontal offset of the axial valley-bounding normal faults result in a fault-accommodated full-spreading rate for this part of the segment of 7.3 cm/yr, slightly higher than estimates of ~6 cm/yr for the entire Juan de Fuca Ridge.

References

Alt, J. C., P. Lonsdale, R. Haymon, and K. Muehlenbachs (1987), Hydrothermal sulfide and oxide deposits on seamounts near 21-degrees-N, East Pacific Rise, *Geological Society of America Bulletin, 98*(2), 157-168.

Baker, E. T., and C. R. German (2004), On the global distribution of hydrothermal vent fields, *Mid-Ocean Ridges: Hydrothermal Interactions between the Lithosphere and Oceans*, *148*, 245-266.

Barclay, A. H., and W. S. D. Wilcock (2004), Upper crustal seismic velocity structure and microearthquake depths at the Endeavour Segment, Juan de Fuca Ridge, *Geochemistry Geophysics Geosystems, 5*.

Bohnenstiehl, D. R., R. P. Dziak, M. Tolstoy, C. G. Fox, and M. Fowler (2004), Temporal and spatial history of the 1999-2000 Endeavour Segment seismic series, Juan de Fuca Ridge, *Geochemistry Geophysics Geosystems, 5*.

Butterfield, D. A., R. E. McDuff, M. J. Mottl, M. D. Lilley, J. E. Lupton, and G. J. Massoth (1994), Gradients in the composition of hydrothermal fluids from the Endeavour Segment vent field - Phase-separation and brine loss, *Journal of Geophysical Research-Solid Earth*, *99*(B5), 9561-9583.

Butterfield, D. A., I. R. Jonasson, G. J. Massoth, R. A. Feely, K. K. Roe, R. E. Embley, J. F. Holden, R. E. McDuff, M. D. Lilley, and J. R. Delaney (1997), Seafloor eruptions and evolution of hydrothermal fluid chemistry, *Philosophical Transactions of the Royal Society of London Series a-Mathematical Physical and Engineering Sciences*, *355*(1723), 369-386.

Carbotte, S. M., J. P. Canales, M. R. Nedimovic, H. Carton, and J. C. Mutter (2012), Recent Seismic Studies at the East Pacific Rise 8 degrees 20 '-10 degrees 10 ' N and Endeavour Segment Insights into Mid-Ocean Ridge Hydrothermal and Magmatic Processes, *Oceanography*, *25*(1), 100-112.

Carbotte, S. M., R. S. Detrick, A. Harding, J. P. Canales, J. Babcock, G. Kent, E. Van Ark, M. Nedimovic, and J. Diebold (2006), Rift topography linked to magmatism at the intermediate spreading Juan de Fuca Ridge, *Geology*, *34*(3), 209-212.

Cherkashov, G., et al. (2010), Seafloor Massive Sulfides from the Northern Equatorial Mid-Atlantic Ridge: New Discoveries and Perspectives, *Marine Georesources & Geotechnology*, *28*(3), 222-239.

Clague, D. A., D. W. Caress, H. Thomas, D. Thompson, M. Calarco, J. Holden, and D. Butterfield (2008), Abundance and distribution of hydrothermal chimneys and mounds on the Endeavour Ridge determined by 1-m resolution AUV multibeam mapping surveys., *Eos, Transactions, American Geophysical Union 89*(53: Fall Meeting Supplement Abstract V41B-2079).

Converse, D. R., H. D. Holland, and J. M. Edmond (1984), Flow-rates in the axial hot springs of the East Pacific Rise (21-degrees-N) - Implications for the heat budget and the formation of massive sulfide deposits, *Earth and Planetary Science Letters*, *69*(1), 159-175.

Davis, E., and H. Elderfield (2004), *Hydrogeology of the oceanic lithosphere*, Cambridge University Press.

de Ronde, C. E. J., et al. (2005), Evolution of a submarine magmatic-hydrothermal system: Brothers volcano, southern Kermadec arc, New Zealand, *Economic Geology*, *100*(6), 1097-1133.

Delaney, J., R. McDuff, V. Robigou, A. Schultz, M. Smith, J. Wells, V. Atnipp, and J. McClain (1990), Covariation in microseismicity and hydrothermal output in the Endeavour vent field (abstr.), *Eos, 71*, 1609.

Delaney, J. R., V. Robigou, R. E. McDuff, and M. K. Tivey (1992), Geology of a vigorous hydrothermal system on the Endeavour Segment, Juan de Fuca Ridge, *Journal of Geophysical Research-Solid Earth*, *97*(B13), 19663-19682.

Ditchburn, R. G., C. E. J. de Ronde, and B. J. Barry (2012), Radiometric Dating of Volcanogenic Massive Sulfides and Associated Iron Oxide Crusts with an Emphasis on Ra-226/Ba and Ra-228/Ra-226 in Volcanic and Hydrothermal Processes at Intraoceanic Arcs, *Economic Geology*, *107*(8), 1635-1648.

Embley, R. W., W. W. Chadwick, I. R. Jonasson, D. A. Butterfield, and E. T. Baker (1995), Initial results of the rapid response to the 1993 Coaxial event - relationships between hydrothermal and volcanic processes, *Geophysical Research Letters*, *22*(2), 143-146.

Glickson, D. A., D. S. Kelley, and J. R. Delaney (2006), The Sasquatch Hydrothermal Field: Linkages Between Seismic Activity, Hydrothermal Flow, and Geology, *American Geophysical Union, Fall Meeting 2006, Abstract #V23B-0614*.

Glickson, D. A., D. S. Kelley, and J. R. Delaney (2007), Geology and hydrothermal evolution of the Mothra Hydrothermal Field, Endeavour Segment, Juan de Fuca Ridge, *Geochemistry Geophysics Geosystems*, *8*.

Goldstein, S. J., M. T. Murrell, D. R. Janecky, J. R. Delaney, and D. A. Clague (1991), Geochronology and petrogenesis of MORB from the Juan de Fuca and Gorda Ridges by U-238 Th-230 disequilibrium, *Earth and Planetary Science Letters*, *107*(1), 25-41.

Grasty, R. L., C. W. Smith, J. M. Franklin, and I. R. Jonasson (1988), Radioactive orphans in barite-rich chimneys, Axial Caldera, Juan-de-Fuca Ridge, *Canadian Mineralogist*, *26*, 627-636.

Hannington, M., C. De Ronde, and S. Petersen (2005), Sea-Floor Tectonics and Submarine Hydrothermal Systems, edited, pp. 111-141, Economic Geology 100th Anniversary Volume.

Hannington, M., J. Jamieson, T. Monecke, S. Petersen, and S. Beaulieu (2011), The abundance of seafloor massive sulfide deposits, *Geology*, *39*(12), 1155-1158.

Hooft, E. E. E., et al. (2010), A seismic swarm and regional hydrothermal and hydrologic perturbations: The northern Endeavour segment, February 2005, *Geochemistry Geophysics Geosystems*, *11*.

Johnson, H. P., M. A. Tivey, T. A. Bjorklund, and M. S. Salmi (2010), Hydrothermal circulation within the Endeavour Segment, Juan de Fuca Ridge, *Geochemistry Geophysics Geosystems*, *11*.

Johnson, H. P., M. Hutnak, R. P. Dziak, C. G. Fox, I. Urcuyo, J. P. Cowen, J. Nabelek, and C. Fisher (2000), Earthquake-induced changes in a hydrothermal system on the Juan de Fuca mid-ocean ridge, *Nature*, *407*(6801), 174-177.

Kadko, D., and D. A. Butterfield (1998), The relationship of hydrothermal fluid composition and crustal residence time to maturity of vent fields on the Juan de Fuca Ridge, *Geochimica Et Cosmochimica Acta*, *62*(9), 1521-1533.

Kadko, D., R. Koski, M. Tatsumoto, and R. Bouse (1985), An estimate of hydrothermal fluid residence times and vent chimney growth-rates based on Pb-210-Pb ratios and

mineralogic studies of sulfides dredged from the Juan-de-Fuca Ridge, *Earth and Planetary Science Letters*, *76*(1-2), 35-44.

Kappel, E. S., and W. B. F. Ryan (1986), Volcanic episodicity and a nonsteady state rift-valley along northeast Pacific spreading centers - evidence from Sea Marc-I, *Journal of Geophysical Research-Solid Earth and Planets*, *91*(B14), 13925-13940.

Karsten, J. L., J. R. Delaney, J. M. Rhodes, and R. A. Liias (1990), Spatial and temporal evolution of magmatic systems beneath the Endeavour Segment, Juan de Fuca Ridge - Tectonic and petrologic constraints, *Journal of Geophysical Research-Solid Earth and Planets*, *95*(B12), 19235-19256.

Kelley, D. S., J. R. Delaney, and D. R. Yoerger (2001), Geology and venting characteristics of the Mothra hydrothermal field, Endeavour segment, Juan de Fuca Ridge, *Geology*, *29*(10), 959-962.

Kelley, D. S., J. A. Baross, and J. R. Delaney (2002), Volcanoes, fluids, and life at mid-ocean ridge spreading centers, *Annual Review of Earth and Planetary Sciences*, *30*, 385-491.

Kelley, D. S., et al. (2012), Endeavour Segment of the Juan de Fuca Ridge: one of the most remarkable places on Earth, *Oceanography*, *25*(1), 44-61.

Kim, K. H., and G. M. McMurtry (1991), Radial growth-rates and Pb-210 ages of hydrothermal massive sulfides from the Juan de Fuca Ridge, *Earth and Planetary Science Letters*, *104*(2-4), 299-314.

Kreemer, C., W. E. Holt, and A. J. Haines (2003), An integrated global model of present-day plate motions and plate boundary deformation, *Geophysical Journal International*, *154*(1), 8-34.

Kristall, B., D. S. Kelley, M. D. Hannington, and J. R. Delaney (2006), Growth history of a diffusely venting sulfide structure from the Juan de Fuca Ridge: A petrological and geochemical study, *Geochemistry Geophysics Geosystems*, *7*.

Kristall, B., D. Nielsen, M. D. Hannington, D. S. Kelley, and J. R. Delaney (2011), Chemical microenvironments within sulfide structures from the Mothra Hydrothermal Field: Evidence from high-resolution zoning of trace elements, *Chemical Geology*, *290*(1-2), 12-30.

Kuznetsov, V., F. Maksimov, A. Zheleznov, G. Cherkashov, V. BeL'Tenev, and L. Lazareva (2011), Th-230/U chronology of ore formation within the Semyenov hydrothermal district (13 degrees 31 ' N) at the Mid-Atlantic Ridge, *Geochronometria*, *38*(1), 72-76.

Kuznetsov, Y., G. A. Cherkashev, V. E. Bel'tenev, A. Y. Lein, F. E. Maximov, V. V. Shilov, and T. V. Stepanova (2007), The Th-230/U dating of sulfide ores in the ocean: Methodical possibilities, measurement results, and perspectives of application, *Doklady Earth Sciences*, *417*(8), 1202-1205.

Lalou, C., E. Brichet, and R. Hekinian (1985), Age dating of sulfide deposits from axial and off-axial structures on the East Pacific Rise near 12-degrees-50'N, *Earth and Planetary Science Letters*, *75*(1), 59-71.

Lalou, C., U. Munch, P. Halbach, and J. L. Reyss (1998), Radiochronological investigation of hydrothermal deposits from the MESO zone, Central Indian Ridge, *Marine Geology*, *149*(1-4), 243-254.

Lalou, C., J. L. Reyss, E. Brichet, P. A. Rona, and G. Thompson (1995), Hydrothermal activity on a 10(5)-year scale at a slow-spreading ridge, TAG hydrothermal field, mid-Atlantic Ridge 26-degrees-N, *Journal of Geophysical Research-Solid Earth*, *100*(B9), 17855-17862.

Lalou, C., J. L. Reyss, E. Brichet, M. Arnold, G. Thompson, Y. Fouquet, and P. A. Rona (1993), New-age data for mid-Atlantic Ridge hydrothermal sites - TAG and Snakepit chronology revisited, *Journal of Geophysical Research-Solid Earth*, *98*(B6), 9705-9713.

Langmuir, C., et al. (1997), Hydrothermal vents near a mantle hot spot: The Lucky Strike vent field at 37 degrees N on the Mid-Atlantic Ridge, *Earth and Planetary Science Letters*, *148*(1-2), 69-91.

Larson, B. I., M. D. Lilley, and E. J. Olson (2009), Parameters of subsurface brines and hydrothermal processes 12-15 months after the 1999 magmatic event at the Main Endeavor Field as inferred from in situ time series measurements of chloride and temperature, *Journal of Geophysical Research-Solid Earth*, *114*.

Lilley, M. D., D. A. Butterfield, J. E. Lupton, and E. J. Olson (2003), Magmatic events can produce rapid changes in hydrothermal vent chemistry, *Nature*, *422*(6934), 878-881.

Lowell, R. P., P. A. Rona, and R. P. Vonherzen (1995), Sea-floor hydrothermal systems, *Journal of Geophysical Research-Solid Earth*, *100*(B1), 327-352.

Macdonald, K. C. (1982), Mid-ocean ridges - fine scale tectonic, volcanic and hydrothermal processes within the plate boundary zone, *Annual Review of Earth and Planetary Sciences*, *10*, 155-190.

Moore, W. S., and D. Stakes (1990), Ages of barite-sulfide chimneys from the Mariana Trough, *Earth and Planetary Science Letters*, *100*(1-3), 265-274.

Munch, U., C. Lalou, P. Halbach, and H. Fujimoto (2001), Relict hydrothermal events along the super-slow Southwest Indian spreading ridge near 63 degrees 56 ' E - mineralogy, chemistry and chronology of sulfide samples, *Chemical Geology*, *177*(3-4), 341-349.

Petersen, S., K. Kuhn, T. Kuhn, N. Augustin, R. Hekinian, L. Franz, and C. Borowski (2009), The geological setting of the ultramafic-hosted Logatchev hydrothermal field (14 degrees 45 ' N, Mid-Atlantic Ridge) and its influence on massive sulfide formation, *Lithos*, *112*(1-2), 40-56.

Proskurowski, G., M. D. Lilley, and T. A. Brown (2004), Isotopic evidence of magmatism and seawater bicarbonate removal at the endeavour hydrothermal system, *Earth and Planetary Science Letters*, *225*(1-2), 53-61.

Reyes, A. O., W. S. Moore, and D. S. Stakes (1995), Th-228/Ra-228 ages of a barite-rich chimney from the Endeavour Segment of the Juan-de-Fuca Ridge, *Earth and Planetary Science Letters*, *131*(1-2), 99-113.

Riddihough, R. (1984), Recent movements of the Juan-de-Fuca plate system, *Journal of Geophysical Research*, *89*(NB8), 6980-6994.

Robigou, V., J. R. Delaney, and D. S. Stakes (1993), Large massive sulfide deposits in a newly discovered active hydrothermal system, the Highrise Field, Endeavour Segment, Juan-de-Fuca Ridge, *Geophysical Research Letters*, *20*(17), 1887-1890.

Seyfried, W. E., J. S. Seewald, M. E. Berndt, K. Ding, and D. I. Foustoukos (2003), Chemistry of hydrothermal vent fluids from the Main Endeavour Field, northern Juan de Fuca Ridge: Geochemical controls in the aftermath of June 1999 seismic events, *Journal of Geophysical Research-Solid Earth*, *108*(B9).

Shilov, V. V., V. E. Bel'tenev, V. N. Ivanov, G. A. Cherkashev, Rozhdestvenskaya, II, I. F. Gablina, I. G. Dobretsova, E. V. Narkevskii, A. N. Gustaitis, and V. Y. Kuznetsov (2012), New hydrothermal ore fields in the Mid-Atlantic Ridge: Zenith-Victoria (20 degrees 08 ' N) and Petersburg (19 degrees 52 ' N), *Doklady Earth Sciences*, *442*(1), 63-69.

Solomon, S. C., P. Y. Huang, and L. Meinke (1988), The seismic moment budget of slowly spreading ridges, *Nature*, *334*(6177), 58-60.

Sours-Page, R., K. T. M. Johnson, R. L. Nielsen, and J. L. Karsten (1999), Local and regional variation of MORB parent magmas: evidence from melt inclusions from the Endeavour Segment of the Juan de Fuca Ridge, *Contributions to Mineralogy and Petrology*, *134*(4), 342-363.

Stakes, D., and W. S. Moore (1991), Evolution of hydrothermal activity on the Juan-de-Fuca Ridge - observations, mineral ages, and Ra isotope ratios, *Journal of Geophysical Research-Solid Earth*, *96*(B13), 21739-21752.

Tivey, M. K., and J. R. Delaney (1986), Growth of large sulfide structures on the Endeavour Segment of the Juan-de-Fuca Ridge, *Earth and Planetary Science Letters*, *77*(3-4), 303-317.

Tivey, M. K., D. S. Stakes, T. L. Cook, M. D. Hannington, and S. Petersen (1999), A model for growth of steep-sided vent structures on the Endeavour Segment of the Juan de Fuca Ridge: Results of a petrologic and geochemical study, *Journal of Geophysical Research-Solid Earth*, *104*(B10), 22859-22883.

Van Ark, E. M., R. S. Detrick, J. P. Canales, S. M. Carbotte, A. J. Harding, G. M. Kent, M. R. Nedimovic, W. S. D. Wilcock, J. B. Diebold, and J. M. Babcock (2007), Seismic structure of the Endeavour Segment, Juan de Fuca Ridge: Correlations with seismicity and hydrothermal activity, *Journal of Geophysical Research-Solid Earth*, *112*(B2).

Volpe, A. M., and S. J. Goldstein (1993), Ra-226 Th-230 disequilibrium in axial and off-axis midocean ridge basalts, *Geochimica Et Cosmochimica Acta*, *57*(6), 1233-1241.

Von Damm, K. L. (1990), Seafloor hydrothermal activity - black smoker chemistry and chimneys, *Annual Review of Earth and Planetary Sciences*, *18*, 173-204.

Wilcock, W. S. D., S. D. Archer, and G. M. Purdy (2002), Microearthquakes on the Endeavour segment of the Juan de Fuca Ridge, *Journal of Geophysical Research-Solid Earth*, *107*(B12).

Wilcock, W. S. D., E. E. E. Hooft, D. R. Toomey, P. R. McGill, A. H. Barclay, D. S. Stakes, and T. M. Ramirez (2009), The role of magma injection in localizing black-smoker activity, *Nature Geoscience*, *2*(7), 509-513.

Table 4.1: ^{226}Ra activities and Ba content for "zero-age" hydrothermal sulfide samples.

Sample #	Vent Field	Structure	Lattitude	Longitude	Ba (wt.%)	^{226}Ra activity (Bq/kg)	^{226}Ra/Ba
ALV2449-1	MEF	Grotto	47.94911	-129.09868	1.6	1908.02 ± 6.69	1193
ALV4448-2211	MEF	TP	47.94898	-129.09885	0.9	1312.83 ± 5.46	1521
ALV4517-1718	MEF	Crypto	47.95008	-129.09696	0.7	1006.21 ± 4.73	1433
ALV4446-1735	MEF	Salut	47.94646	-129.09939	1.2	1759.90 ± 6.02	1479
ALV4452-1706	MEF	Hulk	47.95022	-129.09712	0.4	453.70 ± 2.94	1203
ALV4438-1816	MEF	Bastille	47.94789	-129.09954	0.3	415.05 ± 2.58	1348
ALV4525-0134	MEF	Dante	47.94948	-129.09778	0.7	971.53 ± 4.71	1363
ALV4449-1630	MEF	Hulk	47.95005	-129.09689	2.1	2670.88 ± 7.74	1254
ALV4517-1703	MEF	E. of Hulk	47.95012	-129.09696	0.5	725.05 ± 4.03	1549
ALV2461-R13 TIP	High Rise	Baltic	47.96796	-129.08747	4.6	6134.65 ± 14.65	1334
ALV2463-R5c3	High Rise	E. of Ventnor	47.968818	-129.08707	1.8	2411.88 ± 9.35	1340
D264-R3	S. of Salty Dawg	Marias	47.97601	-129.08115	0.7	1754.61 ± 113.47	2635

[1] Samples starting with 'ALV' or 'D' were collected using the *ALVIN* submersible or ROV *Dock Ricketts*, respectively. The three or four digits that immediately follow refer to the dive number for when the sample was collected. The number after the dash is either the sample number for that dive or the time at which the sample was collected (four digits).

Table 4.2: ^{226}Ra/Ba ages for inactive hydrothermal sulfides samples

Sample #[1]	Field	Lattitude	Longitude	Ba (wt.%)	^{226}Ra activity (Bq/kg)	Age[2] (years)
Active Vent Fields						
FINN-SPH	Mothra	47.92376	-129.10900	4.9	5837.28 ± 14.17	157 ± 127
ALV4450-1829	Mothra	47.92388	-129.10906	22.1	27894.95 ± 26.25	23 ± 127
ALV 2072-7	MEF	47.94911	-129.09868	5.0	5839.18 ± 12.33	202 ± 127
ALV3616-03	MEF	47.94732	-129.09911	0.1	127.19 ± 1.92	611 ± 132
ALV 3581-R-1	MEF	47.94719	-129.09891	33.0	27738.96 ± 49.15	961 ± 127
ALV 3589-R2	MEF	47.94921	-129.09797	11.0	8735.04 ± 24.37	1093 ± 127
ALV 2068-1	MEF	47.94781	-129.09955	23.0	21788.54 ± 37.51	686 ± 127
ALV 2072-1B	MEF	47.94911	-129.09868	7.5	5960.71 ± 11.87	1091 ± 127
TIVEY MISC-2	MEF	Dredge sample		33.0	20149.55 ± 38.15	1699 ± 127
HYS 278-4	MEF	47.94921	-129.09797	1.3	1068.59 ± 5.50	1013 ± 128
ALV2404-4	MEF	47.94178	-129.09743	0.9	753.19 ± 4.07	946 ± 128
ALV2415-1D(3)	MEF	47.94975	-129.09695	2.7	2493.30 ± 7.52	744 ± 127
ALV2408-1A	MEF	47.94975	-129.09743	1.7	1338.46 ± 8.98	1044 ± 128
ALV2452-2	MEF	47.94786	-129.09851	1.7	786.17 ± 4.50	2272 ± 128
ALV4438-1635	MEF	47.94745	-129.09725	0.8	501.40 ± 3.89	1530 ± 128
ALV4446-1628	MEF	47.94642	-129.09725	1.3	950.00 ± 4.43	1194 ± 127
ALV3587-R-1	MEF	47.94608	-129.09936	6.1	4628.02 ± 12.34	1198 ± 127
TIVEY-MISC 1	MEF	47.94921	-129.09797	0.9	681.05 ± 3.11	1139 ± 127
HYS 280-16	MEF	47.94921	-129.09797	1.1	961.13 ± 4.63	872 ± 127
TIVEY MISC 7	MEF	Dredge sample		1.1	1121.55 ± 4.58	516 ± 127
ALV 1452-1A	MEF	47.94921	-129.09797	12.0	6207.94 ± 18.68	2082 ± 127
ALV1452-2	MEF	47.94921	-129.09797	8.5	8431.70 ± 16.46	579 ± 127
J2-59-4 Misc	MEF	47.94755	-129.09918	1.0	874.15 ± 5.41	848 ± 128
ALV2461-R13/1	High Rise	47.96796	-129.08747	0.3	307.41 ± 2.46	345 ± 128
ALV2463-R3-3	High Rise	47.96778	-129.08928	22.0	19469.19 ± 43.03	843 ± 127
ALV 2460-R2-14a	High Rise	47.96882	-129.08707	2.6	2652.88 ± 8.11	514 ± 127
ALV 2463-R4-pc	High Rise	47.96778	-129.08928	26.0	26222.69 ± 46.25	541 ± 127
ALV2461-R13/4	High Rise	47.96796	-129.08747	5.6	6263.84 ± 16.96	302 ± 127
ALV2460-R3-3c	High Rise	47.96882	-129.08707	1.0	984.95 ± 6.33	549 ± 128
ALV2461-R6-4	High Rise	47.96846	-129.08734	1.5	1488.56 ± 6.97	578 ± 127
ALV2461-R13-4-BOT	High Rise	47.96796	-129.08747	1.0	1055.93 ± 6.87	365 ± 128
ALV2461-R13/3	High Rise	47.96796	-129.08747	1.1	1178.97 ± 6.77	401 ± 128
ALV2464-R8-1b	High Rise	47.96846	-129.08734	1.1	1080.05 ± 6.45	603 ± 128
ALV2461-R11-9	High Rise	47.96688	-129.08734	1.2	1169.15 ± 7.39	621 ± 128
ALV2927-A	High Rise	47.96846	-129.08734	2.7	2604.45 ± 9.34	644 ± 127
ALV2460-R3-3	High Rise	47.96882	-129.08707	1.2	1149.55 ± 5.69	660 ± 127

ALV3000-SpireB	Salty Dawg	47.98213	-129.07584	2.2	2294.38	±	7.87	464	±	127
ALV 3622-01A	Sasquatch	47.99667	-129.06637	5.4	3650.29	±	9.74	1465	±	127
ALV4451-1725	Sasquatch	47.99666	-129.06668	0.2	194.33	±	2.52	718	±	130
Axial valley floor, outside active fields										
R1384-1009-Ba	S. of Mothra	47.90583	-129.12194	0.4	252.45	±	3.57	1315	±	131
ALV2467-R9	N. of Clam Bed	47.96440	-129.09110	8.7	5771.96	±	20.14	1494	±	127
ALV2467-R3	N. of MEF	47.95556	-129.09580	26.5	14566.33	±	36.38	1942	±	127
ALV2467-R2	N. of MEF	47.95500	-129.09500	23.1	11503.51	±	27.36	2170	±	127
ALV2464-R5-3	N. of High Rise	47.97060	-129.08810	1.7	1272.49	±	6.78	1229	±	128
D265-R8	N. of Sasquatch	47.99877	-129.06266	2.3	1618.78	±	106.3	1321	±	198
Eastern half-graben										
D266-R9		47.958965	-129.08401	2.5	904.46	±	65.97	2926	±	211
D266-R5		47.956874	-129.08483	0.6	339.8	±	21.48	1706	±	193
D266-R4		47.956927	-129.08545	9.9	5802.44	±	381.89	1794	±	198
Outside axial valley										
D264-R22		47.948285	-129.10773	6.1	618	±	43.1	5853	±	205

[1] Samples starting with 'ALV' or 'D' were collected using the *ALVIN* submersible or ROV *Doc Ricketts*, respectively. The three or four digits that immediately follow refer to the dive number for when the sample was collected. The number after the dash is either the sample number for that dive or the time at which the sample was collected (four digits).

[2] The reported sample ages and their associated uncertainties are absolute values directly from the decay equation and propagation of analytical uncertainties (see Appendix F). Ages are reported in the text with a precision that that reflects an 8% coefficient of variability, based on repeat analyses of IAEA standard soil #375.

Table 4.3: Cumulative horizontal offsets of normal faults within axial valley.

Cross-section	Pacific Plate		Juan de Fuca Plate		Central Horst		TOTAL
	n	(m)	n	(m)	n	(m)	(m)
A-A'	6	215	7	210			425
B-B'	4	225	4	210			435
C-C'	3	145	4	185	2	100	430
Average	4	195	5	200	2	100	430

Figure 4.1

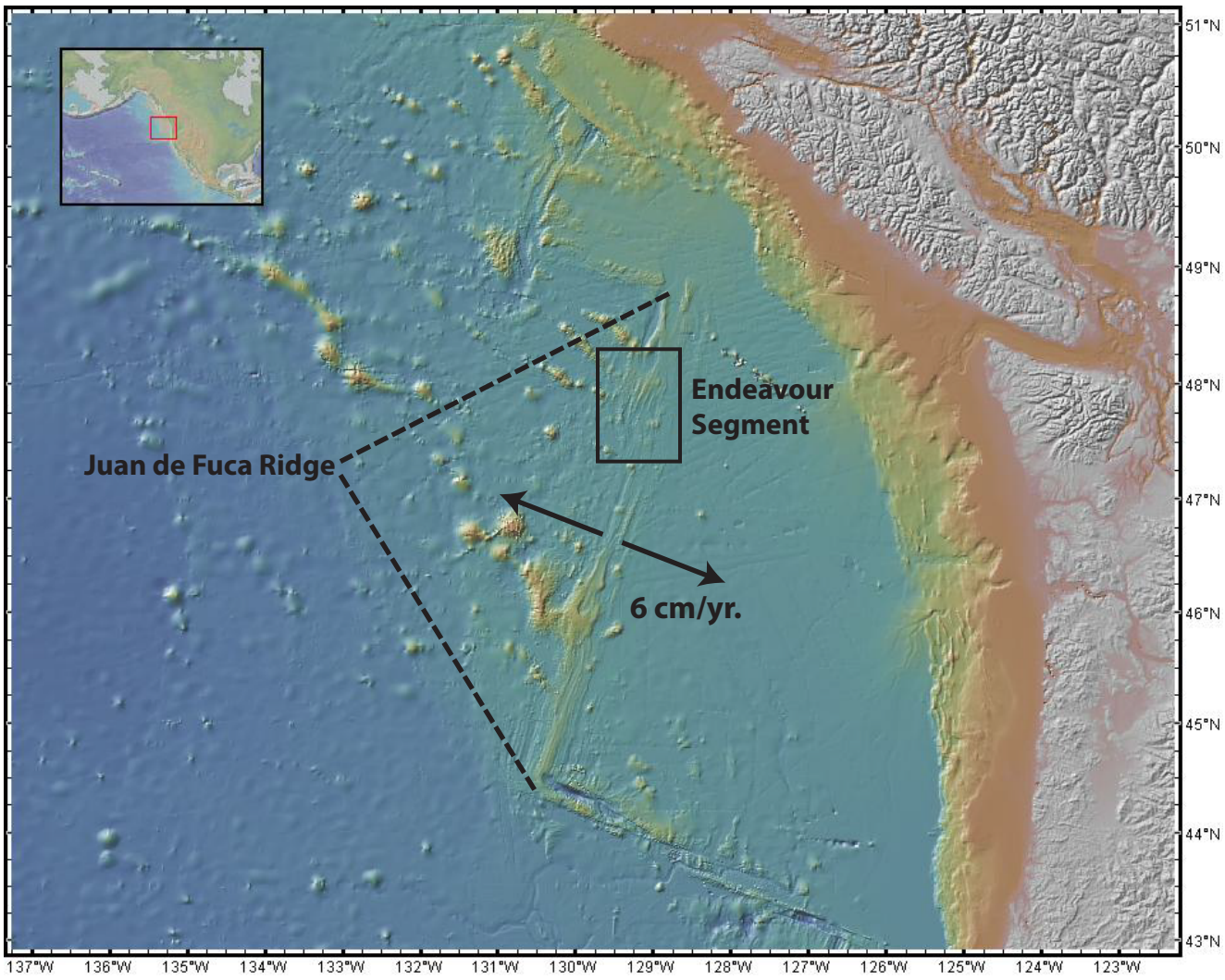

Figure 4.1: Map of the NW Pacific Ocean, east of Washington State, showing the location of the Endeavour Segment (black box) on the Juan de Fuca Ridge. The ridge separates the Pacific plate from the Juan de Fuca plate and is spreading at a full rate of ~6 cm/yr [Riddihough, 1984; Goldstein et al., 1991]. Bathymetry is from Smith and Sandwell v9.1 [1997].

Figure 4.2

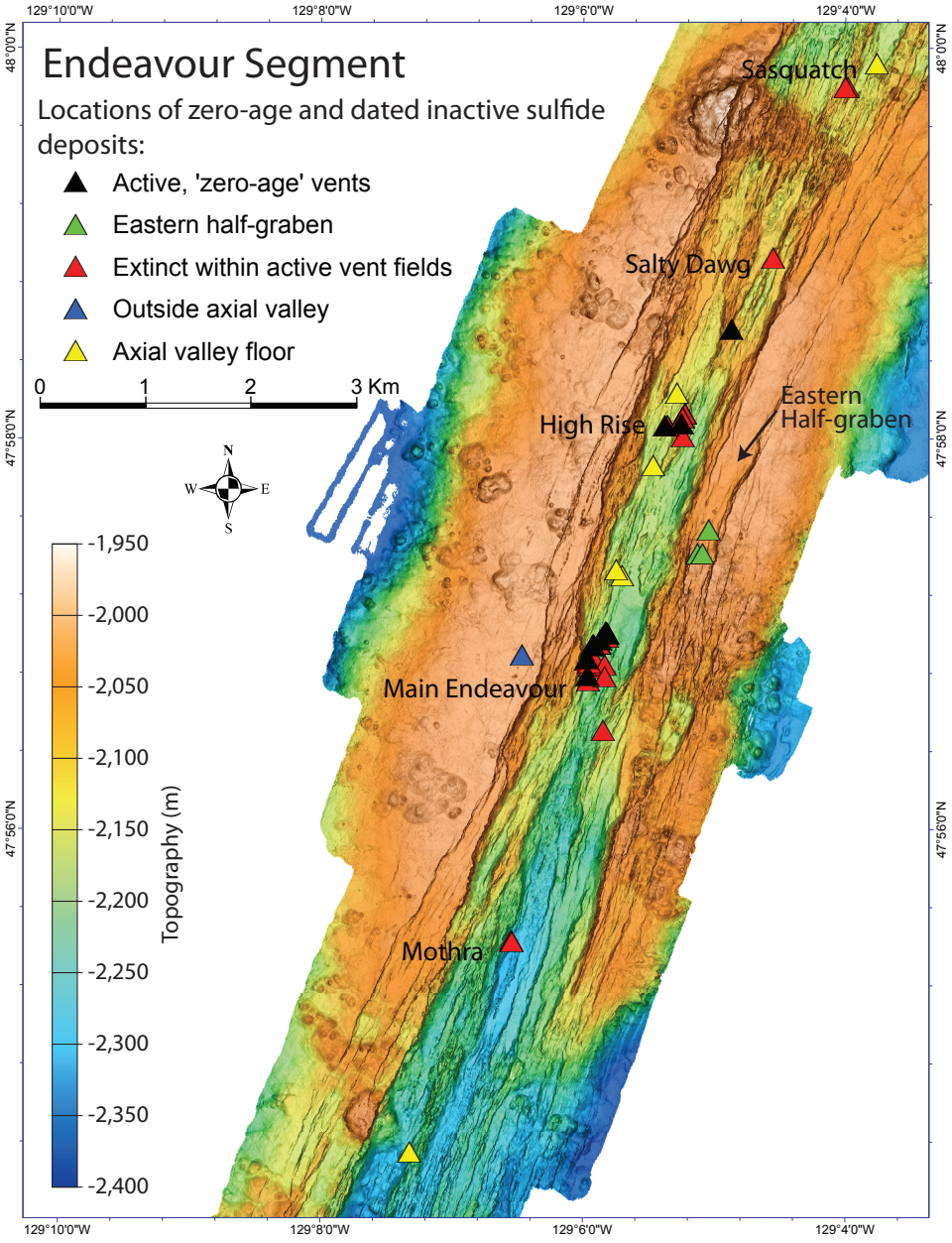

Figure 4.2: Detailed bathymetric map of the Endeavour Segment, with locations of the active vent fields and the hydrothermal sulfide samples dated in this study. The majority of samples were collected from active vent fields or inactive sites on the axial valley floor. Three samples were collected from a half-graben on the eastern valley wall, and a single sample was collected from outside the axial valley, on the western volcanic ridge. Bathymetry is 1-meter resolution, collected between 2008 and 2011 using the Monterey Bay Aquarium Research Institute (MBARI) autonomous underwater vehicle (AUV) D. Allan B.

Figure 4.3

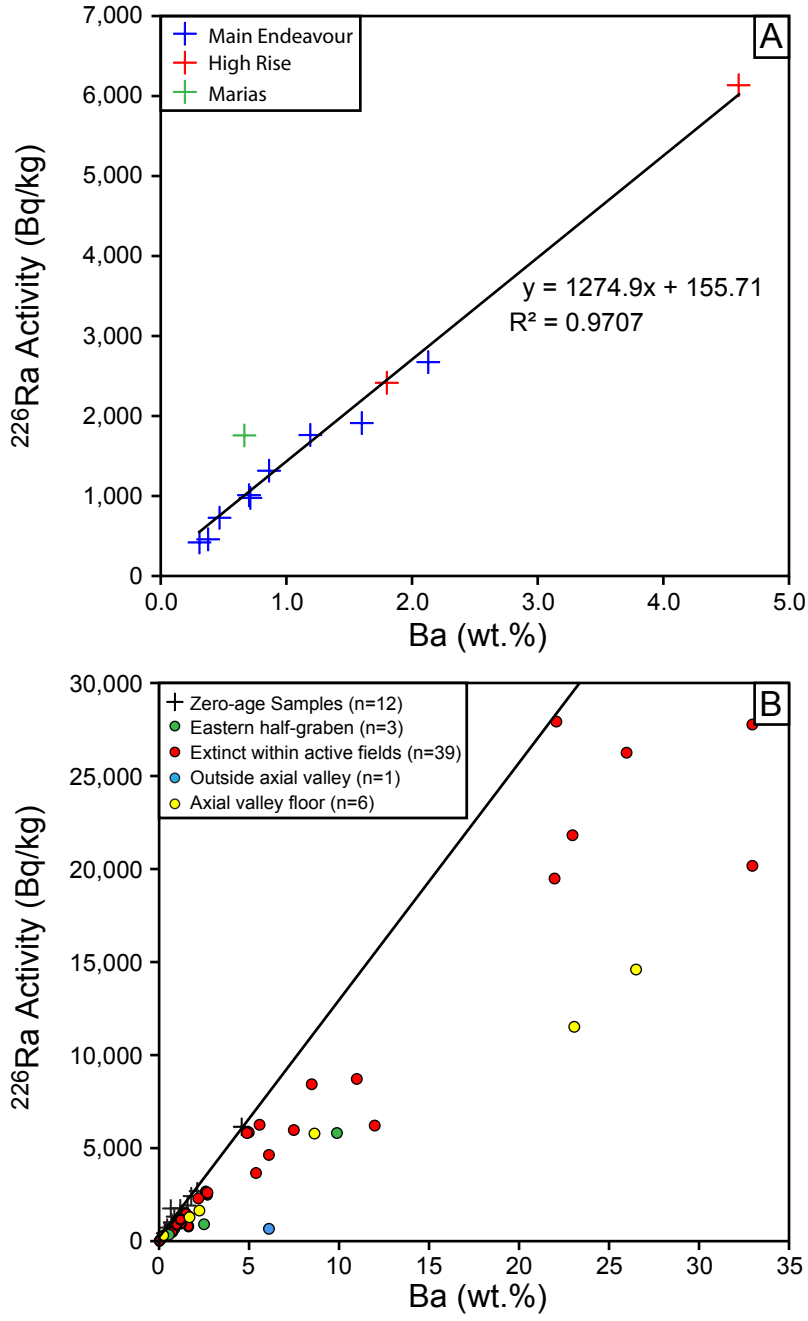

Figure 4.3: A: 226Ra activity versus Ba content for 'zero-age' samples from the Endeavour Segment. The slope of the linear regression line represents the initial 226Ra/Ba value (N_0) for all inactive sulfides along the Endeavour Segment. The uncertainty for N_0 is calculated from the standard deviation of the slope of the regression line. B: 226Ra activity versus Ba content for inactive samples from the Endeavour Segment. Solid line represents zero-age values (from A). As samples age, their 226Ra/Ba ratio will follow a vertical path downward from their initial ratio, located on the solid line. For both A and B, uncertainties are smaller than the size of the symbol.

Figure 4.4

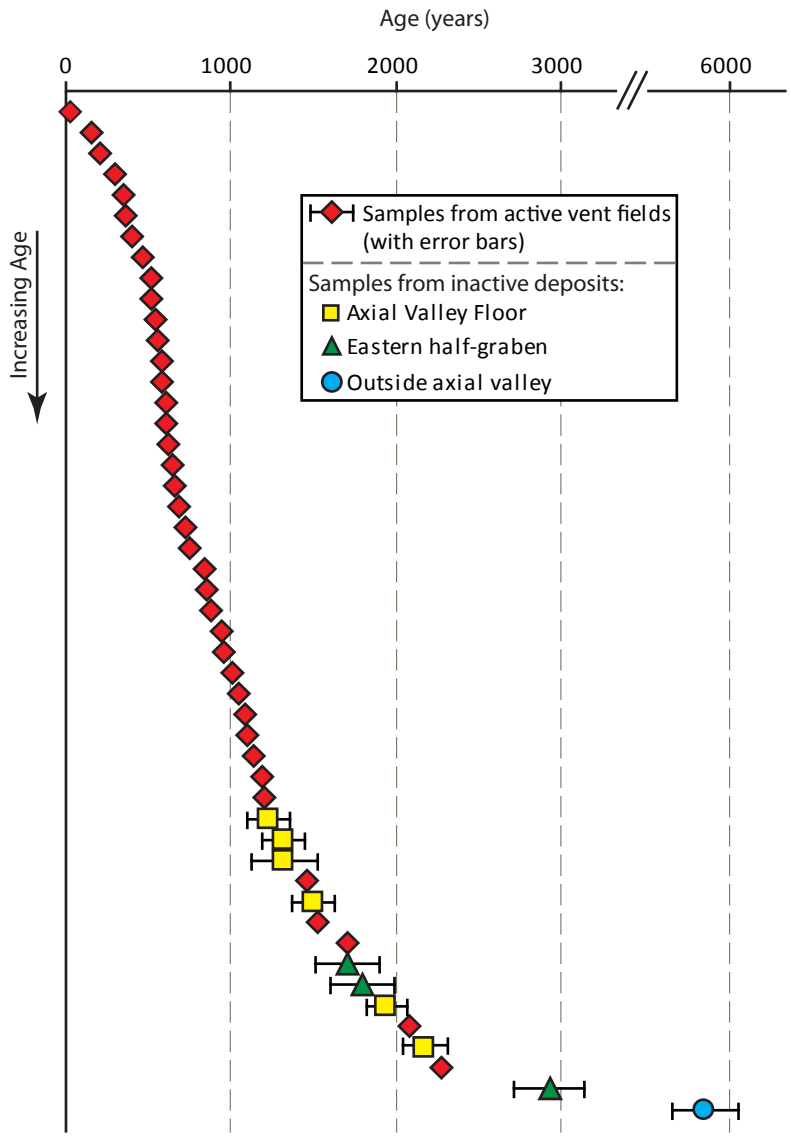

Figure 4.4: Age distribution of hydrothermal sulfide samples from the Endeavour Segment. Forty-eight of forty-nine samples are younger than 3,000 years. The oldest sample, ~6,000 years old is twice as old as the next oldest sample, and is from outside the axial valley. Samples younger than ~1,300 years are all from the active vent fields.

Figure 4.5

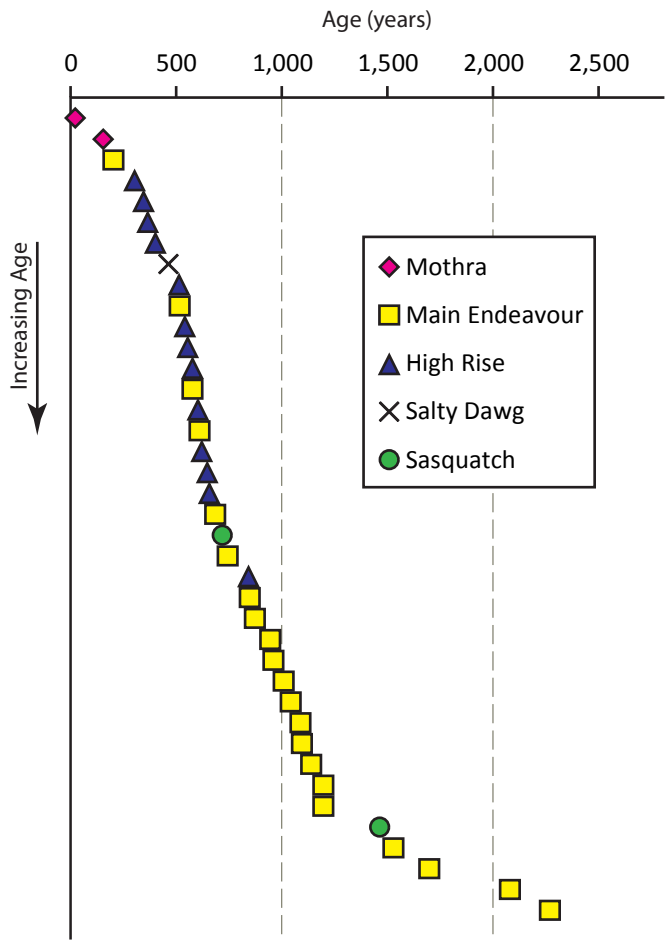

Figure 4.5: Age distribution of hydrothermal sulfides from the five active vent fields. For both MEF and High Rise Fields, sulfide precipitation has been relatively continuous since the earliest recorded evidence of venting at each respective site, suggesting a static upflow zone over the lifespan of these vent fields.

Figure 4.6

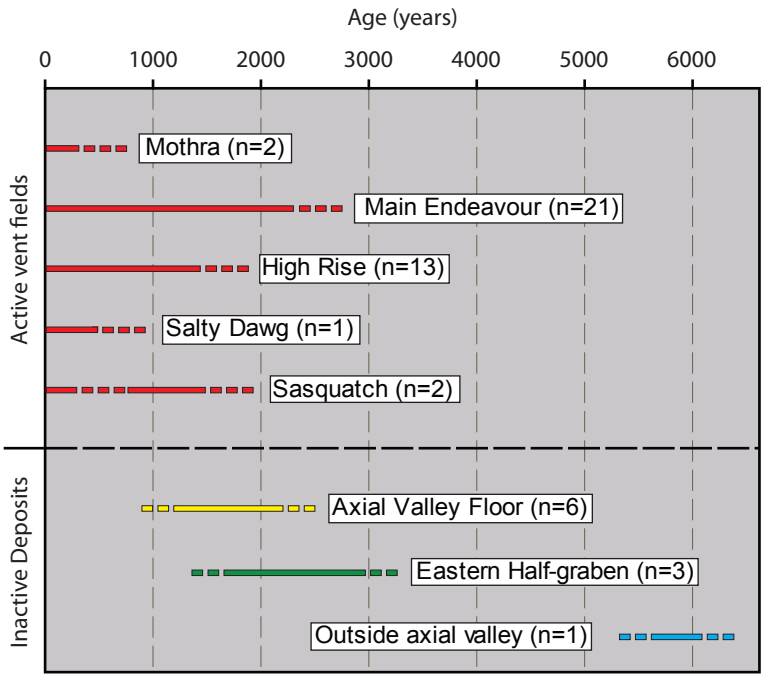

Figure 4.6: Summary of deposit ages, subdivided by vent field (top) and location on the ridge outside of the active vent fields (bottom). Solid line segments represent age ranges constrained by sulfide ages. Dashed lines segments for the active vent fields indicate that the oldest ages represent minimum ages for the vent fields. The dashed segment between ~0 – 700 years for the Sasquatch field indicates that no samples were collected from this active field that are younger than ~700 years. The ages of the inactive deposits are generally older, and their timelines remain open ended until more samples can be dated.

Figure 4.7

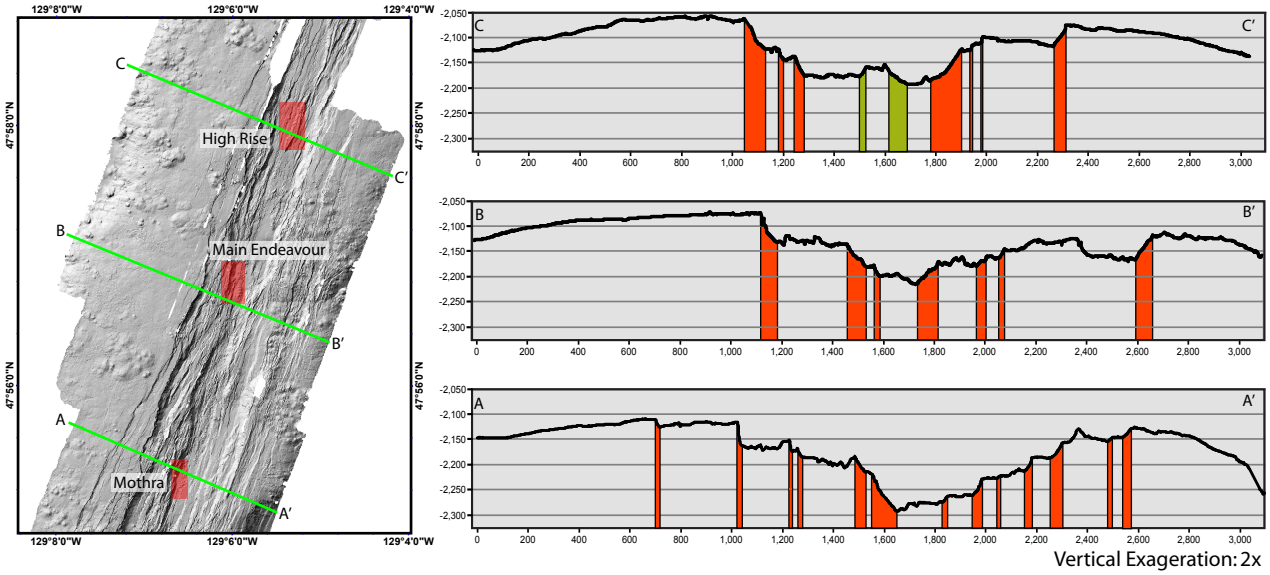

Figure 4.7: Hill-shaded map of the central Endeavour Segment showing locations of cross-sections. Shaded areas show total horizontal offset for each fault on the valley walls (orange) and the central graben in section C-C′ (green). Total offsets summarized in Table 3.

Figure 4.8

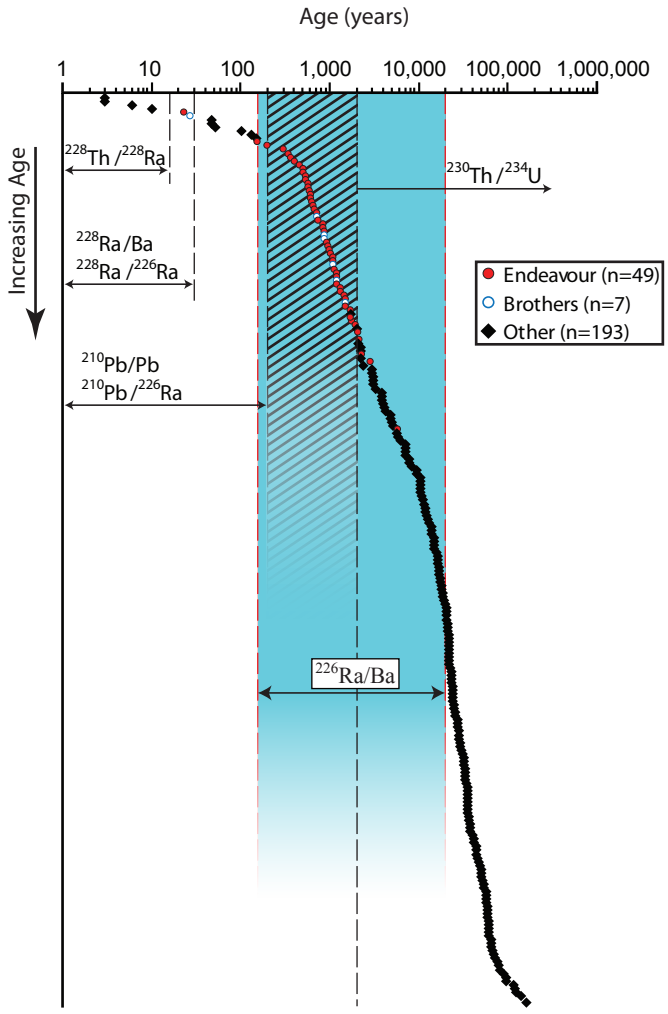

Figure 4.8: Age distribution of 249 sulfides from 18 seafloor hydrothermal deposits around the world. The oldest sulfide dated so far is only 176,200 years old, from the Petersburg site, Mid-Atlantic Ridge [Shilov et al., 2012]. The effective age ranges for different U-series isotope systems are indicated, with the 226Ra/Ba system highlighted in blue. Samples from Endeavour (this study) and Brothers [de Ronde et al., 2005] are the only samples dated using the 226Ra/Ba system. All other samples were dated using the shorter-lived systems for younger samples, or 230Th/234U for older samples. The black hatched pattern shows the age gap between other U-series systems that is effective bridged by the 226Ra/Ba system. Data from [Lalou and Brichet, 1982; Grasty et al., 1988; Lalou et al., 1995; Lalou et al., 1996; Lalou et al., 1998; de Ronde et al., 2005; Cherkashov et al., 2010; Kuznetsov et al., 2011; Wang et al., 2012]

Figure 4.9

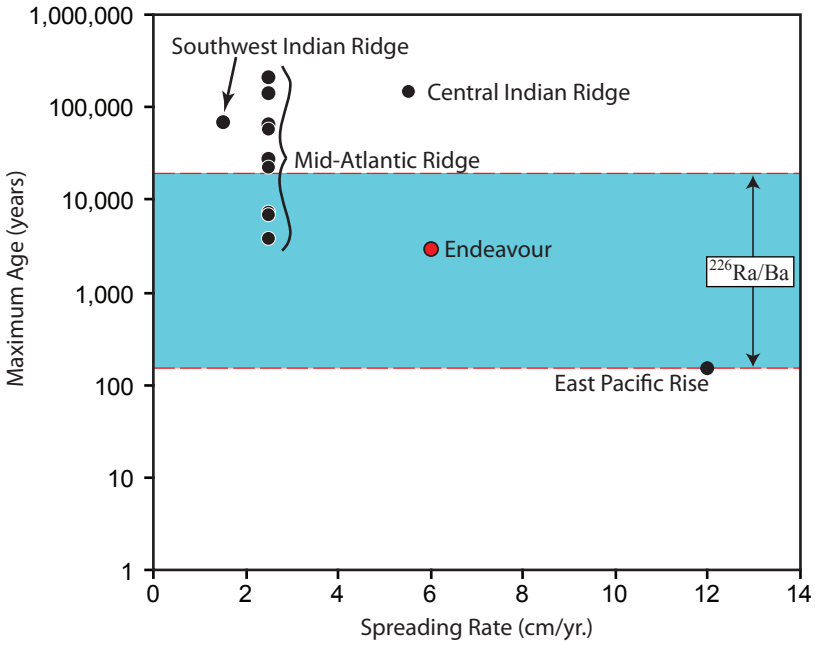

Figure 4.9: Plot of the maximum sulfide ages recorded from sulfide deposits within the axial valleys of mid-ocean ridges and spreading rate, with the maximum age from Endeavour of 5,853 years highlighted in red. Older deposits tend to occur on slower spreading ridges. The effective age range for the 226Ra/Ba technique is highlighted in blue. Data sources are the same as in Figure 7.

CHAPTER 5

VOLUMES, TONNAGES AND MASS ACCUMULATION RATES OF HYDROTHERMAL SULFIDE ALONG THE ENDEAVOUR SEGMENT, JUAN DE FUCA RIDGE

Abstract

A growing interest in seafloor hydrothermal sulfide deposits as an economic resource for Cu, Zn, Pb, Au and Ag has resulted in recent efforts to determine the amount and distribution of these deposits on the modern seafloor. Seafloor sulfide deposits are commonly located by the detection of hydrothermal plumes in the water column, followed by visual surveys. These methods, however, are ineffective for finding hydrothermally-inactive sulfide deposits, which may contain a significant amount of the seafloor sulfide 'resource'. Here, we present results from recent high-resolution, autonomous underwater vehicle-based mapping of the hydrothermally-active Endeavour Segment of the Juan de Fuca Ridge, in the Northeast Pacific Ocean. Analysis of the ridge bathymetry resulted in the location of 581 individual sulfide deposits along 24 km of ridge length. Sulfide deposits were distinguished from volcanic and tectonic features based on their characteristics of their surface morphology, such as shape and slope angles. Volume calculations for the hydrothermal deposits result in a total volume of 372,500 m^3, for an equivalent mass of ~1.2 Mt of sulfide within the ridge's axial valley. Much of this total resource is from previously undiscovered inactive deposits outside the main active vent fields. The calculated sulfide resource represents a four-fold increase over previous sulfide estimates for the Endeavour Segment, which were based largely on accumulations from within the active fields. These results suggest that recent global seafloor sulfide resource estimates, which were based mostly on the sizes and distribution of hydrothermally-active deposits, may be similarly underestimating the amount of sulfide along the spreading ridges, arcs and back-arc basins of today's oceans.

1. Introduction

Estimates of the rate of sulfide accumulation on the seafloor can be made from measurements of the chemical composition and flux of hydrothermal fluids at sites of active venting. However, over the life-span of a hydrothermal system, fluid composition and discharge rates can vary and measurements of vent fluid properties provide only a snapshot of the nature of hydrothermal activity in a given area (Butterfield et al., 1997; Embley et al., 1995; Hooft et al., 2010; Johnson et al., 2000; Kelley et al., 2012; Lilley et al., 2003; Seyfried et al., 2003). The sulfide deposits that form at sites of high-temperature venting on the seafloor provide a time-integrated record of the transfer of mass and heat to the seafloor from the underlying crust and, with age constraints from radiometric dating, the rates at which these processes occur (Humphris and Cann, 2000; Lalou et al., 1993a). An investigation of the hydrothermal mass flux at the scale of a ridge segment or larger, with potentially multiple active and formerly active, but now extinct, hydrothermal systems, requires knowing how much sulfide has accumulated in a given area. Active hydrothermal systems can be detected by their hydrothermal plumes in the water column (Baker and German, 2004). However, a complete visual survey (e.g., with a manned-submersible, ROV, camera-tow or autonomous instrument with a downward-facing camera) would be required to fully document all sulfide accumulation along a ridge segment, in order to locate the inactive deposits that have no associated hydrothermal plume. The time and cost for such an endeavor, however, would be prohibitive at the ridge segment scale. High-resolution (1 m) mapping of the seafloor, acquired using autonomous underwater vehicles (AUVs) provides an alternative method for identifying hydrothermal deposits on the seafloor that can be completed within days and does not rely on direct visual observation of the seafloor. This

method relies instead on the morphology of sulfide deposits (chimneys and mounds), relative to the volcanic and tectonic features that can dominate the seafloor morphology along mid-ocean ridges. Here, we present results from the analysis of hydrothermal sulfide distribution along the Endeavour Segment of the Juan de Fuca Ridge compiled from high-resolution AUV mapping. The volume and surface footprint of sulfide deposits along the segment, combined with previously determined ages of the deposits, allow for the determination of the rate of sulfide deposition at the ridge segment scale, and the efficiency of metal accumulation relative to estimated total metal flux to the seafloor along the segment.

2. Geologic Setting

The Juan de Fuca Ridge lies 500 km off the Oregon coast in the northeast Pacific Ocean and extends 500 km NNE towards Vancouver Island (Fig. 5.1). The ridge is spreading at a full-rate of 6 cm/yr and separates the Pacific Plate to the west from the smaller Juan de Fuca Plate to the east (Riddihough, 1984). The Endeavour Segment forms a 90 km section towards the north end of the Juan de Fuca Ridge (Fig. 5.1). The central portion of the Endeavour Segment is a 15 km-long, 4 km wide volcanic ridge that shallows to the north and south from a central high 2,050 meters below sea level (Delaney et al., 1992). The volcanic high is bisected by an axial valley that varies in width from 500 to 1000 m and consists of a central graben with a series of half-grabens forming step-wise valley walls that rise up 200 m from the valley floor (Fig. 5.2) (Delaney et al., 1992; Kappel and Ryan, 1986; Wilcock et al., 2009). There are five active vent fields within the axial valley, spaced over 15 km of ridge length with sites of minor venting between the active fields and abundant inactive sites of former venting (Delaney et al., 1992; Glickson et al., 2006; Kelley et al., 2002; Kelley et al.,

2012; Robigou et al., 1993). Age determinations of hydrothermal barite within sulfide deposits indicate that hydrothermal venting within the axial valley has been ongoing for at least the past ~3,000 years (Jamieson et al., 2013). The abundance of inactive sulfide deposits located along the Endeavour Segment, and age distribution of sulfides from active and inactive vent fields is evidence of a dynamic history of hydrothermal activity along the segment.

3. Methods

High-resolution bathymetry of the Endeavour Segment was collected with the AUV *D. Allan B.* with a Reson 7125 200 kHz multibeam sonar (Caress et al., 2008). This system generates 256 1° x 1° beams across a 135° swath, resulting in a 1.0 m resolution map with 10 cm vertical precision from a height of 50 m above the seafloor, at a speed of 3 knots. Eight ~18-hour surveys, along 23.8 km of ridge length, covering a total area of 61.93 km^2 were carried out in 2008 from the R/V *Atlantis* and in 2011 from the R/V *Zephyr*. The high resolution of these surveys allows for the identification of individual sulfide edifices that would not be detectable at lower resolutions typical of ship-based sonar systems.

Hydrothermal sulfide deposits within the mapped area were identified manually from the resulting bathymetric data. Sulfide edifices at Endeavour are positive features on the seafloor that generally have a rounded to sub-rounded footprint and steep sides (Figs. 5.3 and 5.4). They can often be distinguished from volcanic mounds (which are also commonly circular) by their steep and irregular sides, relative to the low angle of repose of erupted basalt on the seafloor (Fig. 5.4). There are, however, instances when volcanic structures on

the seafloor can have steep sides that exceed their normal angle of repose. Basalt pillars that result from collapsed lava lakes are steep-sided but generally have a very small footprint so that they are represented by only a single data point at 1 m resolution. For this reason, positive anomalies that are represented by only 1 data point are not included in the inventory, unless the height of the anomaly exceeds the maximum level of the former lava lake, which is also commonly distinguishable on the bathymetric map. Features less than 2 m in height were also not included in the inventory, to avoid inclusion of anomalies resulting from data artifacts and non-hydrothermal structures that could be confused for chimneys. Prior knowledge of the locations and morphologies of known sulfide deposits from past ROV and *ALVIN* dives were used to validate as many of the identified structures as possible (Delaney et al., 1992; Robigou et al., 1993).

The volume of each edifice was determined by first outlining the sulfide footprint in the bathymetric data (Fig. 5.3). A GIS-based volume calculator was then used to determine the volume of material above a horizontal cut-off datum by determining the height of the sulfide above the datum for each data point within the outline. For sulfide edifices that grew on a horizontal substrate, the datum elevation was taken as the inferred base of the edifice on the basaltic substrate (Fig. 5.3A). For edifices that occur on non-horizontal substrates, the datum level was estimated by choosing a mid-point elevation so that the amount of sulfide material cut off below the datum was compensated for the amount of basaltic material above the datum that was included in the volume determination (Fig. 5.3B). The Because only sulfide that has precipitated on or above the seafloor can be identified in the bathymetry, sulfide that precipitated below the seafloor is not accounted for in the volume determinations.

4. Results

The surface footprint and volume for 581 individual sulfide edifices were determined from the high-resolution bathymetry (Fig. 5.2, Supplementary Table 5.1). Multiple structures with several individual peaks that share a common or overlapping sulfide base were considered as a single edifice. The average height, footprint area and volume for the sulfide edifices at Endeavour are 9 m, 201 m^2, and 641 m^3 respectively. The total sulfide footprint within the ~20 km^2 surveyed area is 116,900 m^2, or 0.6% of the total map area. The total cumulative volume of hydrothermal deposits is 372,500 m^3. From a cumulative frequency distribution plot for volumes (Fig. 5.5), the median sulfide volume is 187 m^3, and the upper 10th percentile is 1,225 m^3. The mapped area includes parts of the eastern and western volcanic ridge outside of the axial valley. Thirteen sulfide edifices, totalling 8,320 m^3, or 2% of the total sulfide volume, were identified along the western ridge.

The sulfide edifices at Endeavour can be characterized as either a vent structure or mound, based on their morphology. Of the 581 individual edifices, 507 are classified as vents, which are steep-sided and irregularly shaped (Fig. 5.6A), and on average have a height to basal radius ratio greater than 1 (basal radius is calculated from the area of the edifice's footprint, assuming a circular base). The total volume of the vents is 206,300 m^3. Although 87% of all sulfide edifices are classified as vents, they only account for 55% of the total volume of sulfide. Mounds, which are generally much bigger than the vents, have an average volume of 2,246 m^3, compared to 407 m^3 for vents, and account for the remaining 45% of sulfide material. Mounds are generally circular with a shallow slope (Fig. 5.6B) and a height/radius

ratio of less than 1. The largest edifice so far discovered at Endeavour is the Sweetland Mound, with a height of 26m, footprint of 6,500 m^2 and a volume of 52,535 m^3.

Twenty percent of the mapped edifices are from the five main active vent fields, accounting for 25% of the total sulfide volume. A further 19 deposits from outside the active vent fields have been visually confirmed as hydrothermal in origin during ROV dives, resulting in a total of 138 or 24% confirmed sulfide structures, accounting for 43% of the total sulfide volume. All remaining sulfide edifices are inferred from the high-resolution map. Two structures that were initially thought to be hydrothermal in origin were confirmed by ROV dives as volcanic features. A large mound was visually identified as a basalt pillow mound with diffuse hydrothermal activity on its flanks and a tall basalt pillar was originally identified as a tall, single sulfide chimney.

Reported dry bulk density measurements for samples collected from MEF and High Rise vary between 3.04 and 3.78 g/cm^3 (Tivey et al., 1999). Lower densities for seafloor sulfide precipitates are reported from the East Pacific Rise and Southern Explorer Ridge (1.95 to 2.3 g/cm^3) (Alton et al., 1989) and the Solwara I deposit in the Bismarck Sea (2.24 g/cm^3 ; (Lipton, 2012). The elevated density of Endeavour sulfide structures may be due to the elevated barite and silica abundance typical of Endeavour hydrothermal deposits (Tivey et al., 1999). For this study we apply the average dry bulk density for samples reported by Tivey et al. (1999) of 3.1 g/cm^3, which results in a total sulfide tonnage of 1.15 Mt for the 581 sulfide edifices identified along the Endeavour Segment. From a cumulative frequency distribution plot for tonnage, the median deposit is 580 tonnes, and the upper 10th percentile

is 3,484 tonnes (Fig. 5.5). The Sweetland Mound has a converted tonnage of 162,860 tonnes, representing 14% of the total sulfide in the surveyed area.

5. Discussion

5.1 Previous mapping of sulfides at Endeavour

Previous attempts to map the sulfide edifices along the Endeavour Segment have focused on the active vent fields (Delaney et al., 1992; Glickson et al., 2006; Robigou et al., 1993). Detailed maps of sulfide distribution within the Main Endeavour and High Rise Fields were compiled from observations of twenty-five and nine *ALVIN* dives, respectively (Fig. 5.6) (Delaney et al., 1992; Robigou et al., 1993). A map of the Mothra Field was compiled from two *ALVIN*, 12 ROV dives and several local bathymetric surveys with resolution of up to 1 m. A comparison of the size and shape of sulfide structures identified in the high-resolution AUV bathymetry to visually mapped structures can be considered an evaluation of both mapping methods. For the three map areas, all the major sulfide edifices that were visually mapped were identified in the high-resolution bathymetry (Fig. 5.6). Several edifices were also identified from the bathymetric data that were not visually mapped, including a 50 m long edifice NW of Hulk in the Main Endeavour Field. In many cases, the footprints of the visually-mapped sulfide edifices are larger than what is outlined from the bathymetry. The offset in location for many of the structures is likely a result of the difficulties associated with precise navigation on the seafloor.

For the Main Endeavour Field, Grotto, Lobo and Dante all match up very well with regards to both surface footprint and location (Fig. 5.6A) when comparing the different mapping

techniques. Hulk and Crypto overlap in terms of location but have a significantly larger visually-mapped footprint than what can be inferred from the AUV bathymetry. This may be a result of low-relief sulfide deposition around the steep-sided main venting structures that is lower than the 2 m topographic expression required to identify sulfide edifices using the AUV bathymetric data, or the inclusion of sulfide debris in the visual mapping. Sulfide structures are identified by both methods at the Dudley and TP sites, and an inactive site 45 m ENE of Dudley. However, for these sites, the shape and location of the sulfide footprints do not match as well as they do for sites such as Dante or Grotto. The large sulfide edifice 75 m NW of Hulk that was identified in the AUV bathymetry but not by the *ALVIN* surveys may be due to the limited survey coverage in that area during *ALVIN* dives, which often focus primarily on locations of active venting (Delaney et al., 1992).

For the High Rise Field, the locations of the major sulfide edifices (e.g., Godzilla, Boardwalk, Baltic) agree reasonably well using both mapping methods (Fig. 5.6B). However, unlike the Main Endeavour Field, where the footprints of the sulfide edifices determined from the bathymetric data were either similar or smaller than those that were visually-mapped, the footprints of the edifices at High Rise can be significantly larger (e.g., Ventnor) or smaller (e.g., Godzilla/Bambi), relative to the visual observations, suggesting no systematic bias towards larger or smaller sized sulfide edifices when comparing mapping methods. Sulfide edifices appearing larger may be a result of sulfide accumulation in the ~20 years between the *ALVIN* and AUV surveys. The Godzilla edifice is also known to have collapsed in 1995-1996 (Kelley et al., 2012). It is unlikely that temporal changes would result in a decrease in edifice footprint, or significant change in location of an edifice (Jamieson et al., 2013).

Unlike the Main Endeavour and High Rise maps, the Mothra map was compiled using both visual surveys and local high-resolution bathymetric mapping (Glickson et al., 2007), resulting in complete overlap for sulfide edifice locations between the two maps (Fig. 5.6C). The much larger sulfide footprints from the visual surveys reflects the inclusion of sulfide debris and hydrothermal sediments surrounding the edifices (Glickson et al., 2007).

5.2 Hydrothermal mounds

Distinguishing between mounds of hydrothermal versus volcanic origin using only bathymetric data is commonly difficult, due to the similarities in size and shape of both types of mound. In general, however, hydrothermal mounds at Endeavour can be distinguished by their irregular shape, and commonly have multiple peaks, relative to more uniform volcanic mounds (Fig. 5.4 A,B). These characteristics, in conjunction with visual confirmation by ROV of several mounds identified in the bathymetric data, were used to distinguish the 29 sulfide mounds within the map area. However, the composition (and genetic origin) of several mounds within the mapped area remain unresolved, including a 50 m long mound 25 m southeast of the main hydrothermal complex within the Salty Dawg Field (Fig. 5.4C) and a cluster of several 50 m-plus mounds, southeast of the Main Endeavour Field, on the eastern axial half-graben (Fig. 5.4D).

The discovery of the large "Sweetland" hydrothermal mound during an ROV dive in 2011 was especially surprising because hydrothermal features of this size and morphology had never been encountered along the Endeavour Segment up to this point. The mound was discovered while the ROV was traversing south from east of the High Rise Field, in order to

investigate two chimney structures that were identified in the high-resolution bathymetry and were situated on the eastern flank of what was at that point thought to be a volcanic mound, based on its size and relatively smooth, uniform surface (Fig. 5.7). Upon approaching the mound, the substrate changed from pillow basalts to hydrothermal sediments with some sulfide debris (Fig. 5.7; Fig 5.8 A,B). For the purposes of volume and tonnage estimates, only the exposed sulfide mound (Fig 5.8C) (outlined by a dashed yellow line in Figure 5.7) is considered. However, if the material in the region that is identified by the absence of basalt (within the black dashed lines in Figure 5.7) is also considered to be sulfide, the estimated tonnage of the mound would increase ~240%, from 162,859 tonnes to 392,615 tonnes, and would represent 28% of the total sulfide inventory at Endeavour.

Large sulfide mounds are commonly associated with slow-spreading ridges and their associated long-lived hydrothermal systems (e.g., the TAG and Krasnov Fields on the Mid-Atlantic Ridge), relative to the smaller deposits associated with fast-spreading ridges such as the East Pacific Rise (EPR) (Hannington et al., 2005; Kuznetsov et al., 2006). At Endeavour, which has a intermediate spreading rate, sulfide structures documented from within the active fields have morphologies that are transitional between the small, slender edifices along the axis of the EPR and the large, broad mounds along the Mid-Atlantic Ridge (Hannington et al., 2005; Rona et al., 1993; Tivey et al., 1999). The immediate permeability of the underlying substrate may be an important control on deposit morphologies, with mounds forming on substrates with higher permeabilities that result in branching flow pathways and distributed venting at the surface, and steep-sided vent edifices forming on substrates with low permeabilities that result in highly focused discharge at the surface (Hannington et al., 1995). However, the factors that control whether hydrothermal sulfide deposition along

Endeavour Segment results in the formation of steep sided edifices typical of the active vent fields (e.g. Fig. 5.3), or shallow-sloped mounds (e.g. Fig. 5.4) remain unclear. The ^{226}Ra/Ba ages of two samples collected from the top of the Sweetland Mound (Figs. 5.7 and 5.8D) and from the top of the westernmost sulfide spire on the eastern flank of the mound (Fig. 5.7) have ages of ~1,800 ± 200 and 1,716 ± 190 years, respectively (Jamieson et al., 2013). These ages are similar to or younger than minimum ages of samples from several of the steep-sided sulfide edifices at the Main Endeavour Field, suggesting that steep-sided vent edifices do not simply evolve into mounds over a prolonged period of time.

5.3 Mass-accumulation rates

Age constraints from ^{226}Ra/Ba dating of hydrothermal barite from sulfide edifices both within and outside of the active vent fields at Endeavour allows for the determination of the rate at which sulfide has accumulated within the axial valley of the Endeavour Segment (Jamieson et al., 2013). The oldest sample from a vent field provides a minimum age for that field. Minimum ages for the active vent fields, and for the entire axial valley are summarized in Table 2. For the active vent fields, the accumulation rates, calculated from the minimum age and estimated tonnage, are thus considered maximum accumulation rates.

The Main Endeavour and High Rise Fields have similar accumulation rates of 50 and 75 tonnes per year, respectively. The large number of samples dated from these vent sites (21 for Main Endeavour and 13 for High Rise) provides a higher degree of confidence in the maximum age for each field and hence a higher confidence in their calculated mass accumulation rates. The continuous spectrum of sample ages from the oldest age up to the present indicates that these fields have been continuously active throughout their venting

history (Jamieson et al., 2013). The Mothra and Salty Dawg Fields have calculated mass accumulation rates that are significantly higher than those calculated for the Main Endeavour and High Rise Fields. With only two and one sample dated from each site, respectively, the high accumulation rate values are likely a result of the fact that the reported minimum ages for these fields are artificially low due to limited age constraints for these fields. Conversely, the Sasquatch Field, with only two dated samples has a calculated accumulation rate of only 2 tonnes per year. This is especially surprising considering that a single chimney within the field grew up to 10 m in one year (Kelley et al., 2012). The low rate may be an indication that venting within the Sasquatch field has been periodic, with intervals of little to no sulfide accumulation on the seafloor. Surveys of the Sasquatch Field indicate that venting may have been reactivated since 2000, after a hiatus of undetermined length (Glickson et al., 2006). Further collection and dating of samples from this vent field would be required to test this hypothesis.

The sulfide mass accumulation rate for the entire Endeavour axial valley is ~400 tonnes per year, representing the sum of sulfide deposition from the active vent fields and inactive vent sites over the past ~3,000 years. The accumulation rate is the result of the combination of total hydrothermal discharge, metal and sulfur concentrations within the hydrothermal fluid and the amount of sulfide that is precipitated at the vent site, relative to what is ejected into the water column (% depositional efficiency). Reported total end-member metal (Fe+Cu+Zn) and reduced sulfur concentrations from five active vent edifices from the Main Endeavour Field, measured in 1999, varied between 291 and 832 ppm and average 630 ppm (Seyfried et al., 2003). Considering black smoker vents typically discharge at a rate of 1-2 kg/s, the metal and sulfur flux from a single vent at Main Endeavour would be ~32 tonnes

per year (Converse et al., 1984; Von Damm, 1990). The Main Endeavour Field is estimated to have >100 active chimneys (Kelley et al., 2012). Assuming ~200 active black smoker chimneys within the axial valley at a given time, with vent fluid compositions similar to those measured at the Main Endeavour field, the total metal and sulfur flux to the seafloor would be a combined 6,400 tonnes per year. If only 386 tonnes per year of this total flux is precipitated as sulfide minerals on the seafloor, the remaining 6,014 tonnes per year would have been discharged as 'smoke' into the overlying water column, resulting in a sulfide depositional efficiency of 6%. Previous estimates of depositional efficiency range from 30% at TAG (Humphris and Cann, 2000) to a global average for all mid-ocean ridges of <0.3% (Hannington, 2011).

Sulfide accumulation rates can be determined for other hydrothermal deposits on the seafloor, for which both tonnage and age constraints are known. Rates for 15 deposits (Table 3) were determined from recent compilations of both deposit sizes (Hannington et al., 2010) and deposit ages (Jamieson et al., 2013). Accumulation rates vary from a high of ~800 tonnes/year (12°50′N EPR) to 1 tonne/year (Kairei). For younger hydrothermal systems, such as 12°50′N and Endeavour, the calculated rates can be considered instantaneous rates because hydrothermal activity at these sites have likely been continuous over the age of the systems (Jamieson et al., 2013; Lalou et al., 1985). For older active and inactive deposits, hydrothermal activity may have been punctuated by periods of inactivity, resulting in calculated accumulation rates that are much lower than the rates at which the sulfide accumulated during periods of active venting (Fig. 5.9) (Lalou et al., 1995).

Hannington et al. (1998) estimated a 'corrected' accumulation rate of ~360 tonnes per year for the TAG mound based on the accumulation of 2.7 million tonnes of sulfide over 5,000 to 10,000 years, which is the length of time over which the mound was estimated to be hydrothermally active (Lalou et al., 1995). This 'corrected' value is similar to the rate determined for Endeavour. If the age of the TAG mound (at least 50,000 years old) is used instead, the accumulation rate for the mound would drop to 54 tonnes/year, a value similar to other deposits of that age (Fig. 5.9). The Zenith-Victory Field also has an accumulation rate of ~360 tonnes per year, which is similar to the rate for Endeavour and the 'corrected' rate for TAG. This rate is also much higher than the rates of other deposits of similar age (Fig. 5.9). This may be evidence for continuous hydrothermal activity at Zenith-Victory over its 59,000 year life span. Other variables that could lead to an increased mass accumulation rate include an elevated depositional efficiency, a more vigorous hydrothermal system, venting fluids with elevated metals and sulfur content, or a combination of any of these factors. These variables can also result in low mass accumulation rates such as those for the Kairei and the Logatchev-1 and -2 Fields. The young age of the 12°50′N site makes its calculated accumulation rate particularly susceptible to age uncertainty for the deposit. The high rate of ~800 tonnes per year for this site would be halved to a value similar to that for Endeavour by simply determining that the age of the deposit is ~200 years older than its current minimum age of 170 years (Lalou et al., 1985).

5.4 Implications for the global seafloor sulfide resource

A growing interest in the mining of seafloor hydrothermal deposits for their base (Cu, Zn and Pb) and precious (Au and Ag) metal content was the impetus for an investigation of the global abundance of sulfide deposits on the modern seafloor (Hannington et al., 2010;

Hannington et al., 2011). These studies used a three-part mineral resource assessment, originally designed for land-based ore deposits (Singer and Menzie, 2010), to estimate a total of 600 Mt of sulfide from the neovolcanic zones of the modern ocean floor (Hannington et al., 2011). This resource estimate utilized a database of all hydrothermal systems that have so far been documented on the seafloor to determine the size and spatial distribution of deposits (Beaulieu, 2012). From this database, a tonnage model for seafloor sulfide deposits was generated from a subset of 62 deposits (including three from the Endeavour Segment) for which deposit size information could be determined from available maps and descriptions (Hannington et al., 2010). For the Endeavour Segment, size estimates for the Mothra, Main Endeavour and High Rise Fields were used, as they were the only sites for which detailed geological maps have been published.

Significant sulfide accumulation can occur below the seafloor from mixing of infiltrated cold seawater with hydrothermal fluid before the fluid discharges at the seafloor. The amount of subseafloor precipitation is controlled by factors such as water depth (due to boiling), and the porosity and permeability of the substrate (Doyle and Allen, 2003; Hannington et al., 1995). A limitation of using bathymetry for a resource estimate is that the evaluation of the extent of sulfide deposition is limited to sulfide that has precipitated on the seafloor and forms a positive relief feature on the substrate. Extensive drilling of the Solwara 1 deposit in the Manus Basin has produced the most comprehensive delineation of a seafloor sulfide deposit to date that, crucially, includes information on the extent of sulfide precipitation below the seafloor (Lipton, 2012). High-resolution mapping and drilling of the Solwara 1 deposit has lead to a National Instruments 43-101-compliant resource estimate of 2.5 Mt of sulfide over an area of 90,000 m^2, or ~27 t/m^2 (Lipton, 2012). A similar calculation for Endeavour

Segment using the total sulfide footprint and estimated tonnage from the bathymetric data results in a tonnage-area ratio of 10 t/m^2, with the ratio being essentially the same for mounds and vents. The Solwara 1 deposit formed on a volcanic mound that is composed of andesitic and dacitic volcanic rocks and volcaniclastic sediments (Lipton, 2012). The footwall of the deposit is highly altered and locally brecciated and the resulting increased permeability enhances the degree of subseafloor sulfide precipitation, and a high tonnage to area ratio. At Endeavour, evidence from exposed stockwork upflow zones, magnetic 'burn holes' and focused discharge sites all point to limited local infiltration of seawater and precipitation of sulfide minerals occurring predominantly at the seafloor-seawater interface, resulting in a comparatively lower tonnage to footprint ratio (Delaney et al., 1992; Kelley et al., 2012; Tivey and Johnson, 2002; Tivey and Delaney, 1986)

The majority of the deposits in the global database were originally discovered by the detection of hydrothermal plumes above and down-current from actively venting sites (e.g., Baker et al., 1995; Baker and German, 2004), and as a result, only 56 of the 595 deposits in the global database are classified as 'inactive' (Beaulieu, 2012). Similarly, at Endeavour, although inactive sulfide deposits have been noted outside of the active vent fields, detailed descriptions of sulfide edifices have been largely restricted to edifices within the active fields (Delaney et al., 1992; Glickson et al., 2006; Glickson et al., 2007; Kelley et al., 2012; Kelley et al., 2001; Robigou et al., 1993; Tivey and Delaney, 1986). The total estimated (surface) sulfide tonnage from high-resolution bathymetry of 1.2 Mt has resulted in a four-fold increase in the sulfide resource for the Endeavour Segment, compared to a previous estimate of 0.3 Mt that was limited to only the well-documented active fields (Hannington et al., 2010). Thus, the current global inventory of hydrothermal deposits on the seafloor may be

similarly biased towards active systems, and the 600 Mt global estimate should be considered a minimum. Using the Endeavour Segment as a guide, the ability to assess the contribution of inactive deposits to a global seafloor sulfide resource estimate suggest that up to 2,400 Mt of sulfide may exist within the neovolcanic zones of the modern ocean floor. The tonnage model of a 2,400 Mt resource would have a median value of ~0.3 Mt, which is still considerably less than the tonnage models for the Kuroko- and Cyprus-type deposits (Hannington et al., 2010).

6. Conclusions

High-resolution bathymetric maps generated by AUV surveys provide a quick, reliable and cost-effective method for locating both active and inactive hydrothermal sulfide deposits on the seafloor at the ridge-segment scale. Analysis of a 62 km^2 1-m resolution map from 8 surveys of the Endeavour Segment resulted in the identification of 581 individual sulfide edifices along 24 km of ridge length. The identification of several previously un-mapped sulfide edifices in the well explored Main Endeavour and High Rise vent fields illustrates the advantages of this method over more traditional methods of plume detection and visual mapping of the seafloor in order to identify hydrothermal deposits. However, visual confirmation of identified sulfide deposits is still an important part of any seafloor survey. The total surface sulfide tonnage within this area of 1.2 Mt, estimated from the total volume of sulfide of ~372,500 m^3, represents the first comprehensive ridge segment scale sulfide resource estimate.

The Sweetland Mound, with a diameter of ~90 m and a height of 26 m is the largest single sulfide accumulation so far discovered along the Endeavour Segment, and the first large mound-like hydrothermal feature discovered along the segment. The morphology of the mound is more typical of volcanic mounds in the area and its chance discovery by ROV suggests that other mounds identified in the bathymetry that were originally interpreted to be volcanic in origin may in fact be hydrothermal as well, which would further increase the total sulfide resource for the ridge segment.

The sulfide mass accumulation rate for the Endeavour axial valley of ~400 tonnes per year is comparable to the TAG and Zenith-Victory deposits on the Mid-Atlantic Ridge. Based on the metal and sulfur contents of endmember vent fluids from the Main Endeavour Field, this represents a sulfide depositional efficiency of ~5%.

The inclusion of both active and inactive deposits has resulted in a resource estimate that is four times higher than previous estimates that focused largely on active deposits located by plume detection. A global seafloor sulfide resource estimate that also was based largely on active deposits may also be underestimating the total sulfide resource by a similar factor.

REFERENCES

Alton, M.C.C., Dobby, G.S., Scott, S.D., 1989. Potential for processing seafloor massive sulfides by magnetic separation. Marine Mining 8, 163-172.

Baker, E., German, C., Elderfield, H., 1995. Hydrothermal plumes over spreading center axes: Global distribution and geological inferences. Geophysical Monograph 91, 47-71.

Baker, E.T., German, C.R., 2004. On the global distribution of hydrothermal vent fields. Mid-Ocean Ridges: Hydrothermal Interactions between the Lithosphere and Oceans 148, 245-266.

Beaulieu, S., 2012. InterRidge Global Database of Active Submarine Hydrothermal Vent Fields, Version 2.2.

Butterfield, D.A., Jonasson, I.R., Massoth, G.J., Feely, R.A., Roe, K.K., Embley, R.E., Holden, J.F., McDuff, R.E., Lilley, M.D., Delaney, J.R., 1997. Seafloor eruptions and evolution of hydrothermal fluid chemistry. Philosophical Transactions of the Royal Society of London Series a-Mathematical Physical and Engineering Sciences 355, 369-386.

Caress, D., Clague, D., Thomas, H., Thompson, D., Calarco, M., Holden, J., Butterfield, D., 2008. Tectonic and Volcanic Character of the Endeavour Ridge Axis From 1-m Resolution AUV Multibeam Mapping Surveys. Eos Transactions AGU 89.

Cherkashov, G., Poroshina, I., Stepanova, T., Ivanov, V., BeL'Tenev, V., Lazareva, L., Rozhdestvenskaya, I., Samovarov, M., Shilov, V., Glasby, G.P., Fouquet, Y., Kuznetsov, V., 2010. Seafloor Massive Sulfides from the Northern Equatorial Mid-Atlantic Ridge: New Discoveries and Perspectives. Marine Georesources & Geotechnology 28, 222-239.

Converse, D.R., Holland, H.D., Edmond, J.M., 1984. Flow-rates in the axial hot springs of the East Pacific Rise (21-degrees-N) - Implications for the heat budget and the formation of massive sulfide deposits. Earth and Planetary Science Letters 69, 159-175.

Delaney, J.R., Robigou, V., McDuff, R.E., Tivey, M.K., 1992. Geology of a vigorous hydrothermal system on the Endeavour Segment, Juan de Fuca Ridge. Journal of Geophysical Research-Solid Earth 97, 19663-19682.

Doyle, M.G., Allen, R.L., 2003. Subsea-floor replacement in volcanic-hosted massive sulfide deposits. Ore Geology Reviews 23, 183-222.

Embley, R.W., Chadwick, W.W., Jonasson, I.R., Butterfield, D.A., Baker, E.T., 1995. Initial results of the rapid response to the 1993 Coaxial event - relationships between hydrothermal and volcanic processes. Geophysical Research Letters 22, 143-146.

Glickson, D.A., Kelley, D.S., Delaney, J.R., 2006. The Sasquatch Hydrothermal Field: Linkages Between Seismic Activity, Hydrothermal Flow, and Geology. American Geophysical Union, Fall Meeting 2006 Abstract #V23B-0614.

Glickson, D.A., Kelley, D.S., Delaney, J.R., 2007. Geology and hydrothermal evolution of the Mothra Hydrothermal Field, Endeavour Segment, Juan de Fuca Ridge. Geochemistry Geophysics Geosystems 8.

Hannington, M., 2011. Comments on "What processes at mid-ocean ridges tell us about volcanogenic massive sulfide deposits" by LM Cathles. Mineralium Deposita 46, 659-663.

Hannington, M., De Ronde, C., Petersen, S., 2005. Sea-Floor Tectonics and Submarine Hydrothermal Systems. Economic Geology 100th Anniversary Volume, pp. 111-141.

Hannington, M., Galley, A., Herzig, P., Petersen, S., 1998. Comparison of the TAG mound and stockwork complex with Cyprus-type massive sulfide deposits., in: Herzig, P., Humphris, S., Miller, D., Zierenberg, R. (Eds.), Proceedings of the Ocean Drilling Program, Scientific Results.

Hannington, M., Jamieson, J., Monecke, T., Petersen, S., 2010. Modern sea-floor massive sulfides and base metal resources: towards an estimate of global sea-floor massive sulfide potential. Society of Economic Geologists Special Publication 15, 111-141.

Hannington, M., Jamieson, J., Monecke, T., Petersen, S., Beaulieu, S., 2011. The abundance of seafloor massive sulfide deposits. Geology 39, 1155-1158.

Hannington, M., Jonasson, I., Herzig, P., Petersen, S., 1995. Physical and chemical processes of seafloor mineralization at mid-ocean ridges. Geophysical Monograph 11, 115-157.

Hooft, E.E.E., Patel, H., Wilcock, W., Becker, K., Butterfield, D., Davis, E., Dziak, R., Inderbitzen, K., Lilley, M., McGill, P., Toomey, D., Stakes, D., 2010. A seismic swarm and regional hydrothermal and hydrologic perturbations: The northern Endeavour segment, February 2005. Geochemistry Geophysics Geosystems 11.

Humphris, S.E., Cann, J.R., 2000. Constraints on the energy and chemical balances of the modern TAG and ancient Cyprus seafloor sulfide deposits. Journal of Geophysical Research-Solid Earth 105, 28477-28488.

Jamieson, J., Hannington, M., Clague, D., Kelley, D., Delaney, J., Holden, J., Tivey, M., Kimpe, L., 2013. Sulfide geochronology along the Endeavour Segment of the Juan de Fuca Ridge. Geochemistry Geophysics Geosystems.

Johnson, H.P., Hutnak, M., Dziak, R.P., Fox, C.G., Urcuyo, I., Cowen, J.P., Nabelek, J., Fisher, C., 2000. Earthquake-induced changes in a hydrothermal system on the Juan de Fuca mid-ocean ridge. Nature 407, 174-177.

Kappel, E.S., Ryan, W.B.F., 1986. Volcanic episodicity and a nonsteady state rift-valley along northeast Pacific spreading centers - evidence from Sea Marc-I. Journal of Geophysical Research-Solid Earth and Planets 91, 13925-13940.

Kelley, D.S., Baross, J.A., Delaney, J.R., 2002. Volcanoes, fluids, and life at mid-ocean ridge spreading centers. Annual Review of Earth and Planetary Sciences 30, 385-491.

Kelley, D.S., Carbotte, S.M., Caress, D.W., Clague, D.A., Delaney, J.R., Gill, J.B., Hadaway, H., Holden, J.F., Hooft, E.E.E., Kellogg, J.P., Lilley, M.D., Stoermer, M., Toomey, D., Weekly, R., Wilcock, W.S.D., 2012. Endeavour Segment of the Juan de Fuca Ridge One of the most remarkable places on Earth. Oceanography 25, 44-61.

Kelley, D.S., Delaney, J.R., Yoerger, D.R., 2001. Geology and venting characteristics of the Mothra hydrothermal field, Endeavour segment, Juan de Fuca Ridge. Geology 29, 959-962.

Kuznetsov, V., Cherkashev, G., Lein, A., Shilov, V., Maksimov, F., Arslanov, K., Stepanova, T., Baranova, N., Chernov, S., Tarasenko, D., 2006. Th-230/U dating of massive sulfides from the Logatchev and Rainbow hydrothermal fields (Mid-Atlantic Ridge). Geochronometria 25, 51-55.

Kuznetsov, V., Maksimov, F., Zheleznov, A., Cherkashov, G., BeL'Tenev, V., Lazareva, L., 2011. Th-230/U chronology of ore formation within the Semyenov Hydrothermal District (13 degrees 31 ' N) at the Mid-Atlantic Ridge. Geochronometria 38, 72-76.

Lalou, C., Brichet, E., Hekinian, R., 1985. Age dating of sulfide deposits from axial and off-axial structures on the East Pacific Rise near 12-degrees-50'N. Earth and Planetary Science Letters 75, 59-71.

Lalou, C., Munch, U., Halbach, P., Reyss, J.L., 1998. Radiochronological investigation of hydrothermal deposits from the MESO zone, Central Indian Ridge. Marine Geology 149, 243-254.

Lalou, C., Reyss, J.L., Brichet, E., 1993a. Actinide-series disequilibrium as a tool to establish the chronology of deep-sea hydrothermal activity. Geochimica Et Cosmochimica Acta 57, 1221-1231.

Lalou, C., Reyss, J.L., Brichet, E., Arnold, M., Thompson, G., Fouquet, Y., Rona, P.A., 1993b. New-age data for mid-Atlantic Ridge hydrothermal sites - TAG and Snakepit chronology revisited. Journal of Geophysical Research-Solid Earth 98, 9705-9713.

Lalou, C., Reyss, J.L., Brichet, E., Rona, P.A., Thompson, G., 1995. Hydrothermal activity on a 10(5)-year scale at a slow-spreading ridge, TAG hydrothermal field, mid-Atlantic Ridge 26-degrees-N. Journal of Geophysical Research-Solid Earth 100, 17855-17862.

Lilley, M.D., Butterfield, D.A., Lupton, J.E., Olson, E.J., 2003. Magmatic events can produce rapid changes in hydrothermal vent chemistry. Nature 422, 878-881.

Lipton, I., 2012. Mineral Resource Estimate - Solwara Project, Bismarck Sea, PNG: Canadian NI 43-101 Technical Report for Nautilus Minerals Inc., 240 p.

Riddihough, R., 1984. Recent movements of the Juan-de-Fuca plate system. Journal of Geophysical Research 89, 6980-6994.

Robigou, V., Delaney, J.R., Stakes, D.S., 1993. Large massive sulfide deposits in a newly discovered active hydrothermal system, the Highrise Field, Endeavour Segment, Juan-de-Fuca Ridge. Geophysical Research Letters 20, 1887-1890.

Rona, P.A., Hannington, M.D., Raman, C.V., Thompson, G., Tivey, M.K., Humphris, S.E., Lalou, C., Petersen, S., 1993. Active and relict sea-floor hydrothermal mineralization at the TAG hydrothermal field, Mid-Atlantic Ridge. Economic Geology and the Bulletin of the Society of Economic Geologists 88, 1989-2017.

Seyfried, W.E., Seewald, J.S., Berndt, M.E., Ding, K., Foustoukos, D.I., 2003. Chemistry of hydrothermal vent fluids from the Main Endeavour Field, northern Juan de Fuca Ridge: Geochemical controls in the aftermath of June 1999 seismic events. Journal of Geophysical Research-Solid Earth 108.

Shilov, V.V., Bel'tenev, V.E., Ivanov, V.N., Cherkashev, G.A., Rozhdestvenskaya, II, Gablina, I.F., Dobretsova, I.G., Narkevskii, E.V., Gustaitis, A.N., Kuznetsov, V.Y., 2012.

New hydrothermal ore fields in the Mid-Atlantic Ridge: Zenith-Victoria (20 degrees 08 ' N) and Petersburg (19 degrees 52 ' N). Doklady Earth Sciences 442, 63-69.

Singer, D., Menzie, W., 2010. Quantitative mineral resource assessments - an integrated approach. Oxford University Press.

Tivey, M.A., Johnson, H.P., 2002. Crustal magnetization reveals subsurface structure of Juan de Fuca Ridge hydrothermal vent fields. Geology 30, 979-982.

Tivey, M.K., Delaney, J.R., 1986. Growth of large sulfide structures on the Endeavour Segment of the Juan-de-Fuca Ridge. Earth and Planetary Science Letters 77, 303-317.

Tivey, M.K., Stakes, D.S., Cook, T.L., Hannington, M.D., Petersen, S., 1999. A model for growth of steep-sided vent structures on the Endeavour Segment of the Juan de Fuca Ridge: Results of a petrologic and geochemical study. Journal of Geophysical Research-Solid Earth 104, 22859-22883.

Von Damm, K.L., 1990. Seafloor hydrothermal activity - black smoker chemistry and chimneys. Annual Review of Earth and Planetary Sciences 18, 173-204.

Wang, Y.J., Han, X.Q., Jin, X.L., Qiu, Z.Y., Ma, Z.B., Yang, H.L., 2012. Hydrothermal Activity Events at Kairei Field, Central Indian Ridge 25 degrees S. Resource Geology 62, 208-214.

Wilcock, W.S.D., Hooft, E.E.E., Toomey, D.R., McGill, P.R., Barclay, A.H., Stakes, D.S., Ramirez, T.M., 2009. The role of magma injection in localizing black-smoker activity. Nature Geoscience 2, 509-513.

Table 5.1: Volumes and estimated tonnages of sulfide edifices from the Endeavour Segment

Location	n	Volume (m^3)	Tonnage[1] (tonnes)
Active vent fields			
Mothra	29	9,857	30,557
Main Endeavour	38	36,758	113,950
High Rise	31	20,756	64,344
Salty Dawg	14	24,386	75,597
Sasquatch	6	1,142	3,540
Within Axial Valley	568	364,179	1,128,955
Outside Axial Valley	13	8,318	25,786
Total	581	372,500	1,154,700

[1]Calculated from volumes using a density of 3.1 tonnes/m^3 (Tivey et al., 1999)

Table 5.2: Maximum sulfide accumulation rates within the Endeavour axial valley.

Location	# of samples dated[1]	Minimum Age[1] (years)	Tonnage [2] (tonnes)	Accumulation Rate (t/year)
Mothra	2	157 ± 127	30,557	195
Main Endeavour Field	21	2,272 ± 128	113,950	50
High Rise Field	13	843 ± 127	64,344	76
Salty Dawg	1	464 ± 127	75,597	163
Sasquatch	2	1,465 ± 127	3,540	2
Total within axial valley	45	2,926 ± 211	1,128,955	386

[1] ^{226}Ra/Ba ages of hydrothermal barite (Jamieson et al., 2013)

[2] Calculated from total volumes using a density of 3.1 t/m^3 (Tivey et al., 1999)

Table 5.3: Sulfide mass accumulation rates for active and inactive hydrothermal systems on the ocean floor

Deposit	Location	Active?	Age[1]	Tonnage[2] (tonnes)	Accumulation Rate (tonnes/year)
12°50′N	East Pacific Rise	Yes	170[3]	135,000	794
Endeavour	Juan de Fuca	Yes	2,926[4]	1,154,741	395
Logatchev-1	Mid-Atlantic Ridge	Yes	58,200[5]	135,000	2
Logatchev-2	Mid-Atlantic Ridge	Yes	7,000[5]	27,000	4
Rainbow	Mid-Atlantic Ridge	Yes	23,000[5]	810,000	35
Ashadze-1	Mid-Atlantic Ridge	Yes	7,200[5]	1,350,000	188
Ashadze-2	Mid-Atlantic Ridge	Yes	27,300[5]	1,350,000	49
TAG	Mid-Atlantic Ridge	Yes	7,500[6]	2,700,000	360
Zenith-Victoria	Mid-Atlantic Ridge	Yes	59,000[5]	21,073,500	357
Snakepit	Mid-Atlantic Ridge	Yes	4,000[7]	405,000	101
Kairei	Indian Ocean	Yes	96,300[8]	81,000	1
Petersburg	Mid-Atlantic Ridge	No	176,200[9]	2,475,900	14
Krasnov	Mid-Atlantic Ridge	No	119,200[5]	4,050,000	34
Semyenov	Mid-Atlantic Ridge	No	124,000[10]	8,100,000	65
MESO	Central Indian Ridge	No	140,000[11]	1,350,000	10

[1] The reported age for TAG is the estimated number of years for which the mound was hydrothermally active (Hannington et al., 1998)
[2] Tonnage estimates from Hannington et al. (2010) except for TAG (Hannington et al., 1998), Petersburg and Krasnov (Shilov et al., 2012) and Endeavour (this study)
[3] (Lalou et al., 1985)
[4] (Jamieson et al., 2013)
[5] (Cherkashov et al., 2010)
[6] Averaged from estimated range of 5,000 to 10,000 years (Hannington et al., 1998)
[7] (Lalou et al., 1993b)
[8] (Wang et al., 2012)
[9] (Shilov et al., 2012)
[10] (Kuznetsov et al., 2011)
[11] (Lalou et al., 1998)

Figure 5.1

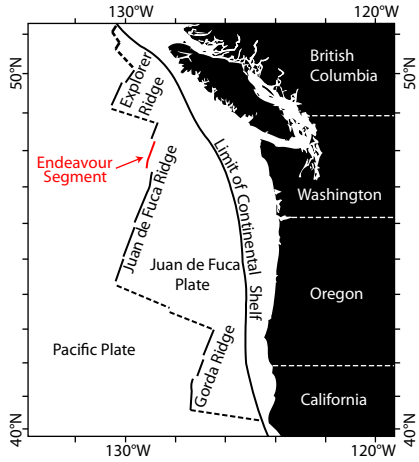

Figure 5.1: Map of the Juan de Fuca Plate showing the location of the Endeavour Segment.

Figure 2

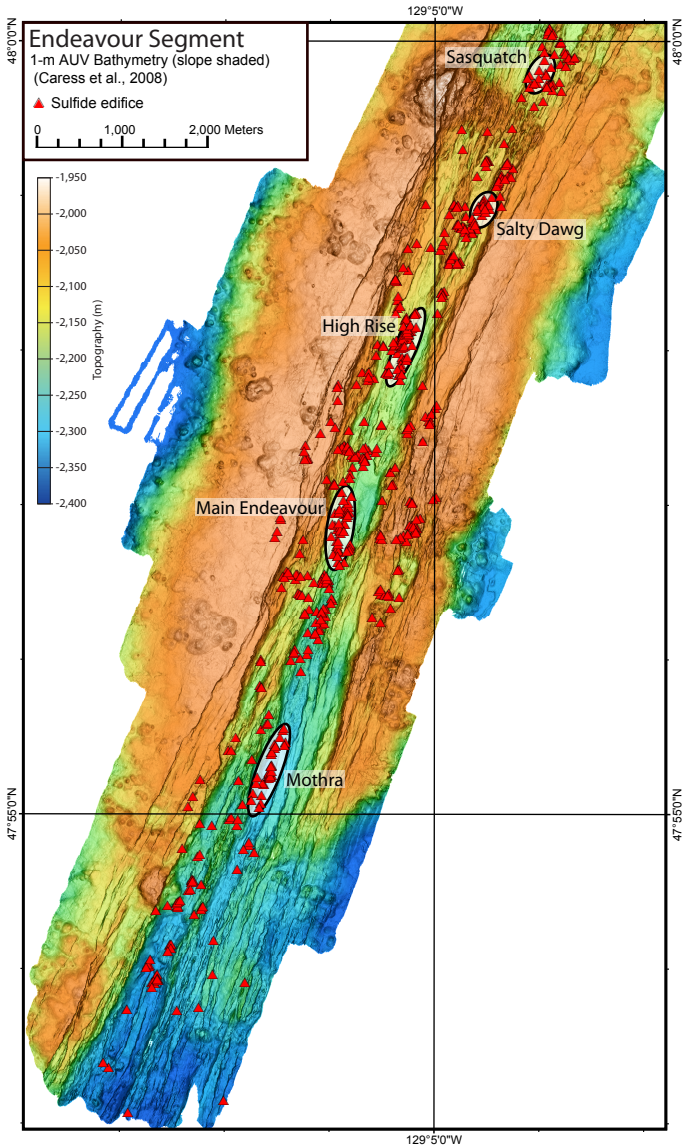

Figure 2: Slope-shaded bathymetric map of the Endeavour Segment, with the locations of 581 hydrothermal sulfide edifices identified in the map area from 1 m resolution bathymetric data. The locations of the five active vent fields are highlighted in white.

Figure 5.3

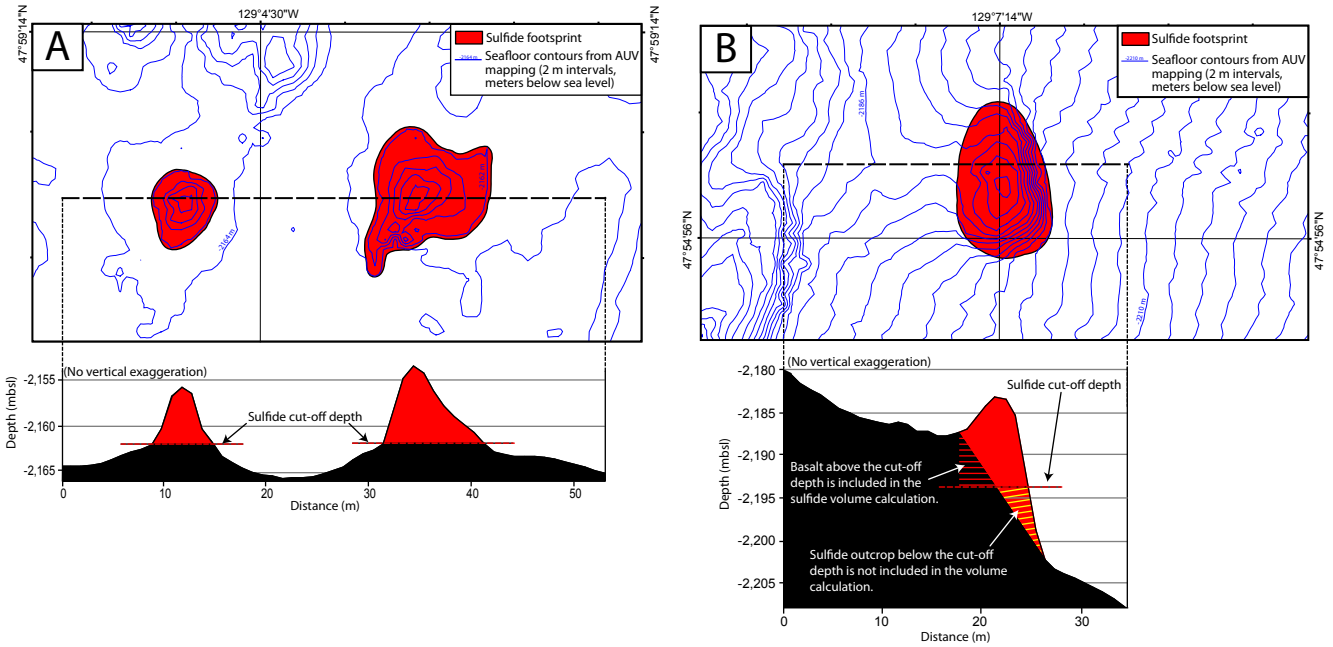

Figure 5.3: The footprints of sulfide edifices (shaded in red) are identified from the bathymetric data based on their morphology (e.g. shape, slope angles). A: For each edifice, the volume of exposed sulfide material above a horizontal datum defined by the basal extent of the edifice was determined using a GIS-based volume calculator. B: For sulfide edifices that occur on sloped surfaces, the depth of the horizontal datum was chosen so that the estimated amount of sulfide material that was cut-off below the datum was balanced by the amount of volcanic substrate above the datum that was included in the volume calculation.

Figure 5.4

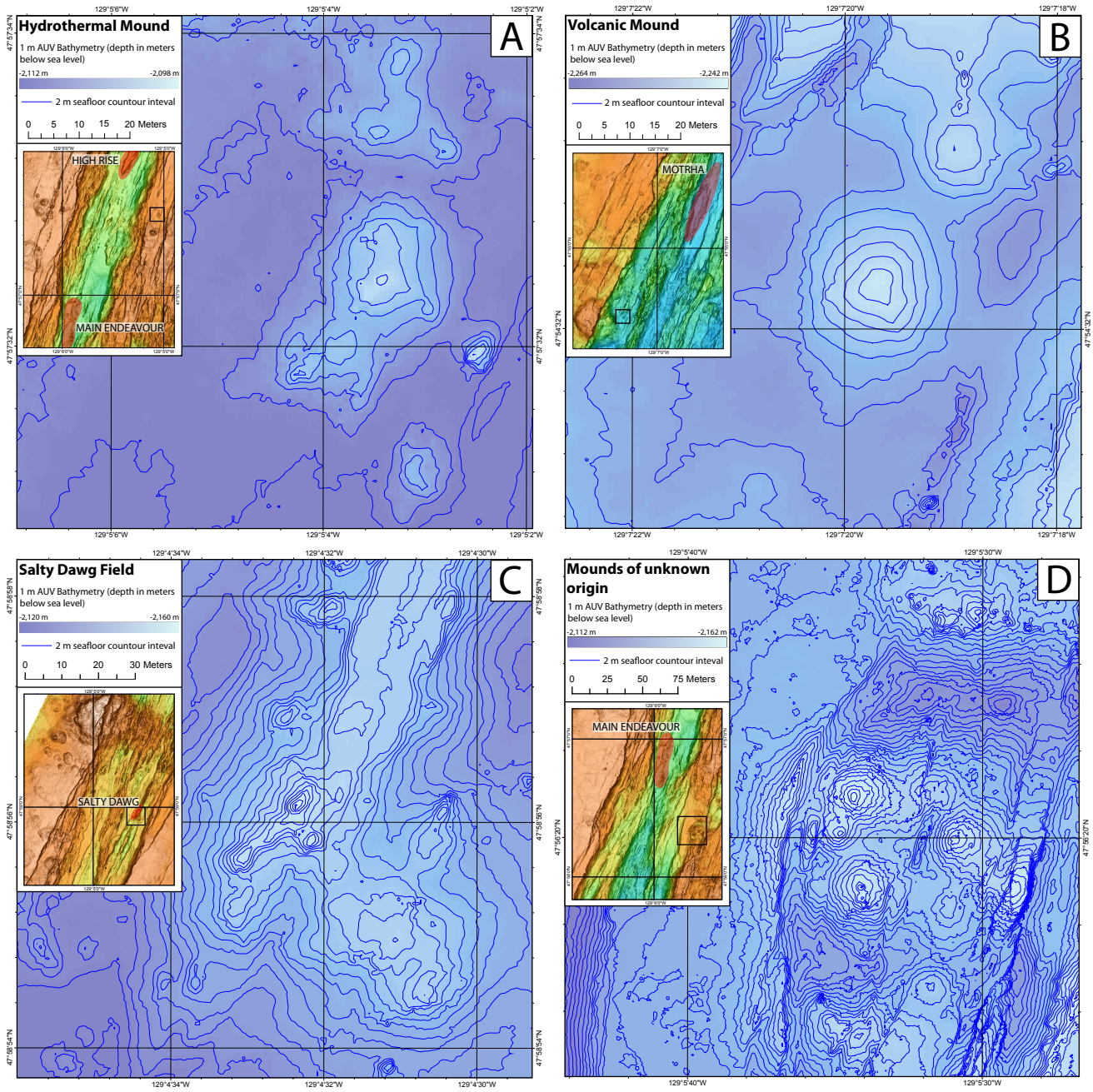

Figure 5.4: Relief maps of mounds from the Endeavour Segment: A) typical sulfide mound, with irregular, jagged contours and multiple peaks; B) typical volcanic mound with smooth contours, relatively constant slope, and a single peak; C) possible large sulfide mound, ~25 m southeast of the main hydrothermal complex at Salty Dawg; D) cluster of mounds of unknown, but possibly hydrothermal origin. Bathymetry from Caress et al. (2008)

Figure 5.5

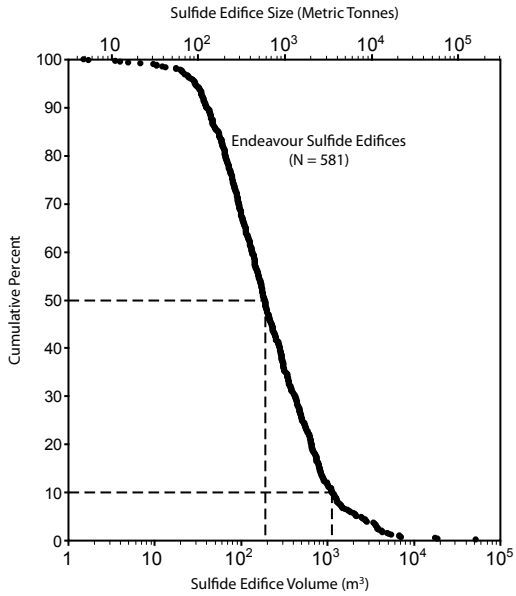

Figure 5.5: Cumulative frequency plot of sulfide edifice volumes and tonnages for the Endeavour Segment. Measured volumes were converted to tonnages using a density of 3.1 tonnes/m3 (Tivey et al., 1999). The median edifice size (50th percentile) is 187 m3 (580 tonnes) and the upper 10th percentile is 1,225 m3 (3,798 tonnes).

Figure 5.6

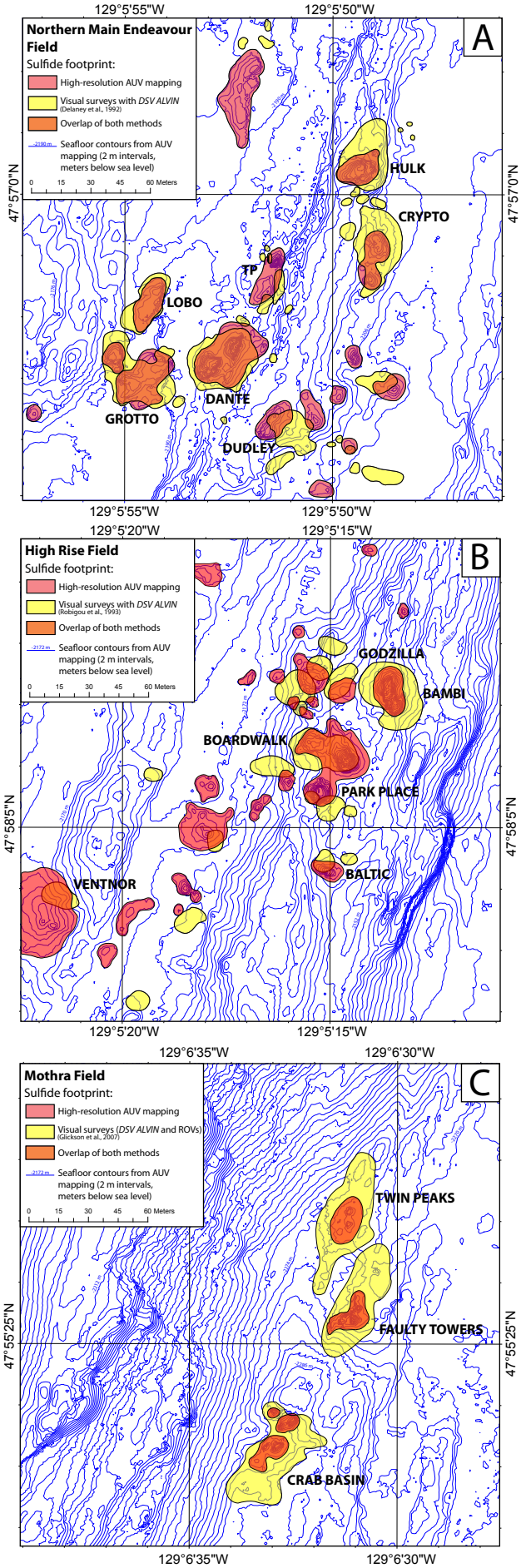

Figure 5.6: Bathymetric maps of sulfide edifice locations within active vent fields at Endeavour. Areas highlighted in red represent sulfide edifices identified from the high-resolution bathymetry and outcrops in yellow are sulfide structures mapped by previous authors based on submersible observations. Areas highlighted in orange represent locations where sulfide mineralization was identified with both mapping methods. A: The Northern Main Endeavour Field was originally mapped by Delaney et al. (1992) from 25 ALVIN dives. B: The High Rise Field was mapped by Robigou et al., (1993) from 9 ALVIN dives. C: The Mothra field was mapped by Glickson et al., (2007) with ALVIN (2 dives), 12 ROV dives, and a local high-resolution bathymetric survey. See text for further discussion.

Figure 5.7

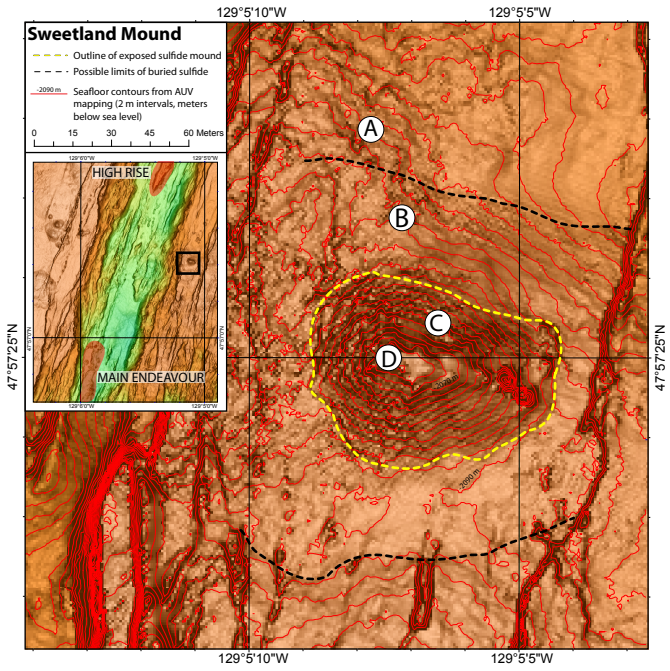

Figure 5.7: Slope-shaded 1 m resolution image of the Sweetland mound, located on the eastern half-graben of the Endeavour axial valley, between the Main Endeavour and High Rise vent fields. The yellow dashed line indicates the outer perimeter of the exposed massive sulfide mound. The black dashed lines show the possible limits of buried sulfide material, based on the presence of hydrothermal sediment, absence of basalt and change in slope of the substrate from relatively flat-lying to gently sloping away from the mound. The letter markers correspond to the locations of photographs in Figure 5.8.

Figure 5.8

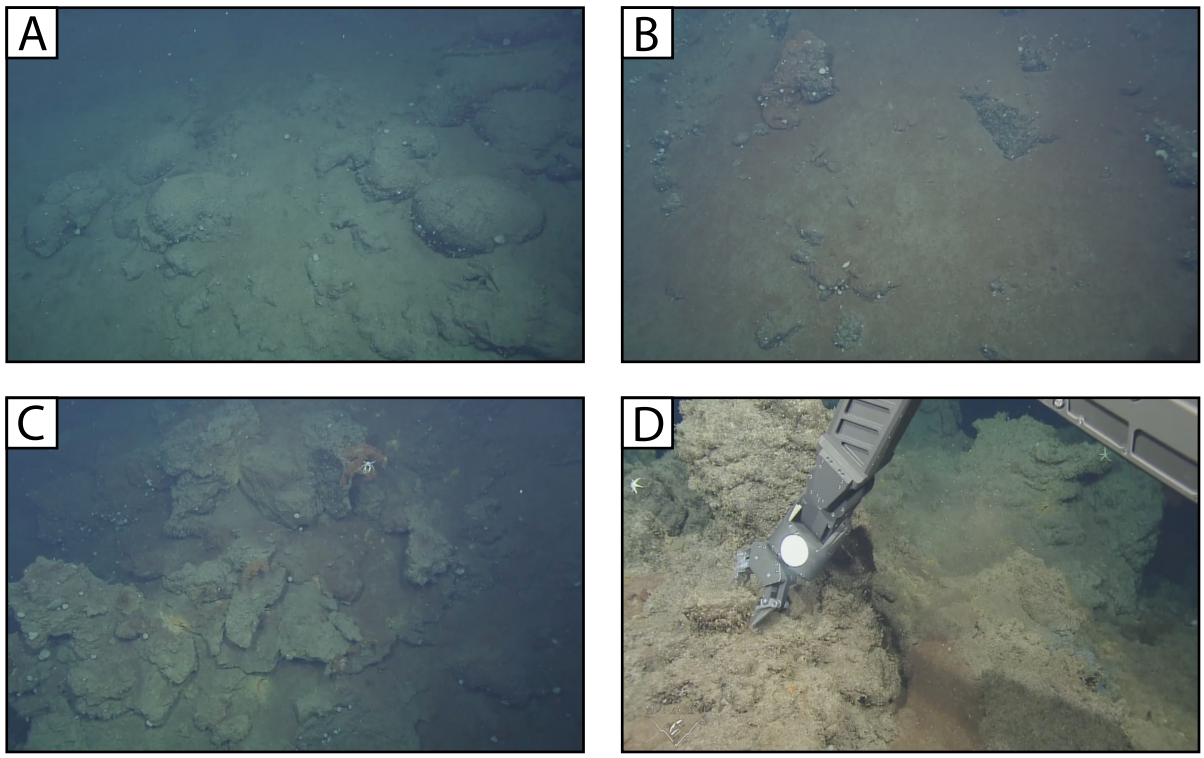

Figure 5.8: Frame grabs from the ROV Doc Ricketts of the Sweetland Mound and surrounding substrate. Letters correspond to map locations in Figure 5.7. A: lightly-sedimented pillow basalts dominate the substrate in the vicinity of the mound; B: dark red/brown hydrothermal sediment with sulfide talus immediately flanking the mound; C: blocky, massive sulfide on the north face of the mound; D: a sulfide sample collected from the top of the mound has an age of 1,797 ± 198 years (Jamieson et al., 2013).

Figure 5.9

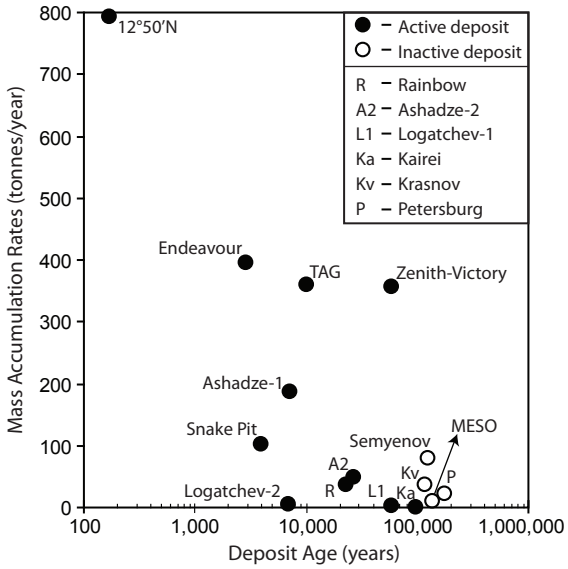

Figure 5.9: Mass accumulation rates for active and inactive hydrothermal systems on the seafloor, plotted relative to the age of the oldest sample dated from each deposit. With the notable exception of the Zenith-Victory site, accumulation rates appear to decrease with age, reflecting the increased likelihood of the rates accounting for periods of hydrothermal inactivity, or in the case of the inactive deposits, possible cessation of hydrothermal activity. Ages and rates from Table 3.

CHAPTER 6

CONCLUSIONS

A clearer understanding of the distribution of hydrothermal sulfide deposits on the seafloor has emerged as a result of the research presented in this thesis. Major active deposits are spaced every ~100 km along the neovolcanic zones of the ocean. The median size of these deposits is ~70,000 tonnes, with 10% of the deposits estimated to be greater than 2 Mt. The sizes of seafloor deposits that are predicted by the tonnage model are significantly smaller than similar land-based volcanogenic massive sulfide deposits. This is likely a result of the inclusion in the tonnage model of deposits on the seafloor that would be considered uneconomic on land and not included in models for land-based deposits. The geological settings, composition and textures of both modern and ancient deposits indicate that the processes responsible for the formation of the largest deposits are similar to those of the smallest deposits. The smaller size estimates predicted by the new seafloor tonnage model, relative to land-based VMS tonnage models, is likely not an indication that sulfide accumulations on the modern seafloor do not have the potential to grow as large as ancient deposits found on land. The similar geological settings, composition and textures of both modern and ancient deposits indicate that the genetic processes responsible for the formation of these deposits have not significantly changed over time. Therefore, the potential to find large (e.g. > 10 Mt) deposits on the modern seafloor may be significant. Global grade models predict median grades of 3.6 wt. % Cu, 7.9 wt. % Zn, 0.4 wt. % Pb, 1.7 g/t Au and 115 g/t Ag. These models show an opposite trend to the tonnage model, with predicted grades that are higher than those for land-based deposits. Typically, only high-grade surface samples are collected from the seafloor, which result in artificially high grades in the model. Grades of samples collected from below the seafloor by drilling are more typical of the grades found in land-based deposits.

The Endeavour Segment contains a fault-bounded axial valley that hosts five major active vent fields, with several smaller sites of active venting, along 15 km of ridge length. The sulfide deposits at Endeavour contain abundant barite, which allowed for the samples to be dated by measuring the decay of radioactive ^{226}Ra concentrated in barite. An investigation into the precipitation of barite within hydrothermal sulfide accumulations confirmed that barite precipitates as a result of the mixing of Ba^{2+}-rich, hot hydrothermal fluid with SO_4^{2-}-rich, cold seawater. The proportions of the two endmember fluids that are present during precipitation, determined from $^{87}Sr/^{86}Sr$ measurements of barite crystals, vary from 19 to 89% hydrothermal fluid. A range of crystal morphologies exhibited by barite within the vent chimneys, from dendritic to euhedral, reflects the degree of supersaturation of the mineralizing fluid, which is controlled by the amount of mixing between the endmember fluids. Because barite is precipitated throughout the paragenesis, at both low and high degrees of mixing, it records the ages of active, high-temperature venting at the discharge sites.

With a half-life of 1,600 years, the $^{226}Ra/Ba$ chronometer is effective for samples with ages of between ~500 to 20,000 years. At Endeavour, venting has been occurring within the current axial valley for at least the past ~5,850 years. Venting at the Main Endeavour and High Rise fields has been spatial static and continuous for the past ~2,300 and 850 years, respectively. This is the first successful application of the $^{226}Ra/Ba$ dating technique to a mid-ocean ridge hydrothermal environment, and indicates that this technique could be a powerful geochronological tool for studying the temporal evolution of seafloor hydrothermal systems. For this technique to be utilized in other locations, three criteria must be met: 1) the deposits must contain enough barite (e.g. >1 wt.% Ba) to generate meaningful analytical

results; 2) there must be active venting in the area in order to obtain initial, zero-age ^{226}Ra/Ba values from which the ages of inactive deposits can be calculated; and 3) if the inactive samples are collected over a wide area, enough active samples, spatially distributed within the area of interest must be collected and analyzed to ensure that the determined initial ^{226}Ra/Ba values are spatially consistent and representative of the entire area of interest. If these criteria are met, this technique bridges an important time gap between shorter- and longer-lived dating systems. The utility of this dating technique is enhanced by the simple and cost effective analytical procedure, which does not require chemical separations, the technique is non-destructive and requires very little sample (<10 g) for analysis.

Inactive deposits may be just as important as active deposits for the understanding of the magnitude and importance of seafloor hydrothermal activity, from the ridge segment to global scale. Active systems provide instantaneous information on the attributes of a hydrothermal system such as fluid temperature, flux and composition. However, these attributes can change significantly, even over short periods of time. Sulfide deposition at the discharge sites of currently-active hydrothermal systems may also not be representative of the total depositional history within the area of interest since the onset of hydrothermal activity, as discharge sites may change location with time, and the number of active hydrothermal systems may have been higher, or lower, in the past. A high-resolution bathymetric map, generated from eight near-bottom AUV multibeam surveys, allowed for the identification of nearly 600 individual hydrothermal sulfide structures within the axial valley of the Endeavour Segment. Nearly 80% of these structures had not previously been documented despite 30 years of exploration within the axial valley using manned submersible and remotely-operated vehicles. There are two main reasons for this: Firstly, in

the past, scientists have focused primarily on active hydrothermal systems. Secondly, sulfide deposits associated with active systems are significantly easier to detect and locate than inactive deposits. Improvements in technology for the generation of high-resolution maps, such as the use of autonomous underwater vehicles, will allow for the enhanced ability to detect and quantify the amount of inactive deposits, using methods such as those outlined in Chapter 5. The significant increase in total sulfide now documented at Endeavour implies that a similar proportion of sulfide deposition in other well-explored areas has also remained undetected. Accounting for undetected, inactive sulfide deposits would not significantly change the tonnage model for seafloor deposits. It would, however, significantly change the amount of total sulfide on the seafloor. The increased total resource, along with the evidence that the deposits may be more closely spaced than what is estimated from only the active deposits, may generate increased interest in the economic viability of seafloor deposits for their base and precious metal content.

Analysis of the total volume and tonnage of the sulfide deposits at Endeavour result in a four-fold increase in known resource from a previous estimate of 0.3 Mt to 1.2 Mt. Included in the new discoveries was a large inactive sulfide mound with a basal diameter of ~90 m, similar to mounds found on the Mid-Atlantic Ridge. This mound, which contains 14% of the known sulfide at Endeavour, is a unique feature along the segment, as hydrothermal edifices at Endeavour are more commonly smaller and steep-sided. A mass accumulation rate of ~400 t/year were calculated from a combination of the sulfide tonnage estimates and the age constraints on hydrothermal activity within the ridge segment. Estimates of mass accumulation rates for other deposits on the Mid-Atlantic Ridge, for which the sizes and ages are well known, are generally lower. This likely reflects the periodicity of long-lived

hydrothermal systems, in which there are long periods of hydrothermal quiescence with no sulfide accumulation.

The calculated sulfide depositional efficiency of 6% indicates that the genesis of much larger deposits than those found so far on the seafloor could result from a much higher depositional efficiency. Increased permeability within the substrate due to fracturing/faulting or sediment cover could significantly increase the amount of sulfide that precipitates at or below the seafloor, and sites with these features may be more prospective for the discovery of large deposits.

APPENDICES

APPENDIX A – Seafloor hydrothermal sulfide deposit names

Each name below corresponds to the numbered location on the map in Figure 2.1

Intracontinental rifts
1. Atlantis II Deep, Red Sea
2. Thetis, Nereus, Gypsum Deeps
3. Kebrit Deep, Red Sea
4. Shaban Deep, Red Sea

Slow-spreading mid-ocean ridges
5. Rainbow Field, Mid-Atlantic Ridge
6. Broken Spur, Mid-Atlantic Ridge
7. TAG Mound, Mid-Atlantic Ridge
8. MIR Zone, Mid-Atlantic Ridge
9. Alvin Zone, Mid-Atlantic Ridge
10. 24°30'N, Mid-Atlantic Ridge
11. Snakepit Field, Mid-Atlantic Ridge
12. Zenith-Victory, Mid-Atlantic Ridge
13. Krasnov, Mid-Atlantic Ridge
14. Logatchev Field, Mid-Atlantic Ridge
15. 13°30'N Semyenov, Mid-Atlantic Ridge
16. Ashadze Field, Mid-Atlantic Ridge
17. 5°S, Mid-Atlantic Ridge
18. 8°18'S, Mid-Atlantic Ridge
19. Mt. Jourdanne, Southwest Indian Ridge
20. Segment 28, Southwest Indian Ridge
21. Segment 27, Southwest Indian Ridge
22. 13°E, Southwest Indian Ridge
23. Gakkel Ridge, Arctic Ocean
24. Aurora Field, Arctic Ocean
25. Lena Trough, N. Mid-Atlantic Ridge
26. Mohns-Knipovich Ridge
27. Mohns Ridge
28. Northern Kolbeinsey Ridge

Intermediate-rate mid-ocean ridges
29. JX/MESO Zone, Central Indian Ridge
30. EX/FX Zone, Central Indian Ridge
31. Kairei Field, Central Indian Ridge
32. Edmond Field, Central Indian Ridge
33. Galapagos Rift, 86°W
34. Galapogos Rift, 89°30'W
35. Galapogos Rift, 90°33'W
36. Galapogos Rift, Navidad
37. Galapogos Rift, Pinguinos, Iguanas
38. West Galapagos Rift, 91°50'W
39. West Galapagos Rift, 102°W
40. Southern Explorer Ridge
41. High-Rise, Endeavour Ridge
42. Main Field, Endeavour Ridge
43. CoAxial Site, Juan de Fuca Ridge
44. North Cleft, Juan de Fuca Ridge
45. South Cleft, Juan de Fuca Ridge
46. North Gorda Ridge

Fast-spreading mid-ocean ridges
47. 9°45'N, EPR Flank
48. 10°20'N, EPR Flank
49. 21°N, Northern EPR
50. 12°50'N, Northern EPR
51. 12°42'N, Northern EPR
52. 11°32'N, EPR Seamount
53. 11°30'N, Northern EPR
54. 11°N, Northern EPR
55. 9-10°N, Northern EPR
56. 1°44'N, AHA Field, EPR
57. 7°00'S, Southern EPR
58. 7°24'S, Southern EPR
59. 14°00'S, Southern EPR
60. 15°00'S, Southern EPR
61. 16°43'S, Southern EPR
62. 17°12'S, Southern EPR
63. 17°26'S, Southern EPR
64. 17°27'S, Southern EPR
65. 17°34'S, Southern EPR
66. 18°00'S, Southern EPR
67. 18°11'S, Southern EPR
68. 18°26'S, Southern EPR
69. 18°36'S, Southern EPR
70. 20°00'S, Southern EPR
71. 20°40'S, Southern EPR
72. 20°50'S, Southern EPR
73. 21°25'S, Southern EPR
74. 21°33'S, Southern EPR
75. 21°50'S, Southern EPR
76. 22°30'S, Southern EPR
77. 22°58'S, Easter Microplate
78. 23°30'S, Southern EPR
79. 26°10'S, Southern EPR
80. 31°09'S, Southern EPR
81. 31°51'S, Southern EPR
82. 37°40'S, Pacific-Antarctic Ridge
83. 37°48'S, Pacific-Antarctic Ridge

Off-axis volcanoes
84. Green Seamount
85. 14°N, Northern EPR
86. 13°N, Northern EPR
87. 23°19'S, Southern EPR
88. Pito Seamount

Sedimented ridges and related rifts
89. Middle Valley (Bent Hill, ODP Mound)
90. Escanaba Trough
91. Guaymas Basin
92. Grimsey Hydrothermal Field

Ridge-hotspot intersections
93. Axial Seamount, Juan de Fuca Ridge
94. Lucky Strike, Azores
95. Menez Gwen, Azores

Intraplate volcano
96. Loihi Seamount, Hawaii

Intraoceanic arcs
97. Sunrise Deposit, Izu-Bonin Arc
98. Kita Bayonnaise, Izu-Bonin Arc
99. Hakurei Deposit, Izu-Bonin Arc
100. Myonjinsho, Izu-Bonin Arc
101. Suiyo Seamount, Izu-Bonin Arc
102. Kaikata Seamount, Izu-Bonin Arc
103. East Diamante, Mariana Arc
104. Volcano 1, Tonga-Tofua Arc
105. Volcano 19, Tonga-Tofua Arc
106. Monowai Caldera, Kermadec Arc
107. Clark Seamount, Kermadec Arc
108. Rumble II West, Kermadec Arc
109. Brothers, Kermadec Arc

Intraoceanic back-arc basins
110. Sumisu Rift, Izu-Bonin Arc
111. Alice Springs, Mariana Trough
112. 18°13'N, Central Mariana Trough
113. 18°02'N, Central Mariana Trough
114. 13°N, Southern Mariana Trough
115. Forecast Field, Southern Mariana Arc
116. Fryer Site, Southern Mariana Arc
117. Archean Seamount, Southern Mariana
118. Pika Seamount, Southern Mariana Arc
119. Sonne99 Corner Mound, North Fiji Basin
120. Sonne99 Yogi Mound, North Fiji Basin
121. White Lady, North Fiji Basin
122. Pere Lachaise, North Fiji Basin
123. Kaiyo Field, North Fiji Basin
124. Papatua Site, Northern Lau Basin
125. Kings Triple Junction, Northern Lau
126. MTJ Caldera, Mangatolo Triple Junction
127. Northeast Lau Spreading Center
128. Maka Volcano, Northeast Lau Basin
129. Plume Site, Northeast Lau Basin
130. Niua Site, Northeast Lau Basin
131. Fonualei Rift, Northeast Lau Basin
132. Central Lau Basin
133. Kilo Moana, Southern Lau Basin
134. Tow Cam Field, Southern Lau Basin
135. ABE, CDE Fields, Southern Lau Basin
136. White Church, Southern Lau Basin
137. Tui Malila, Southern Lau Basin
138. Mariner, Southern Lau Basin
139. Vai Lili Field, Southern Lau Basin
140. Hine Hina, Southern Lau Basin
141. Western Manus Basin (Solwara 11)
142. Mata Na Taru, Western Manus Basin
143. Central Manus Basin
144. 3°22'S, Central Manus Basin
145. Central Manus Basin (Solwara 10)
146. Vienna Woods, Manus Basin
147. Central Manus Basin (Solwara 2)
148. Central Manus Basin (Solwara 3)

Transitional island arcs and back-arc rifts
149. Pacmanus, Eastern Manus (Solwara 4)
150. Solwara 6, 7, 8, Eastern manus Basin
151. Desmos Cauldron, E. Manus Basin
152. Solwara 12, 13, Eastern Manus Basin
153. Solwara 1, 5, Eastern Manus Basin
154. SuSu Knolls, Eastern Manus (Solwara 9)
155. Palinuro Seamount, Tyrrhenian Sea
156. Panarea Seamount, Tyrrhenian Sea
157. Calypso Vents, Taupo Zone

Intracontinental back-arc rifts
158. Minami-Ensei, Okinawa Trough
159. North Iheya, Okinawa Trough
160. Clam Site, Okinawa Trough
161. Izena Cauldron, Okinawa Trough
162. Hatoma Knoll, S. Okinawa Trough
163. Yonaguni Knoll, S. Okinawa Trough

Volcanic rifted margins
164. Franklin Seamount, Woodlark Basin
165. Bransfield Strait, Antarctica

APPENDIX B – Seafloor hydrothermal sulfide deposit area estimates

The footprint areas for seafloor sulfide deposits are estimates based on maps and descriptions of the deposits or vent fields from published reports. In many cases, the estimated areas are order-of-magnitude estimates, and the uncertainties can be significant. For this reason, many estimated areas are assigned area 'bins', based on the descriptions and maps of the hydrothermal sulfide distribution. Below is a compilation of maps of the hydrothermal fields, from which information for sulfide footprints are taken.

MID-ATLANTIC RIDGE

Krasnov (Izu-Bonin Arc)

Location: 16.640N, -46.475E
Area: 150,000 m^2
Reference: (Cherkashov et al., 2008)

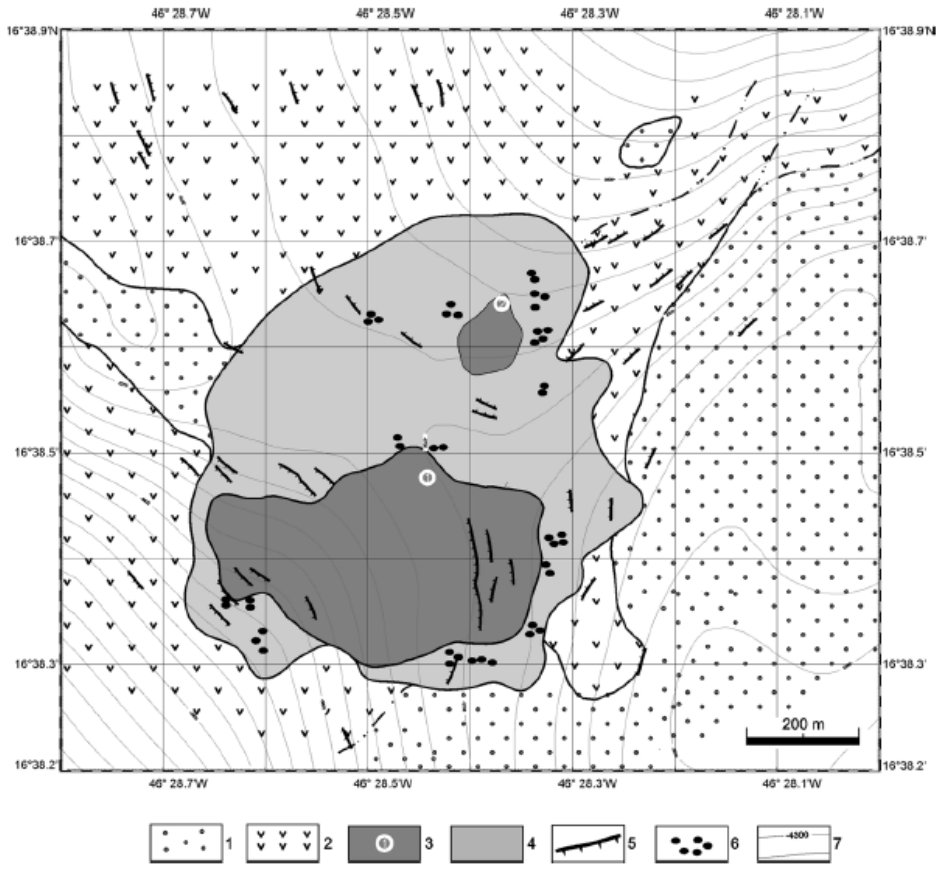

Figure 6. Krasnov hydrothermal field: 1 – Pelagic calcareous non-metalliferous sediments, 2 – Basalts, 3 – Sulfide deposits (with numbers), 4 – Metalliferous sediments, 5 – Escarp zones, 6 – Fe-Mn crusts, and 7 – Isobath (meters).

Ashadze-1

Location: 13.000N, -44.833E
Area: 30,000 m^2
Reference: (Cherkashov et al., 2008)

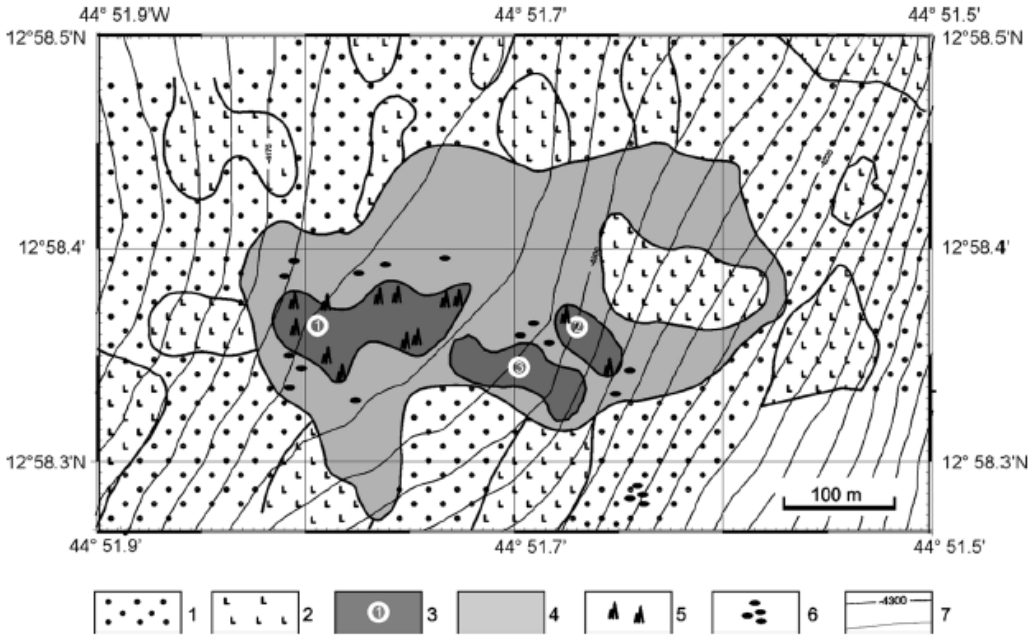

Figure 4. Ashadze-1 hydrothermal site: 1 – Pelagic calcareous non-metalliferous sediments, 2 – Gabbro and peridotites, 3 – Sulfide deposits (with numbers), 4 – Metalliferous sediments (Fe + Mn > 10%), 5 – Sulfide chimneys, 6 – Fe-Mn crusts, and 7 – Isobath (meters).

Ashadze-2

Location: 13.000N, -44.833E
Area: 30,000 m^2
Reference: (Cherkashov et al., 2008)

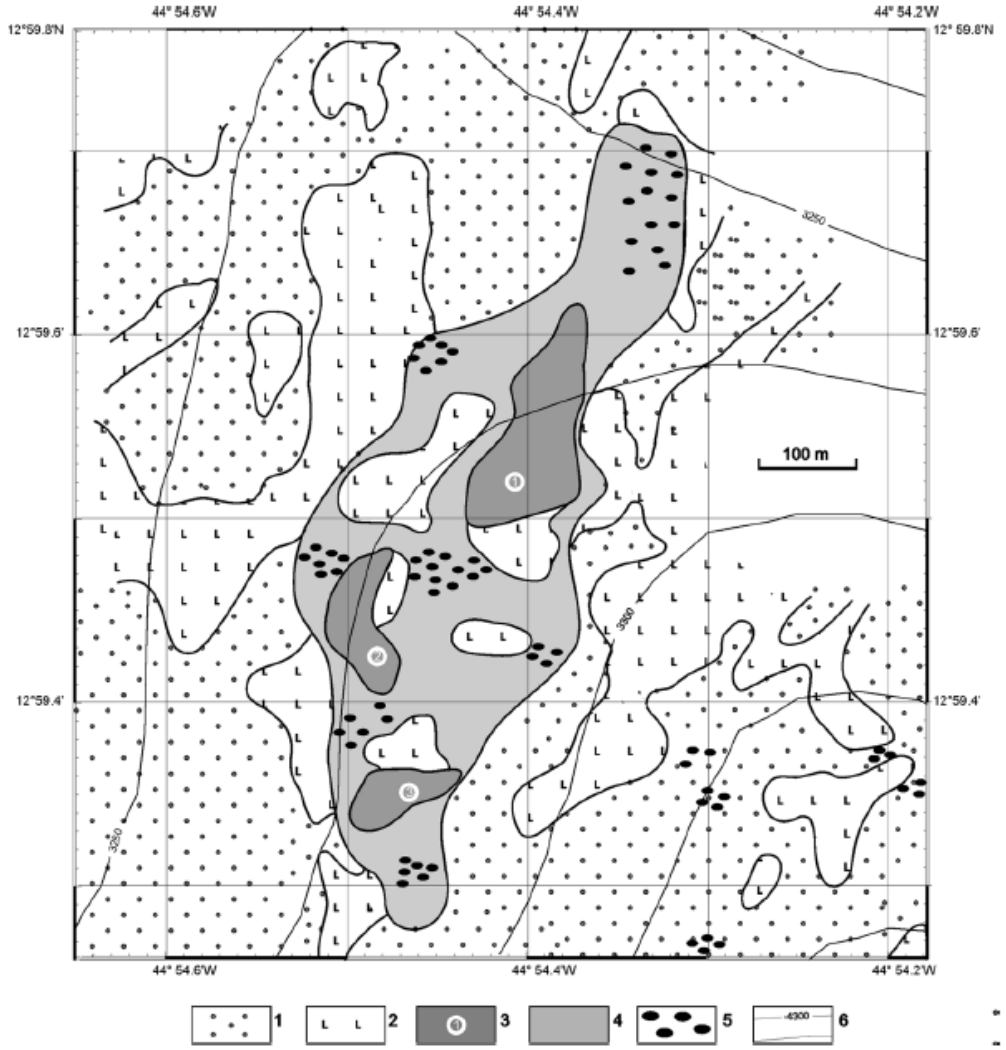

Figure 5. Ashadze-2 hydrothermal site: 1 – Pelagic calcareous non-metalliferous sediments, 2 – Gabbro and peridotites, 3 – Sulfide deposits (with numbers), 4 – Metalliferous sediments (Fe – Mn > 10%), 5 – Fe-Mn crusts, and 6 – Isobath (meters).

Broken Spur

Location: 29.167N, -43.167E
Area: 1,000 m^2
Reference: (Bogdanov et al., 2008)

"Owing to the observations from the *Alvin* and *Mir* manned submersibles, over 10 hydrothermal mounds were discovered within the Broken Spur hydrothermal vent field within an area approximately 10 x 10^2 m^2 in size." "The most representative structure among them is the Wasps' Nest Mound 15-20 m high and 8-10 m across."

TAG (Trans-Atlantic Geotraverse)

Location: 26.133N, -44.817E
Area: 30,000 m^2
Reference: (Rona et al., 1993; White et al., 1998)

"The New mound has a diameter of ~150-200 m…" "The Southern mound is ~200 m…" "The Double mound, previously thought to be the southernmost mound of the Alvin relict zone, is approximately 80 x 150 m in size…" (White et al, 1998)

"The active mound is a steep-sided structure measuring about 200 m in diameter" (Rona et al., 1993)

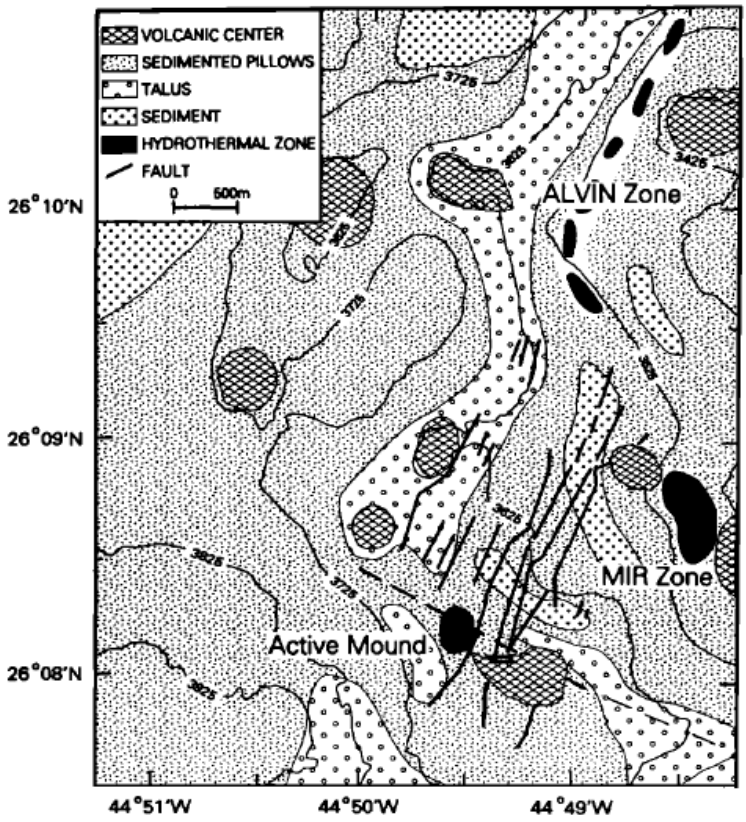

Snakepit

Location: 23.6367N, -44.950E
Area: 5,000 m^2
Reference: (Karson and Brown, 1989)

TABLE 1
Parameters for calculating the volume of the Snake Pit sulfides

Data		Source
Sulfide sediments (maximum)		
length	800 m	ANGUS Runs 1–3, ALVIN Dive 1683
width	200 m	ALVIN Dives 1679–1680, ODP[a,b]
thickness	4 m	ODP[1]
volume	640 000 m^3	
Massive sulfides (Mounds):		
length	40 m	ALVIN Dive 1683
width	20 m	ALVIN Dive 1683
thickness	45 m	ALVIN Dive 1683
volume per mound[c]	24 000 m^3	
number of mounds	6	ALVIN Dive 1683, ANGUS Run 1
volume of massive sulfides	144 000 m^3	
Total volume of sulfides	784 000 m^3 (maximum)	

[a] ODP Leg 106 Scientific Party, 1986.
[b] ODP Legs 106/109 Scientific Party (in press).
[c] 0.67 × rectangular volume.

Semyenov

Location: 23.636N, -44.950E
Area: 350,000 m^2
Reference: (Cherkashov et al., 2010)

Table 4. Parameters of the Northern Equatorial MAR SMS deposits

Deposit (A–active, I–inactive)	Latitude (N)	Water depth (meters)	Estimated size parameters of deposit		
			Square Km^2	Thickness m	Resources mln. Tones
Ashadze-1 (A)	12° 58.5′	4200	0.058	10	1.74
Ashadze-2 (A)	12° 59.5′	3250	0.106	20	5.70
Semyenov (I)	13° 31′	2400–2600	0.361	10	13.66 (?)
Logatchev-1 (A)	14° 45′	2900–3100	0.032	15	2.00
Logatchev-2 (A)	14° 43′	2720	0.007	10	0.25
Krasnov (I)	16° 38′	3700–3750	0.161	25	13.95
Zenith-Victoria (I)	20° 08′	2370–2390	0.495	8	11.00
Puy des Folles (?)	20° 30.5′	1940–2000	0.858	4	10.00
TAG (Active mound) (A) (Hannington et al. 1998)	26° 08′	3670	0.031	40–50	4.0
Solwara-1 (A) (www.nautilusminerals.com)					1.2

Turtle Pits

Location: 4.810S, -12.374E
Area: 500 m^2
Reference: (Haase et al., 2007)

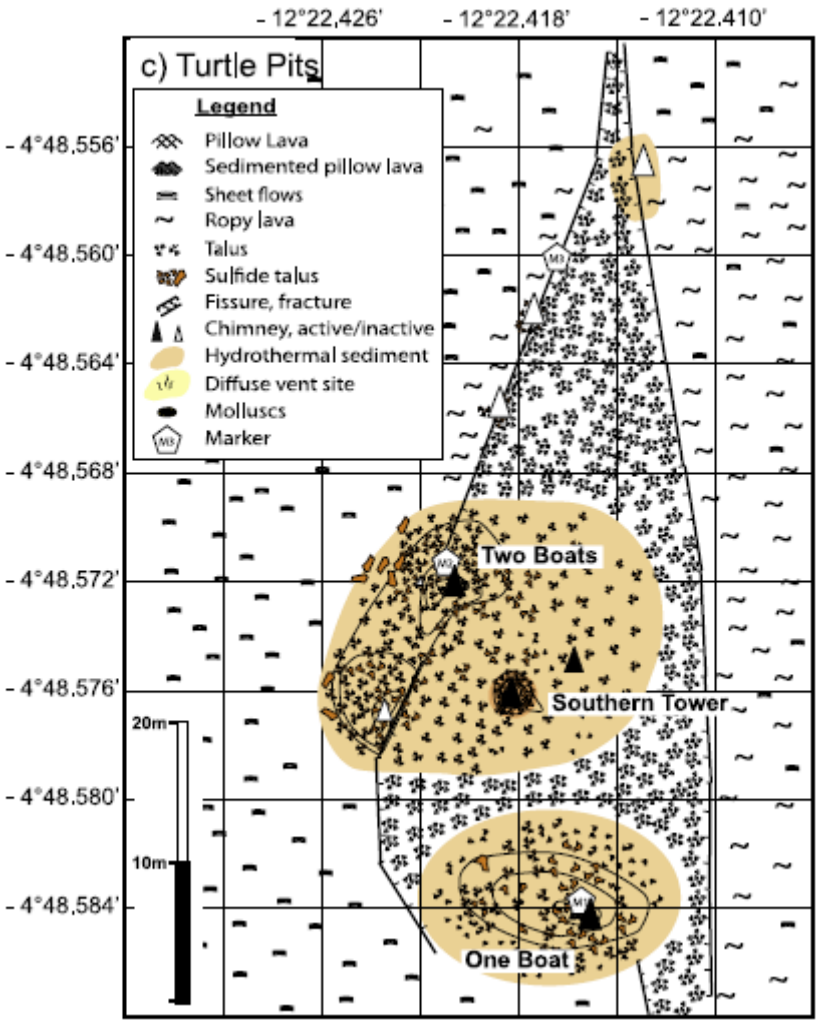

Lucky Strike

Location: 4.810S, -12.374E
Area: 3,000 m^2
Reference: (Langmuir et al., 1997)

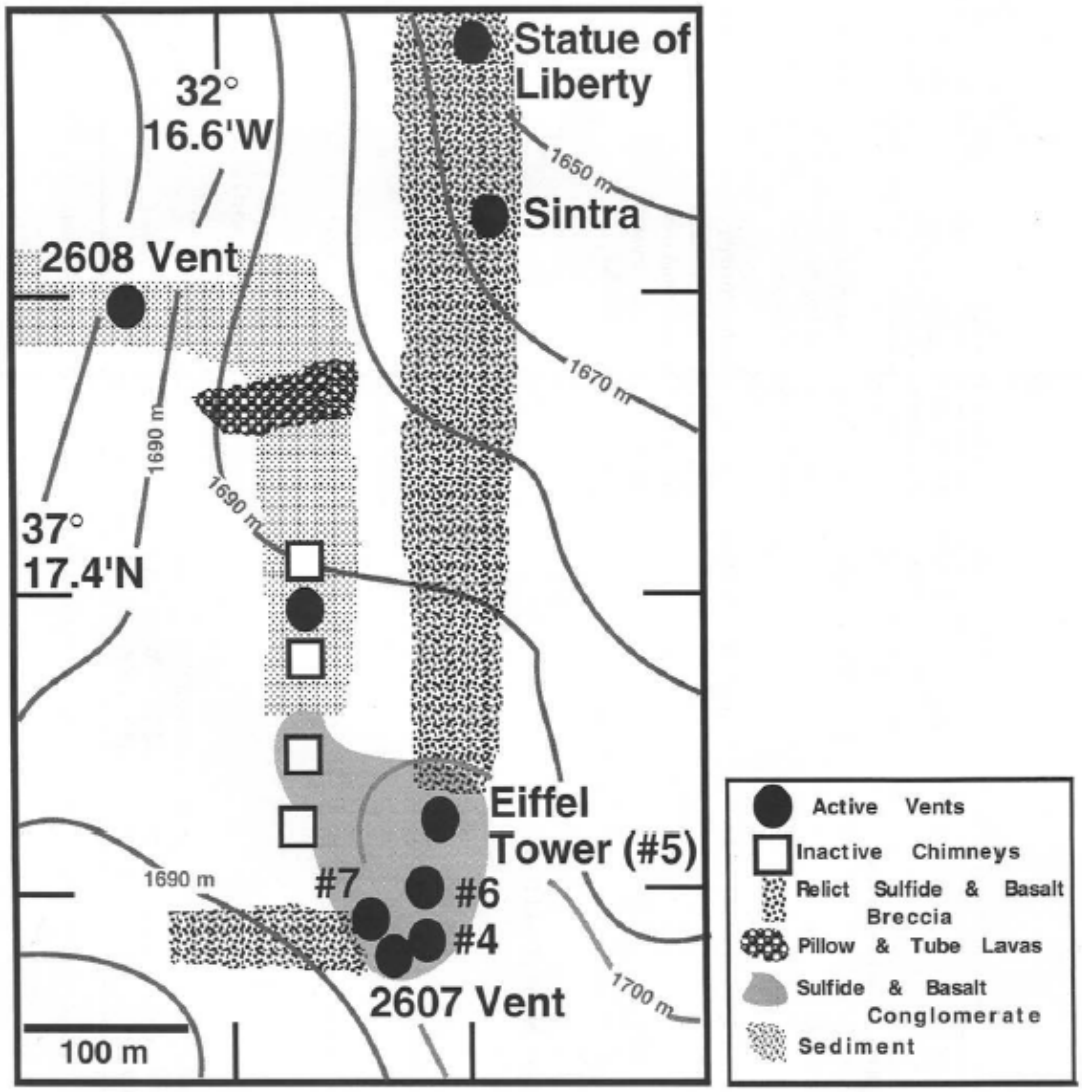

Fig. 4. Close-up map of the Lucky Strike vent sites sampled by *Alvin*.

Table 2
Morphology and mineralogy of active vent sites in the Lucky Strike hydrothermal field

Vent site	Location		Depth (m)	Morphologic characteristics	Fluid temperatures	Mineralogy [a]
Northern region of vent field						
Statue of Liberty (Marker #1)	37°17.59′N	32°16.49′W	1646	2 m wide active flange at base of a mound consisting of inactive chimney spires ~2–3 m high	Fluid pooled beneath flange: 156–200°C	Flange: bar with mar ± pyr. and sph Chimney spires: cpyr, mar,sph, bar; some late silica
Sintra (Marker #5)	37°17.55′N	32°16.48′W	1646	Spire ~5 m high; active on one side, inactive on the other. Smaller (<1 m) inactive chimneys around base. Talus apron (30 m in diameter) of massive sulfide blocks	Both low temperature diffuse flow (8–14°C), and 197–212°C focused flow on active side of spire	Inactive side: pyr + cpyr; outer oxidized layer with ata and non; Active side: conduit lined with mar, minor cpyr and sph; outer wall of mar, bar and sph; mid-wall of mar + bar + anhy with minor sph
Southern region of vent field						
2608 Vent	37°17.50′N	32°16.64′W	1715	Single spire ~10 m high	Focused flow: 333°C	All locations have interior chimney walls of massive cpyr with variable amounts of pyr.
Eiffel Tower	37°17.33′N	32°16.51′W	1700	Tapered spire ~20 m high; active on one side, inactive on the other	Focused flow up to 325°C	Outer chimney walls: pyr and anhy with minor sph and mar.
Mounds (#4)	37°17.27′N	32°16.51′W	1706	All mounds sites are small chimneys (<1 m high) with outer diameters of <10 cm on top of small (<1–3 m diameter) sulfide mounds	Focused flow: 292°C	Trace amounts of bor, cov, dig, late amorphous silica and bar (in some samples)
Mounds (#6)	37°17.30′N	32°16.52′W	1704		Focused flow: 298°C	
Mounds (#7)	37°17.28′N	32°16.54′W	1708		Focused flow: 297°C	
2607 Vent	37°17.27′N	32°16.53′W	1706		Focused flow: 319°C	

[a] pyr = pyrite; mar = marcasite; bar = barite; cpyr = chalcopyrite; sph = sphaerite; dig = digenite; cov = covellite; any = anhydrite; ata = atacamite; non = nontronite.

Rainbow:

Location: 36.233N, -35.900E
Area: 60,000 m^2
Reference: (Marques et al., 2006)

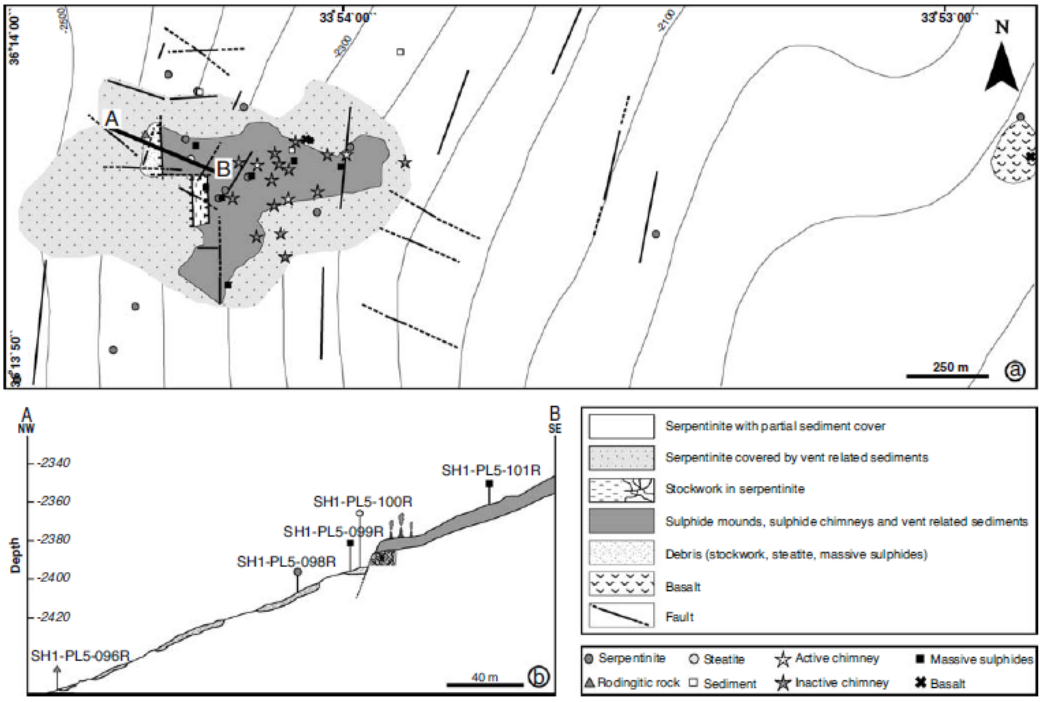

Fig. 2 **a** Geological map of the Rainbow vent field area with sample location (geology and sample location from direct observations during IRIS and SEAHMA1 cruises and FLORES cruise report; bathymetric data and ADELIE software from IFREMER). *Line AB* is the cross-section represented in subpanel b. **b** Interpretative geological cross-section with no vertical exaggeration, representing location of samples collected during dive SH1-PL5 of the SEAHMA1 cruise

Logatchev:

Location: 14.717N, -44.933E
Area: 150,000 m^2
Reference: (Kuznetsov et al., 2006)

"The total area of the Logatchev-1 field is about 0.3 km^2 and it incorporates 15 hydrothermal mounds. The largest one (called IRINA II) is about 200 m long and up to 100 m wide and has black and white smoker chimneys at its top. The Logatchev-2 hydrothermal field is located on the same eastern slope of rift valley as Logatchev-1. The field area totals 0.15 km^2 and includes six hydrothermal mounds. The largest one is about 150 m long and up to 80 m wide."

EAST PACIFIC RISE

13°N East Pacific Rise Seamount

Location: 12.717N, -103.850E
Area: 40,000 m^2
Reference: (Fouquet et al., 1996)

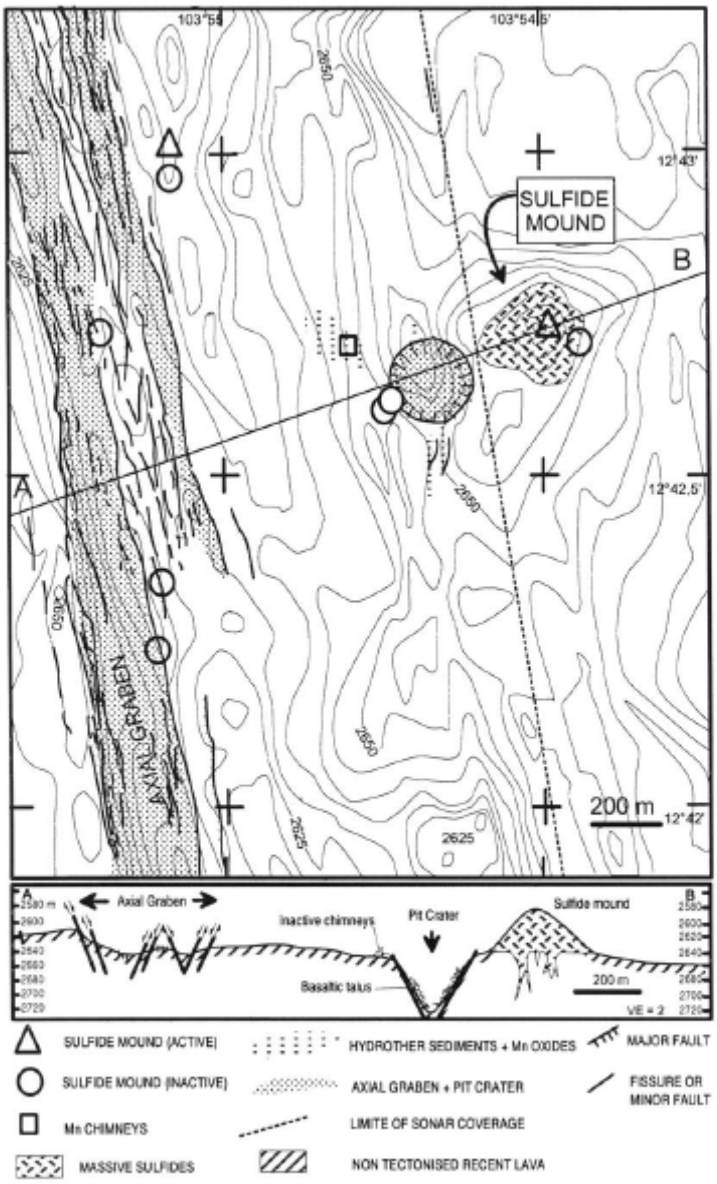

Fig. 3. SeaBeam bathymetric map of the axis and the marginal high (see location on Fig. 1). Tectonic features observed on the side scan sonar image and hydrothermal fields are superimposed. Note the good correspondence between the elongated depression of the Seabeam map and the circular pit crater on the sonar image.

13°N (12°50N) EPR

Location: 12.833N, -103.950E
Area: 5,000 m^2
Reference: (Fouquet et al., 1988)

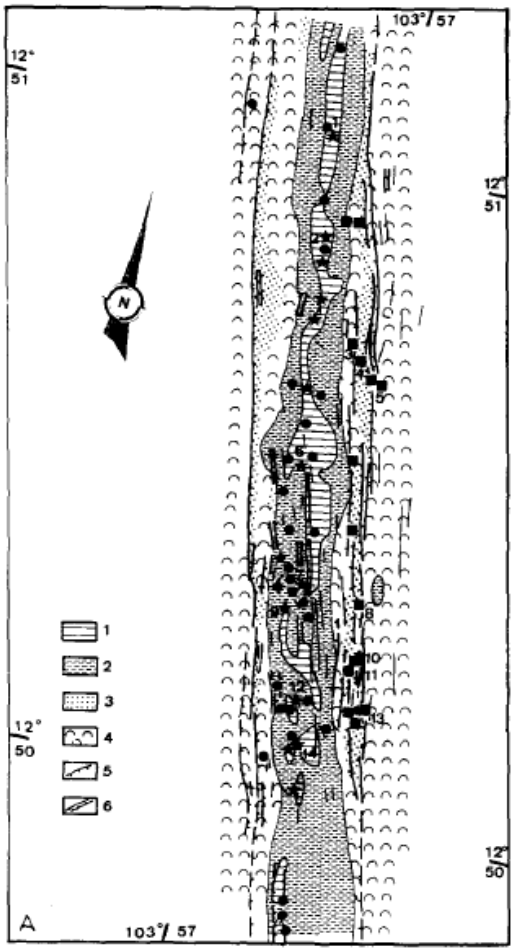

Number	Sample	Type	T°C
1	"Chandelier"		
	Cy 84-13-1	Ib	335
	Cy 84-17-1a	IVa	
	Cy 84-17-1b	IVa	
	Cy 84-17-2	IVb	
2	"Cathédrales"		
	Cy 82-18-2	IIIb	27
	Cy 84-13-2	IVb	
3	Cy 84-29-2	VIIa	
	Cy 84-29-3	VII	
4	Cy 84-27-2	IVa	
	Cy 84-27-3	VIIa	
	Cy 84-27-4	VIIa	
	Cy 84-27-5	VIa	
	Cy 84-29-4	VIIa	
	Cy 84-29-5	Vb	
5	Cy 84-29-6	Vb	
	Cy 84-29-7	Vb	
6	"Chain Site"		
	Cy 82-16-2	Ia	319
	Cy 82-25-1	IIb	
	Cy 82-25-2	Ia	
	Cy 82-25-3	IIb	
	Cy 82-30-1	Ib	
	Cy 82-30-2	Ia	
	Cy 82-30-3	Ib	
	Cy 82-30-7	Ia	
	Cy 84-17-3	IIIb	
	Cy 84-20-1	Ia	
7	Cy 82-27-5	IVb	
	Cy 82-25-6	II	
8	Cy 82-13-1	VIa	
9	"Tour de Pise"		
	Cy 82-03-2	Ia	310
	Cy 82-03-3	Ia	
	Cy 82-30-4	Ia	
	Cy 82-30-6(1)	Ia	
	Cy 82-30-6(2)	Ia	
	Cy 82-16-1	IVa	
10	Cy 82-25-9	VIIa	
11	Cy 82-25-7	IVb	
	Cy 82-25-8	II	
12	Cy 82-10-1	IVa	
	Cy 82-13-4	IIIa	
13	Cy 82-30-5	IVa	
14	Cy 82-03-1	Ia	283

Fig.2.A. Geological map of site A (located in Fig.1 (modified from Gente et al., 1986)) and detailed location of the collected samples. *1*=lavas lakes; *2*=lobate flows; *3*=talus; *4*=pillow lavas; *5*=graben wall; *6*=axial fissure. Stars—active; dots—inactive hydrothermalism at the axis; squares—inactive hydrothermalism on the top of the graben wall. B. Type of sulfide samples collected at site A. The numbers on the left coincide with those in Fig.2A.

21°N Green Seamount

Location: 20.783N, -109.267E
Area: 300 m^2
Reference: (Alt et al., 1987)

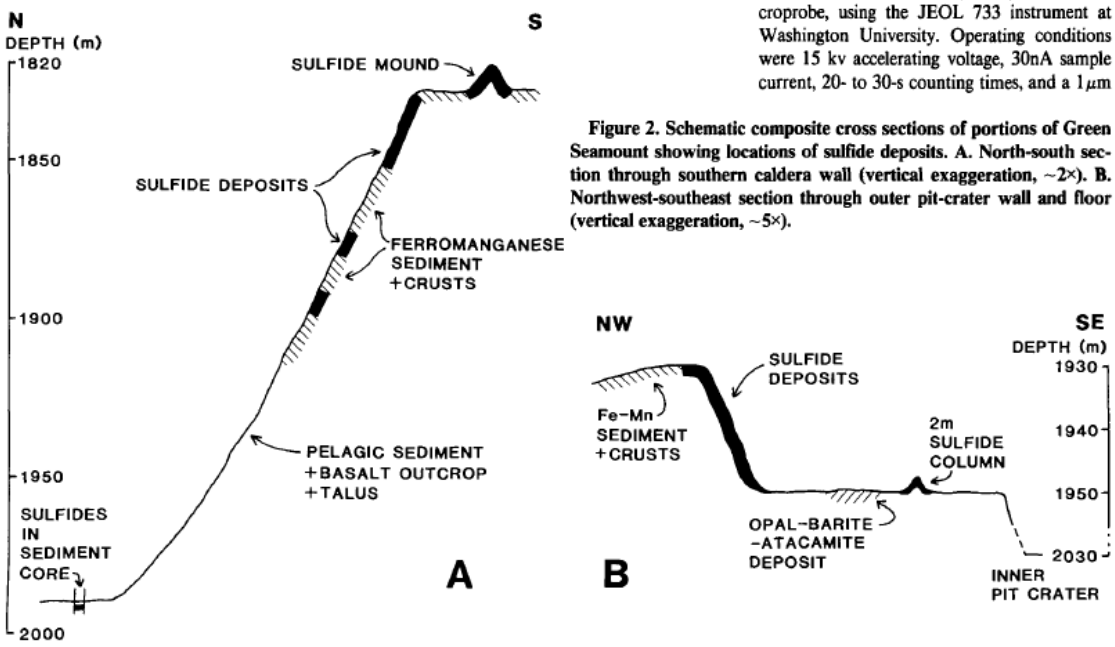

croprobe, using the JEOL 733 instrument at Washington University. Operating conditions were 15 kv accelerating voltage, 30nA sample current, 20- to 30-s counting times, and a 1 μm

Figure 2. Schematic composite cross sections of portions of Green Seamount showing locations of sulfide deposits. A. North-south section through southern caldera wall (vertical exaggeration, ~2×). B. Northwest-southeast section through outer pit-crater wall and floor (vertical exaggeration, ~5×).

Galapagos Rift

Location: 0.750N, -85.833E
Area: 30,000 m^2
Reference: (Embley et al., 1988)

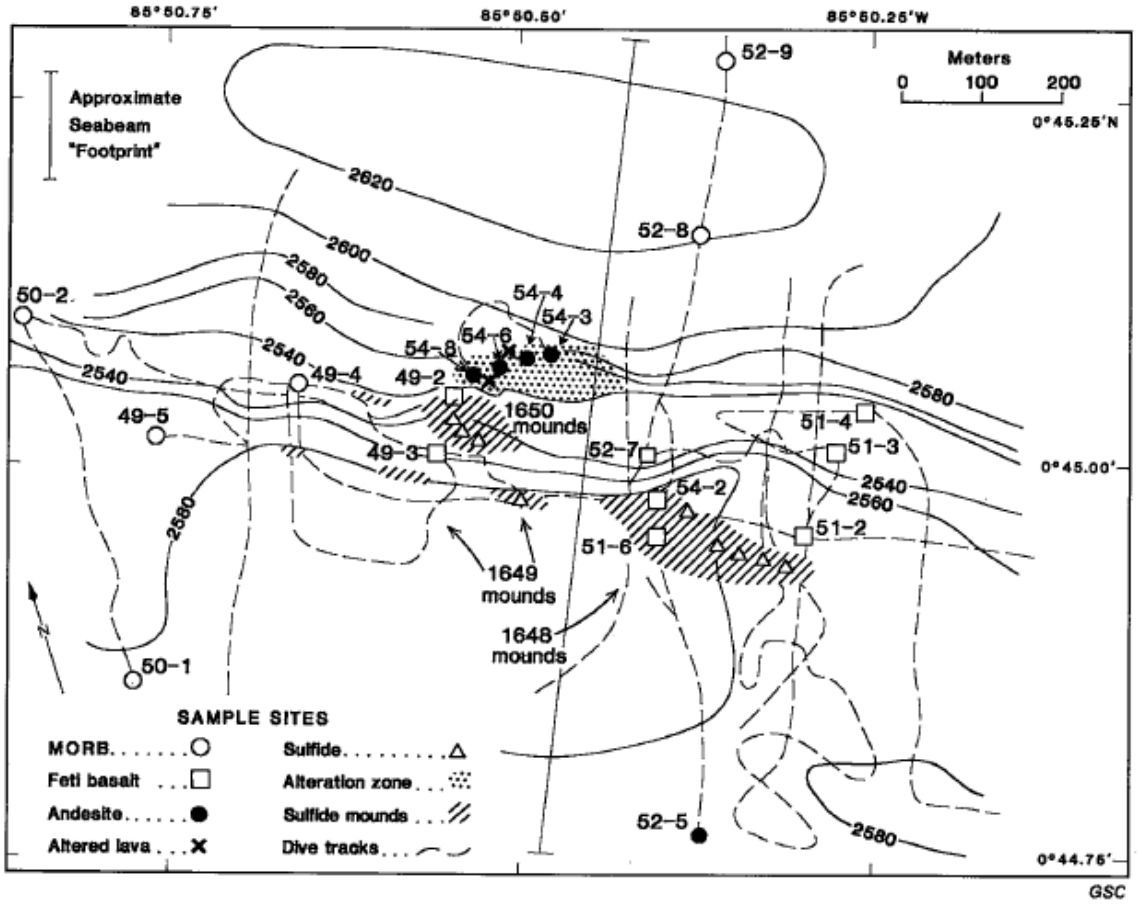

FIG. 4. Detailed bathymetry of dive area showing dive tracks, location of samples (*e.g.*, 54-4 designates Dive 1654, station 4), and lava types. Samples 1654-6, 7, 8 all are from the same site; 1655-1 not located for space reasons. Samples on wall projected to 2537 m (horst top). Box on Figure 3 shows area covered on map. Depths (m) based on ALVIN pressure gauge. N–S line indicates position of cross-section in Figure 5.

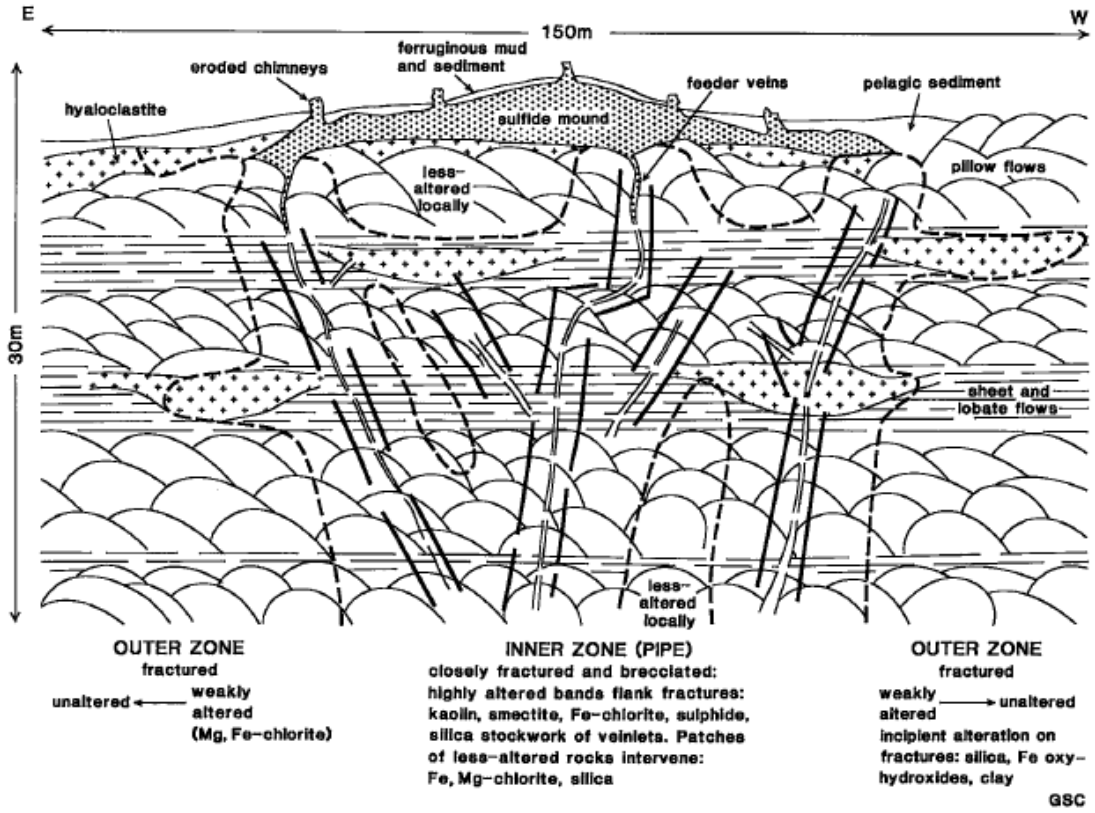

FIG. 8. Schematic section of the north wall (central horst) in the vicinity of the alteration zone, depicting structural and petrological features and their relationships to sulfide mounds. Reconstruction is based on visual observations, video, and still photography from ALVIN dives.

JUAN DE FUCA RIDGE

Mothra

Location: 47.820N, -129.105E
Area: 5,000 m^2
Reference: (Glickson et al., 2007)

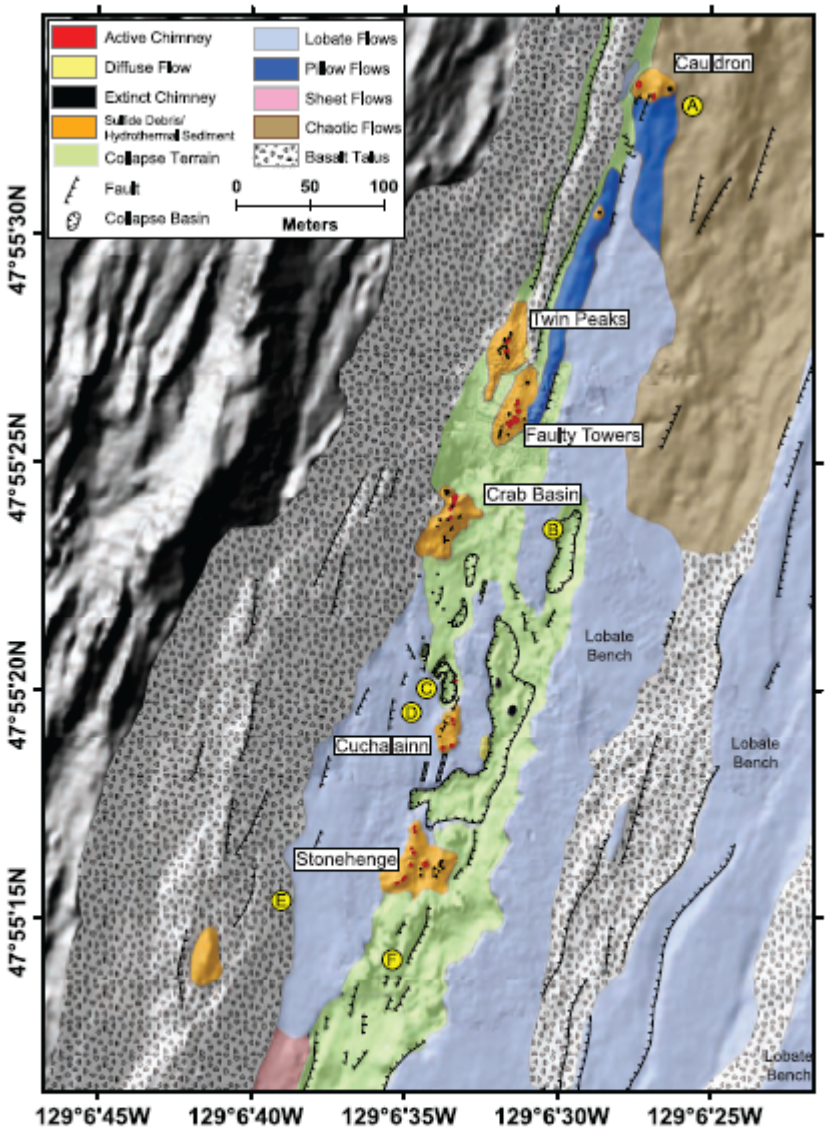

Figure 4. Geology of the Mothra Field created from analyses of visual imagery on 14 *Alvin* and ROV dives and coregistered scanning sonar and multibeam bathymetry. Major basaltic flow morphologies include lobate, pillow, ropy sheet, and chaotic flows, in addition to basalt talus and collapse terrain. The six labeled active sulfide clusters contain active and extinct chimneys and localized areas of diffuse flow. They are enclosed by sulfide talus and hydrothermal sediment. Extinct sulfide chimneys are far more numerous than shown, but most are too small or too poorly located to be accurately represented. Patches of diffuse flow are also more numerous than shown, but they are typically enclosed within the areas delineated by sulfide talus and hydrothermal sediment. Circled letters correspond to the locations of photographs shown in Figure 5.

Main Endeavour

Location: 47.950N, -129.100E
Area: 5,000 m^2
Reference: (Delaney et al., 1992)

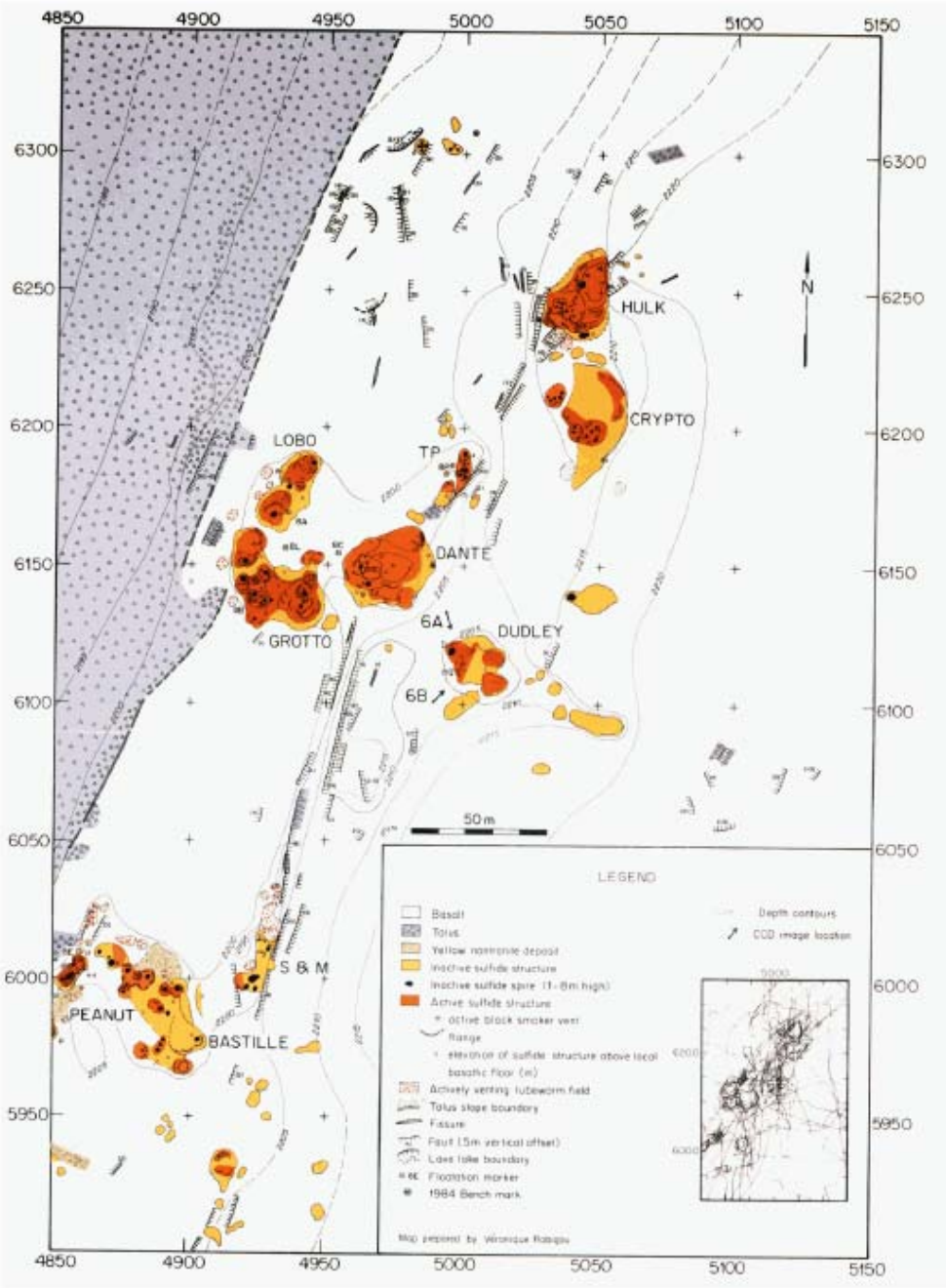

Plate 1. Geologic map of the Endeavour vent field, scale 1:1,250. This map was prepared from 25 Alvin dives in the Endeavour area (see track line inset). X (4850 E to 5150 E) and Y (5900 N to 6350 N) coordinates correspond to the transponder grid coordinates in m established during the summer 1988 dive program. All locations are based on in-hull navigation system described in text. The 5-m depth contours are drawn from the 1-m grid of the seafloor obtained by merging altitude and depth records from the submersible with the in-hull navigation records. The two small arrows located to the north and southwest of the "Dudley" sulfide structure indicate the position of the submersible on the basaltic floor while taking the CCD images of the sulfide structure shown in Figure 5.

High Rise

Location: 47.967N, -129.092E
Area: 3,000 m^2
Reference: (Robigou et al., 1993)

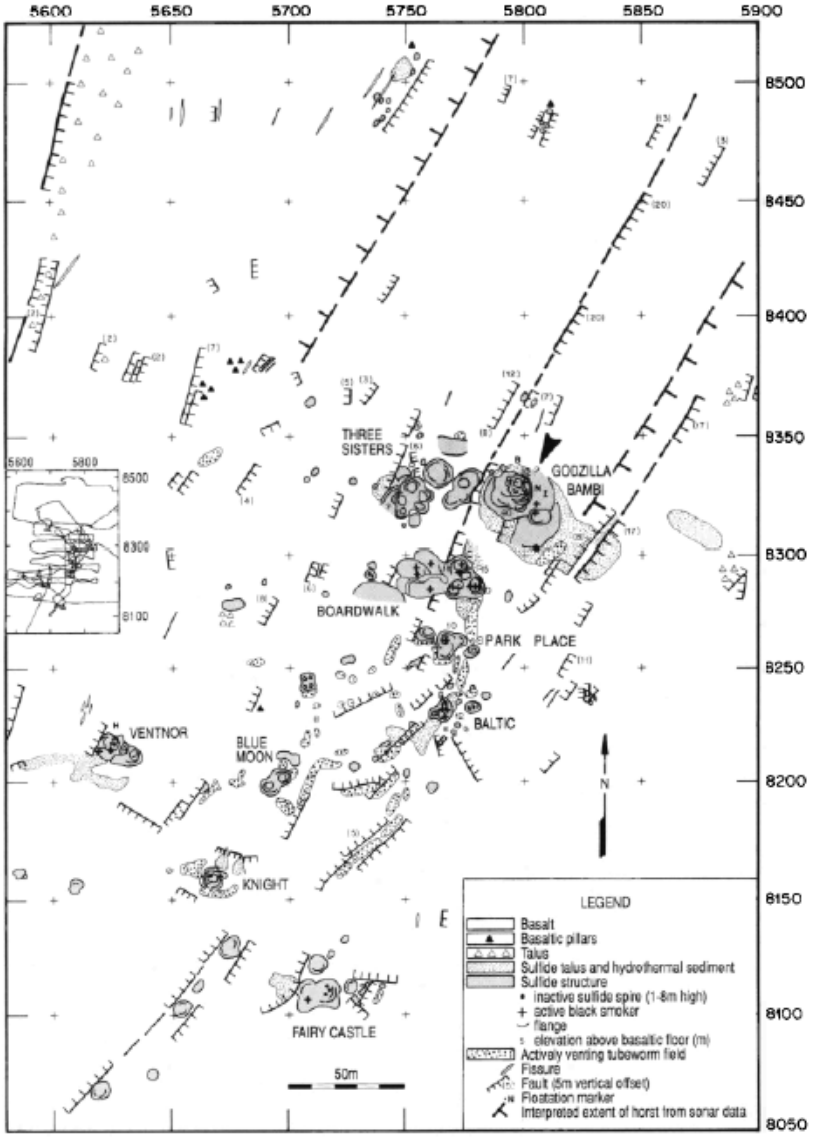

Fig. 3. Detailed geological map of the High-Rise vent field. The map was prepared from 9 dives during 1991 Atlantis II-Alvin legs 125-28 and 125-32 (J.R. Delaney), leg 125-30 (R. Lutz) and leg 125-33 (D.Stakes). All locations and sulfide structure elevations from the basaltic floor are based on in-hull navigation system [Delaney et al., 1992]. The black arrow indicates the position from which the drawing of the Godzilla structure was composed (Cover).

Southern Explorer Ridge

Location: 49.750N, -130.250E
Area: 5,000 m^2
Reference: (Tunnicliffe et al., 1986)

"One large deposit (Magic Mountain) is 200-250 m in diameter and hosts active hydrothermal vents at temperatures up to 306°C."

Middle Valley

Location: 48.433N, -128.683E
Area: 50,000 m^2
Reference: (Houghton et al., 2004)

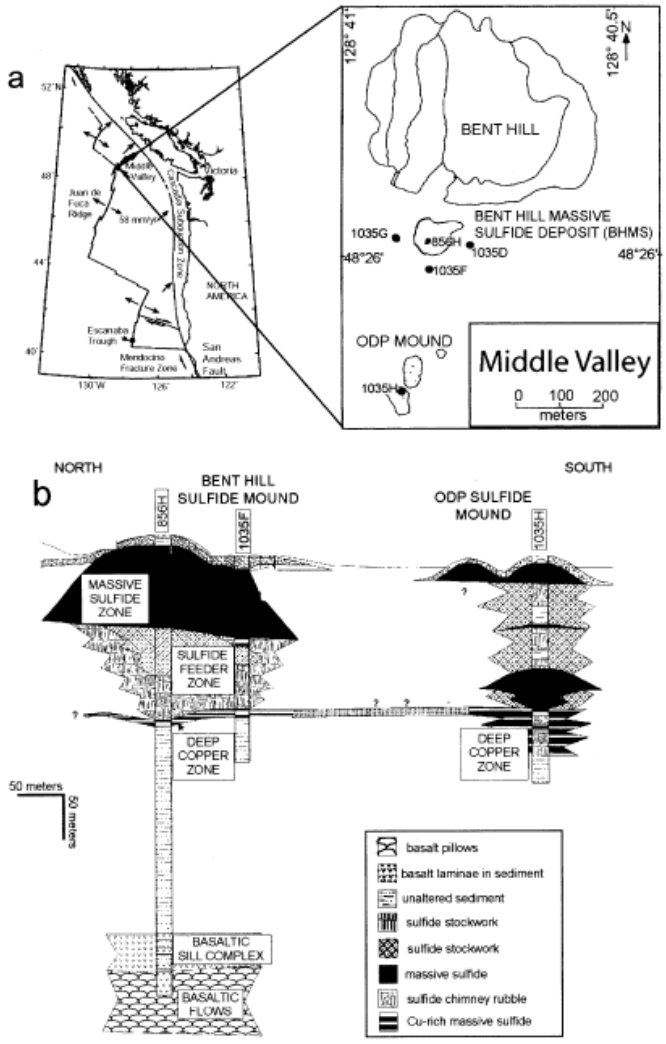

Fig. 1. (a) Map of the Middle Valley area on the Juan de Fuca Ridge with enlarged schematic diagram of the Bent Hill site showing some of the cores drilled during ODP Leg 169. Both east-west and north-south transects were made across the BHMS deposit. (b) Cross section of the BHMS and ODP Mound deposits. The BHMS deposit consists of a single massive sulfide zone and underlying feeder zone. The ODP Mound deposit, in contrast, contains three massive sulfide and feeder zone sets. Both deposits have a thin deep copper zone at the base, depicted here as possibly a continuous stratigraphic unit.

Guaymas Basin

Location: 27.017N, -111.417E
Area: 15,000 m^2
Reference: (Koski et al., 1985)

"More than 100 hydrothermal deposits, 10-100 m in diameter, are mapped in the area shown by Figure 2"

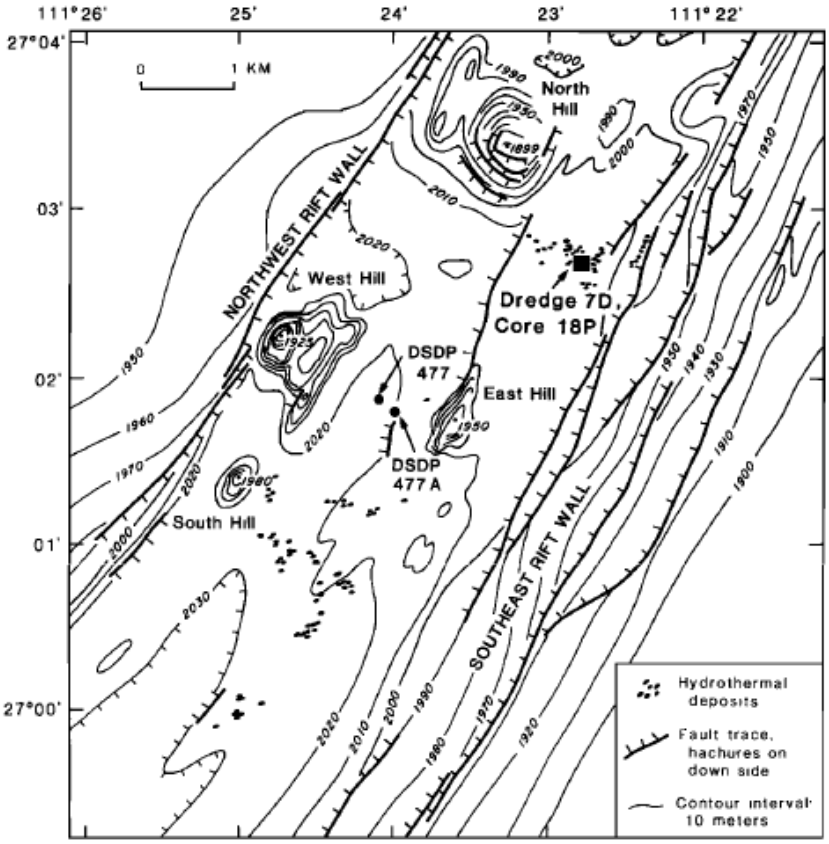

Fig. 2. Bathymetric and structural map of the Southern Trough showing the distribution of hydrothermal deposits, DSDP sites 477 and 477A and dredge site 7D. Uplifts on the valley floor are thought to be caused by shallow emplacement of pluglike intrusions [*Lonsdale and Lawver*, 1980].

Escanaba Trough

Location: 41.000N, -127.494E
Area: 1,000 m^2
Reference: (Fouquet et al., 1998)

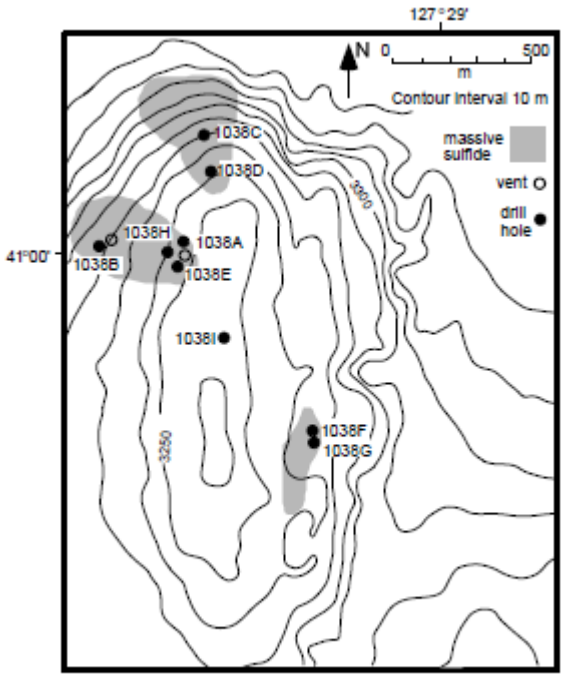

Figure 1. Location map showing the nine holes drilled at Central Hill, and the extent of massive sulfide on the seafloor.

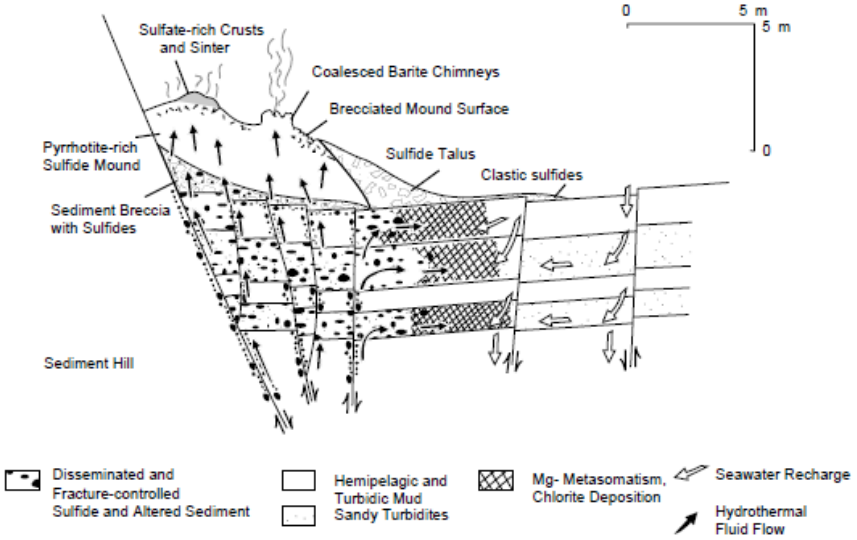

Figure 4. Generalized model for hydrothermal discharge and deposition of sulfide mounds at the margin of an uplifted sediment hill. The evolution of a sulfide mound includes initial precipitation of sulfate crust and chimneys, main-stage deposition of the pyrrhotite-rich sulfide assemblage below the sulfate carapace, inflationary growth during ongoing cementation, recrystallization and replacement within the mound, brecciation and degradation of the mound by mass wasting, and renewed precipitation of sulfate and sulfide from fluids discharging through the mound surface. The bounding fault structure and sediment breccia deposits provide cross-stratal permeability for hydrothermal fluids. Fluids migrate laterally along porous sandy units in the turbidite section. Subsurface mixing of hydrothermal fluid and seawater along faults and within permeable beds results in disseminated and fracture-controlled sulfide mineralization, Mg metasomatism, and chlorite formation in the sediment (Zierenberg et al., 1993).

INDIAN OCEAN

MESO Zone

Location: 23.393S, 69.242E
Area: 40,000 m^2
Reference: (Halbach et al., 1998)

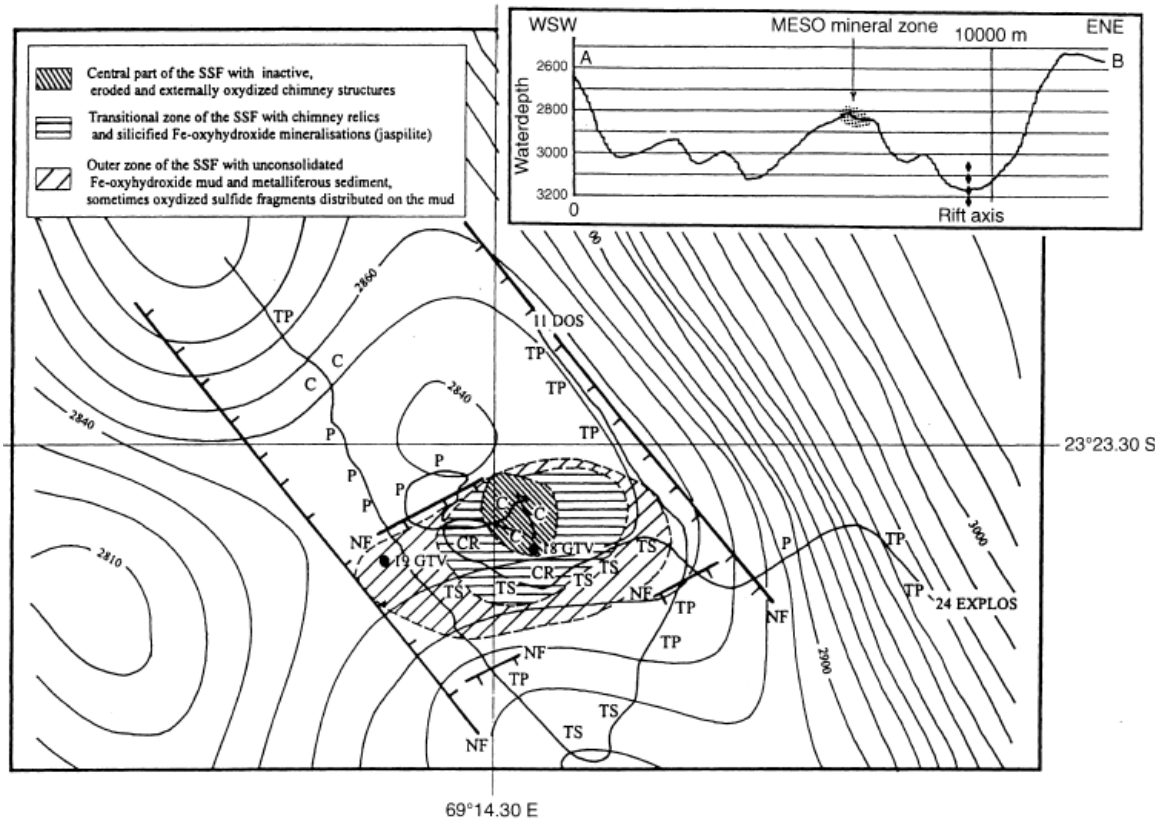

Kairei Field

Location: 25.317S, 70.033E
Area: 3,000 m^2
Reference: (Gallant and Von Damm, 2006)

"Hydrothermal venting is focused within an ~80 by 40 m area that trends WNW. There are three mounds with active high-temperature vents within a larger area of weathered sulfides."

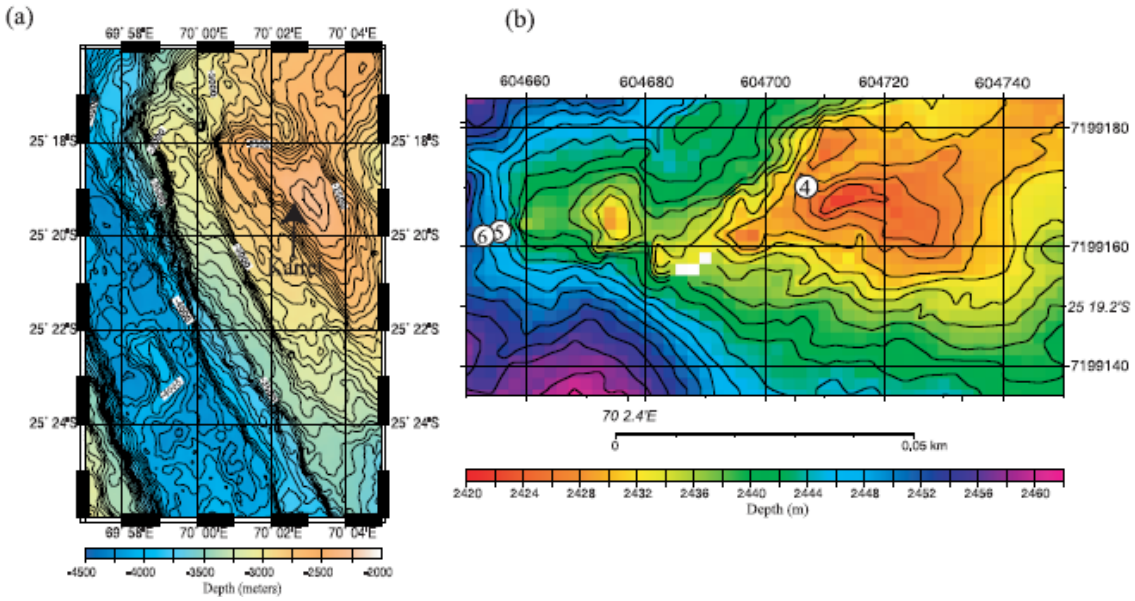

Figure 2. (a) Bathymetric map showing the location of the Kairei vent field (50 m contours). (b) Relative locations of the individual vents sampled within the Kairei field in *Jason* x-y coordinates (meters). (c) Bathymetric map showing the location of the Edmond vent field (20 m contours). (d) Relative locations of the individual vents sampled within the Edmond field superimposed on bathymetry (10 m contours). All bathymetry is based on SeaBeam data. Maps are courtesy of D. Fornari.

Edmond Field

Location: 23.867S, 69.600E
Area: 6,000 m^2
Reference: (Gallant and Von Damm, 2006)

"Although the area of extinct sulfide structures and talus is larger (~100 m by 60 m) than at Kairei, the area of high-temperature venting is slightly smaller (~40 m^2) and consists of a wider range of high-temperature vent chimney morphologies and more extensive diffuse flow than at Kairei."

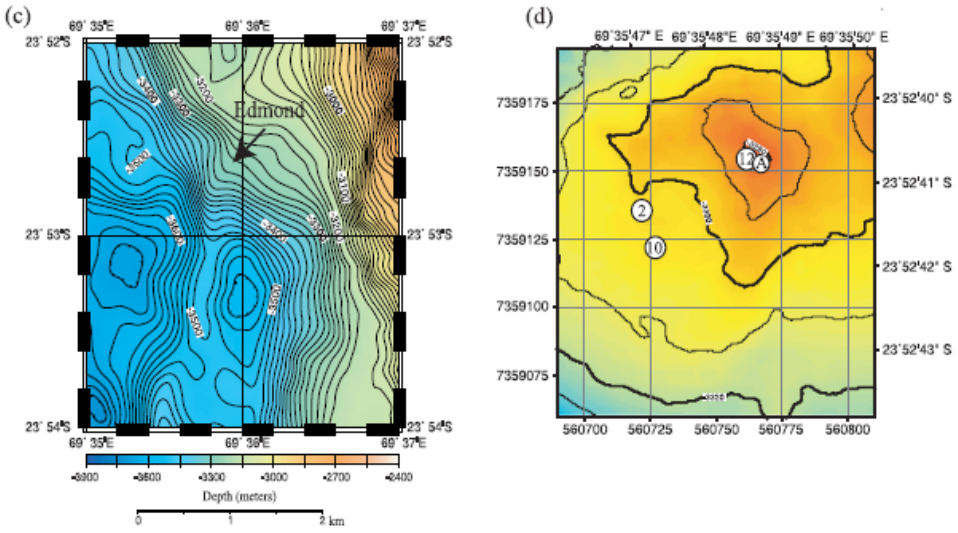

Figure 2. (a) Bathymetric map showing the location of the Kairei vent field (50 m contours). (b) Relative locations of the individual vents sampled within the Kairei field in *Jason* x-y coordinates (meters). (c) Bathymetric map showing the location of the Edmond vent field (20 m contours). (d) Relative locations of the individual vents sampled within the Edmond field superimposed on bathymetry (10 m contours). All bathymetry is based on SeaBeam data. Maps are courtesy of D. Fornari.

IZU-BONIN ARC

Sunrise

Location: 32.100N, 139.867E
Area: 150,000 m^2
Reference: (Iizasa et al., 1999)

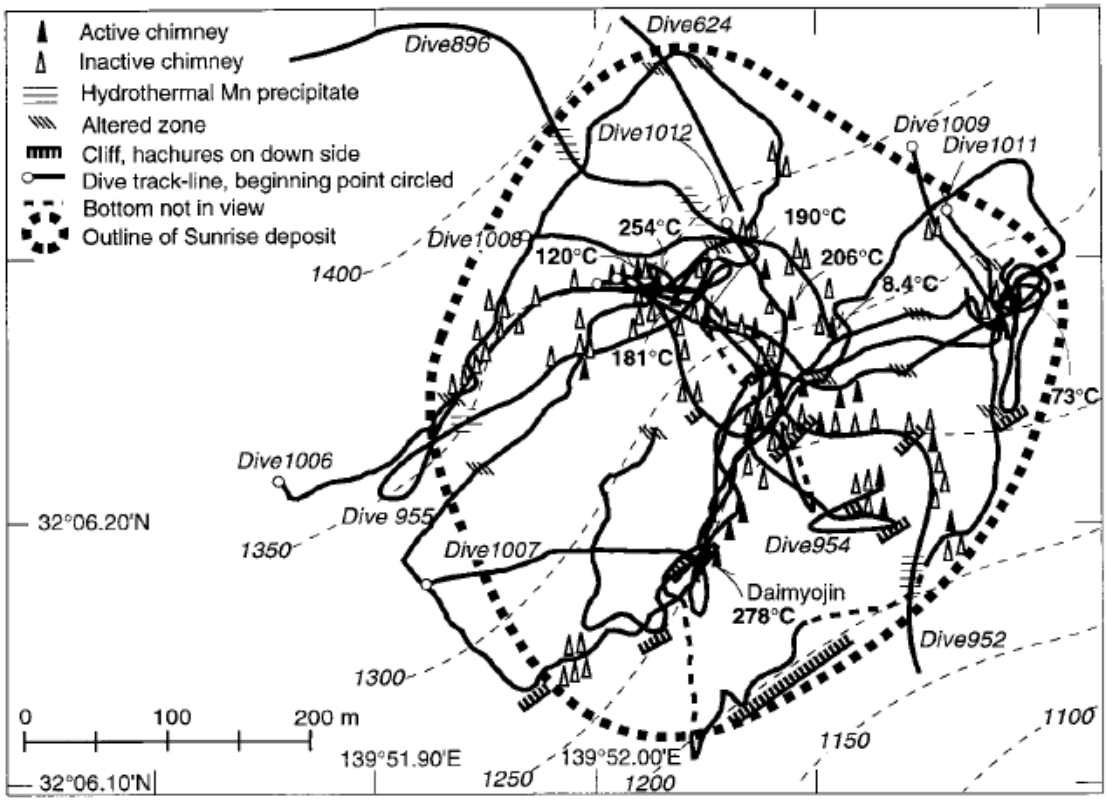

Fig. 2. Map of the Sunrise deposit. Hydrothermal fluid temperatures are shown at selected chimneys; the highest observed temperature, 278°C, was measured at the top of a 30-m-high sulfide chimney informally called Daimyojin ("Big Myojin"). Contour interval, 50 m.

Suiyo Seamount

Location: 28.567N, 140.650E
Area: 3,000 m^2
Reference: (Glasby et al., 2000)

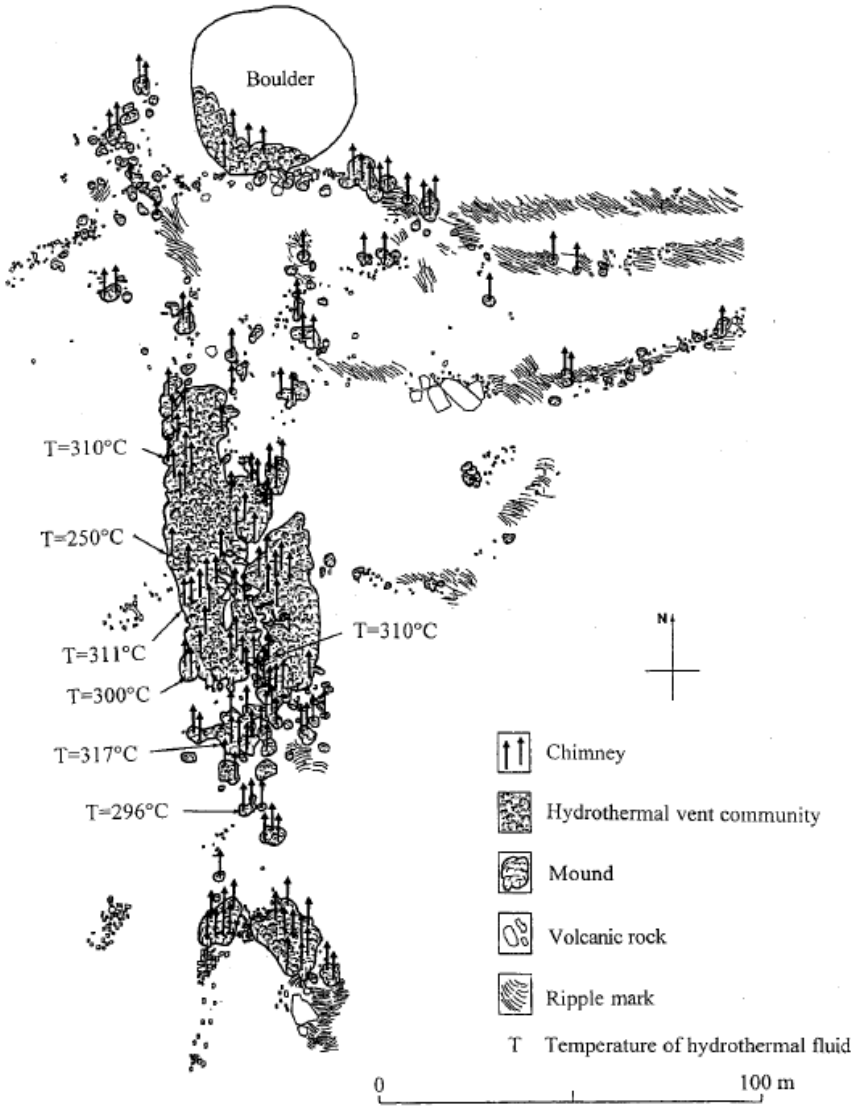

Figure 6. Schematic map showing the distribution of hydrothermal chimneys and mounds on the caldera floor of the western peak of Suiyo Seamount (modified from Watanabe et al., 1994: Figure 4).

North Fiji Basin

Location: 16.983S, 173.917E
Area: 3,000 m^2
Reference: (Bendel et al., 1993)

"The hydrothermal field is located in the central part of the axial graben and is about 50 m in diameter. Deposits consist of metalliferous sediment blanketing the basalt and individual inactive spires up to 8 m high. One small sulfide mound, 7 m in diameter and 5 m thick, was examined in detail."

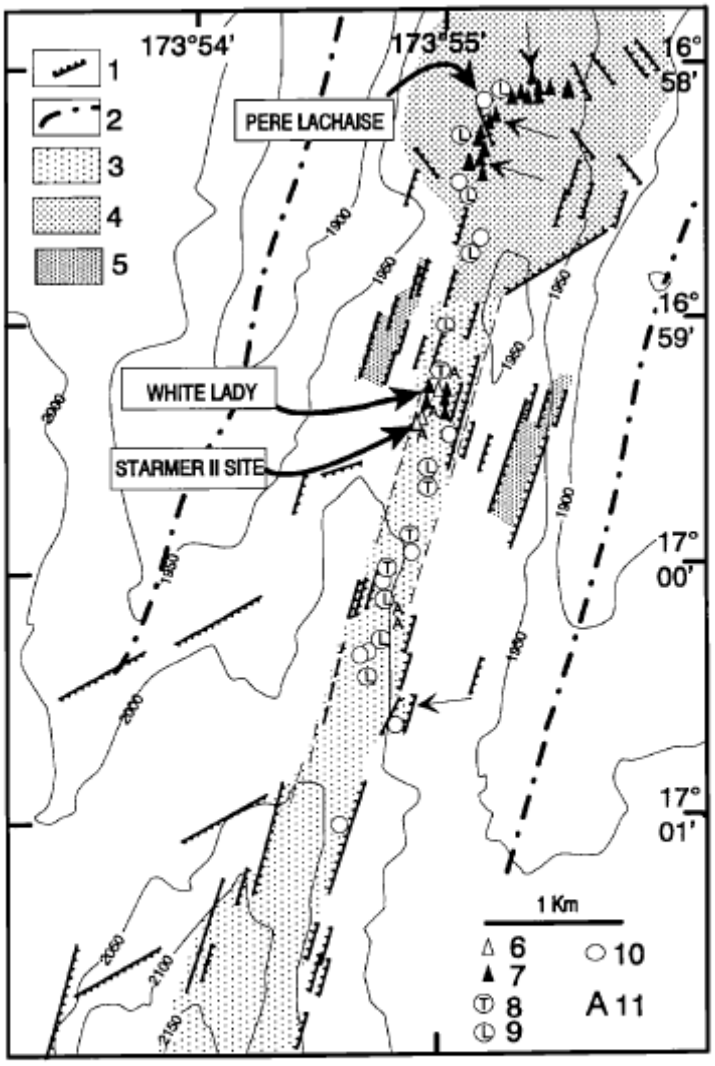

FIG. 4. Structural sketch map from dives observations (modified after Auzende et al., in press). 1 = normal fault, 2 = crest, 3 = main axial graben, 4 = intersection zone, 5 = secondary graben, 6 = active hydrothermal sites, 7 = fossil chimneys, 8 = temperature anomaly, 9 = lava lake, 10 = yellow hydrothermal staining, 11 = mussels and gastropods (alive at the White Lady and Starmer II sites); Small arrrows = sampling areas out of the White Lady site.

Brothers Seamount (Kermadec Arc)

Location: 34.850S, 179.067E
Area: 5,000 m^2
Reference: (de Ronde et al., 2005)

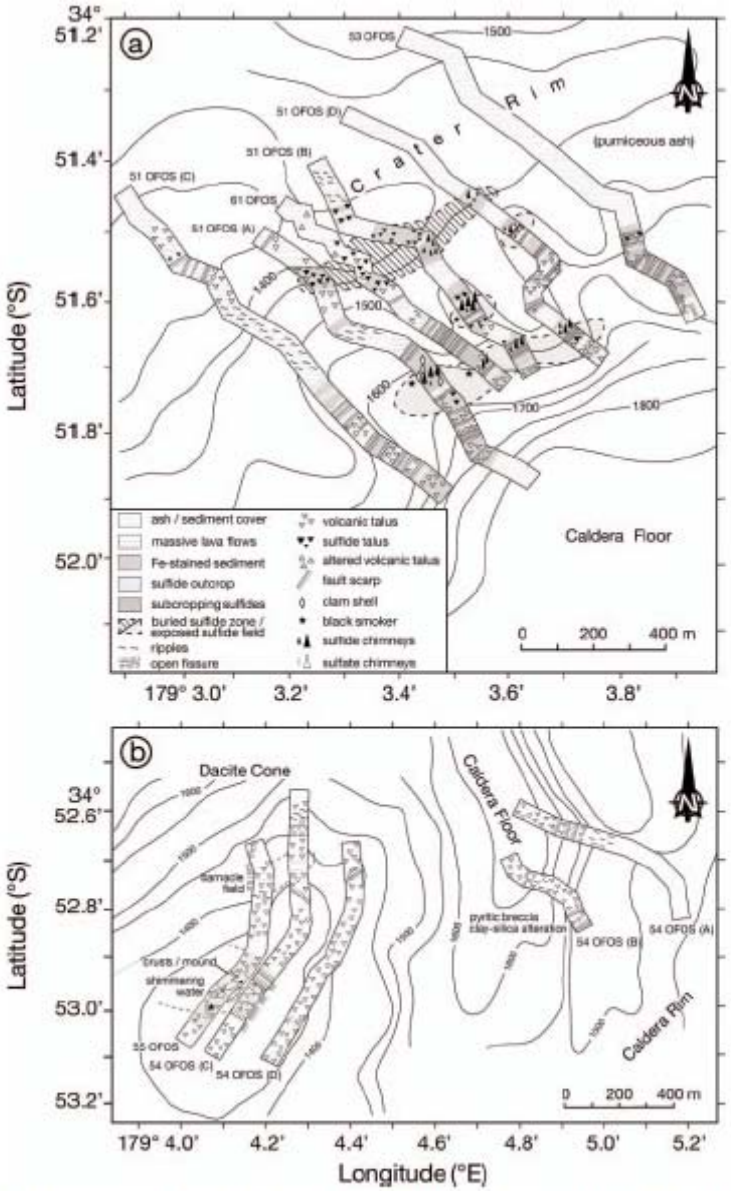

FIG. 7. a. Geology of the northwest caldera site constructed from towed video camera observations (contoured depth in meters). The caldera wall is relatively steep and is largely covered by ash and/or sediment although massive lava flows are seen locally (see Fig. 3). Two large zones containing relict chimneys and spires and subcropping massive sulfides were seen; one nearer the caldera floor and the other nearer the caldera rim. Actively venting chimneys were seen in the lower zone and part way up the caldera wall. b. Observations in towed camera surveys over the cone and southeast caldera sites. Only minor evidence was seen for past hydrothermal activity at the latter site. No actively venting chimneys were observed over the cone site, although several black smoker plumes were seen in 1999 as were abundant vent shrimp and pieces of hydrothermally altered rock (see Fig. 3). Diffuse venting and a large field of barnacles were seen down the northeast flank of the cone.

Palinuro Seamount (Tyrrhenian Sea)

Location: 39.533N, 14.700E
Area: 3,000 m^2
Reference: (Eckhardt et al., 1997)

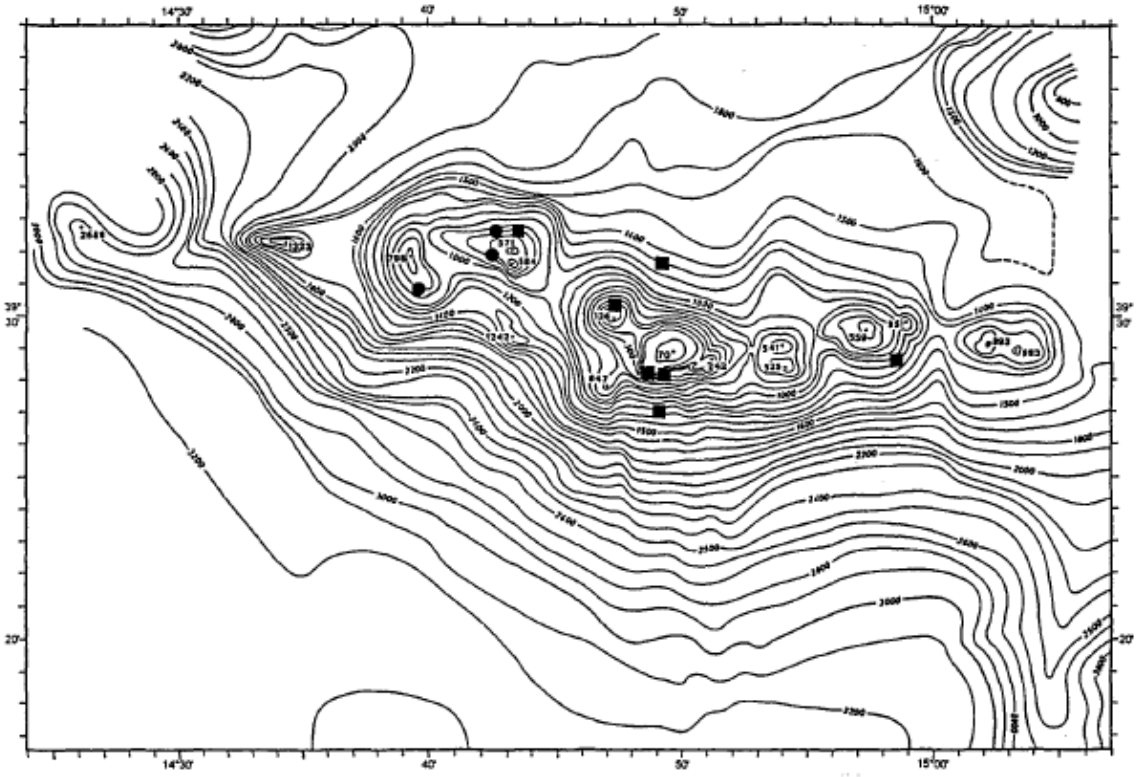

Figure 2. Schematic bathymetric chart of Palinuro Seamount contured at an interval of 100 m. Dots denote the occurrence of hydrothermal sulfide minerals and squares hydrothermal manganese crusts. (After Fabbri et al., 1973.)

Izena Cauldron (Jade) (Okinawa Trough)

Location: 27.267N, 127.083E
Area: 5,000 m^2
Reference: (Marumo and Hattori, 1999)

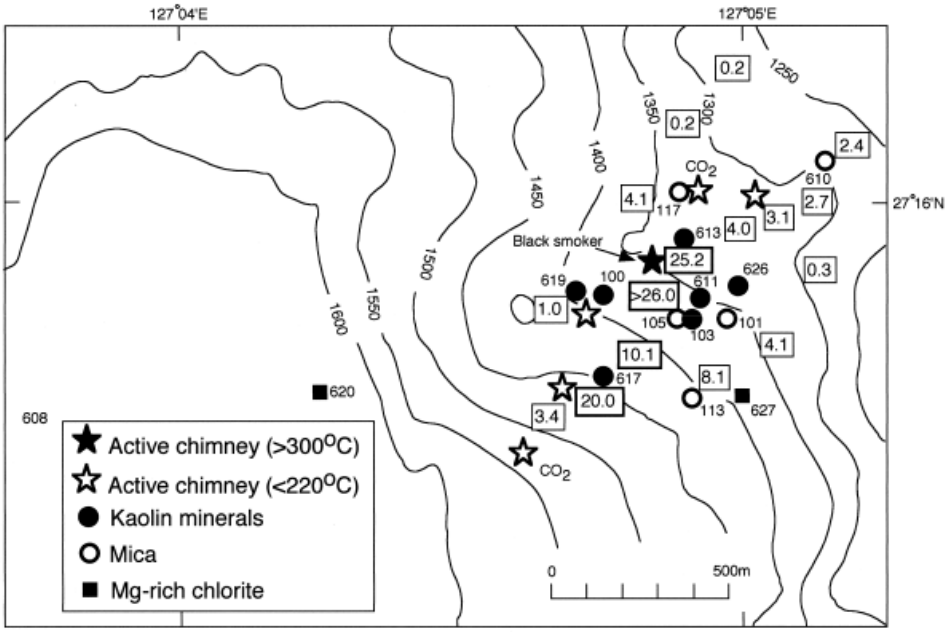

Fig. 1-3. Bathymetric map of the Jade field with the distribution of clay minerals. The sites for the gravity cores are numbered from 608 to 627 and those for the grab samplers from 100 to 117. Numbers in squares are heat flow values in kmW/m^2 (Kinoshita, 1990).

MANUS BASIN

Solwara 1

Location: 3.783S, 152.083E
Area: 90,000 m^2
Reference: (Lipton, 2012)

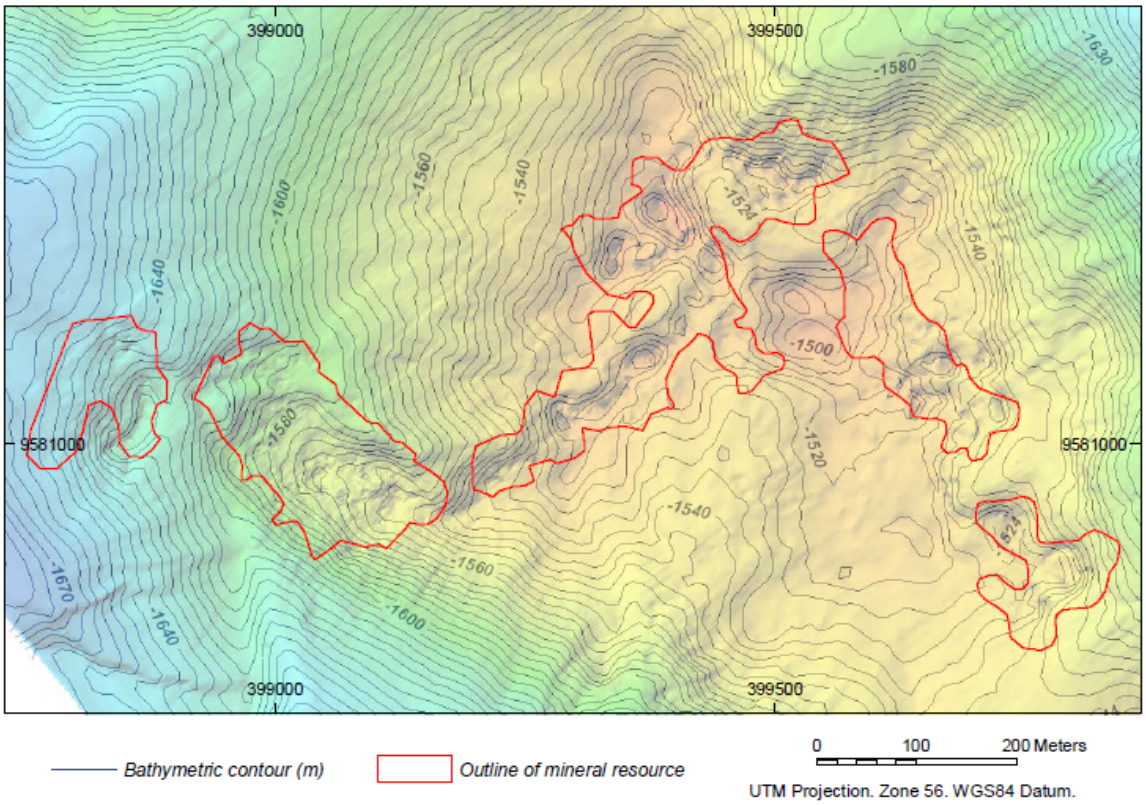

Figure 7-1 Plan showing bathymetric contours and outline of mineral resources

Solwara 4 (Pacmanus)

Location: 3.733S, 151.667E
Area: 15,000 m^2
Reference: (Beaudoin et al., 2007)

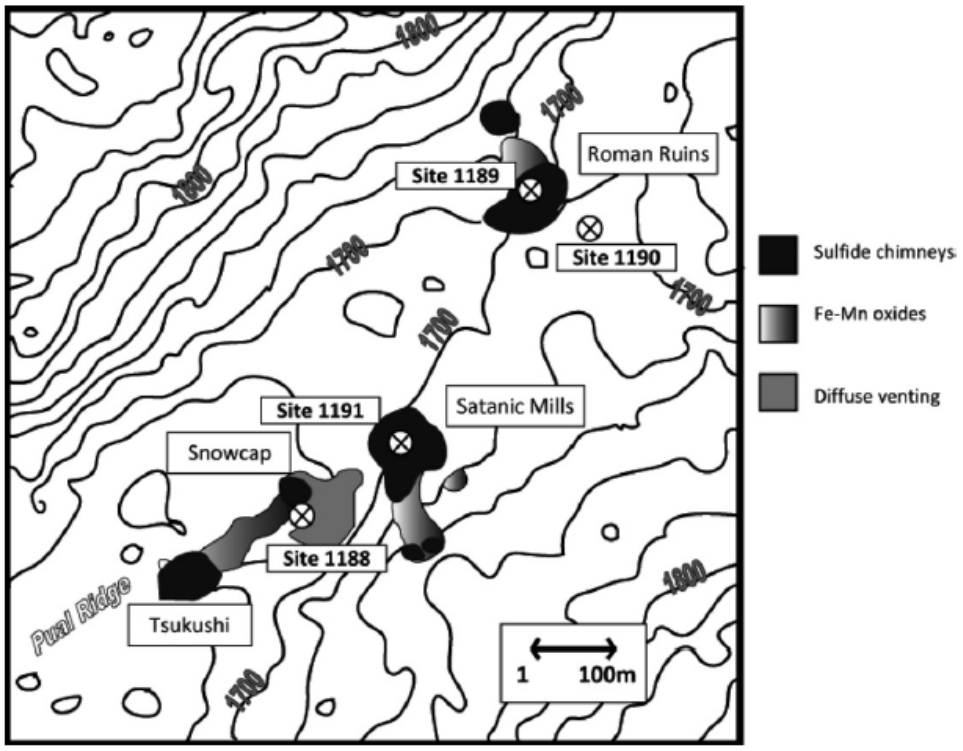

Fig. 2. Location of hydrothermal deposits comprising the PACMANUS hydrothermal area. ODP Leg 193 drill sites 1188, 1189, 1190 and 1191 are shown. Map modified from Binns et al. (2002).

Solwara 5

Location: 3.783S, 152.067E
Area: 15,000 m^2
Reference: (Lipton, 2012)

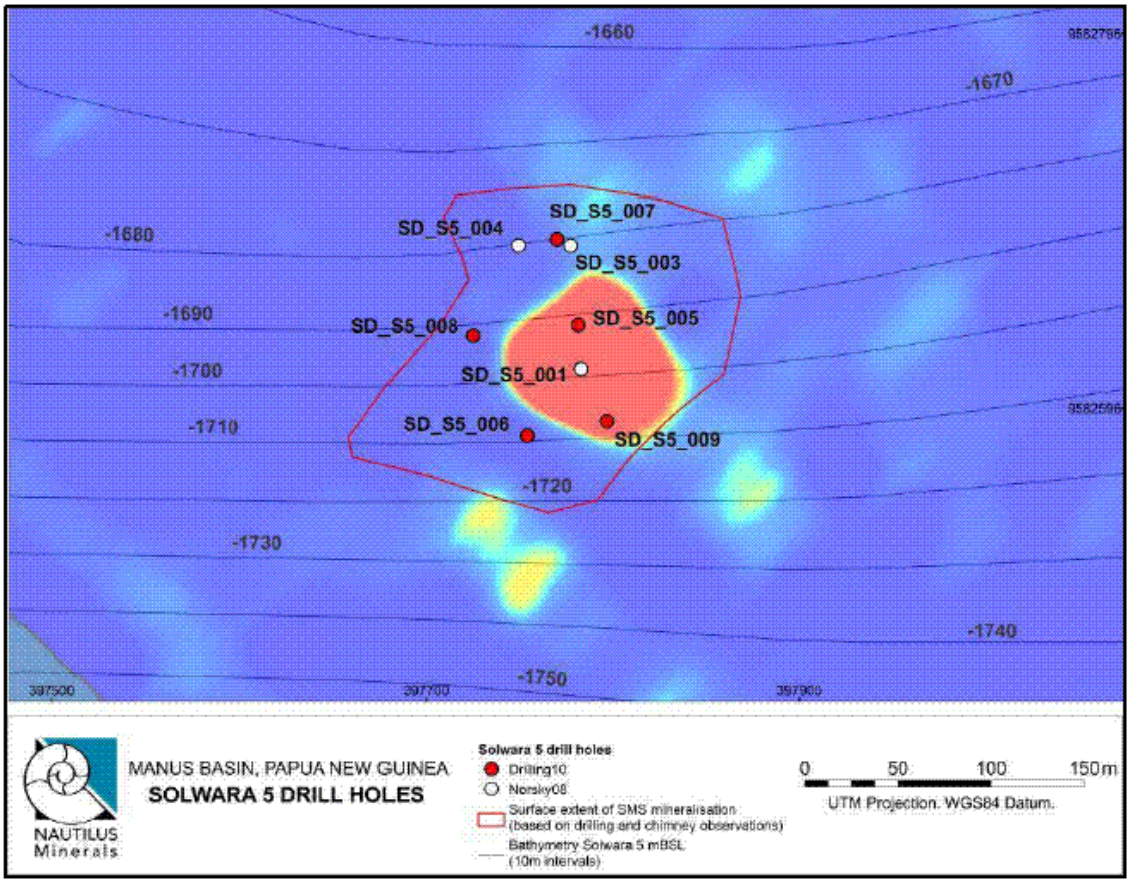

Figure 41: Location of drillholes at Solwara 5

Solwara 6

Location: 3.733S, 151.683E
Area: 3,000 m^2
Reference: (Lipton, 2012)

"The field is inactive, covering an area of approximately 50 m by 50 m, with the standing chimneys formed in clusters and individual chimneys up to several metres in height. The standing chimneys are surrounded by piles of collapsed chimney debris, and the chimney field is sediment covered."

Solwara 7

Location: 3.717S, 151.667E
Area: 15,000 m^2
Reference: (Lipton, 2012)

“The area is a highly active hydrothermal field with a strike length of 200 m and 20 to 25 m wide.” “The area is characterized by a large variety of chimney styles, ranging from narrow, tall and fragile black smokers up to 18 m high, to collapsed and broken tree-trunk like formations, to classic beehive chimneys, to white anhydrite chimneys. The chimneys occur in clusters of dozens, and are surrounded by large mounds of collapsed chimney rubble forming piles at least two or three metres high in some places.”

References:

Alt, J.C., Lonsdale, P., Haymon, R., Muehlenbachs, K., 1987. Hydrothermal sulfide and oxide deposits on seamounts near 21-degrees-N, East Pacific Rise. Geological Society of America Bulletin 98, 157-168.

Beaudoin, Y., Scott, S.D., Gorton, M.P., Zajacz, Z., Halter, W., 2007. Effects of hydrothermal alteration on Pb in the active PACMANUS hydrothermal field, ODP leg 193, Manus Basin, Papua New Guinea: A LA-ICP-MS study. Geochimica Et Cosmochimica Acta 71, 4256-4278.

Bendel, V., Fouquet, Y., Auzende, J.M., Lagabrielle, Y., Grimaud, D., Urabe, T., 1993. The White-Lady hydrothermal field, North Fiji Back-arc Basin, Southwest Pacific. Economic Geology and the Bulletin of the Society of Economic Geologists 88, 2237-2249.

Bogdanov, Y.A., Lein, A.Y., Maslennikov, V.V., Li, S., Ul'yanov, A.A., 2008. Mineralogical-Geochemical Features of Sulfide Ores from the Broken Spur Hydrothermal Vent Field. Oceanology 48, 679-700.

Cherkashov, G., Bel'tenev, V., Ivanov, V., Lazareva, L., Samovarov, M., Shilov, V., Stepanova, T., Glasby, G.P., Kuznetsov, V., 2008. Two New Hydrothermal Fields at the Mid-Atlantic Ridge. Marine Georesources & Geotechnology 26, 308-316.

Cherkashov, G., Poroshina, I., Stepanova, T., Ivanov, V., BeL'Tenev, V., Lazareva, L., Rozhdestvenskaya, I., Samovarov, M., Shilov, V., Glasby, G.P., Fouquet, Y., Kuznetsov, V., 2010. Seafloor Massive Sulfides from the Northern Equatorial Mid-Atlantic Ridge: New Discoveries and Perspectives. Marine Georesources & Geotechnology 28, 222-239.

de Ronde, C.E.J., Hannington, M.D., Stoffers, P., Wright, I.C., Ditchburn, R.G., Reyes, A.G., Baker, E.T., Massoth, G.J., Lupton, J.E., Walker, S.L., Greene, R.R., Soong, C.W.R., Ishibashi, J., Lebon, G.T., Bray, C.J., Resing, J.A., 2005. Evolution of a submarine magmatic-hydrothermal system: Brothers volcano, southern Kermadec arc, New Zealand. Economic Geology 100, 1097-1133.

Delaney, J.R., Robigou, V., McDuff, R.E., Tivey, M.K., 1992. Geology of a vigorous hydrothermal system on the Endeavour Segment, Juan de Fuca Ridge. Journal of Geophysical Research-Solid Earth 97, 19663-19682.

Eckhardt, J.D., Glasby, G.P., Puchelt, H., Berner, Z., 1997. Hydrothermal manganese crusts from Enarete and Palinuro Seamounts in the Tyrrhenian Sea. Marine Georesources & Geotechnology 15, 175-208.

Embley, R.W., Jonasson, I.R., Perfit, M.R., Franklin, J.M., Tivey, M.A., Malahoff, A., Smith, M.F., Francis, T.J.G., 1988. Submersible investigation of an extinct hydrothermal system on the Galapagos Ridge - Sulfide mounds, stockwork zone, and differentiated lavas. Canadian Mineralogist 26, 517-539.

Fouquet, Y., Auclair, G., Cambon, P., Etoubleau, J., 1988. Geological setting and mineralogical and geochemical investigations on sulfide deposits near 13-degrees-N the East Pacific Rise. Marine Geology 84, 145-178.

Fouquet, Y., Knott, R., Cambon, P., Fallick, A., Rickard, D., Desbruyeres, D., 1996. Formation of large sulfide mineral deposits along fast spreading ridges. Example from off-axial deposits at 12 degrees 43'N on the east Pacific rise. Earth and Planetary Science Letters 144, 147-162.

Fouquet, Y., Zierenberg, R., Miller, D., 1998. Proceedings of the Ocean Drilling Program, Initial Reports.

Gallant, R.M., Von Damm, K.L., 2006. Geochemical controls on hydrothermal fluids from the Kairei and Edmond Vent Fields, 23 degrees-25 degrees S, Central Indian Ridge. Geochemistry Geophysics Geosystems 7.
Glasby, G.P., Iizasa, K., Yuasa, M., Usui, A., 2000. Submarine hydrothermal mineralization on the Izu-Bonin Arc, south of Japan: An overview. Marine Georesources & Geotechnology 18, 141-176.
Glickson, D.A., Kelley, D.S., Delaney, J.R., 2007. Geology and hydrothermal evolution of the Mothra Hydrothermal Field, Endeavour Segment, Juan de Fuca Ridge. Geochemistry Geophysics Geosystems 8.
Haase, K.M., Petersen, S., Koschinsky, A., Seifert, R., Devey, C.W., Keir, R., Lackschewitz, K.S., Melchert, B., Perner, M., Schmale, O., Suling, J., Dubilier, N., Zielinski, F., Fretzdorff, S., Garbe-Schonberg, D., Westernstroer, U., German, C.R., Shank, T.M., Yoerger, D., Giere, O., Kuever, J., Marbler, H., Mawick, J., Mertens, C., Stober, U., Ostertag-Henning, C., Paulick, H., Peters, M., Strauss, H., Sander, S., Stecher, J., Warmuth, M., Weber, S., 2007. Young volcanism and related hydrothermal activity at 5 degrees S on the slow-spreading southern Mid-Atlantic Ridge. Geochemistry Geophysics Geosystems 8.
Halbach, P., Blum, N., Munch, U., Pluger, W., Garbe-Schonberg, D., Zimmer, M., 1998. Formation and decay of a modern massive sulfide deposit in the Indian ocean. Mineralium Deposita 33.
Houghton, J.L., Shanks, W.C., Seyfried, W.E., 2004. Massive sulfide deposition and trace element remobilization in the Middle Valley sediment-hosted hydrothermal system, northern Juan de Fuca Rdge. Geochimica Et Cosmochimica Acta 68, 2863-2873.
Iizasa, K., Fiske, R.S., Ishizuka, O., Yuasa, M., Hashimoto, J., Ishibashi, J., Naka, J., Horii, Y., Fujiwara, Y., Imai, A., Koyama, S., 1999. A Kuroko-type polymetallic sulfide deposit in a submarine silicic caldera. Science 283, 975-977.
Karson, J.A., Brown, J.R., 1989. Geologic setting of the Snake Pit hydrothermal site - an active vent field on the Mid-Atlantic Ridge. Marine Geophysical Researches 10, 91-107.
Koski, R.A., Lonsdale, P.F., Shanks, W.C., Berndt, M.E., Howe, S.S., 1985. Mineralogy and geochemistry of a sediment-hosted hydrothermal sulfide deposit from the Southern Trough of Guaymas Basin, Gulf of California. Journal of Geophysical Research-Solid Earth and Planets 90, 6695-6707.
Kuznetsov, V., Cherkashev, G., Lein, A., Shilov, V., Maksimov, F., Arslanov, K., Stepanova, T., Baranova, N., Chernov, S., Tarasenko, D., 2006. Th-230/U dating of massive sulfides from the Logatchev and Rainbow hydrothermal fields (Mid-Atlantic Ridge). Geochronometria 25, 51-55.
Langmuir, C., Humphris, S., Fornari, D., VanDover, C., VonDamm, K., Tivey, M.K., Colodner, D., Charlou, J.L., Desonie, D., Wilson, C., Fouquet, Y., Klinkhammer, G., Bougault, H., 1997. Hydrothermal vents near a mantle hot spot: The Lucky Strike vent field at 37 degrees N on the Mid-Atlantic Ridge. Earth and Planetary Science Letters 148, 69-91.
Lipton, I., 2012. Mineral Resource Estimate - Solwara Project, Bismarck Sea, PNG: Canadian NI 43-101 Technical Report for Nautilus Minerals Inc., 240 p.
Marques, A.F.A., Barriga, F., Chavagnac, V., Fouquet, Y., 2006. Mineralogy, geochemistry, and Nd isotope composition of the Rainbow hydrothermal field, Mid-Atlantic Ridge. Mineralium Deposita 41, 52-67.

Marumo, K., Hattori, K.H., 1999. Seafloor hydrothermal clay alteration at Jade in the back-arc Okinawa Trough: Mineralogy, geochemistry and isotope characteristics. Geochimica Et Cosmochimica Acta 63, 2785-2804.
Robigou, V., Delaney, J.R., Stakes, D.S., 1993. Large massive sulfide deposits in a newly discovered active hydrothermal system, the Highrise Field, Endeavour Segment, Juan-de-Fuca Ridge. Geophysical Research Letters 20, 1887-1890.
Rona, P.A., Hannington, M.D., Raman, C.V., Thompson, G., Tivey, M.K., Humphris, S.E., Lalou, C., Petersen, S., 1993. Active and relict sea-floor hydrothermal mineralization at the TAG hydrothermal field, Mid-Atlantic Ridge. Economic Geology and the Bulletin of the Society of Economic Geologists 88, 1989-2017.
Tunnicliffe, V., Botros, M., Deburgh, M.E., Dinet, A., Johnson, H.P., Juniper, S.K., McDuff, R.E., 1986. HYDROTHERMAL VENTS OF EXPLORER RIDGE, NORTHEAST PACIFIC. Deep-Sea Research Part a-Oceanographic Research Papers 33, 401-412.
White, S.N., Humphris, S.E., Kleinrock, M.C., 1998. New observations on the distribution of past and present hydrothermal activity in the TAG area of the mid-Atlantic ridge (26 degrees 08 ' N). Marine Geophysical Researches 20, 41-56.

APPENDIX C – Sulfide Geochemistry

Sample	Field	Cu	Fe	Zn	Pb	S	SiO2	Ba	MgO	CaO	Cd	Sr
Method		ICP-ES	INAA	ICP-ES	ICP-MS	LECO	ICP-ES	INAA	ICP-ES	ICP-ES	ICP-MS	ICP-ES
Detection Limit		0.001 wt.%	0.02 wt.%	0.0005 wt.%	0.0002 wt.%	0.01 wt.%	0.01 wt.%	0.005 wt.%	0.01 wt.%	0.01 wt.%	0.2 ppm	10 ppm
		wt%	wt%	wt%	wt%	wt%	wt%	wt%	wt.%	wt.%	ppm	ppm
ALV3622-01A	Sasquatch	1.74	12.20	15.70	0.11	18.20	31.20	5.40	0.34	0.21	479	1990
ALV3622-01F	Sasquatch	1.72	23.60	23.60	0.03	40.10	3.10	0.04	0.50	0.01	902	27
ALV3622-1	Sasquatch	1.90	19.10	31.80	0.02	38.90	4.00	0.00	0.14	0.01	1032	11
ALV3622	Sasquatch	1.76	17.80	34.10	0.03	39.50	1.50	0.00	0.05	0.01	1168	
ALV3000C	Salty Dawg	0.44	35.30	14.30	0.11	39.00	4.00	1.70	0.04	0.08	591	365
ALV3000-GrendleA	Salty Dawg	0.07	33.10	9.44	0.06	41.70	7.30	0.18	0.07	0.04	264	98
ALV3000-SpireB	Salty Dawg	0.16	28.60	18.00	0.08	36.50	6.50	2.20	0.06	0.11	465	443
ALV2460-R2-14a	High Rise	0.71	11.05	0.86	0.01	13.60	61.90	2.60	0.13	0.06	25	440
ALV2460-R2-14b	High Rise	0.83	16.16	15.60	0.22	24.80	33.70	0.58	0.02	0.04	398	65
ALV2460-R2-15	High Rise	1.20	19.93	14.00	0.03	28.70	22.30	0.86	0.08	0.07	457	250
ALV2460-R3-3	High Rise	2.60	33.50	11.70	0.09	32.70	8.71	1.20	0.05	0.10	356	400
ALV2460-R3-3c	High Rise	2.50	31.82	11.10	0.08	31.90	9.50	0.98	0.02	0.17	316	350
ALV2460-R3-5	High Rise	1.10	22.73	8.30	0.02	32.10	9.70	0.75	0.23	6.45	265	730
ALV2462-R6-1d2	High Rise	10.10	27.98	0.47	0.12	32.30	2.09	0.07	0.22	0.09	165	28
ALV2462-R7-1b	High Rise	2.00	30.78	7.90	0.06	33.30	2.51	0.60	0.16	4.26	232	420
ALV2460-R4-1c	High Rise	0.89	34.27	12.40	0.00	45.40	0.96	0.02	0.02	0.05	453	10
ALV2460-R5	High Rise	0.56	2.60	0.50	0.00	22.50	1.60	0.04	0.96	26.27	25	2100
ALV2461-R4d	High Rise	3.30	43.09	0.10	0.00	49.40	0.25	0.01	0.02	0.05	25	10
ALV2461-R1b2	High Rise	1.00	27.35	13.40	0.15	37.30	12.10	0.73	0.02	0.07	347	290
ALV2461-R3c1	High Rise	1.00	31.96	16.90	0.01	43.50	1.18	0.01	0.02	0.04	450	160
ALV2464-R6-2c	High Rise	1.00	21.89	28.40	0.08	32.90	6.36	0.62	0.02	0.19	1063	250
ALV2461-R12-2	High Rise	0.63	31.61	10.90	0.22	34.60	2.30	0.28	0.02	1.78	208	200
ALV2461-R13 TIP	High Rise	0.26	23.22	6.30	0.35	27.80	13.40	4.60	0.02	0.21	84	1000
ALV2461-R13-4-BOT	High Rise	1.10	20.84	20.90	0.65	31.50	15.60	0.97	0.02	0.06	580	350
ALV2461-R13/1	High Rise	0.82	28.68	13.60	0.26	35.80	12.20	0.28	0.02	0.06	274	120
ALV2461-R13/2	High Rise	0.59	31.12	9.20	0.16	38.80	14.00	0.32	0.02	0.04	151	110
ALV2461-R13/3	High Rise	0.58	24.83	11.30	0.53	32.40	21.50	1.10	0.02	0.07	192	280
ALV2461-R13/4	High Rise	0.08	21.82	4.30	1.61	25.20	28.10	5.60	0.02	0.20	25	950
ALV2461-R11-9	High Rise	0.85	22.94	18.20	0.10	30.80	10.00	1.20	0.02	1.19	642	380
ALV2462-R1a	High Rise	1.10	33.08	12.40	0.06	33.50	0.95	0.76	0.10	0.44	403	240
ALV2462-R1b	High Rise	0.08	0.43	0.31	0.00	22.90	1.08	0.04	0.72	26.49	25	2500
ALV2462-R1c	High Rise	1.30	34.41	10.40	0.06	39.10	5.13	0.62	0.09	0.13	300	210
ALV2463-R1-2	High Rise	0.80	36.16	6.00	0.13	40.80	1.81	0.01	0.11	0.10	88	10
ALV2463-R2-1a	High Rise	5.10	30.98	0.16	0.00	24.50	32.90	0.01	0.07	0.09	25	10
ALV2463-R3-3	High Rise	0.26	2.38	0.90	0.41	9.85	37.85	22.00	0.46	0.20	25	3650

Sample	Field	Cu	Fe	Zn	Pb	S	SiO2	Ba	MgO	CaO	Cd	Sr
ALV2463-R4-pc	High Rise	0.01	0.46	0.04	0.02	10.50	22.00	26.00	0.05	0.22	25	5700
ALV2463-R5c3	High Rise	0.46	18.67	4.00	0.01	23.20	49.20	1.80	0.05	0.09	125	290
ALV2463-R6-misc	High Rise	5.40	33.36	0.78	0.01	43.60	1.12	0.00	0.06	0.04	25	10
ALV2461-R10b2	High Rise	4.40	42.25	0.34	0.01	47.70	0.25	0.02	0.05	0.06	25	10
ALV2461-R6-4	High Rise	1.20	26.65	19.10	0.14	36.00	2.71	1.50	0.02	0.22	483	370
ALV2461-R7c2	High Rise	0.31	26.37	10.40	0.37	35.20	17.60	1.70	0.02	0.10	133	440
ALV2461-R8-3	High Rise	0.01	0.15	0.01	0.00	20.00	2.24	0.03	4.11	22.92	25	2200
ALV2464-R8-1b	High Rise	0.51	34.76	10.20	0.23	39.50	5.38	1.10	0.07	0.13	186	370
ALV2464-R5-3	High Rise	0.48	13.78	28.90	0.13	31.00	9.37	1.70	0.02	0.08	759	380
ALV1417-1b b2	High Rise	4.40	42.66	0.26	0.01	51.00	0.84	0.03	0.20	0.11		11
ALV1417-2a b5	High Rise	9.70	27.13	6.70	0.01	37.00	16.10	2.10	0.19	0.12		540
ALV1417-1c b22	High Rise	3.90	43.08	0.16	0.00	48.80	6.01	0.47	0.15	0.07		91
ALV1417-1d b7	High Rise	0.04	44.20	0.02	0.00	50.90	4.84	0.00	0.16	0.04		11
ALV1417-c b9	High Rise	0.04	46.15	0.10	0.01	53.20	0.63	0.01	0.14	0.07		
ALV1417-1e	High Rise	1.60	44.62	0.34	0.00	52.70	0.48	0.00	0.16	0.06		
ALV1417-2b	High Rise	0.71	41.19	0.08	0.01	46.60	10.10	0.02	0.16	0.06		14
ALV1417-5b b12	High Rise	0.12	16.50	2.00	7.10	27.00	23.40	0.00	0.17	0.30		
ALV1417-5c b13	High Rise	0.12	16.50	19.80	6.60	26.90	23.90	0.00	0.17	0.29		24
ALV1417-5a b11	High Rise	0.12	16.57	20.30	7.00	27.10	23.60	0.00	0.16	0.29		
ALV1417-5d b14	High Rise	0.12	16.71	20.40	6.30	27.50	23.60	0.01	0.17	0.27		24
ALV2451-1	High Rise	1.21	29.90	19.10	0.05	39.60	0.60	0.03	0.27	1.46	596	92
ALV3003	High Rise	1.58	34.90	9.38	0.05	33.70	13.80	0.87	0.05	0.42	270	204
ALV2461-R-3	High Rise	1.53		13.00	0.35	35.20	13.10		0.09	0.07	314	334
ALV2461-R-3-2	High Rise	3.20		13.90	0.01	42.80	1.50		0.02	0.01	458	5
ALV2929	High Rise	2.36	1.33	0.29				0.03	0.02	29.00		2300
ALV2463-R2-3	High Rise	2.36		0.27	0.01	50.90	0.80		0.07	0.02	8	5
ALV2463-R5c2	High Rise	0.14		4.40	0.02	33.00	18.60		0.02	0.04	254	715
ALV2927-A	High Rise	0.29	33.90	10.50	0.23	41.30	6.10	2.70	0.02	0.10	150	1190
ALV2927-B	High Rise	20.70	36.50	0.03	0.00	40.50	0.25		0.02	0.07	1.7	5
ALV2936-A	High Rise	0.60	35.70	13.60	0.15	42.60	5.00	0.26	0.02	0.05	346	146
ALV2936-B	High Rise	0.02	48.70	0.39	0.07	50.00	0.25	1.15	0.08	0.08	2	591
ALV2460 B	High Rise	0.35			0.10		21.30	0.44			184	10
ALV2460 E	High Rise	1.17	14.40	30.00	0.09		25.30	0.08			888	10
ALV2464 B	High Rise	0.79	11.00	53.20	0.01		4.50	0.00			1550	10
ALV2464 F-V	High Rise	5.40	47.30	3.91	0.01		4.10	0.01			121	10
ALV2462 A1	High Rise	5.50	28.10	1.22	0.34		25.50	4.07			22	1480
ALV2463 A	High Rise	10.00	42.10	0.86	0.01		0.40	0.01			37	10
ALV2463 F	High Rise	10.00	37.60	0.58	0.01		1.90	0.00			23	10
ALV2461 A	High Rise	0.28	9.22	2.68	0.13		52.70	8.87			85	2800
ALV2461 E	High Rise	0.24	17.50	1.34	0.54		52.90	0.63			11	215
ALV2467-R1exc	Clam Bed	2.20	10.07	0.77	0.00	26.10	0.26	0.04	0.70	20.85	25	1900
ALV2467-R1-1b3	Clam Bed	0.70	37.14	6.50	0.03	31.00	0.25	0.05	0.05	0.65	235	65

Sample	Field	Cu	Fe	Zn	Pb	S	SiO2	Ba	MgO	CaO	Cd	Sr
ALV2467-R1-14d	Clam bed	3.70	36.02	9.40	0.04	33.90	0.25	0.07	0.05	2.46	250	230
ALV2467-R4-misc	Clam Bed	0.19	39.31	0.44	0.02	46.00	0.26	0.01	0.06	0.04	0.25	10
ALV2467-R3	Clam Bed	0.02	9.55	1.60	0.36	16.60	21.95	26.50	0.05	0.15	25	2000
HYS-350-02(?)	Clam Bed	0.21	7.63	2.11	0.54			25.00	0.27	0.27	18.2	990
ALV2463-R7-6B	Clam Bed	0.84	19.00	8.03	3.02		12.70	0.22		0.01	138	
ALV2463-R7-6C	Clam Bed	0.27	5.50	2.49	1.39		45.90	10.70		0.45	33	3610
ALV2463-R7-6G	Clam Bed	0.10	2.61	1.05	0.35		28.60	30.50		0.01	10	8900
ALV2467-R1	Clam Bed	2.64	17.63	3.61	0.04	26.90	3.40		0.45	16.60	142	2190
ALV2465-R1-6c	Main Endeavour	1.60	30.36	8.30	0.24	33.40	19.00	0.76	0.01	0.12	219	210
ALV2466-b	Main Endeavour	0.54	30.36	14.80	0.15	38.70	1.13	0.17	0.10	2.46	508	220
ALV2466-c	Main Endeavour	0.43	32.17	10.00	0.13	41.10	10.30	0.20	0.05	0.06	298	80
ALV2466-R1-4b	Main Endeavour	0.42	45.18	0.47	0.05	46.90	0.25	0.01	0.07	0.09	25	28
ALV2466-R3	Main Endeavour	0.56	35.18	9.60	0.06	45.40	1.12	0.33	0.01	0.04	420	81
ALV2466-R3-1b1	Main Endeavour	0.39	24.90	9.20	0.06	31.80	27.40	0.45	0.01	0.07	409	120
ALV2466-R3-1b2	Main Endeavour	0.15	30.32	8.00	0.00	37.05	16.65	0.37	0.02	0.06	25	115
ALV2466-R4	Main Endeavour	0.70	25.95	4.70	0.03	35.00	0.70	0.02	0.26	9.71	234	650
ALV2466-R5-8/1	Main Endeavour	2.50	34.20	9.80	0.12	34.60	3.63	0.43	0.01	0.12	382	190
ALV2466-R5-8/2	Main Endeavour	0.67	35.04	9.60	0.06	39.00	0.25	0.02	0.01	1.78	376	120
ALV2466-R5-8/3	Main Endeavour	0.44	36.72	9.70	0.06	38.70	0.25	0.02	0.01	0.06	318	10
ALV2466-R5-8/4	Main Endeavour	0.30	27.49	12.70	0.25	32.40	15.90	0.61	0.01	0.09	331	190
ALV2465-R3-2a	Main Endeavour	2.80	8.11	0.11	0.00	25.10	1.50	0.03	1.04	21.35	25	2000
ALV2465-R2-1e	Main Endeavour	11.70	24.69	0.27	0.00	31.30	0.25	0.01	0.23	5.50	25	460
ALV2465-R2-2a2	Main Endeavour	2.20	15.88	0.94	0.01	26.80	0.85	0.04	0.62	18.56	54	1600
ALV2465-R2-2d2	Main Endeavour	0.21	4.54	0.09	0.00	24.60	0.25	0.09	0.12	25.49	25	2000
ALV2465-R2-3b	Main Endeavour	7.10	20.07	0.85	0.01	31.60	0.77	0.06	0.40	11.85	25	1100
ALV2465-R2b	Main Endeavour	0.85	32.80	9.20	0.07	31.60	1.27	0.04	0.16	1.48	358	100
ALV2449-1	Main Endeavour	0.21	37.42	4.50	0.05	36.80	5.82	1.60	0.01	0.09	104	290
ALV2450-2	Main Endeavour	1.60	45.32	5.40	0.02	38.50	0.25	0.24	0.01	0.05	90	65
ALV2452-1	Main Endeavour	2.20	37.42	2.50	0.02	31.30	1.14	0.02	0.49	1.15	86	97
HYS-278-01	Main Endeavour	0.29	33.20	8.61	3.93	30.77	17.24	0.98	0.03	0.04	57.9	227
HYS-278-02a	Main Endeavour	0.59	17.00	26.00	0.92	35.92	18.22	1.20	0.10	0.06	438.2	350
HYS-278-02b	Main Endeavour	0.42	23.64	19.00	2.79	34.43	9.29	0.85	0.03	0.04	192.2	406
HYS-278-09a	Main Endeavour	4.88	47.29	0.05	0.00	51.64	0.86	0.00	0.03	0.01	0.25	6
HYS-278-09b	Main Endeavour	2.96	49.92	0.31	0.02	52.95	1.44	0.00	0.03	0.01	8.9	3
HYS-278-10	Main Endeavour	15.07	42.49	0.05	0.01	46.07	0.31	0.06	0.02	0.01	0.7	16
HYS-278-14a	Main Endeavour	6.51	47.15	0.02	0.01	50.89	0.33	0.00	0.03	0.01	0.25	2
HYS-278-14b	Main Endeavour	3.92	48.43	0.15	0.01	53.26	0.42	0.00	0.02	0.01	6.4	2
HYS-278-16	Main Endeavour	0.94	34.03	0.61	0.01	38.23	16.88	2.80	0.07	0.04	23.5	238
HYS-347-01	Main Endeavour	0.01	50.70	0.97	0.04			1.80	0.05	0.08	0.25	167
HYS-347-02	Main Endeavour	1.50	43.40	7.18	0.02			0.01	0.03	1.07	155.6	105
HYS-350-01	Main Endeavour	0.65	50.20	4.29	0.03			0.24	0.07	1.13	99	162
HYS-350-02	Main Endeavour	0.84	36.90	6.41	0.02			0.02	0.07	1.63	190.3	161

Sample	Main Endeavour	Cu	Fe	Zn	Pb	S	SiO2	Ba	MgO	CaO	Cd	Sr
HYS-355-01	Main Endeavour	13.70	12.10	33.00	0.01			0.05	0.02	0.11	1420.4	6
HYS-355-02	Main Endeavour	5.72	6.42	33.00	0.01			0.00	0.02	0.03	1545.9	2
HYS-355-B	Main Endeavour	0.28	24.30	5.76	1.94			4.80	1.77	5.83	44	761
HYS-363-01A	Main Endeavour	2.72	6.62	48.00	0.00			0.02	0.02	1.47	1677.1	141
HYS-363-01B	Main Endeavour	1.34	20.30	9.79	0.33			11.00	0.05	0.40	199	226
HYS-363-01C	Main Endeavour	3.55	13.50	36.00	0.63			0.01	0.03	0.33	1038.7	33
ALV2453-3	Main Endeavour	4.00	41.83	4.20	0.02	35.60	0.26	0.01	0.02	0.06	123	10
G2 mucus	Main Endeavour		0.33	0.02				0.00		1.00		50
ALV2066-3	Main Endeavour	7.38	20.60	4.48	0.01	26.80	0.90	0.02	0.62	17.20	284	1140
ALV2066-4A	Main Endeavour	0.57	31.40	10.20	0.13	36.00	10.30	0.52	0.10	0.28	312	251
ALV2066-4B	Main Endeavour	0.60	32.30	13.90	0.07	33.70	7.20	0.00	0.09	0.23	478	15
ALV2066-5	Main Endeavour	0.29	3.16	4.60	0.02	24.00	0.25	0.00	0.02	34.10	265	856
ALV2066-6	Main Endeavour	0.54	34.40	17.00	0.17	39.80	0.70	0.00	0.10	0.16	475	22
ALV2406-1A	Main Endeavour	2.72	35.70	11.80	0.07	36.30	3.90	0.12	0.02	0.18	335	107
ALV2406-1B	Main Endeavour	15.20	31.00	0.50	0.00	32.00	1.10	0.00	0.42	8.71	26	375
ALV2408-1A	Main Endeavour	0.06	40.40	0.87	0.10	47.70	2.30	1.65	0.05	0.11	16	813
ALV2408-1B	Main Endeavour	0.76	22.30	28.00	0.07	32.50	2.60	0.00	0.06	1.62	773	125
ALV2413-2	Main Endeavour	1.03	36.70	12.10	0.03	45.10	0.25	0.00	0.05	0.09	263	5
ALV2061-2A	Main Endeavour	0.70	36.30	0.28	0.01	31.50	0.25	0.02	0.14	5.83	7.1	399
ALV2061-2B	Main Endeavour	0.47	39.10	7.10	0.03	38.90	0.25	0.03	0.12	1.04	255	74
ALV2465-R2A	Main Endeavour	21.00		0.29	0.00	30.60	0.70	0.00	0.45	8.93	16	700
ALV2073-1	Main Endeavour	1.08	10.20	1.00	0.02	25.20	0.25	0.11	0.07	25.80	39	1970
ALV2448-1	Main Endeavour	2.97	35.90	2.46	0.02	31.20	1.20	0.00	0.62	4.94	76	332
ALV2072-1B	Main Endeavour	0.11	36.70	0.44	0.02	43.40	0.25	7.50	0.10	0.19	12	6440
ALV2072-7	Main Endeavour	0.72	23.10	11.70	0.10	30.50	12.60	5.00	0.02	0.15	377	3170
ALV2409-1B	Main Endeavour	1.41	43.80	6.22	0.04	35.00	2.90	0.08	0.02	0.04	188	19
ALV2998-A	Main Endeavour	19.30	18.20	21.70	0.00	35.40	1.80	0.00	0.02	0.04	840	5
ALV2998-B	Main Endeavour	3.98	6.05	48.10	0.17	33.40	1.70	0.55	0.02	0.39	1077	133
ALV-Grotto-Sep95	Main Endeavour	0.23	46.90	0.15	0.03	51.90	0.25	0.00	0.09	0.01	4.1	5
ALV2063-1B	Main Endeavour	0.31	31.90	14.20	0.07	38.80	0.25	0.09	0.05	0.41	172	85
ALV2068-1	Main Endeavour	0.14	11.60	0.38	0.21	19.70	22.60	23.00	0.18	0.34	7.7	12800
ALV2411-1A	Main Endeavour	1.19	5.97	0.54	0.00	22.80	0.25	0.04	2.01	30.70	16	2950
ALV2411-2	Main Endeavour	1.04	43.50	5.09	0.02	32.60	0.25	0.00	0.02	0.11	119	5
ALV2997AH	Main Endeavour	4.07	10.70	0.26	0.00	25.90	0.80	0.04	1.54	27.00	6	2090
ALV3588-A	Main Endeavour	23.70	17.60	4.22	0.00	28.40	2.90	0.20	1.42	10.30	179	804
ALV3588-B (R1)	Main Endeavour	2.76	4.33	0.24	0.00	23.70	0.25	0.03	2.63	32.40	8.6	2780
ALV3588-R2A	Main Endeavour	4.30	31.20	12.50	0.04	35.90	0.70	0.58	0.06	6.28	384	957
ALV3588-R2B	Main Endeavour	0.91	35.50	7.57	0.11	41.80	10.20	0.93	0.06	0.03	237	337
ALV3609-01A	Main Endeavour	7.62	16.10	0.18	0.00	28.90	0.25	0.00	0.17	23.20	4.2	1490
ALV2452-2	Main Endeavour	3.83	6.79	44.20	0.14	31.60	3.80	1.65	0.05	0.03	885	373
HYS-278-11	Main Endeavour	4.50	39.50	0.01	0.01	46.40	0.25	0.00	0.02	0.01	0.7	5
ALV3572-R1	Main Endeavour	0.86	35.10	21.10	0.24	36.30	0.90	0.15	0.08	0.03	425	27

Sample	Main Endeavour	Cu	Fe	Zn	Pb	S	SiO2	Ba	MgO	CaO	Cd	Sr
ALV3005A	Main Endeavour	0.80	29.00	4.10	0.03	37.80	0.25	0.32	0.09	11.70	75	921
ALV3005B	Main Endeavour	4.39	46.20	2.85	0.02	42.00	0.25	0.04	0.07	0.02	66	23
ALV3569-R1-A	Main Endeavour	20.80	22.50	0.09	0.01	29.90	0.25	0.03	1.79	11.20	2	688
ALV3569-R1-B	Main Endeavour	7.21	36.20	9.18	0.06	44.10	0.25	0.56	0.11	0.21	255	156
ALV3570-R2	Main Endeavour	3.99	37.00	9.49	0.03	38.30	0.25	0.48	0.15	2.99	344	321
ALV3570-R2D	Main Endeavour	11.40	15.80	3.41	0.01	28.20	0.25	0.12	0.32	20.00	140	1620
ALV3623-02	Main Endeavour	3.18	40.10	5.39	0.03	48.50	0.25	0.02	0.11	0.01	131	5
ALV2453-2 (puffer)	Main Endeavour	9.14	42.10	0.94	0.01	46.00	0.25	0.00	0.02	0.51	20	32
ALV3586-R-1A	Main Endeavour	8.41	45.30	2.19	0.02	39.90	0.25	0.00	0.28	0.23	63	22
ALV3586-R-1B	Main Endeavour	9.11	45.50	0.28	0.03	37.70	3.50	0.02	1.72	0.32	5.3	29
J2-59-2	Main Endeavour	29.00	26.30	0.13	0.00	33.50	0.60	0.11	0.12	3.76	3.6	336
J2-59-4 Misc	Main Endeavour	0.50	39.00	8.26	0.05	46.40	0.25	0.99	0.02	0.05	233	561
J2-59-4D	Main Endeavour	1.93	32.40	19.20	0.05	35.90	0.60	0.00	0.02	0.04	705	5
ALV3581-R-1	Main Endeavour	0.39	3.03	12.60	0.09	19.70	0.25	33.00	0.02	0.67	138	9250
ALV3581-R-2	Main Endeavour	4.57	15.40	3.60	0.01	27.80	0.25	0.07	1.30	22.60	116	1860
ALV2412-1	Main Endeavour	0.82	34.60	10.90	0.07	43.30	0.25	0.22	0.06	0.03	224	102
ALV2998-Salut (1of2)	Main Endeavour	5.63	36.20	2.43	0.04	36.80	2.70	0.15	0.47	6.09	25	557
ALV2998-Salut (2of2)	Main Endeavour	8.90	33.40	2.10	0.02	36.80	1.20	0.22	0.38	6.44	44	630
ALV3616-03	Main Endeavour	0.55	15.90	40.40	0.05	35.20	0.25	0.13	0.06	0.02	1360	56
ALV3587-R-1	Main Endeavour	1.95	0.31	53.70	0.15	30.50	0.25	6.10	0.02	0.07	1723	1150
ALV3587-R-2	Main Endeavour	1.94	1.65	12.70	0.01	23.80	1.10	0.03	0.82	29.10	715	2580
ALV3616-A	Main Endeavour	1.38	0.94	58.50	0.22	31.70	0.25	0.79	0.08	0.05	1644	256
ALV3616-B	Main Endeavour	13.90	2.58	41.80	0.20	29.50	0.25	4.10	0.02	0.09	1477	975
ALV2419-1	Main Endeavour	11.70	36.90	0.11	0.01	43.30	0.25	0.02	0.08	0.04	2.8	5
ALV2419-2	Main Endeavour	4.00	31.50	0.57	0.01	33.40	0.90	0.02	0.36	10.80	13	795
ALV2404-1	Main Endeavour	1.12	35.60	10.80	0.03	32.50	0.25	0.00	0.07	1.00	319	83
ALV2404-3A	Main Endeavour	2.04	34.60	19.20	0.05	36.30	0.25	0.00	0.02	0.02	521	5
ALV2404-3B	Main Endeavour	0.02	44.30	0.62	0.11	49.90	0.25	0.28	0.12	0.07	4.9	130
ALV2404-4	Main Endeavour	1.73	9.99	29.00	0.13	27.30	21.70	0.89	0.07	0.03	840	357
ALV2414-1	Main Endeavour	3.15	39.00	2.34	0.03	36.00	0.25	0.08	0.20	5.91	73	462
ALV2415-1D(1)	Main Endeavour	1.11	22.90	25.20	0.12	38.30	3.00	0.87	0.06	0.08	862	443
ALV2415-1D(2)	Main Endeavour	3.41	26.00	22.90	0.07	37.70	1.70	0.00	0.02	0.10	825	5
ALV2415-1D(3)	Main Endeavour	0.10	35.50	6.69	0.24	44.60	4.10	2.70	0.02	0.10	80	1300
ALV2418-1	Main Endeavour	7.63	38.80	0.14	0.01	47.20	0.25	0.01	0.07	0.01	3.6	5
ALV2420-1B	Main Endeavour	1.14	30.20	22.40	0.02	34.20	1.00	0.06	0.02	1.18	856	105
ALV2420A	Main Endeavour	0.61	24.20	23.30	0.14	38.30	0.60	0.37	0.02	0.27	637	241
ALV2420B	Main Endeavour	0.67	10.80	3.45	0.00	26.00	0.25	0.02	0.23	27.70	150	1820
ALV2453-1A	Main Endeavour	1.73	43.60	0.33	0.03	46.50	6.80	0.04	0.11	0.07	6.9	15
ALV2453-1B	Main Endeavour	0.95	49.00	2.18	0.02	38.40	0.25	0.02	0.08	1.11	64	81
ALV2996MEF	Main Endeavour	1.68	53.30	2.41	0.01	40.10	0.25	0.00	0.08	0.01	57	5
ALV3589-R2	Main Endeavour	0.19	23.00	3.25	0.09	27.10	25.80	11.00	0.02	0.17	112	5570
ALV3612-01	Main Endeavour	1.53	14.50	0.72	0.01	27.10	1.30	0.02	2.30	26.00	30	2040

Sample	Main Endeavour	Cu	Fe	Zn	Pb	S	SiO2	Ba	MgO	CaO	Cd	Sr
ALV3619-01	Main Endeavour	1.87	34.90	16.60	0.02	34.60	0.25	0.00	0.02	0.64	558	46
ALV1439	Main Endeavour	1.31	36.10	19.90	0.05	39.20	0.25	0.30	0.05	0.33	625	193
ALV1445-7	Main Endeavour	21.20	40.50	4.08	0.05	46.90	2.00	0.25	0.05	0.03	151	139
ALV1451-1	Main Endeavour	0.98	38.80	6.95	0.08	42.50	0.90	0.29	0.07	0.33	239	205
ALV1452-1A	Main Endeavour	0.23	17.40	4.61	0.25	24.60	28.90	12.00	0.08	0.25	43	8230
ALV1452-2	Main Endeavour	0.28	23.00	9.59	0.13	31.40	9.60	8.50	0.13	0.16	565	3880
ALV2057	Main Endeavour	5.62	40.80	0.54	0.02	45.30	0.25	0.34	0.14	0.03	13	155
R507-9	Main Endeavour	0.02	0.20	0.60	0.00	21.80	2.70	0.05	1.73	37.80	54	2490
TIVEY MISC-1	Main Endeavour	28.20	29.50	0.02	0.00	31.70	0.70	0.88	0.09	0.09	0.8	971
TIVEY MISC-2	Main Endeavour	0.34	15.80	0.20	0.08	25.20	0.25	33.00	0.06	0.15	4.5	7160
TIVEY MISC-3	Main Endeavour	0.48	40.90	2.28	0.03	46.80	5.90	0.01	0.02	0.03	91	5
TIVEY MISC-4	Main Endeavour	0.45	28.80	14.00	0.26	38.70	10.00	0.58	0.05	0.07	727	496
TIVEY MISC-5	Main Endeavour	18.70	30.20	0.12	0.01	32.80	1.60	0.17	0.02	7.22	4.1	657
TIVEY MISC-6	Main Endeavour	4.71	41.30	2.94	0.02	45.00	6.20	0.10	0.02	0.01	137	35
TIVEY MISC-7	Main Endeavour	0.64	34.80	6.91	0.10	41.50	7.80	1.10	0.02	0.02	203	444
TT 170-66D B112A	Main Endeavour	0.90	39.60	7.52	0.05	44.40	1.30	0.03	0.05	0.01	342	5
TT 170-66D B30-A	Main Endeavour	0.22	33.70	11.60	0.11	41.10	4.90	0.06	0.02	0.01	294	27
TT 170-66D B9-B	Main Endeavour	0.33	34.60	13.10	0.06	37.30	7.20	0.00	0.09	0.03	391	13
TT 170-66D B19-B2	Main Endeavour	0.70	38.40	0.40	0.01	38.50	2.90	0.02	0.02	0.01	14	15
TT 170-66D B1-B2	Main Endeavour	2.71	35.70	2.00	0.01	31.80	1.50	0.00	0.02	0.01	83	5
TT 170-66D R2	Main Endeavour	0.61	29.20	12.20	0.08	28.70	0.60	0.00	0.02	0.01	453	5
TT 170-66D 1B	Main Endeavour	0.53	32.10	6.88	0.11	35.00	10.90	0.38	0.05	0.07	259	140
TT 170-66D EXIT CH 1	Main Endeavour	0.69	26.60	14.40	0.10	27.80	18.50	0.03	0.06	0.02	446	5
TT 170-66D AIS Inner 1	Main Endeavour	0.66	40.80	0.20	0.02	44.00	7.30	0.05	0.02	0.02	5.6	19
TT 170-66D AIS 9T 1	Main Endeavour	0.48	31.30	11.50	0.10	36.10	13.80	0.03	0.02	0.01	332	11
TT 170-66D AIS Slab 1	Main Endeavour	0.65	26.90	9.45	0.07	31.10	19.80	0.05	0.02	0.01	301	18
TT 170-66D EXIT CH 2	Main Endeavour	0.75	27.30	14.60	0.10	27.30	18.30	0.00	0.02	0.13	440	5
TT 170-66D AIS Inner 2	Main Endeavour	0.59	36.20	0.16	0.01	42.30	5.90	0.04	0.02	0.01	5.1	16
TT 170-66D AIS 9T 2	Main Endeavour	0.48	30.40	11.50	0.10	36.30	13.50	0.00	0.02	0.01	321	10
TT 170-66D AIS Slab 2	Main Endeavour	0.66	26.50	9.34	0.07	31.30	19.80	0.05	0.02	0.01	296	16
Pisces 1B	Main Endeavour	0.02	32.50	0.11	0.00	0.59	36.90	0.00	1.41	0.43	4.1	149
HYS 270-1	Main Endeavour	1.86	44.60	0.26	0.01	51.00	0.80	0.00	0.02	0.04	5.8	5
HYS 278-4	Main Endeavour	1.01	32.40	1.07	0.04	31.70	26.90	1.30	0.07	0.04	43	438
HYS 278-14	Main Endeavour	3.00	43.10	0.30	0.03	48.70	0.25	0.00	0.06	0.02	11	5
HYS 280-16	Main Endeavour	6.04	26.30	1.44	0.02	29.80	23.30	1.10	0.02	0.01	67	537
HYS 278-9	Main Endeavour	0.96	45.00	0.37	0.04	47.00	1.40	0.00	0.05	0.01	15	5
HYS 278-3	Main Endeavour	0.11	24.60	3.26	0.32	28.60	33.10	0.01	0.02	0.26	33	21
ALV2466 A	Main Endeavour	0.17	30.40	9.84	2.49		32.40	0.89		0.06	36	311
ALV2466 E	Main Endeavour	0.27	29.60	12.20	0.27		25.20	1.13		0.04	155	282
ALV1445-3A	Main Endeavour	31.60		0.07	0.01		1.40			1.52		
ALV1445-3B	Main Endeavour	1.11		0.36	0.03		3.80			8.36		
ALV1445-3C	Main Endeavour	1.64		0.53	0.05		6.80			6.80		

Sample	Main Endeavour	Cu	Fe	Zn	Pb	S	SiO2	Ba	MgO	CaO	Cd	Sr
ALV1445-3D	Main Endeavour	1.02		0.24	0.05		3.35			3.35		
Endv-1. vent	Main Endeavour	30.20		0.40	0.00			0.01				
ALV1419-1b b3	Main Endeavour	0.73	42.73	0.08	0.00	49.10	10.40	0.02	0.15	0.03		11
ALV1419-2 b10	Main Endeavour	0.03	46.15	0.08	0.01	53.20	0.64	0.01	0.14	0.01		
ALV1418-8b b6	Main Endeavour	1.50	44.41	0.58	0.02	52.30	2.49	0.01	0.17	0.06		1
ALV1418-1d b2	Main Endeavour	1.50	45.24	0.34	0.00	53.10	0.25	0.01	0.16	0.06		
ALV1418-1d b5	Main Endeavour	0.51	38.46	0.03	0.00	44.50	15.30	1.40	0.14	0.04		210
ALV1418-3a	Main Endeavour	0.49	38.95	0.03	0.00	45.50	14.70	1.40	0.14	0.04		210
ALV1419-1a b2	Main Endeavour	0.33	36.64	5.80	0.13	43.60	7.36	1.30	0.20	0.13		470
ALV1418-6b b9	Main Endeavour	0.69	24.83	25.10	0.28	35.90	6.16	1.30	0.18	0.12		370
ALV1417-1b b8	Main Endeavour	0.73	25.24	25.20	0.23	38.10	6.10	1.20	0.19	0.16		410
ALV1417-1c b2	Main Endeavour	1.60	23.57	2.40	0.03	29.30	27.70	8.90	0.19	0.10		2200
ALV1417-1a b2	Main Endeavour	0.17	19.79	1.50	0.09	25.50	25.00	8.80	0.15	0.14		2000
ALV1419-1d b31	Main Endeavour	0.10	6.19	2.10	0.11	13.80	39.10	22.00	0.12	0.23		4300
ALV1419-1h b4	Main Endeavour	0.03	2.41	0.62	0.13	11.60	32.90	32.00	0.09	0.31		6900
ALV1418-1e b2	Main Endeavour	0.03	1.57	0.65	0.16	10.80	26.70	37.00	0.03	0.31		6900
ALV1419-1c b2	Main Endeavour	0.03	1.55	0.62	0.13	11.10	27.30	37.00	0.03	0.32		6900
ALV1419-1d b3	Main Endeavour	0.05	0.99	0.72	0.07	11.10	25.80	39.00	0.10	0.29		7400
ALV3570-MISC(A)	Main Endeavour	5.77	26.86	6.18	0.03	36.20	0.25		0.17	10.80	196	872
ALV3570-MISC(B)	Main Endeavour	10.60	37.84	1.45	0.02	42.60	0.25		0.26	2.16	51	147
ALV2450-3b (crust)	Main Endeavour	0.09	35.32	0.57	0.08	41.70	0.25			0.06	3.8	370
ALV1447-1	Main Endeavour	0.00	20.56	0.16	0.00	30.50	1.30		1.65	10.30	7.7	881
ALV2116-R3-H1	Main Endeavour	0.06	0.54	0.04	0.03	11.00	24.50			0.27	1.3	13300
ALV2116-R4a-4	Main Endeavour	0.06	7.83	2.12	0.88	19.30	13.70		0.90	4.41	9.2	11100
ALV2116-4b-1	Main Endeavour	0.03	1.31	0.07	0.03	20.90	0.25			27.10	1.9	7390
ALV2460-R5P1C	Main Endeavour	1.17	5.68	1.04	0.01	23.20	1.80		0.86	31.90	46	2440
ALV2460-R5P2C	Main Endeavour	0.32	1.38	0.18	0.01	22.70	1.20		0.53	38.70	7.4	2700
ALV2460-R5P3B-D	Main Endeavour	0.95	2.78	0.31	0.00	23.20	1.40		1.62	35.70	15	2790
ALV2461-R4-2	Main Endeavour	1.48	38.12	8.77	0.02	47.10	0.70		0.19	0.03	237	5
ALV2461-R10-2	Main Endeavour	5.14	40.71	0.18	0.02	47.40	0.60		0.15	0.08	8.2	17
ALV2463-R2P2B	Main Endeavour	5.07	40.85	0.25	0.01	48.10	0.25		0.02		4.5	5
ALV2464-R4	Main Endeavour	0.12	1.59	0.30	0.05	1.63	50.90		25.40	0.11	0.3	1290
ALV2464-R6-pc	Main Endeavour	1.10	24.83	16.60	0.18	30.60	10.90		0.06	0.09	423	683
ALV2464-R6P1C	Main Endeavour	1.19	29.24	17.90	0.22	34.90	4.20		0.02	0.10	408	1200
ALV2465-R1P1A	Main Endeavour	9.32	23.92	2.45	0.00				1.60	14.80	189	1270
ALV2466-R1	Main Endeavour	0.78	43.29	0.61	0.04	50.20	0.25		0.11	0.02	26	5
ALV2466-R1P3B2	Main Endeavour	0.10	43.64	0.38	0.04	48.80	0.25			0.01	15	5
HYS-356-01A	Mothra	19.50	33.80	4.88				0.05	0.33	2.73	379	226
HYS-356-01B	Mothra	25.00	36.10	0.16				0.00	0.45	1.06	11.2	74
HYS-356-02A	Mothra	0.11	1.37	2.75				0.05	0.75	16.60	193.6	1648
FINN-CPY	Mothra	21.90	25.30	4.67		32.70	8.90	0.75	0.26	0.07	388	293
FINN-SPH	Mothra	0.00	5.58	5.83				4.90		2.00		

Sample	Field	Cu	Fe	Zn	Pb	S	SiO2	Ba	MgO	CaO	Cd	Sr
J2-59-1	Mothra	0.08	0.94	0.97		23.90	0.25	0.04	0.70	37.20	53	2730
J2-52-1	Mothra	19.20	27.30	3.30		35.20	0.90	0.04	0.94	5.84	174	412
FINN-ZN Silica	Mothra	0.40	5.40	5.71		9.00	56.00		4.44	1.69	198	1910
ALV4438-1635	Main Endeavour	0.21	24.60	2.18	0.21	26.90	32.94	0.76	bd	0.01	84	395
ALV4438-1816	Main Endeavour	4.64	31.50	3.33	0.04	40.20	3.29	0.31	bd	4.88	159	566
ALV4438-1816 (outer)	Main Endeavour	2.18	33.10	6.31	0.06	43.40	6.93	0.63	bd	0.01	284	440
ALV4438-1816 (inner)	Main Endeavour	10.00	33.00	2.03	0.03	40.20	4.62	0.35	bd	0.10	121	289
ALV4438-2132	Main Endeavour	4.35	2.73	20.00	21.00	31.80	0.01	0.00	bd	0.01	1540	25
ALV4441-1912	Main Endeavour	0.45	30.40	9.01	0.13	38.30	12.09	0.50	bd	0.01	346	336
ALV4441-2135	Main Endeavour	6.26	34.50	0.09	0.02	43.80	0.98	0.02	bd	3.46	1	188
ALV4446-1628	Main Endeavour	4.04	30.50	9.66	0.06	40.60	8.11	1.25	bd	0.07	261	631
ALV4446-1735	Main Endeavour	1.56	4.86	20.00	21.00	29.10	5.80	1.19	bd	15.67	1200	1580
ALV4448-2211	Main Endeavour	0.53	33.00	3.29	0.05	42.60	6.65	0.86	bd	0.01	93	429
ALV4449-1630	Main Endeavour	0.40	24.80	11.10	0.22	32.80	20.58	2.13	bd	0.24	434	1510
ALV4449-1938	Main Endeavour	1.18	3.86	0.20	0.00	27.40	0.19	0.03	bd	37.21	8	1970
ALV4449-1938 (inner)	Main Endeavour	0.11	0.73	0.68	0.01	25.70	0.24	0.05	bd	39.45	33	1870
ALV4449-1938 (outer)	Main Endeavour	0.48	38.60	0.44	0.03	40.50	0.26	0.03	bd	7.82	17	424
ALV4450-1538	Mothra	0.09	0.91	1.29	0.01	25.60	0.90	0.08	bd	38.89	64	2210
ALV4450-1538 (inner)	Mothra	0.33	19.10	0.83	0.02	34.10	0.01	0.04	bd	24.90	42	1260
ALV4450-1829	Mothra	0.10	4.15	2.19	0.85	7.20	31.66	22.10	bd	0.39	19	10000
ALV4451-1725	Sasquatch	0.14	0.51	1.84	0.02	25.10	0.73	0.21	bd	38.05	104	2260
ALV4452-1706	Main Endeavour	0.57	26.90	11.70	0.16	38.10	0.39	0.38	bd	10.23	418	796
ALV4517-1703	Main Endeavour	1.60	20.50	20.00	20.00	35.40	8.49	0.47	bd	0.01	1000	422
ALV4517-1718	Main Endeavour	0.47	23.00	20.00	20.00	38.10	11.25	0.70	bd	0.01	756	574
ALV4518-1836	Main Endeavour	0.26	0.94	0.06	0.00	24.30	2.29	0.03	bd	38.05	1	2370
ALV4518-1836 (inner)	Main Endeavour	0.44	1.68	0.11	0.00	19.00	4.68	0.02	bd	29.10	4	1690
ALV4518-1836 (outer)	Main Endeavour	0.22	1.03	0.08	0.00	23.20	3.19	0.01	bd	36.09	4	2270
ALV4525-0134	Main Endeavour	0.38	22.00	7.62	0.40	39.40	20.28	0.71	bd	0.06	122	598
ALV2467-R2	N. of MEF	0.14	5.22	10.10	0.85	11.50	25.24	23.10	bd	0.07	49	4560
ALV2467-R9	N. of Clambed	0.18	7.37	15.60	0.69	15.90	30.59	8.65	bd	0.01	84	2240
R1348-1007-Ba	S. of Mothra	4.77	33.20	0.48	0.00	42.90	8.21	0.00	0.01	0.03	21	129
R1348-1007-S	S. of Mothra	2.41	37.70	0.06	0.01	48.00	4.71	0.00	0.01	0.08	4	9
D264-R6	N of MEF	1.20	37.50	2.62	0.04	50.50	0.13	0.04	0.01	0.01	0.4	48
D266-R9	NE of MEF	0.43	29.30	3.04	0.20	30.80	17.99	2.52	0.05	0.35	1.4	1460
D266-R5	NE of MEF	0.38	17.50	28.70	0.25	36.40	7.87	0.48	0.01	0.13	130	250
D265-R3	SE of Sasquatch	4.48	39.90	0.24	0.01	47.50	0.64	0.00	0.15	0.04	0.4	4
D266-R8	NE of MEF	0.04	41.60	0.13	0.02	57.60	0.81	0.00	0.02	0.07	0.4	15
D266-R6	NE of MEF	12.10	35.50	0.02	0.00	46.20	0.51	0.00	0.01	0.07	127	74
D264-R3	N of MEF	1.18	36.80	3.32	0.07	43.40	5.26	0.67	0.01	0.07	0.4	423
D264-R5	N of MEF	1.05	23.10	5.52	0.25	31.30	19.83	2.61	0.13	0.18	1.9	1950
D266-R4	NE of MEF	0.07	29.10	2.48	0.08	38.90	5.97	9.90	0.01	0.11	3.8	2330
D265-R8	NE of Sasquatch	0.44	23.00	14.60	0.25	31.30	10.82	2.25	0.10	0.18	4.6	1190

Sample	Field	Cu	Fe	Zn	Pb	S	SiO2	Ba	MgO	CaO	Cd	Sr
D264-R2	N of MEF	0.74	28.10	16.30	0.02	48.70	0.51	0.00	0.02	0.01	0.4	6
D264-R22	W Ridge Flank	0.82	8.89	0.41	0.07	10.40	52.41	6.12	0.15	0.17	5.3	3630
D265-R4	SE of Sasquatch	3.95	29.60	0.20	0.00	40.00	0.34	0.00	0.07	0.10	0.4	11
D265-R2	SE of Sasquatch	1.73	7.60	24.20	0.01	16.80	45.78	0.00	0.01	0.04	0.4	11

ICP-ES: inductively coupled plasma emission spectrometry
ICP-MS: inductively coupled plasma mass spectrometry
INAA: instrumental neutron activation analysis
LECO:

APPENDIX D: Petrographic Descriptions of barite rich samples from the Endeavour Segment

The following are 22 detailed thin-section descriptions of the samples used in this study.

TIVEY MISC-2

Geochemistry notes: 33wt% Ba, low SiO_2 and CaO.

Initially, it appears that this section did not appear to contain much barite, considering that the bulk sample has the highest wt% Ba in the collection. This sample contains two distinct parts; a denser, lower porosity, sulfide-rich section transitioning abruptly to a more porous, sulfide and barite-rich area that appears crust-like. The first section contains mainly pyrite and marcasite, with minor amounts of chalcopyrite and sphalerite. Pyrite and marcasite occur as blocky, large, euhedral cubic or triangular crystals, as well as smaller more subhedral and massive ones, with botryoidal growth in places. The marcasite crystals are generally smaller in size than pyrite. Minor (<1%) chalcopyrite is present and occurs mainly as chalcopyrite disease within the minor sphalerite observed. Sphalerite is present as small euhedral crystals as well as in association with pyrite, as colloform intergrowths and framboids. Barite occurs minimally in this part of the section as very small, blocky crystals (elongate as well as tabular, ~50 μm in size) within pore spaces, as well as very small circular arrangements of acicular crystals, approximately 50 μm (these appear orange in colour, which is thought to be the result of iron staining).

In the second section of higher porosity, barite is the predominant mineral and occurs as blocky elongate crystals, generally small to medium in size (0.25 to 0.5 mm). These crystals occur both individually and as fans, as well as very small tabular crystals (<0.1mm). Large as well as small acicular crystals growing radially are also present, as well as very small completely spherical clusters of needle-like crystals. Barite also occurs as branching fans of blocky elongate crystals. Barite generally appears to have grown towards open spaces, and any appearance of partial dissolution on the barite crystals, where it occurs, is thought to be inclusions and $AmSiO_2$ coating. Anhydrite content (and CaO wt%) is very low.

Barite generally grows with, and nucleated on, marcasite as a crust, as well as on small spherical sulfides that are likely pyrite aggregates. Sulfides in this part of the sample include pyrite and marcasite, which are also present in the same form in the sulfide-rich

section, although in much smaller amounts. Pore spaces are also filled with a grey to orange-brown fuzzy material which is thought to be amorphous iron oxide.

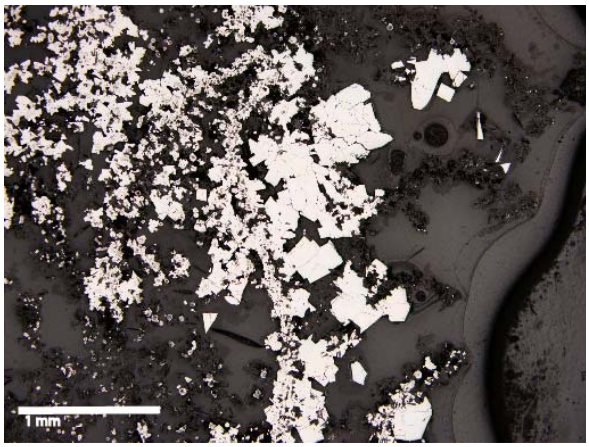

a.

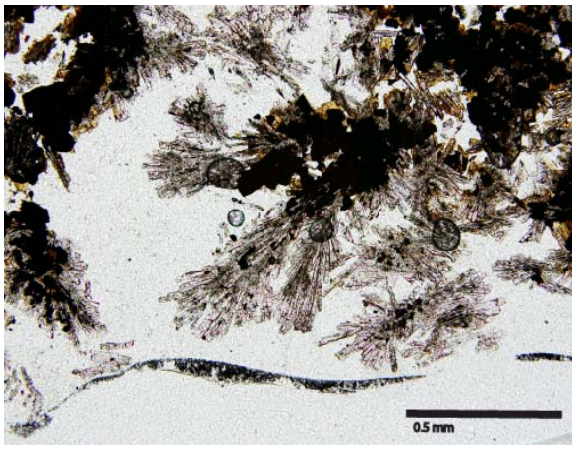

b.

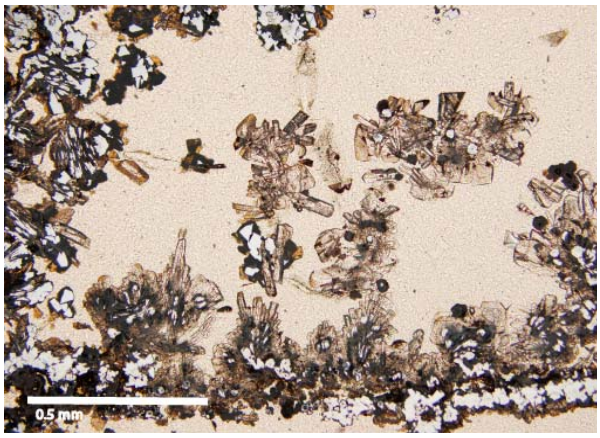

c.

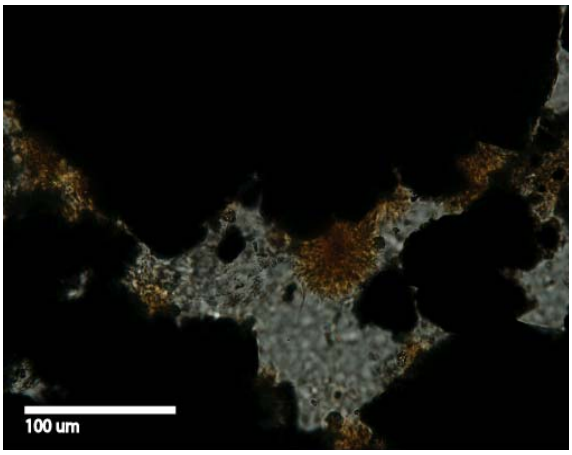

d.

Typical mineral textures from TIVEY MISC 2. a. RL, PPL, shows euhedral pyrite and marcasite, b. TL, PPL shows barite fans, c. TL and RL, PPL, shows small euhedral and tabular barite growing off pyrite and marcasite, d. TL, PPL, shows very small spherical aggregates of barite needles.

ALV 2467-R3 (EN16) _ section 1

Geochemistry notes: 26.5wt% Ba, little CaO, significant silica (24.75 wt% SiO_2).

This section has abundant barite, mainly growing radially off very small sulfide crystals (that appear to be partially dissolved in some cases) or as crusts around holes that may be remnants of fauna (tube worms); some of the barite has grown towards the interior of these structures while other barite has grown on the exterior. In places, acicular barite has grown towards the inside of other empty spaces. Barite crystals are mainly elongate and arranged radially; however, some single blocky elongate crystals are present. Here, the crystals are quite different from the anhydrite crystals seen in other sections; the cleavage is orthogonal but offset and bireflectance is lower first order colours. Some acicular barite is especially pointy and thin. It also occurs as dendritic fans as well as radial spheres of acicular crystals as seen in section ALV 2068-1. “Spherulite-like” barite also present. Sweeping extinction is common in all assemblages of barite in this section.

Any sulfides present (<5%) are distributed randomly or focused near the centre of the section where a channel cutting through the entire section is visible. Marcasite crusts are present, (sub to anhedral), and have thick fractures running through the crystals; in most cases there is evidence of colloform growth. Some of the colloform marcasite contains relict dendrites or acicular crystals; these appear in almost all situations where marcasite crusts are present, and are believed to be barite needles that have grown through the marcasite, or more likely marcasite that has grown between and around the barite. There is a very fine amorphous silica coating over most crystals in the section.

It appears that in general, barite in association with the fossil worm tubes consists of very fine, well-formed blocky crystals that have grown towards the inside while more fan-like, dendritic barite have grown towards the outside.

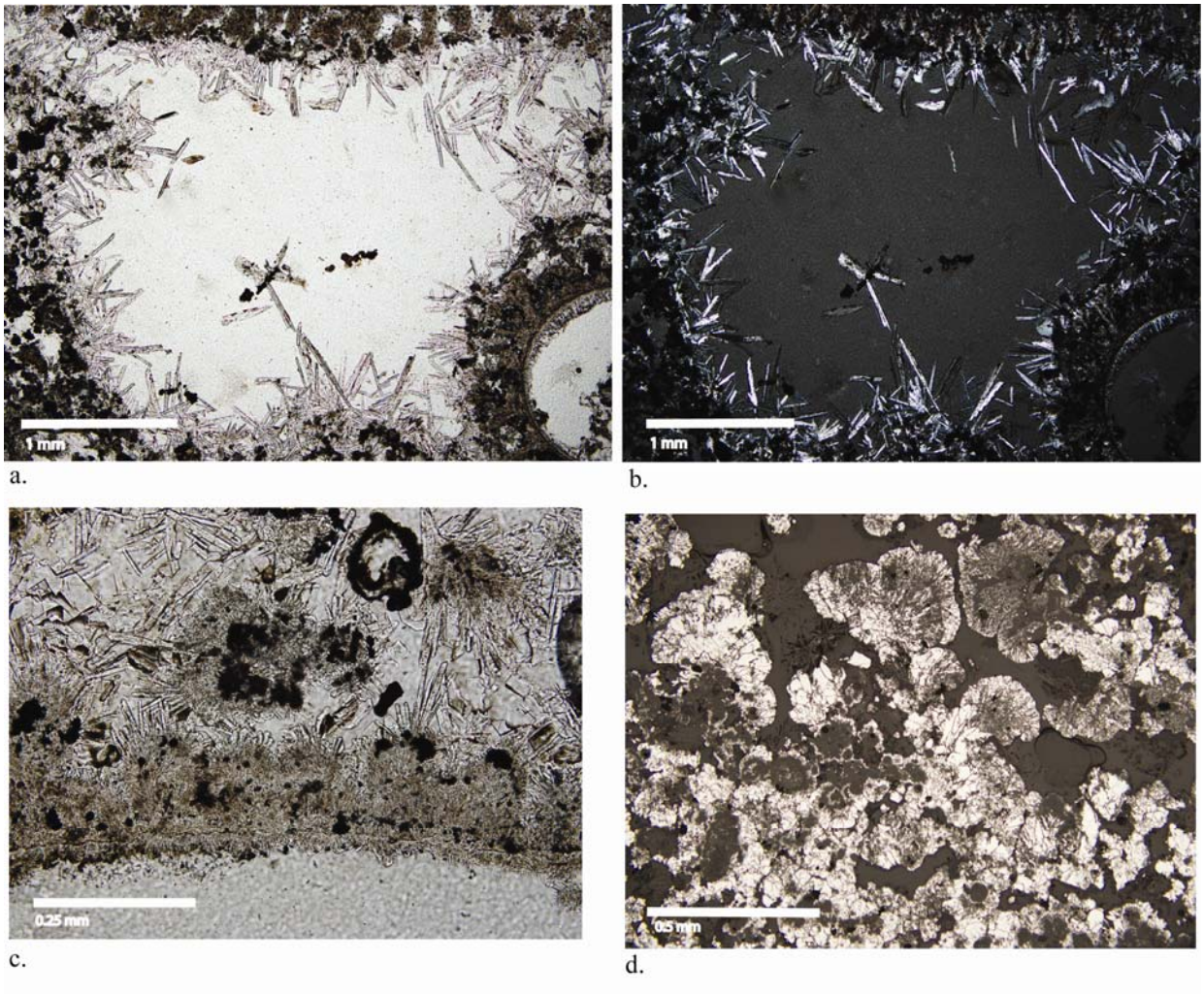

Typical mineral textures from ALV 2467-R3_section 1. a. TL, PPL and b. TL, XL both show elongate barite needles growing into pore space, c. TL, PPL, shows dendritic barite becoming euhedral barite on the exterior of a fossil worm tube, and d. RL, PPL, shows relict needles through marcasite in reflected light.

ALV 2467-R3 (EN16) _ section 2

Geochemistry notes: 26.5wt% Ba, little CaO, significant silica (24.75 wt% SiO_2).

This is the second section from the same sample. Abundant worm tube fossils are also the main feature. In this section the barite has grown towards the inside of worm tubes as blocky elongate crystals of varying sizes, whereas in section 1 the barite has mostly grown towards the outside of the fossil worm tubes as small branching dendrites and acicular crystals. As in other sections, the clear, well-formed crystals nucleated as fine-grained, sulfide-included, masses of grey barite. Any acicular fans of barite are fuzzy with sulfide inclusions (the most common occurrence of barite in this section); all the clear crystals appear to have grown on the small sulfides and are most visible in reflected light.

In contrast to section 1, there are no elongate barite needles. Abundant $AmSiO_2$ coats all other mineral phases. The main sulfide is marcasite and occurs as crusts around holes, with fractures running through. The typical marcasite-barite association is seen here, with barite crystals growing into marcasite, or vice versa. Pyrite is present in small amounts, and almost always has marcasite growing around it. Some pyrite framboids are present, as well as a small amount of sphalerite which occurs as colloform intergrowths with pyrite.

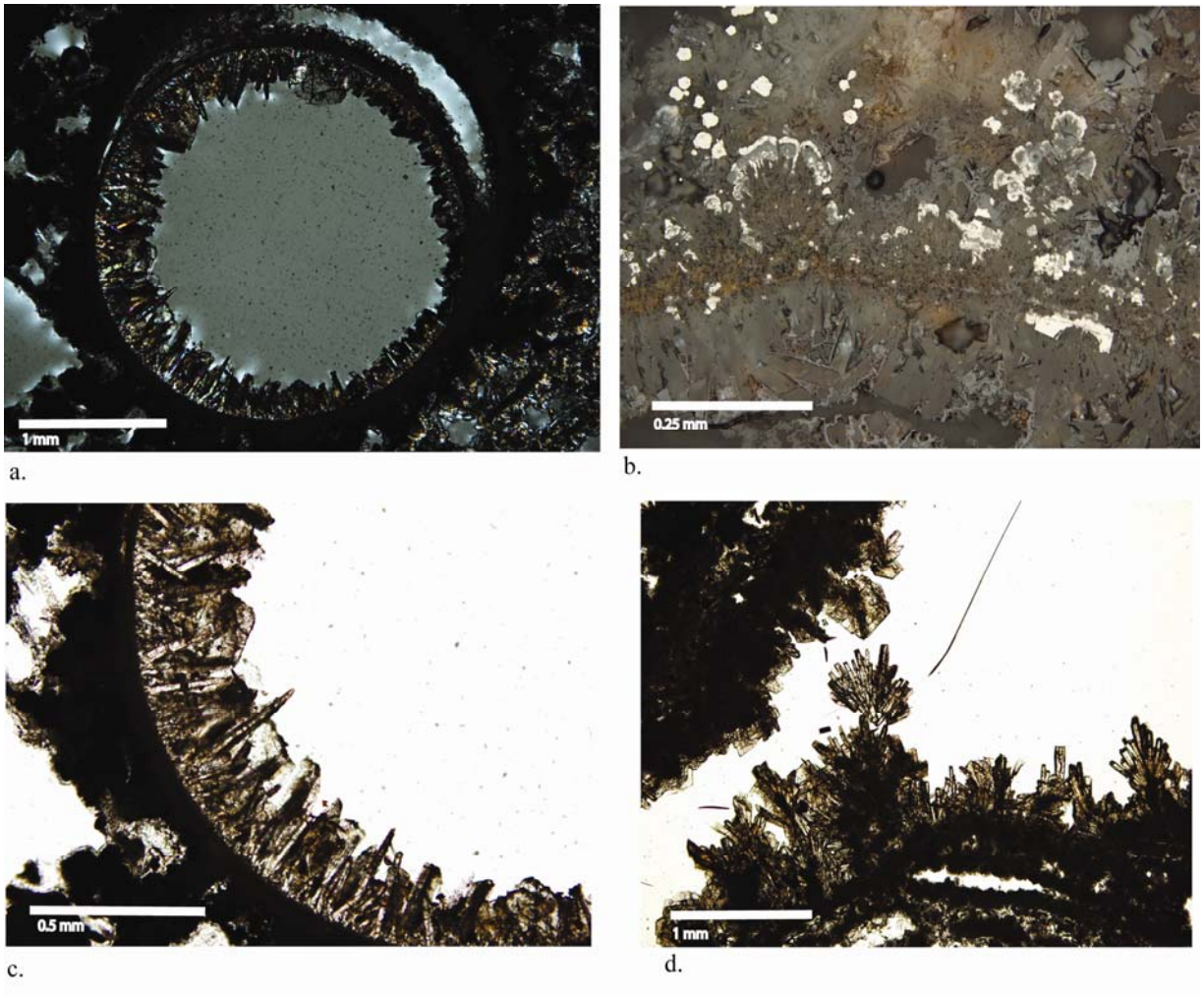

Typical mineral textures from ALV 2467-R3_section 2. a. TL, XL and c. TL, PPL, both show blocky and needle barite growing towards the interior of a fossil worm tube, b. RL, PPL, shows anhedral pyrite overgrowing and intergrowing colloform sphalerite, which in turn surrounds relict needles, and d. TL, PPL, shows blocky barite growing in a radial pattern.

ALV 2463-R4-pc (EN 32)

Geochemistry notes: 26.00 wt% Ba, very little CaO.

This section consists mainly of large elongate blocky barite crystals, some of the largest seen in any of the samples (1 to 2 mm). This allows for close observation of barite characteristics, such as the typical triangular or rectangular terminations as well as the high first order birefringent colours. Almost all of these large barite crystals have grown directly into open spaces; they are larger and blockier than the barite which has grown as aggregates and are more elongate and do not have any apparent preferential orientation. Many barite crystals appear to have grown as extensions of fine barite crystals in fans – these are grey and unclear, likely due to sulfide inclusions. Some crystals appear to have started as dendritic or feathery fans and finished growing as blocky barite crystals. This barite appears to continue growing radially even when it grades outward from acicular to blocky. Some fossil worm tubes are present in this sample, with barite growing on the inner wall of the tube in the same way as sample ALV 2467-R3_section 2, but at a smaller scale.

$AmSiO_2$ spheres are abundant and occur around the barite crystals as thick coatings. Minor sulfides have grown off the barite crystals and are also surrounded by $AmSiO_2$. Very small pyrite crystals are located within minor sphalerite, which occurs as small subhedral crystals.

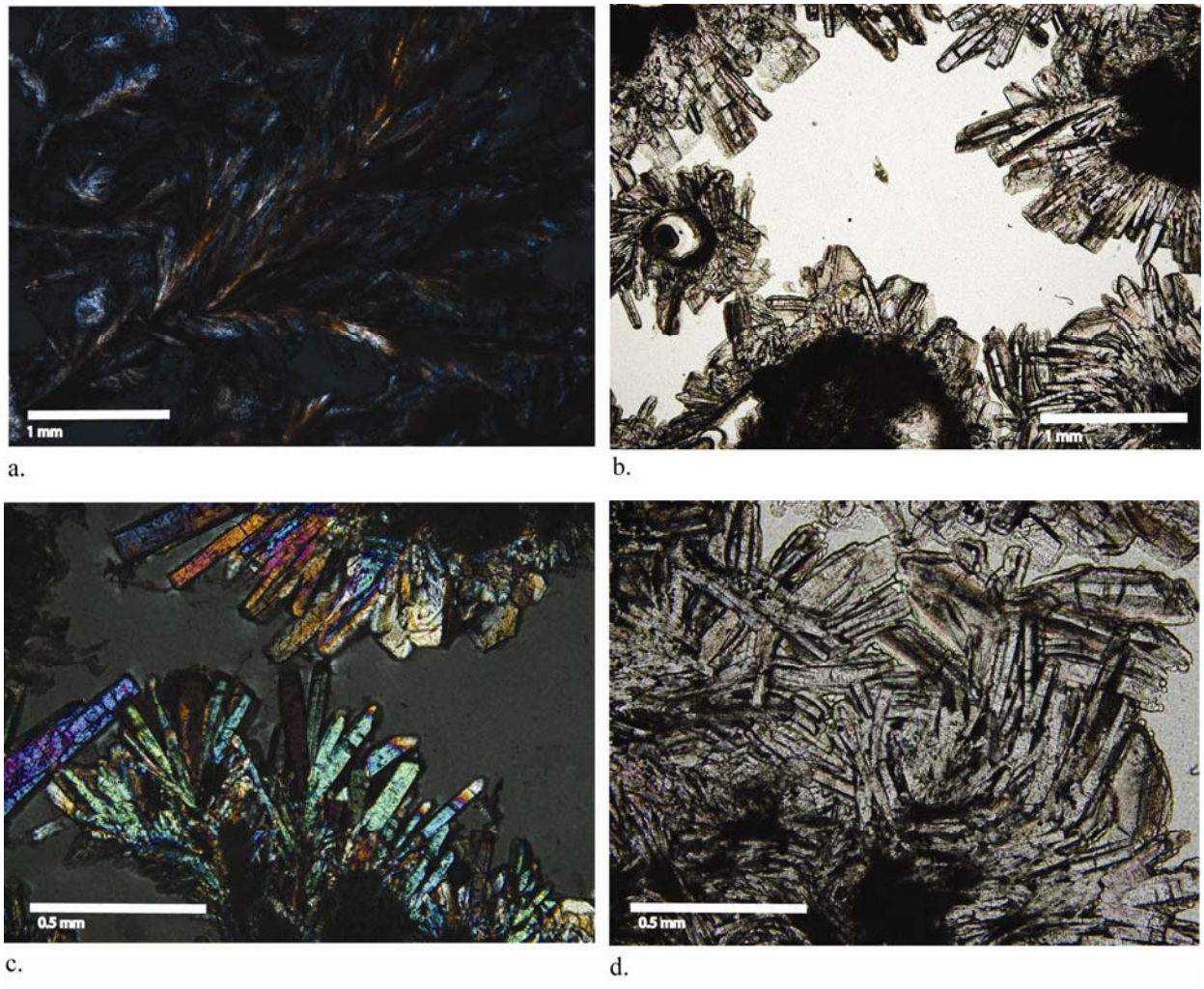

Typical mineral textures from ALV 2463-R4-pc. a. TL, PPL, shows branching dendritic barite under crossed-polars, b. TL, PPL, c. TL, XL, and d. TL, PPL, all show well-formed, euhedral barite.

ALV 2068.1

Geochemistry notes: 23wt% Ba, minor CaO, high silica (22wt%), 11.6wt% Fe.

This section contains abundant $AmSiO_2$ that coats almost all crystals and has preserved the shape of relict anhydrite, barite, or pyrrhotite needles. Most of the section consists of very fine, porous, sulfides and $AmSiO_2$. Sulfides occur as small framboids, botryoidal masses, and as fine-grained aggregates; they include marcasite, pyrite, and minor sphalerite, and occur with what appears to be fine barite crystals.

Marcasite occurs as fairly sub- to euhedral crystals throughout, whereas pyrite occurs as sub- to euhedral crystals, fine framboids, and colloform/botryoidal growths. When marcasite and pyrite occur close to each other, marcasite is usually euhedral whereas pyrite is fine-grained, granular, and colloform. Possible fine-grained sphalerite or wurtzite occur in a dark matrix of uncertain composition.

Barite occurs as both small and large acicular needles growing radially and individually, and as blocky bladed and tabular crystals. Where individual crystals are not visible, barite occurs dendritically, as branching fan-like aggregates with sweeping extinction. The edge of the section contains spherical aggregates of acicular barite with no specific nucleus visible; the centre appears to be a random arrangement of small barite needles that eventually are organized radially towards the outside of the sphere. There is a fairly high abundance of these spheres, and some barite fans are grey and cloudy due to sulfide inclusions.

Barite has grown into open spaces and generally towards the outside of the section. As in many other sections, barite occurs in close association with marcasite; the marcasite has grown around barite, or vice versa. An indistinct, unclear grey material occurs in “trails” through the section. At high magnification (100x) it consists of $AmSiO_2$ and no crystals.

A thick coating of $AmSiO_2$ gives the barite a corroded appearance, which can confuse it with the dissolving or replacement of anhydrite.

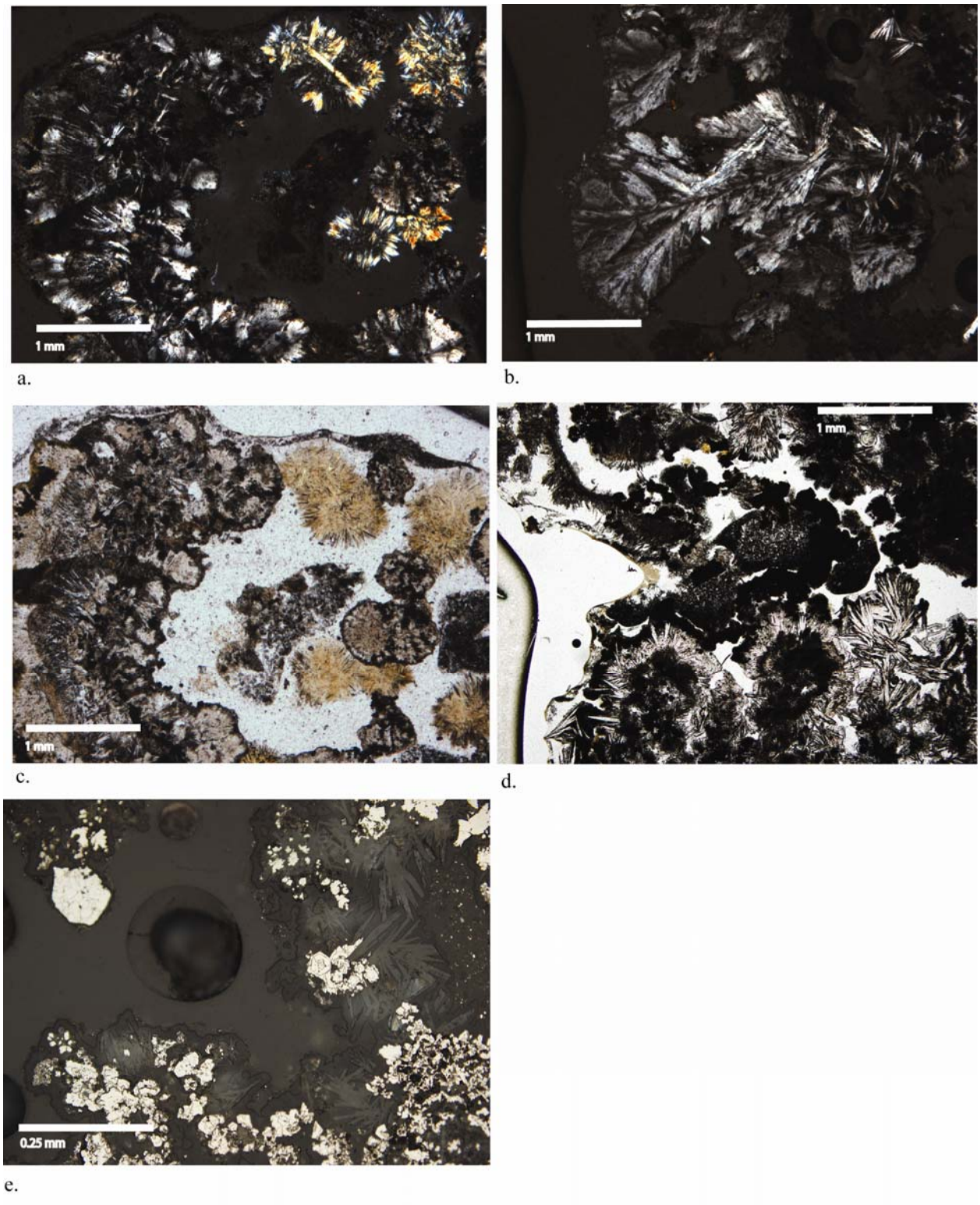

Typical mineral textures from ALV 2068.1. a. TL, XL, and c. TL, PPL, both show arrangements of small acicular barite needles, b. TL, XL, shows a feathery dendritic barite crystal, d. TL, PPL shows radiating acicular barite, and e. RL, PPL, shows marcasite, pyrite, and barite needles in reflected light.

ALV 1452-1A

Geochemistry notes: 12wt% Ba, 28wt% SiO2.

This section shows a general zoning of sulfides, from large subhedral sphalerite, to anhedral colloform/botryoidal marcasite and colloform pyrite (some small euhedral crystals present as well), to a crust of feathery dendritic and acicular barite, as well AmFeO. $AmSiO_2$ has coated everything that is exposed to an open space.

Barite occurs as feathery dendrites on one side of the section, forming a crust which is weakly from feathery fans on the outside, through a layer of unstructured sulfides to fine-grained cloudy barite fans with sulfide inclusions on the inside. Barite also occurs as acicular dendritic fans with fine sulfide inclusions in some cases with an apparently preferred growth direction. In another part of the section, rather than growing off from the sulfides, the radial barite fans have grown into them and appear to originate from a disorganized point of nucleation. Radial barite needles have either grown into the sphalerite, or more likely the sphalerite has grown around the barite, or there is a marcasite crust at the ends of the needles which then grades into the sphalerite. In this area, there are also very small, spherical pyrite framboids consisting of even smaller pyrite crystals; these have been interpreted in other studies as having biological origins.

Within the porous sulfide-rich area with abundant $AmSiO_2$, barite grows as small needle-like crystals in all directions, but generally from the centre of the pore space towards the sulfides. The barite appears to nucleate in open space and then is eventually overgrown by sulfides. Barite does not really occur as tabular crystals in this section but is typically overgrown by marcasite crystals.

Sphalerite occurs as subhedral grains, with strong red internal reflections as well as larger euhedral crystals. Sphalerite is often surrounded by red/orange cloudy iron oxide. Also observed are two large, rounded, subhedral sphalerite crystals surrounded by the tiny spherical pyrite framboids. One crystal is intact and fractured, and the other has been overgrown acicular barite and marcasite crusts as discussed previously. Very fine sphalerite also occurs in the middle pyrite/marcasite section.

Marcasite occurs throughout the section, as subhedral to euhedral crystals, but more commonly as colloform crusts as well as small botryoids. In centre of the section it occurs

also as dendrites that appear to be growing around and/or replacing an acicular mineral that grew radially (possibly dissolved anhydrite).

Pyrite occurs as euhedral crystals or colloform pyrite, and as framboids, and is often associated with marcasite.

Fibers that appear to be extending from the $AmSiO_2$ spheres are most likely bacterial filaments that are coated by silica. Similar translucent filaments as seen in section ALV 2467-R3 and ALV 3589-R2 are commonly nucleation points for growth of barite.

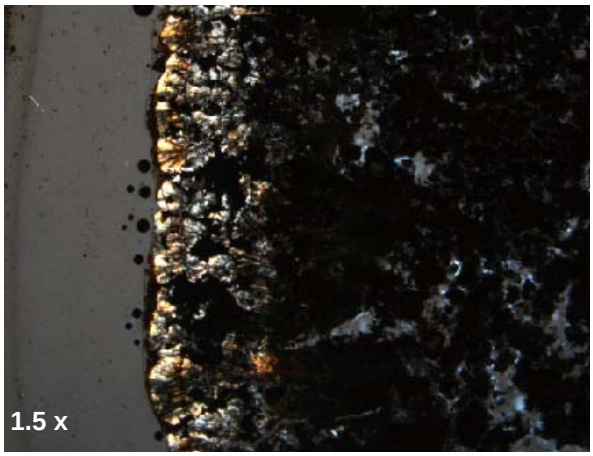

a.

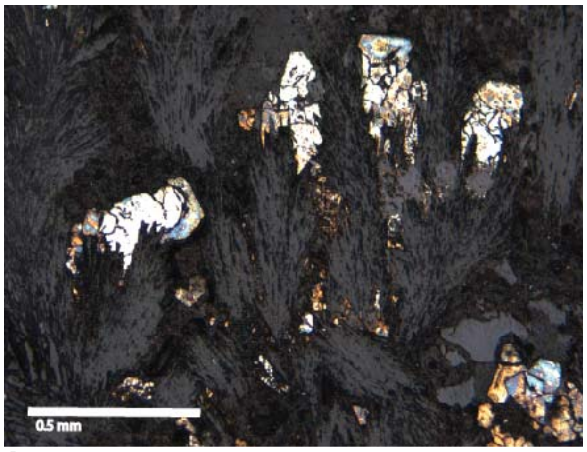

b.

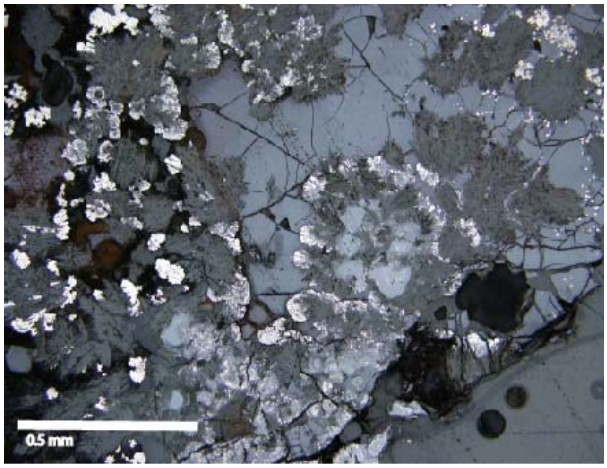

c.

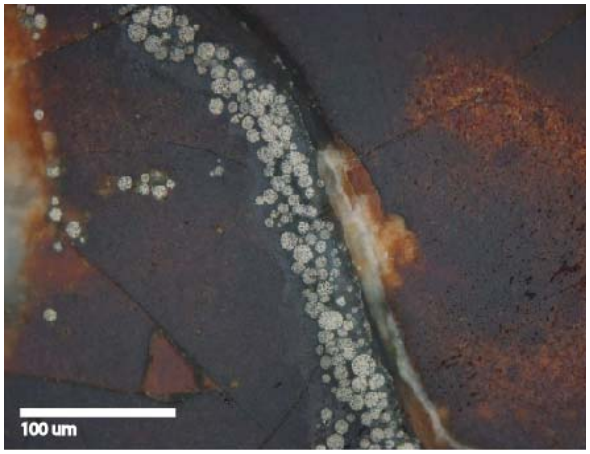

d.

Typical mineral textures from ALV 1452-1A. a. TL, XL, shows dendritic fan barite occurring as a crust, b. RL, PPL, shows barite needles overgrown by pyrite, c. RL, PPL, shows barite needles growing into colloform marcasite and large sphalerite crystals, and d. RL, PPL, shows framboidal pyrite occurring along a fracture in a sphalerite crystal.

ALV 3589-R2

Geochemistry notes: 11% Ba, 23wt% Fe, 25wt% SiO2.

The sulfides are porous and include marcasite and pyrite, with minor sphalerite. Pyrite and marcasite are so similar in terms of morphology, and occur so close together that they are often mistaken if optical properties are not examined. One crystal of chalcopyrite was observed.

Barite crystals look dirty and fractured, but at high magnification appear to contain inclusions and $AmSiO_2$ spheres attached to the surface of the crystal. They occur mainly as blocky elongate crystals rather than needle-like crystals, as well as short elongate crystals, sometimes organized radially and sometimes individually. Fine, “disseminated” barite crystals also occur among sulfides (mainly pyrite), locally as wide tabular crystals in some cases. Intergrowths of these minerals explain the common pyrite/marcasite association with radiating barite needles being overgrown by sulfides.

Pyrite occurs as fairly well-formed sub- to euhedral crystals and is replacing overgrowing what used to be acicular barite or anhydrite. In this section, pyrite occurs more with the replacement of the acicular needles than marcasite does, which was the case for section ALV 1452-1A. Marcasite occurs both as fairly large crystals and also as fine bortyoidal aggregates and crusts that contain pseudomorphs of acicular needles, similar to section ALV 1452-1A. Some of the crystals associated with replacing acicular needles are also marcasite; some are both pyrite and marcasite.

ZnS in this sample occurs mainly as skeletal crystals, possibly of incompletely crystallized hexagonal wurtzite. Elsewhere ZnS occurs as crust, in which case it is difficult to determine if it is sphalerite or wurtzite. These textures are typical of higher-temperature sulfide-rich assemblages.

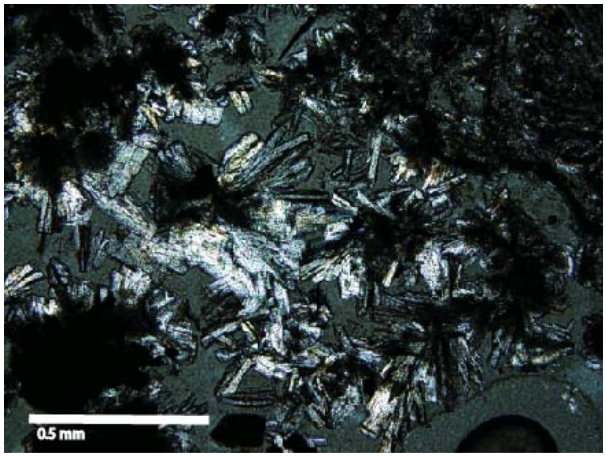

a.

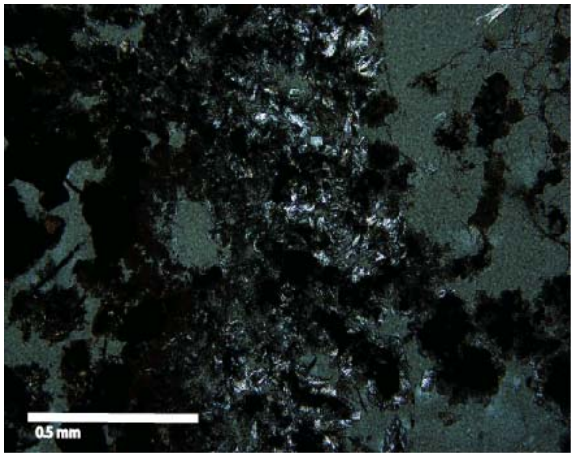

b.

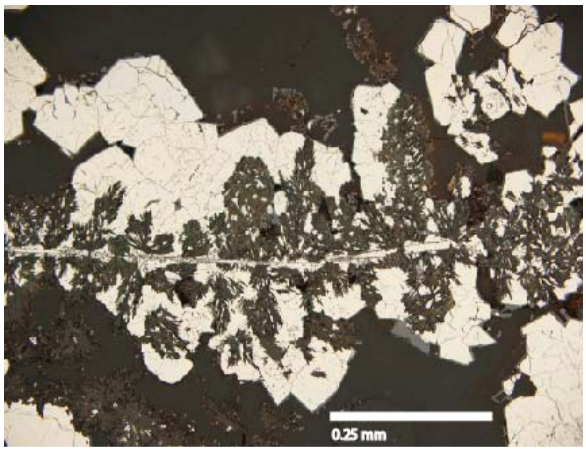

c.

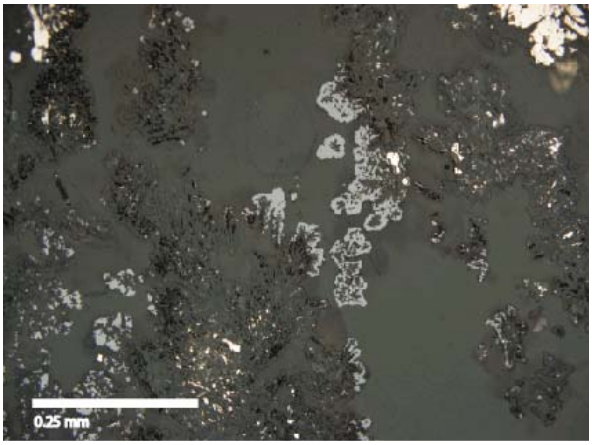

d.

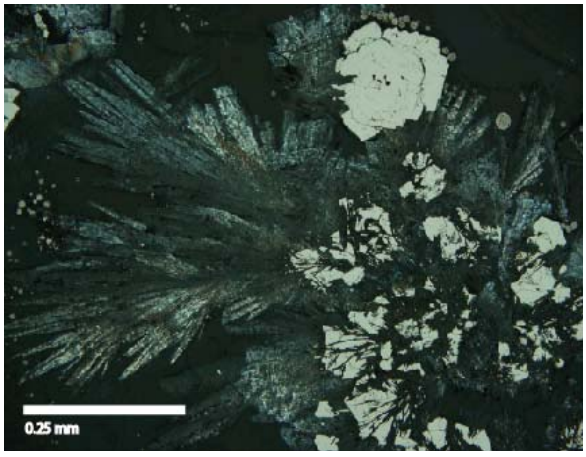

e.

Typical mineral textures from ALV3589-R2. a. TL, XL, shows blocky barite growing off sulfides, b. TL, XL, shows fine barite disseminated among sulfides, c. RL, PPL, shows barite needles overgrown by pyrite and marcasite, d. RL, PPL, shows colloform sphalerite crust, and e. TL and RL, XL, barite needles growing from marcasite.

ALV 1452-2

Geochemistry notes: 23 wt% Fe, 9.59 wt% Zn, 9.60 wt%SiO2, 8.5 wt% Ba and little CaO.

This section contains very little barite, and many crystals appear fractured and/or broken. Much of the white colour of the thin section when viewed without a microscope is silica ($AmSiO_2$).

Barite occurs as pointy, acicular crystals growing radially as well as fine crystals, disseminated among sulfides and amorphous oxides. Many crystals are very small, but still blocky and elongate.

The sulfide assemblage consists of sphalerite or wurtzite, marcasite, pyrite, chalcopyrite (as minor crystals and cpy disease in sphalerite), as well as abundant translucent orange and red amorphous oxide crusts from dissolved sphalerite. Hexagonal wurtzite is also present. Some of these crystals are skeletal and zoned. Most of the sphalerite has been replaced or overgrown and now contains a marcasite outline (faint but distinct anisotropism is seen at 100x), possibly indicating cooling. Marcasite generally occurs as sub- to euhedral crystals or aggregates or crusts. In one area it occurs as fine crystals growing around large subhedral to anhedral rounded pyrite crystals indicating several stages of pyrite-marcasite growth. Pyrite generally occurs as small euhedral crystals or colloform overgrowths and is closely associated with marcasite throughout the section; where they occur together, pyrite is generally towards the inside (i.e., earlier). Some pyrite is rimmed with dendritic/colloform marcasite. Chalcopyrite occurs mainly associated with the sphalerite or wurtzite as chalcopyrite disease; only a few crystals occur individually, but usually in close association with sphalerite and wurtzite. Some crystals occur with fine pyrite framboids and euhedral crystals.

AmSiO2 is present as a fine coat (not as thick as some sections) on most minerals.

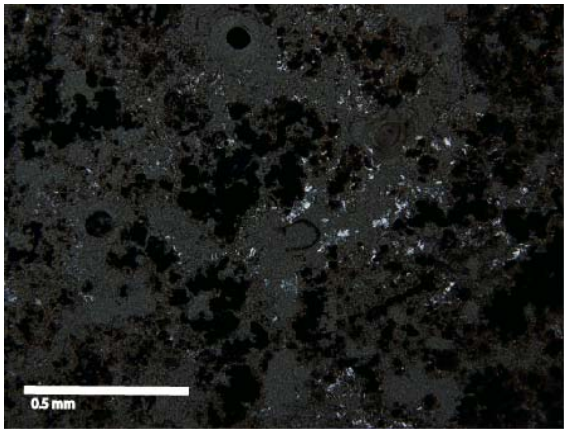

a.

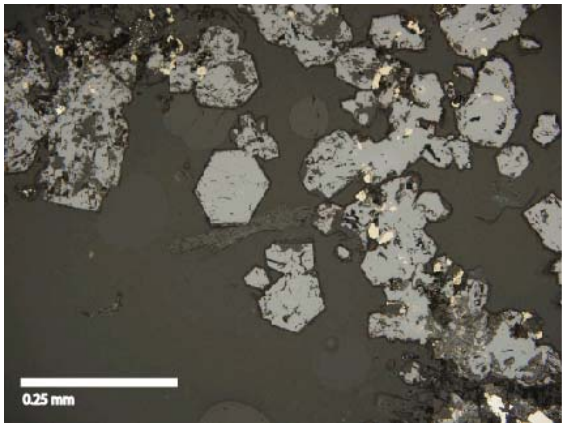

b.

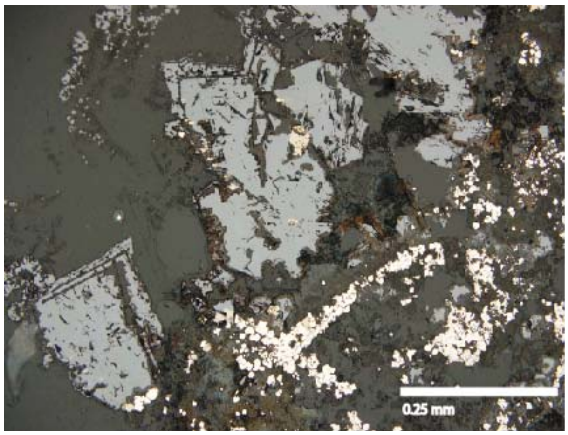

c.

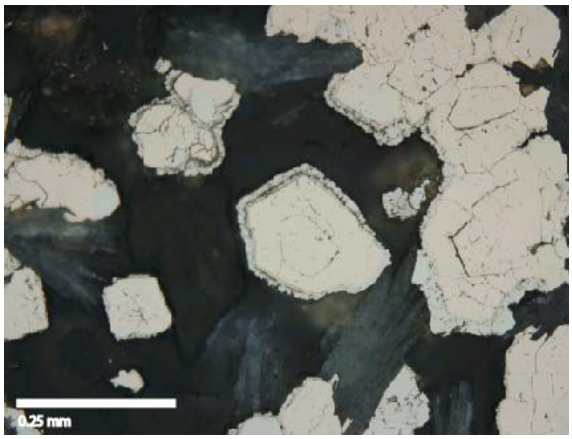

d.

Typical mineral textures from ALV1452-2. a. TL, XL, shows fine blocky barite scattered among sulfides, b. RL, PPL, shows a hexagonal wurtzite crystal in centre, as well as chalcopyrite disease in surrounding ZnS, c. RL, PPL, shows zoned disintegration of ZnS, as well as minor chalcopyrite and pyrite, and d. RL, PPL, shows possibly two generations of pyrite, overgrown with a marcasite crust, and in association with barite needles.

ALV 2072-1B

Geochemistry notes: Abundant Fe (36.7 wt.%), low SiO2, 7.5wt% Ba, low CaO.

The sulfide assemblage includes marcasite (main sulfide), and pyrite, typically with marcasite overgrowing earlier pyrite. There is no visible sphalerite in this section. Amorphous silica also occurs very minimally, as a thin coat.

Barite occurs minimally and as aggregates of small acicular radial crystals. Blocky and tabular forms are rare (if present, they are very small). Very fine barite occurs randomly distributed disseminated in sulfides. Some tabular barite crystals are present, in association with the acicular barite. One zoned, tabular barite crystal is overgrown by radially organized needles overtop. Locally, barite is overgrown by marcasite; this barite is more blocky elongate. Some very fine acicular barite appears to be stained a yellow colour (Fe staining), and is overgrown by other fine acicular barite crystals. This barite appears to have nucleated on and between sulfides and therefore is later than the sulfides.

Marcasite and pyrite occur in close association with each other, marcasite usually as fine crystals distributed throughout larger pyrite crystals; however, it’s difficult in this section to distinguish these two minerals. Pyrite and marcasite form crusts, generally with larger pyrite on the outside and a small layer of marcasite on the inside.

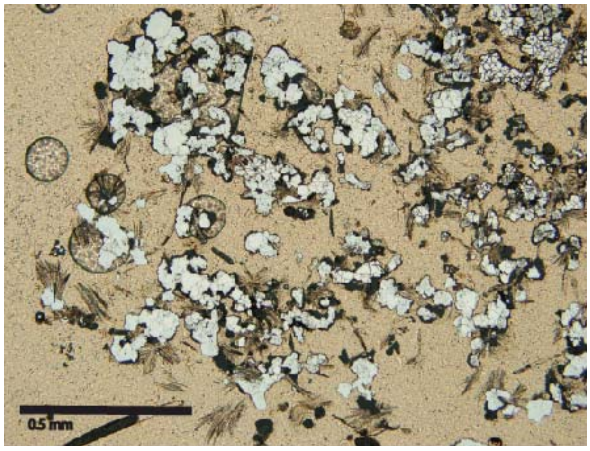

a.

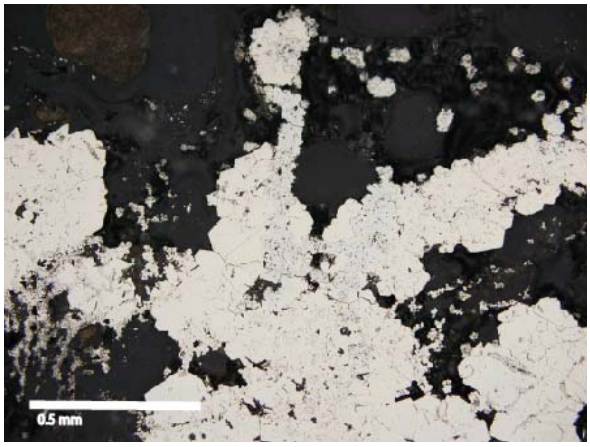

b.

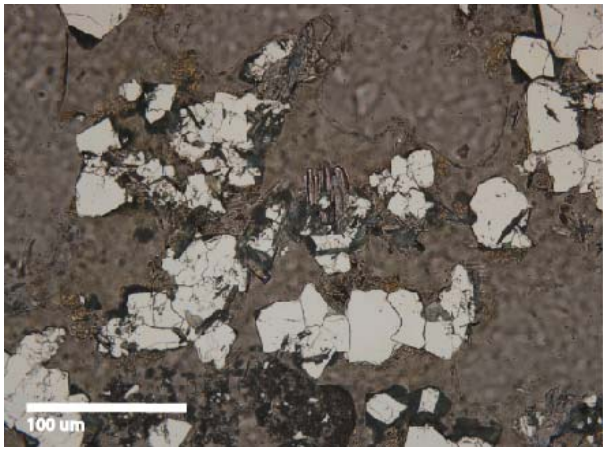

c.

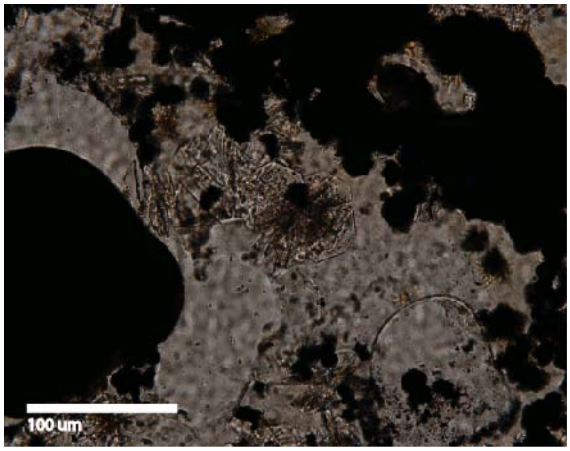

d.

Typical mineral textures from ALV2072-1B. a. RL and TL, PPL, shows acicular barite among subhedral pyrite and marcasite, b. RL, PPL, shows fine anhedral marcasite growing in association with larger more euhedral pyrite, c. RL and TL, PPL, shows very small blocky barite overgrowing marcasite, and d. TL, PPL, shows very small tabular barite in centre.

ALV 3587-R-1

Geochemistry notes: Abundant Zn (53.7wt%), low SiO_2, 6.1wt% Ba, little CaO.

Macroscopically, this section consists of large, porous, branching and dendritic aggregates of sphalerite, the primary sulfide in this section.

Barite occurs as a crust on one side of the section, consisting of small blocky to blocky-acicular crystals. Adjacent to the barite crust, sphalerite crystals are very small and more anhedral. Barite crystals that occur individually are usually blocky, whereas those occurring together or overgrowing sulfides are more acicular and grow radially. Some acicular barite dendrites appear to be partly replaced and have abundant dark grey sulfide inclusions.

There does not appear to be any significant amount of $AmSiO_2$ in the section. It is only visible at high magnification and appears to be coating barite as very small spheres. An unusual, triangular-shaped barite crystal was observed (probably barite but possibly anglesite).

In some cases, sphalerite has overgrown barite crystals. Sphalerite occurs as well-developed, small euhedral crystals as well as dendritic crystals with small euhedral sphalerite crystals in between each fan. In plane-polarized light, a more opaque phase surrounded by a more translucent orange phase can be seen, reflecting zonation of Fe contents in sphalerite. Often the crystals on the outside of the sphalerite aggregates are more euhedral, which would make sense because they have more space to grow. A lot of crystals are triangular, but some do take on a hexagonal shape which would indicate wurtzite. Finally, some sphalerite grains have small inclusions of galena (pink and blue inclusions are likely due to oxidation). Very minor covellite is present, occurring as in section ALV 3622.01A.

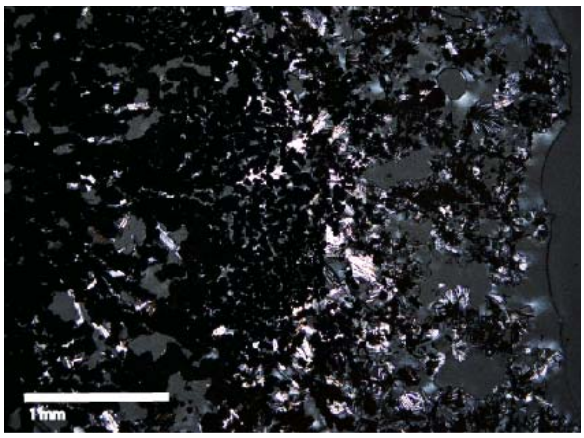

a.

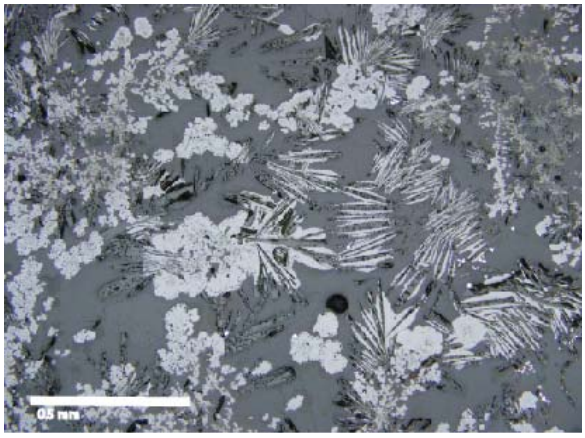

b.

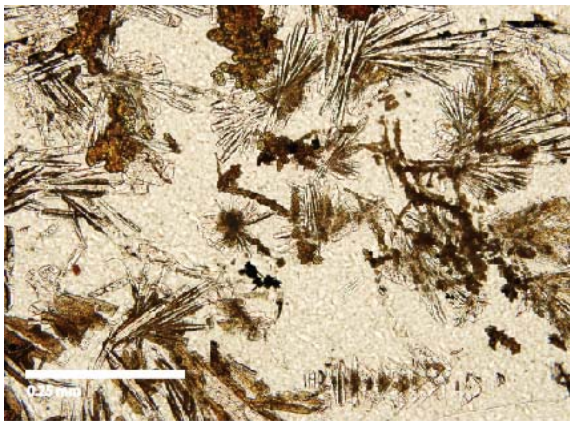

c.

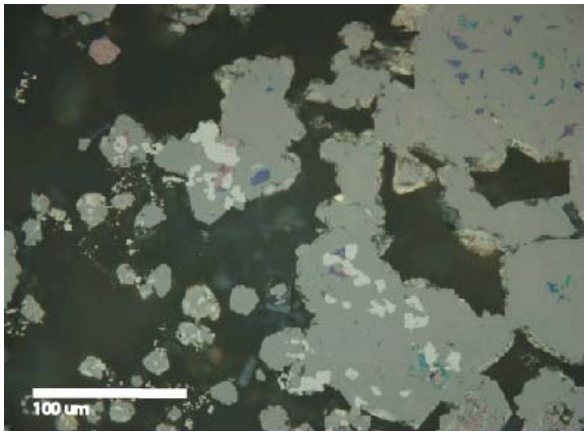

d.

Typical mineral textures from ALV3587-R-1. a. TL, PPL, shows the transition from sphalerite to barite within the sample, with barite occurring as needles and small blocky crystals, b. RL, PPL, shows anhedral sphalerite overgrowing euhedral elongate barite crystals, c. TL, PPL, shows a similar view to b., and d. RL, PPL, shows galena occurring within sphalerite, as well as pink bornite and/or covellite.

ALV 3622-01A

Geochemistry notes: Low Cu, 12 and 15 wt% Fe and Zn, 31.2 wt% SiO2, 5.4 wt% Ba and little CaO.

Macroscopically, this section looks zoned, from the inside of a conduit towards the outside. There is very abundant $AmSiO_2$ that coats the other mineral phases.

Barite lines the central fluid conduit and occurs within pore spaces. It occurs as dendritic fans facing the interior of the conduit, sometimes with $AmSiO_2$ crust. Locally acicular radial crystals appear to have nucleated in open space. Any crystals occurring alone are blocky. Around the conduit, blocky barite is mostly associated with pyrite as radial overgrowths or intergrowths with pyrite +/- sphalerite.

The sphalerite and/or wurtzite occurring in this section is pitted and pock marked, with some covellite replacement. There appear to be some relict hexagonal shapes, likely formerly wurtzite. This sample is described as coming from an old spire. A lot of the leftover sphalerite and/or wurtzite is organized in oddly shaped elongate aggregates only locally containing euhedral forms (relict crystal outlines). Pyrite and marcasite commonly overgrow the sphalerite and/or wurtzite masses.

Marcasite occurs as crusts with pyrite and in close association with pyrite; both occur as euhedral cubes as well as finer sub- to anhedral crystals (framboids and crusts). Pyrite occurs also as very small elongate blocky crystals. Within the section, marcasite and pyrite occur mainly after barite, or with barite, as the layer lining the central orifice.

Covellite replaces sphalerite mostly as the second “zone” from the centre, on both sides of the central orifice.

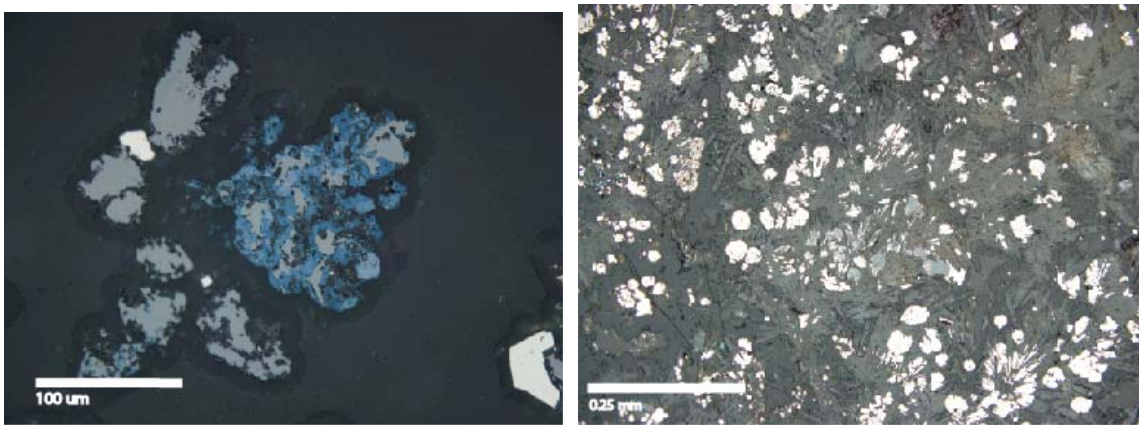

a. **b.**

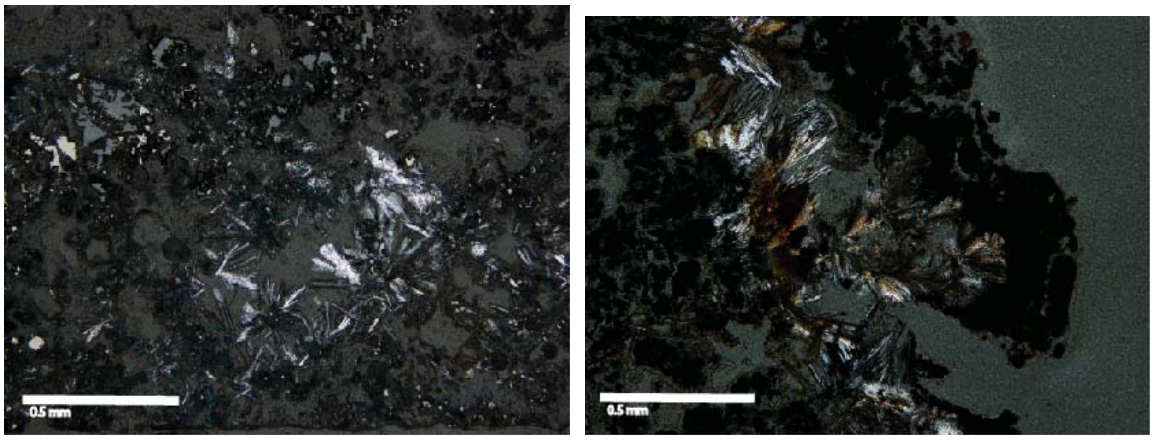

c. **d.**

Typical mineral textures from ALV3622-01A. a. RL, PPL, shows covellite replacement of sphalerite, b. RL, PPL, shows sphalerite, as well as intergrowing marcasite and barite needles, c. TL, XL, shows in white barite needles and small blocky crystals, and d. TL, XL, shows iron stained fine barite needles growing into a barite crust containing sulfide inclusions.

ALV 2072-7

Geochemistry notes: High Fe (23%), med Zn (11%), 12% SiO2, 5% Ba.

This section contains a marcasite-barite intergrowth, with possible worm tube fossils present as well. Barite occurs mainly as cloudy grey branching dendrites, mostly oriented towards the outside of the slide; however, some are facing other directions. Barite is mainly associated with marcasite; the marcasite overgrows the tops of the dendrites and is less abundant at the base. Barite also occurs as acicular crystals, as well as one occurrence of a "spherulite-like" dendrite. On some acicular crystals there appears to be very small rounded sphalerite grains.

Marcasite occurs as large dendritic fan growths facing the outside of the section (away from the centre). These fans have very rounded edges (botryoidal to colloform). In some instances marcasite and sphalerite occur together; euhedral sphalerite is overgrown by rounded marcasite growths.

Sphalerite occurs mostly in the centre of the section as fine rounded crystals or euhedral, angular hexagonal shapes; some well-formed hexagons are present, indicating wurtzite. Chalcopyrite disease and fine pyrite crystals are common among the sphalerite.

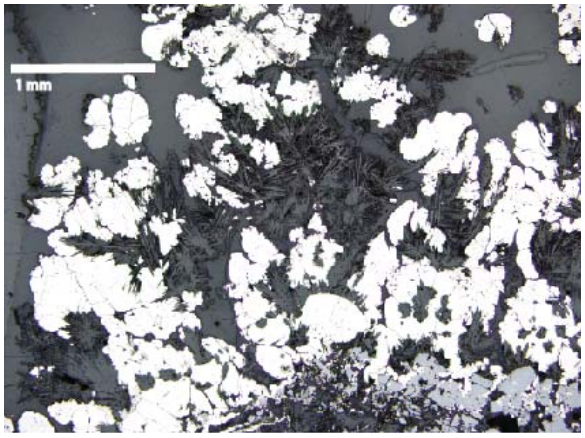

a.

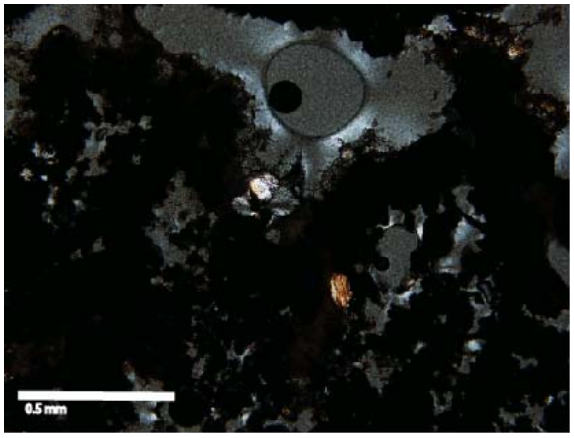

b.

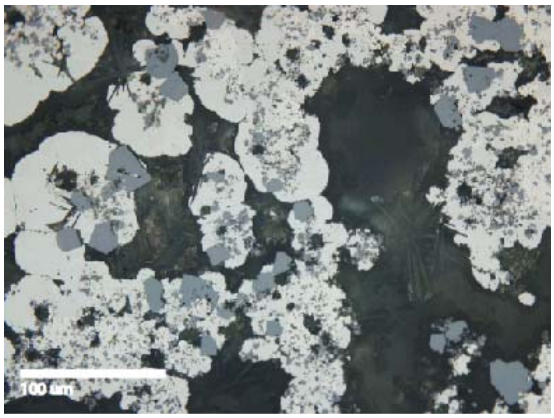

c.

Typical mineral textures from ALV2072-7. a. RL, PPL, shows at the bottom a layer of sphalerite followed by intergrowing marcasite and barite needles, b. TL, XL, shows a needle to spherulite-like barite fan, and c. RL, PPL, shows euhedral sphalerite and/or wurtzite in association with marcasite and needle barite.

ALV 3616-B

Geochemistry notes: Low Fe, med Cu (13%), high Zn (41%), low SiO2, 4.1% Ba, 0.09% CaO.

Macroscopically, the studied section is concentrically zoned: layers alternate from dark brown to brassy. Dark brown layers are less porous than brassy, sulfide-rich layers. This section contains 4.1% Ba and very little CaO. However, the major mineral present does not appear to be barite, rather it greatly resembles anhydrite. Also, when compared to a sample with similar Zn wt% (ALV 2452-2, 44wt% Zn), there is not nearly enough sphalerite or wurtzite present; only small crystals that make up ~20% of the section.

In comparison to other sections with similar amounts of Ba (ALV 2072.7, 5wt% Ba), the unknown mineral is far too abundant in the section to be barite. Barite does not seem to occur significantly at all in this section in the way (i.e. appearance) it does in other sections. The low CaO, 0.09%, also suggests that the unknown mineral cannot be anhydrite, although its habit is very similar to the abundant anhydrite in CaO-rich sections (ALV 3588.BR1, 32.40wt% CaO), which are also very low in Zn and Cd (Kristall et al, 2006).

Kristall et al. (2006) describe the occurrence of Gordaite in a sample from the Mothra vent field. Gordaite is a hydrated zinc-sodium chlorasulfate ($NaZn_4(SO_4)Cl(OH)_6 \times 6H_2O$) that occurs as transparent, platy laths resembling barite or blocky aggregates. The unknown mineral observed in this section is interpreted to be gordaite.

Sphalerite occurs in minor amounts as sub- to anhedral grains, and contain chalcopyrite disease; skeletal and fractured crystals are also present. Pyrrhotite in this section occurs as needles throughout, mainly associated with fine sub to euhhedral pyrite which are fairly euhedral.

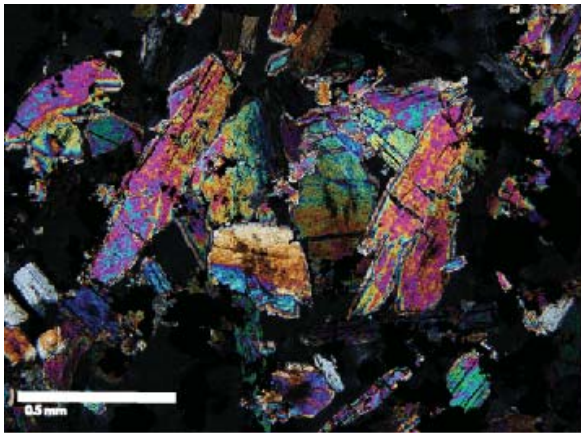

a.

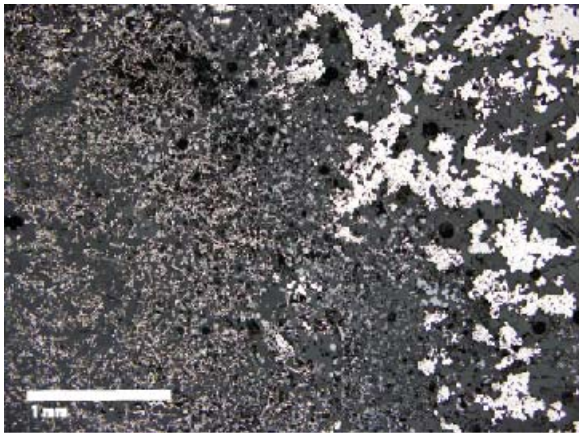

b.

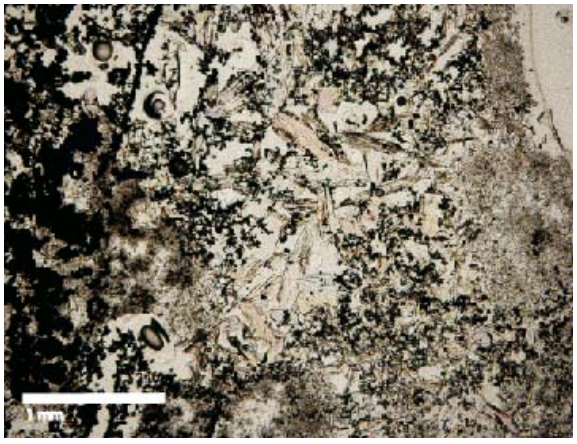

c.

Typical mineral textures from ALV3616-B. a. TL, PPL, shows the unknown mineral, thought to be gordaite, with bright birefringence, b. RL, PPL, shows fine pyrrhotite needles growing among sphalerite and/or wurtzite, with marcasite occurring on the right side, and c. TL, PPL, shows a similar view as a.

ALV 2415-1D(3)

Geochemistry notes: High Fe, med Zn, 2.7% Ba.

The studied section is very similar to section ALV 2408-1A. However, barite is more abundant, and the barite-marcasite association is more common.

Barite occurs as needles between the marcasite-pyrite layers and as fine crystals growing near sulfides on the edge of the crust. Some barite needles occur as small spherical aggregates radiating into open space. Needles of barite can also be seen overgrown by colloform marcasite. This is the most abundant type of barite within the section.

In transmitted light, the original needles are sometimes no longer evident, suggesting that they are casts of a pre-existing acicular mineral within the marcasite, possibly anhydrite.

Sphalerite and/or wurtzite appear to have grown after the pyrite-marcasite as semi-circular colloform layers and as round aggregations.

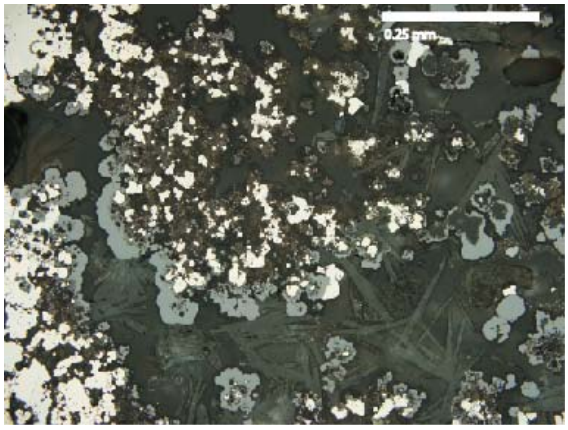

a.

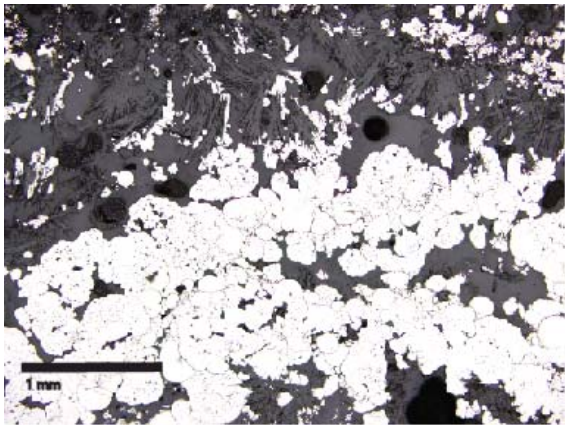

b.

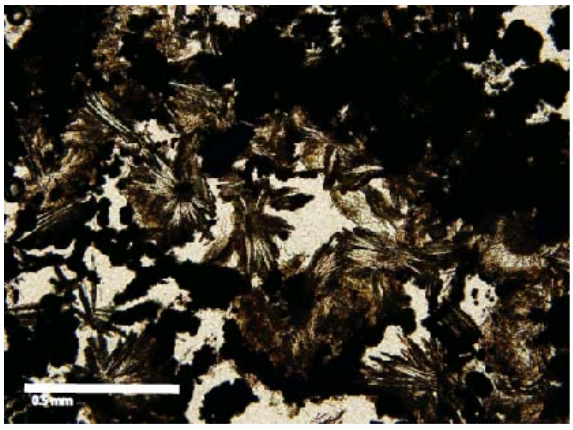

c.

Typical mineral textures from ALV2415-1D(3). a. RL, PPL, shows barite needles, as well as a sphalerite crust overgrowing subhedral marcasite, b. RL, PPL, shows acicular barite at the top in association with botryoidal marcasite in white, and c. TL, PPL, shows acicular barite fuzzy from iron staining and sulfide inclusions growing with sulfides.

ALV 2460-R2-14a (EN 31)

Geochemistry notes: Fe (11%), SiO2 (61%), 2.6% Ba.

Barite occurs mainly as thin elongate, crystals and needles. There are also a few larger, more euhedral crystals. Most crystals have grown into open spaces; all are coated with $AmSiO_2$. One partial “spherulite-like” barite dendrite is present. Where needles are small, they have grown in many different directions. However, some are organized into radial growths nucleated at a common point. Barite is also associated with marcasite, where it is nucleated on the sulfides.

Marcasite occurs sporadically with some intergrown pyrite; it is sometimes difficult to distinguish pyrite from marcasite with low anisotropy. The grains are mainly fine and encrusting. Occasional euhedral cubic crystals are faintly anisotropic, indicating marcasite.

Abundant chalcopyrite occurs in one part of the section as subhedral grains and locally “disseminated” small sub- to anhedral crystals. Traces of subhedral sphalerite are also present.

Amorphous silica coats everything and in some cases appears to contain extremely fine crystal aggregates, possibly barite. $AmSiO_2$ also forms complex, irregular growths in this section, as seen in others. It appears that barite was the last mineral to precipitate, before amorphous silica.

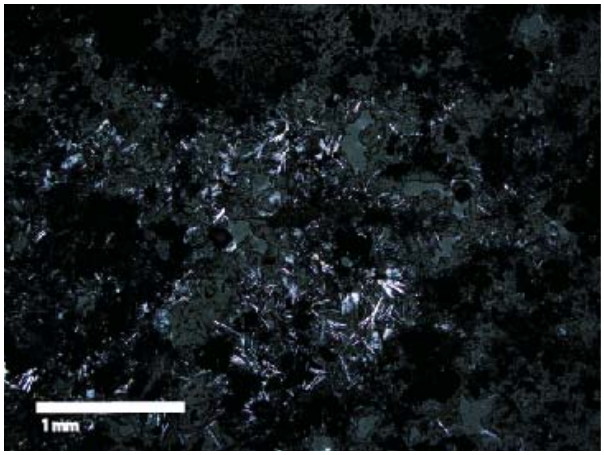

a.

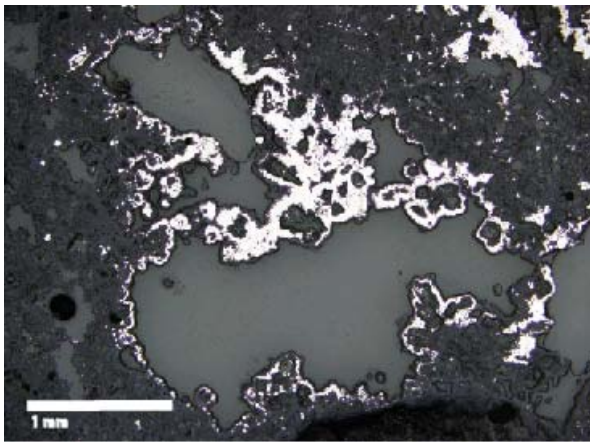

b.

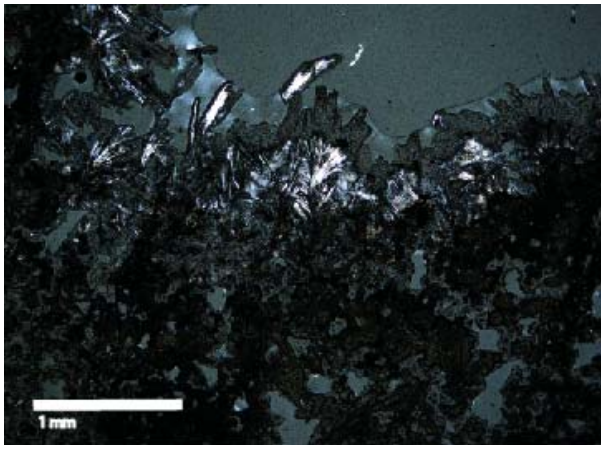

c.

Typical mineral textures from ALV2460-R2-14a. a. TL, XL, shows fine barite needles in grey growing among sulfides, b. RL, PPL, shows a marcasite crust growing in between layers of what appears to be amorphous silica, and c. TL, XL, shows radial fans of needle barite transitioning to blocky crystals.

ALV 3000C

Geochemistry notes: 35% Fe, 14% Zn, low SiO2, 1.7% Ba.

Wurtzite overgrows pyrite and marcasite and forms a crust around the marcasite. At the centre of these growths is open cavity or more zinc sulfide, or relict anhydrite/barite needles.

There is no obvious chalcopyrite in the section; however pyrite is present. Locally, pyrrhotite-marcasite intergrowths have relict needles throughout. These needles were likely anhydrite around which the sulfides grew, before the anhydrite dissolved. Fossilized remnants of vent biology also appear to be present.

The minimal barite in this section occurs almost exclusively in association with marcasite crusts as well as small needle-like crystals in between the marcasite dendrites and in the same general orientation. Some barite fans are completely enclosed in the marcasite, suggesting that the barite is early, although in some cases it appears that that barite has grown through the marcasite layers possibly while the marcasite was precipitating. However, in most cases it appears that the marcasite post-dates the barite.

One “spherulite-like” dendrite of barite was observed. Barite needles and fans are also present; some grew in the same direction as the marcasite crust, some grew laterally.

Pyrrhotite occurs as needles on the inside of the marcasite crust, likely indicating a temperature gradient. AmSiO_2 occurs in this section as a coating, but as very small spheres as opposed to the very large and thicker coatings seen in some previous sections.

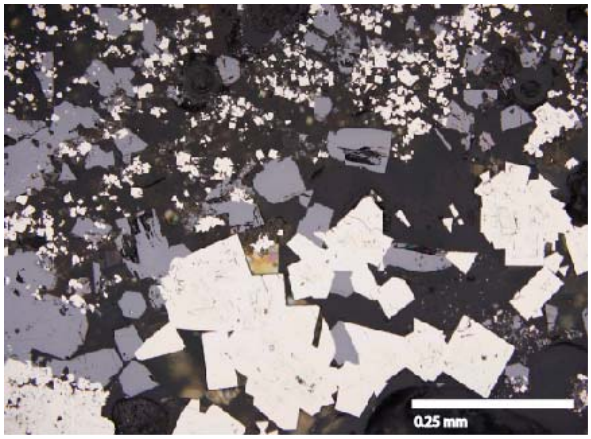

a.

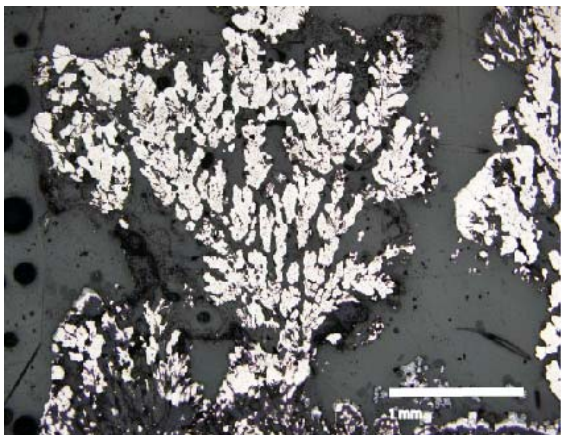

b.

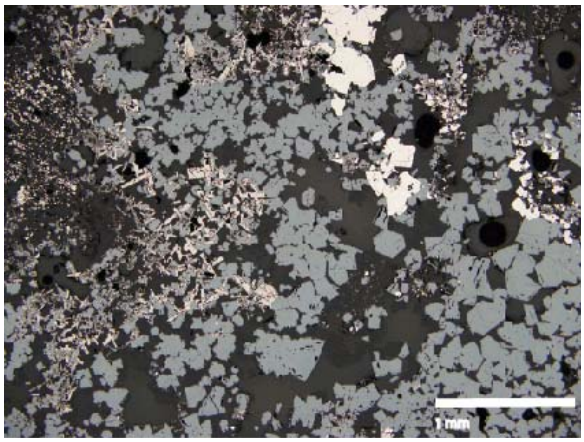

c.

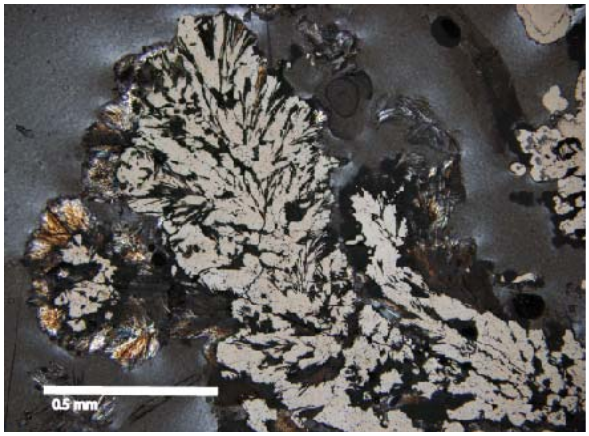

d.

Typical mineral textures from ALV3000C. a. RL, PPL, shows euhedral pyrite and euhedral, but possibly dissolving, wurtzite, b. RL, PPL, shows dendritic marcasite, c. RL, PPL, shows pyrrhotite needles growing in association with wurtzite, as well as euhedral pyrite (white), and d. RL and TL, XL, shows dendritic marcasite growing with barite needles that fan in a radial pattern.

ALV 2408-1A

Geochemistry notes: High Fe, 40%, 1.65% Ba.

This section is very similar to section ALV 2415-1D(3). Pyrite and marcasite occur as colloform and dendritic intergrowths. Barite occurs as needles between the marcasite-pyrite layers (crusts) and as fine crystals near sulfides on the edge of the crust. Some barite needles occur as small spherical aggregates where space permits. Where needles of barite occur in association with the colloform marcasite, they can be seen to have grown from the centre of the marcasite growths; this is the most common type of barite occurrence within the section. Locally, in transmitted light, the original barite appears to have been replaced by silica casts. Sphalerite and/or wurtzite appear to have grown after the pyrite-marcasite in collorform layers and as round aggregations.

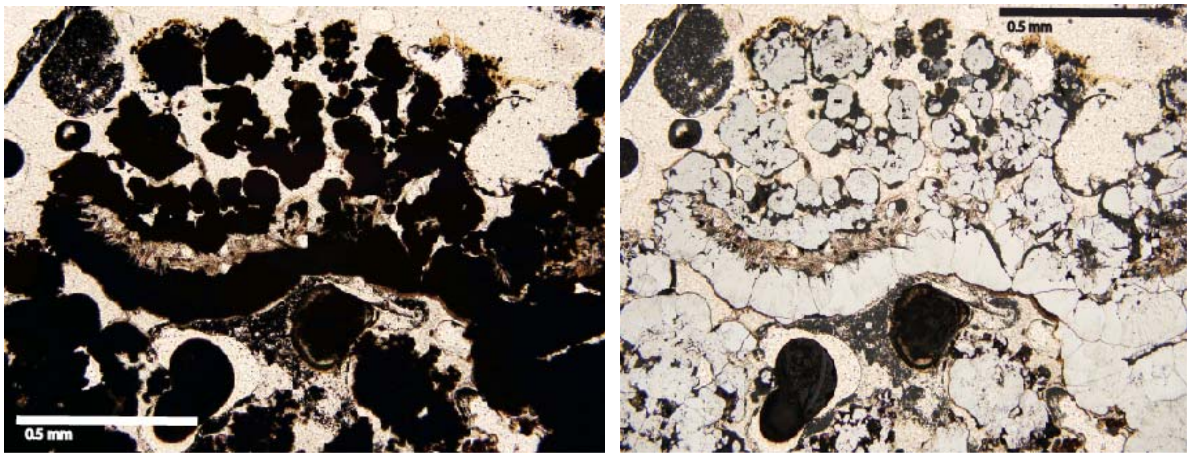

a. **b.**

Typical mineral textures from ALV2408-1A. a. TL, PPL, and b. RL and TL, both show marcasite, in the centre showing a marcasite crust with fine barite needles occurring within it.

ALV 2452-2

Geochemistry notes: 3% Cu, 6% Fe, 44% Zn, 3% SiO2, 1.65% Ba.

Barite occurs around or between sulfides, as small blocky, euhedral crystals. Barite also occurs mainly in the areas that contains marcasite, and not significantly with the large sphalerite crystals. Only minor spherical aggregates of barite occur with the large sphalerite crystals.

From the bottom to the top of the section, a layer of sphalerite and fine pyrite-marcasite grades into a crust of large subhedral crystals. When more euhedral, the crystals tend towards the shape of wurtzite. Some sphalerite is very euhedral (in transmitted plane-polarized light). The sphalerite crystals have chalcopyrite disease throughout. Fine-grained barite appears to be restricted to open spaces between the larger sulfide crystals.

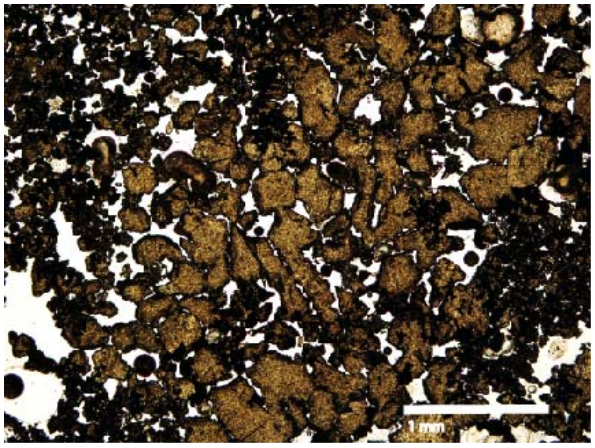

a.

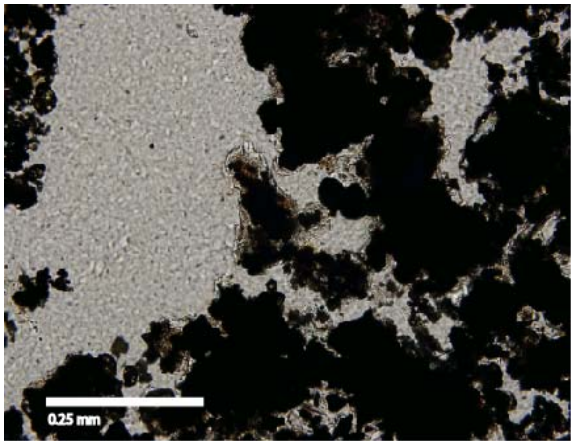

b.

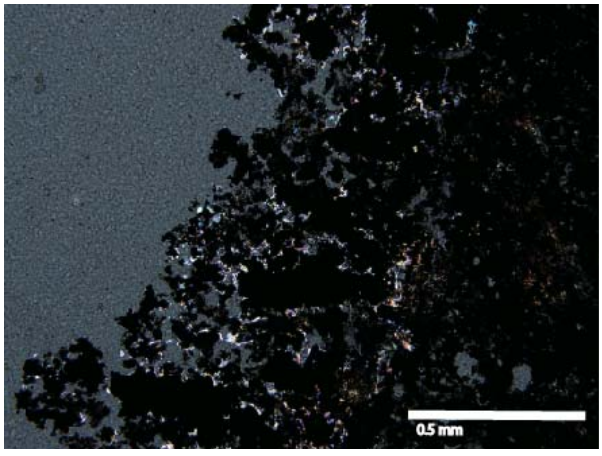

c.

Typical mineral textures from ALV2452-2. a. TL, PPL, shows almost exclusively sphalerite, b. TL, XL, shows very fine barite growing off sulfides, mainly visible in the centre, and c. TL, XL, shows fine barite occurring disseminated among sulfides.

ALV 2449-1_EN08

Geochemistry notes: 37% Fe, 5% SiO2, minimal Cu and Zn, 1.6% Ba.

This section contains almost no barite; the only non-opaque mineral appears to be restricted to minor open spaces between sulfides.

The rest of the section is a crust with alternating layers of large pyrite-marcasite dendrites within finer pyrite-marcasite. There also appears to be some casts of barite or anhydrite; they are “empty” or have been replaced by pyrrhotite and are surrounded by sphalerite or wutzite. These casts are associated with euhedral hexagonal ZnS (wurtzite) that contains some chalcopyrite disease. Chalcopyrite is also intergrown with pyrite.

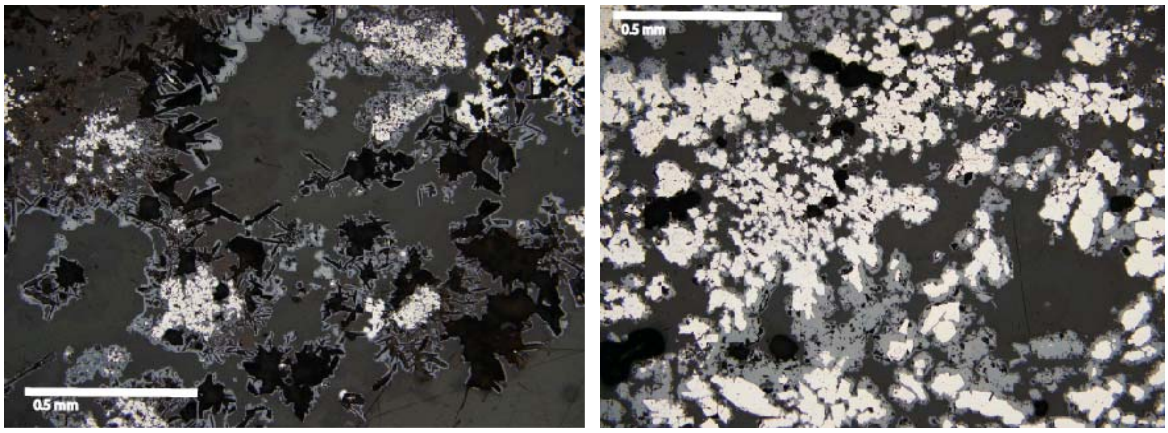

a. **b.**

Typical mineral textures from ALV2449-1. a. RL, PPL, shows needle casts surrounded by sphalerite and amorphous silica, with the white subhedral pyrite, and b. RL, PPL, shows pyrite in some places overgrown with marcasite, with subhedral sphalerite crusts occurring around both.

ALV 2461-R6-4_EN52

Geochemistry notes: 26% Fe, 19% Zn, 1.5% Ba.

The studied section contains anhydrite on one end and barite on the other. This section is very porous and consists of abundant sub- to euhedral sphalerite that contain abundant empty cavities (presumably open space from the interior of the chimney).

There is a fluid conduit running through the section, the right side contains abundant dendritic marcasite. Within this area is where the minor barite occurs, as small crystal needles the grew generally in the same direction as the marcasite. However some grew in the opposite direction, where space allows. Some of the sphalerite appears skeletal, and is associated with small pyrite crystals. Marcasite is bortyoidal in some places and associated with pyrite as well as a pinkish-beige opaque in some places. Chalcopyrite disease is present within sphalerite.

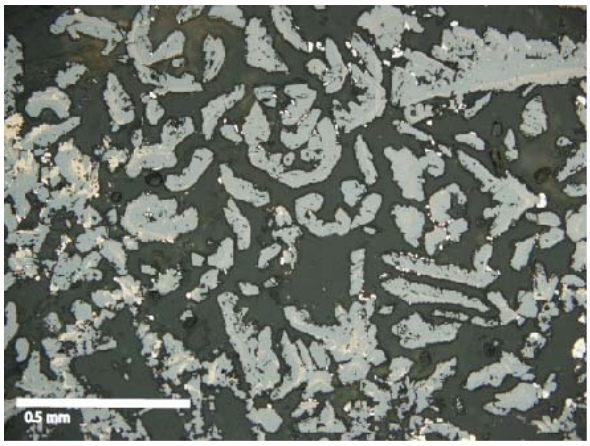

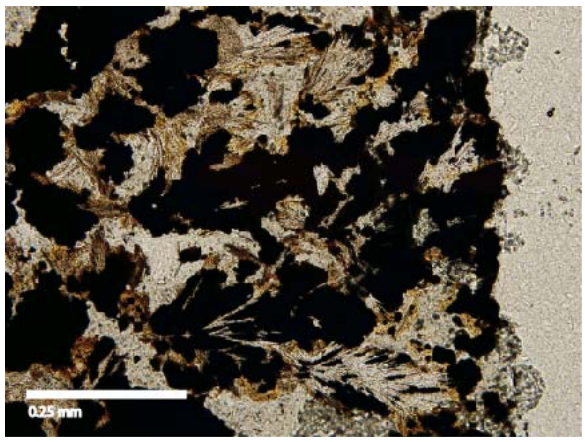

a. **b.**

Typical mineral textures from ALV2461-R6-4. a. RL, PPL, shows what appears to be skeletal sphalerite with chalcopyrite disease, and b. TL, PPL, shows barite needles growing among sulfides.

ALV 2464-R4

Geochemistry notes: 50% SiO_2, 25.4wt% MgO, Low CaO (0.11%).

This sample is from MEF contains many large barite crystals. Ba wt% not available but estimated at at least 25%.

The barite in this section resembles that of sample ALV 2463-R4-pc_EN32; the crystals are large (1 to 1.5mm) to small (<1 mm) blocky and elongate, and large tabular. Unlike other samples the barite crystals do not appear to have nucleated together from a specific site, nor are they oriented in any specific direction, but have grown randomly or rarely in a radial pattern. Some tabular crystals are zoned. A few twinned barite crystals are visible; although massive barite may twin due to deformation, twinning is generally not common.

A notable pyrite framboid occurs with barite needles growing from it. Any sulfides in this section are very small crystals of anhedral pyrite, and subhedral sphalerite, with no marcasite as in other sections. There section is highly porous where more sulfides are present. The sample appears to be held together by amorphous silica in the matrix.

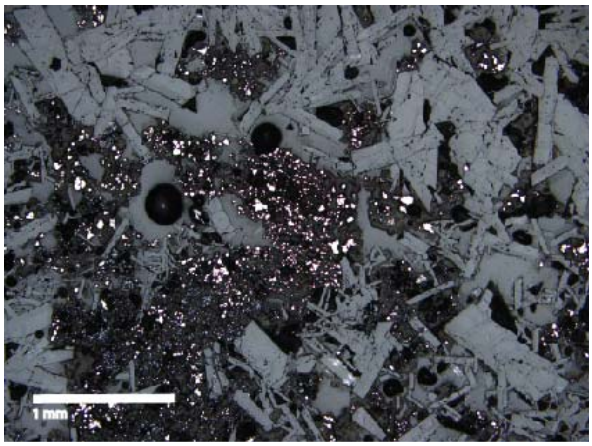

a.

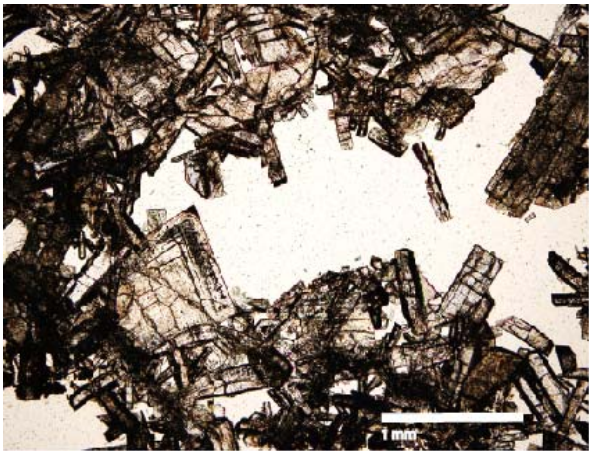

b.

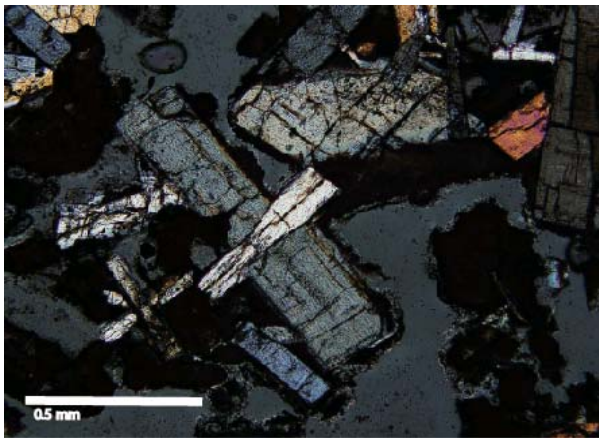

c.



d.

Typical mineral textures from ALV2464-R4. a. RL, PPL, shows blocky barite with small anhedral pyrite and sphalerite, b. TL, PPL, shows large, blocky, euhedral barite with the square crystal in the bottom left quadrant showing what may be zoning, c. TL, XL, shows what appears to be barite twinning, and d. TL, PPL, blocky barite growing radially from a common point.

ALV 4446_1735

Geochemistry notes: 1.19 wt% Ba, 10% Ca, 5% Fe, 10% Zn

This section mainly consists of fine intergrown sphalerite, marcasite and pyrite, with chalcopyrite occurring within the sphalerite. Dendritic sphalerite and fine dendritic pyrite are also present. Sphalerite crystals are generally small, and triangular in shape but still subhedral, although some larger crystals occur in one part of the section. Much of sphalerite is translucent green in TL. One open space is lined with large marcasite crystals, and there are small $AmSiO_2$ spheres abundantly occurring around all material.

Barite is disseminated among sulfides, with Fe stained $AmSiO_2$, and also occurs as small needles alone and in radial aggregates. Many of the needles are cloudy from sulfide inclusions. Small, low birefringent, tabular barite is also present.

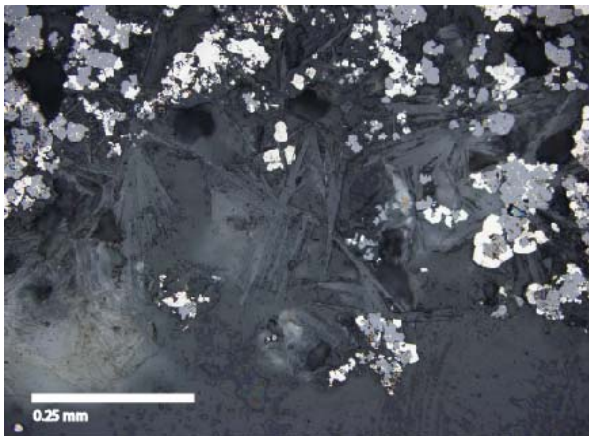

a.

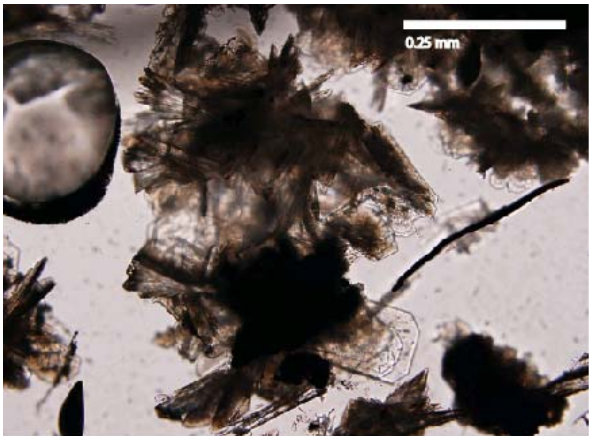

b.

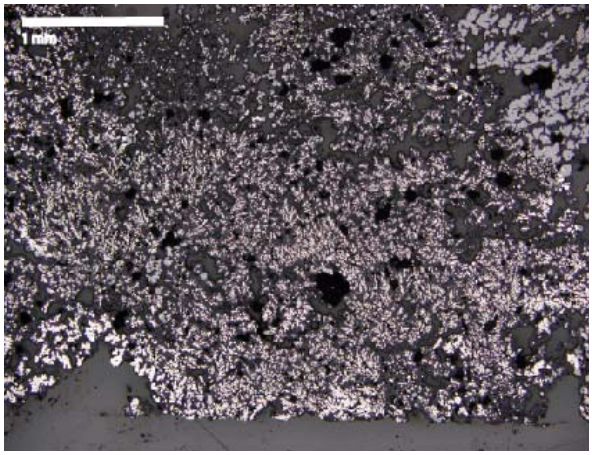

c.

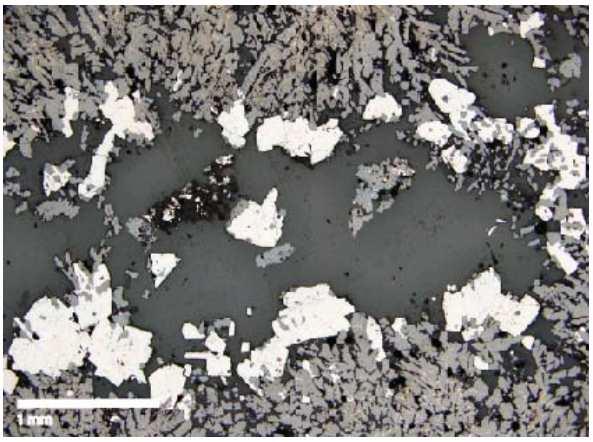

d.

Typical mineral textures from ALV4446-1735. a. RL, PPL, shows barite needles with subhedral pyrite (white) and sphalerite (grey) containing minor chalcopyrite disease, b. TL, PPL, shows very small tabular barite in the bottom right quadrant growing off pyrite, c. RL, PPL, shows very fine dendritic pyrite and subhedral sphalerite, and d. RL, PPL, shows dendritic sphalerite followed in growth by large, euhedral marcasite

Appendix D – Electron Microprobe Analysis Spot Locations



a.

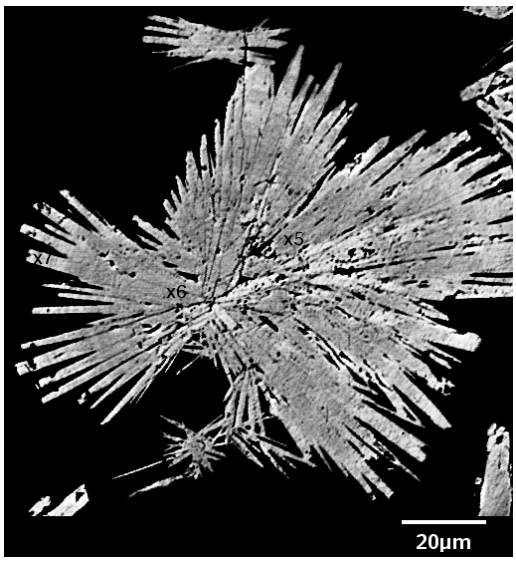

b.



c.

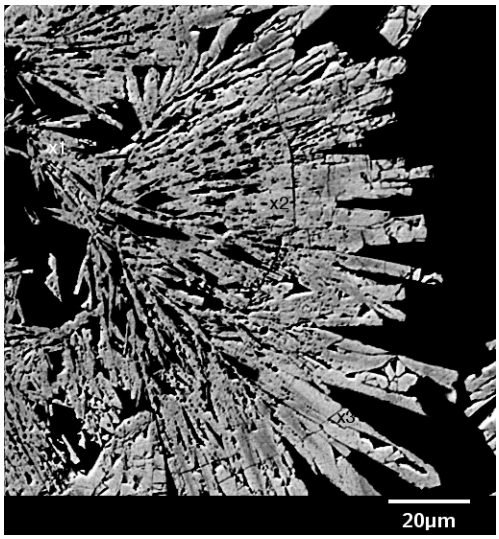

d.

a. Backscattered electron image of sample ALV-2072-7, displaying small and large acicular texture. Average Sr concentration for this sample is 7.3 wt.%. Average Sr/Ba for this sample is 0.09.

b. Second backscattered electron image of sample ALV-2072-7, also displaying acicular texture. Average Sr concentration for this sample is 7.3 wt.%. Average Sr/Ba for this sample is 0.09.

c. Backscattered electron image for sample ALV-2068-1, displaying fine acicular morphology. Average Sr for this sample is 10.0 wt.%. Average Sr/Ba for this sample is 0.12.

d. Backscattered electron image of sample ALV-3589-R2, displaying tabular to dendritic morphology. Average Sr for this sample is 3.6 wt.%. Average Sr/Ba for this sample is 0.04.

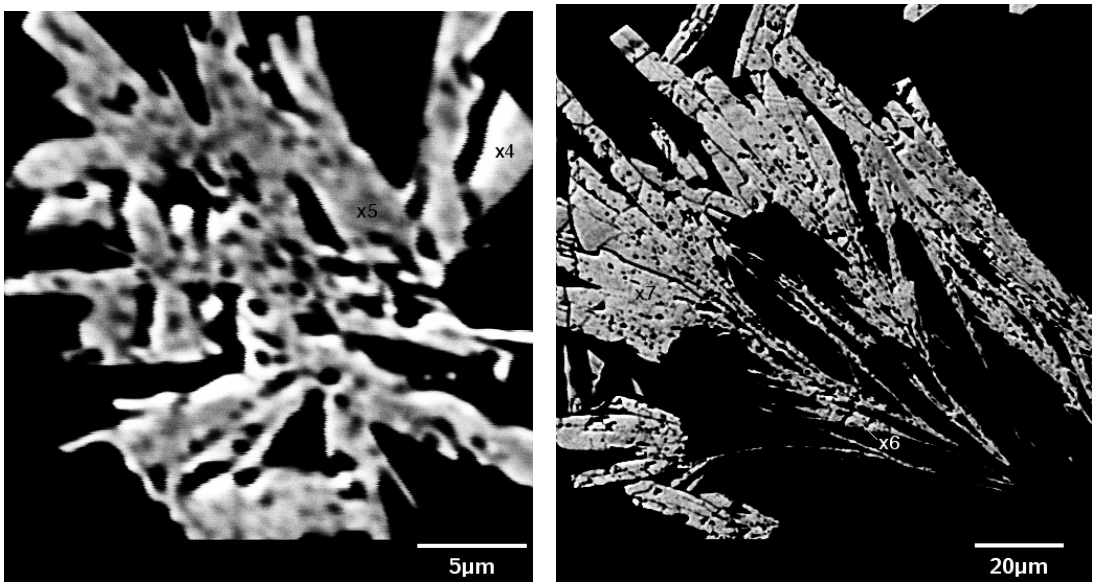

a. b.

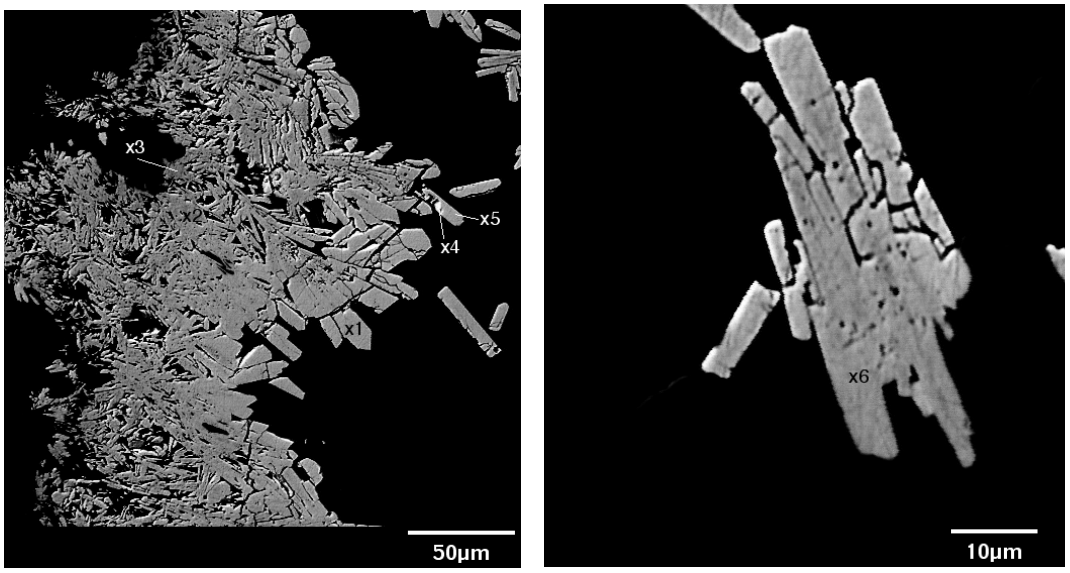

c. d.

a. Second backscattered electron image of sample ALV-3589-R2, displaying dendritic morphology. Average Sr for this sample is 3.6 wt.%. Average Sr/Ba for this sample is 0.04.

b. Third backscattered electron image of sample ALV-3589-R2, showing mostly tabular morphology with some very thin acicular needles. Average Sr for this sample is 3.6 wt.%. Average Sr/Ba for this sample is 0.04.

c. Backscattered electron image of sample TIVEY-MISC-2, displaying small tabular morphology. Average Sr in this sample is 3.1 wt.%. Average Sr/Ba for this sample is 0.03.

d. Second backscattered electron image of sample TIVEY-MISC-2, also showing small tabular morphology. Average Sr in this sample is 3.1 wt.%. Average Sr/Ba for this sample is 0.03.

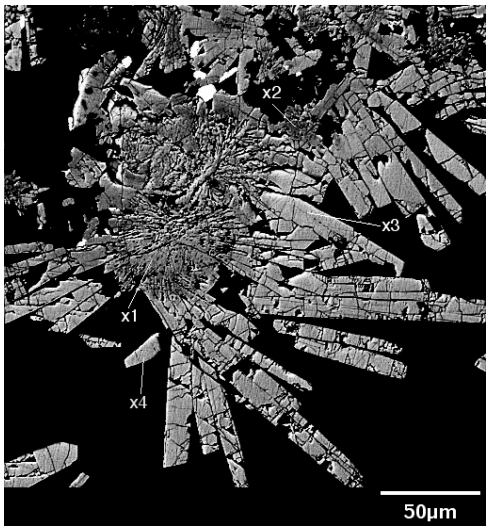

a.

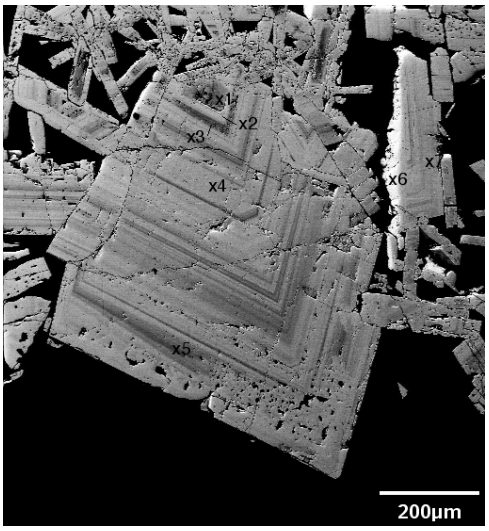

b.

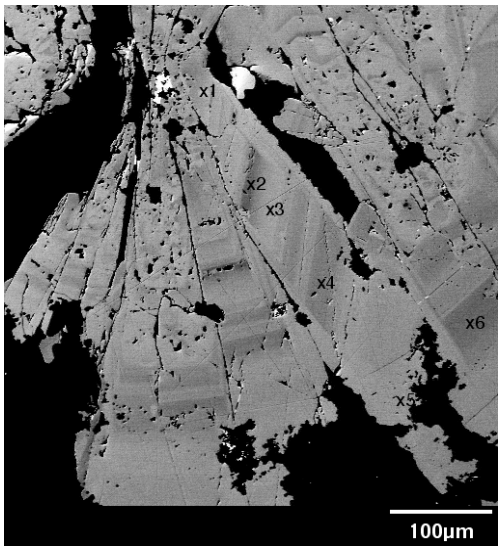

c.

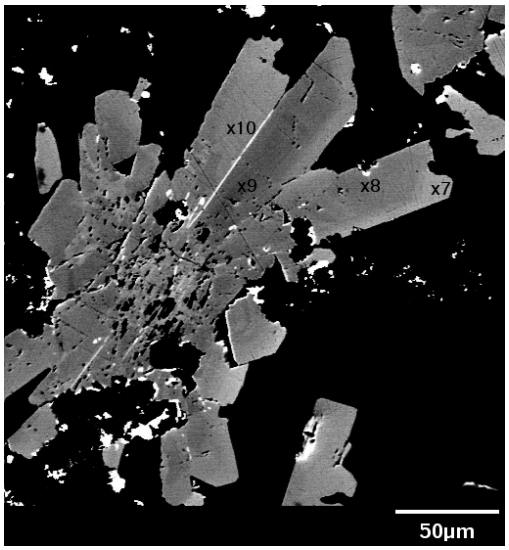

d.

a. Backscattered electron image for sample EN-16, displaying radiating blocky morphology. Average Sr for this sample is 4.0 wt.%. Average Sr/Ba for this sample is 0.04.
b. Backscattered electron image of sample ALV-2464-R4, displaying blocky morphology. Note the large size of the crystals, as well as the distinct zoning seen throughout. Average Sr for this sample is 6.1 wt.%. Average Sr/Ba for this sample is 0.07.
c. Backscattered electron image for sample ALV-2467-R2, displaying blocky morphology. Note some zonation, although not as distinct as in sample ALV-2464-R4. Average Sr for this sample is 4.8 wt.%. Average Sr/Ba for this sample is 0.05.
d. Second backscattered electron image for sample ALV 2467-R2, also showing blocky morphology. Average Sr for this sample is 4.8 wt.%. Average Sr/Ba for this sample is 0.05.

ALV 2072-7:

Location x1: $(Sr_{6.7},Ba_{86.7},Ca_{6.7})SO_4$

Location x2: $(Sr_{6.7},Ba_{86.7},Ca_{6.7})SO_4$

Location x3: $(Sr_{8.9},Ba_{84.4},Ca_{6.7})SO_4$

Location x4: $(Sr_{8.9},Ba_{84.4},Ca_{6.7})SO_4$

Location x5: $(Sr_{6.7},Ba_{88.9},Ca_{04.4})SO_4$

Location x6: $(Sr_{6.7},Ba_{86.7},Ca_{6.7})SO_4$

Location x7: $(Sr_{6.7},Ba_{84.4},Ca_{6.7})SO_4$

ALV 3589-R2:

Location x1: $(Sr_{4.6},Ba_{95.5},Ca_{0.0})SO_4$

Location x2: $(Sr_{2.3},Ba_{97.7},Ca_{0.0})SO_4$

Location x3: $(Sr_{0.0},Ba_{100.0},Ca_{0.0})SO_4$

Location x4: $(Sr_{4.6},Ba_{95.5},Ca_{0.0})SO_4$

Location x5: $(Sr_{7.0},Ba_{93.0},Ca_{0.0})SO_4$

Location x6: $(Sr_{4.7},Ba_{95.4},Ca_{0.0})SO_4$

Location x7: $(Sr_{2.3},Ba_{97.7},Ca_{0.0})SO_4$

ALV 2467-R2

Location x1: $(Sr_{4.6},Ba_{95.5})SO_4$

Location x2: $(Sr_{9.1},Ba_{90.9})SO_4$

Location x3: $(Sr_{2.3},Ba_{97.7})SO_4$

Location x4: $(Sr_{4.7},Ba_{95.4})SO_4$

Location x5: $(Sr_{2.3},Ba_{97.7})SO_4$

Location x6: $(Sr_{6.82},Ba_{93.18})SO_4$

ALV 2068-1:

Location x1: $(Sr_{2.3},Ba_{97.7},Ca_{0.0})SO_4$

Location x2: $(Sr_{10.9},Ba_{78.3},Ca_{10.9})SO_4$

Location x3: $(Sr_{17.8},Ba_{80.0},Ca_{2.2})SO_4$

Location x4: $(Sr_{9.1},Ba_{88.6},Ca_{2.3})SO_4$

EN-16

Location 1: $(Sr_{4.6},Ba_{95.5},Ca_{0.0})SO_4$

Location 2: $(Sr_{7.0},Ba_{93.0},Ca_{0.0})SO_4$

Location 3: $(Sr_{2.3},Ba_{97.7},Ca_{0.0})SO_4$

Location 4: $(Sr_{2.3},Ba_{97.7},Ca_{0.0})SO_4$

Tivey Misc-2:

Location x1: $(Sr_{2.3},Ba_{97.7},Ca_{0.0})SO_4$

Location x2: $(Sr_{4.6},Ba_{95.5},Ca_{0.0})SO_4$

Location x3: $(Sr_{4.6},Ba_{95.5},Ca_{0.0})SO_4$

Location x4: $(Sr_{2.4},Ba_{97.6},Ca_{0.0})SO_4$

Location x5: $(Sr_{2.3},Ba_{97.7},Ca_{0.0})SO_4$

Location x6: $(Sr_{2.3}Ba_{97.7}Ca_{0.0})SO_4$

ALV 2464-R4

Location 1: $(Sr_{6.8},Ba_{90.9},Ca_{2.3})SO_4$

Location 2: $(Sr_{2.3},Ba_{97.7},Ca_{0.0})SO_4$

Location 3: $(Sr_{13.3},Ba_{82.2},Ca_{4.4})SO_4$

Location 4: $(Sr_{4.6},Ba_{95.5},Ca_{0.0})SO_4$

Location 5: $(Sr_{11.4},Ba_{88.6},Ca_{0.0})SO_4$

Location 6: $(Sr_{0.0},Ba_{100.0},Ca_{0.0})SO_4$

Location 7: $(Sr_{4.7},Ba_{95.4},Ca_{0.0})SO_4$

APPENDIX E – Locations and sizes of sulfide edifices along the Endeavour Segment

Number	Longitude	Lattitude	Depth (bottom) (mbsl)	Depth (top) (mbsl)	Height (m)	Footprint (m^2)	Volume (m^3)	Description	Vent Field
1	-129.065092	48.001428	2170	2156	14	88.2	561.2	vent	
2	-129.065086	48.001426	2171	2164	7	74.8	124.2	vent	
3	-129.065278	48.001130	2172	2164	8	209.2	59.5	vent	
4	-129.064536	48.000833	2168	2165	3	146.4	299.8	vent	
5	-129.065354	48.000803	2170	2164	6	148.2	424.5	vent	
6	-129.064669	48.000722	2159	2152	7	44.8	822.0	vent	
7	-129.063462	47.999936	2166	2159	7	80.9	96.5	vent	
8	-129.063230	47.999933	2165	2159	6	60.1	93.1	vent	
9	-129.063360	47.999766	2162	2156	6	139.2	179.9	vent	
10	-129.066258	47.999535	2178	2172	6	38.9	72.7	vent	
11	-129.062671	47.998914	2178	2171	7	95.7	180.4	vent	
12	-129.065879	47.998810	2161	2153	8	122.1	458.2	vent	
13	-129.062564	47.998622	2188	2180	8	109.5	1978.9	vent	
14	-129.064324	47.998601	2179	2172	7	150.3	223.2	vent	
15	-129.062242	47.998581	2178	2173	5	232.3	226.5	vent	
16	-129.061038	47.998307	2156	2149	7	62.7	60.6	mound	
17	-129.061219	47.998203	2150	2146	4	117.5	122.3	mound	
18	-129.062286	47.998199	2177	2165	12	45.4	64.4	vent	
19	-129.062019	47.998181	2156	2151	5	28.1	88.8	vent	
20	-129.061713	47.997950	2148	2144	4	144.7	200.6	vent	
21	-129.065882	47.997930	2129	2125	4	82.0	66.2	vent	
22	-129.063334	47.997563	2165	2153	12	103.7	282.2	vent	
23	-129.062470	47.997283	2160	2158	3	47.0	43.6	vent	
24	-129.064818	47.997214	2171	2164	7	252.2	561.8	vent	
25	-129.066756	47.996932	2232	2226	6	89.9	157.8	vent	Sasquatch
26	-129.065703	47.996513	2159	2151	8	142.2	279.4	vent	Sasquatch
27	-129.065635	47.996397	2163	2158	5	46.3	113.4	vent	Sasquatch
28	-129.068299	47.996377	2171	2167	4	232.6	127.0	vent	
29	-129.066767	47.996006	2154	2148	6	998.8	56.0	mound	Sasquatch
30	-129.068600	47.995977	2147	2130	17	25.8	277.8	vent	
31	-129.063488	47.995622	2161	2154	7	115.6	108.8	vent	
32	-129.067078	47.995538	2167	2163	4	35.4	69.5	vent	
33	-129.067470	47.995447	2151	2146	4	82.1	97.3	vent	
34	-129.067872	47.995416	2152	2141	11	243.3	500.9	mound	Sasquatch
35	-129.064579	47.995395	2157	2151	6	38.3	90.4	vent	
36	-129.065225	47.995350	2162	2151	11	125.0	344.6	vent	
37	-129.065506	47.995340	2156	2147	9	71.5	105.6	vent	
38	-129.064843	47.995264	2144	2132	12	37.2	3660.6	mound	
39	-129.065149	47.995240	2157	2150	7	156.8	284.9	vent	
40	-129.065332	47.995216	2163	2151	12	90.8	355.8	vent	
41	-129.065490	47.995119	2152	2148	4	97.8	43.0	vent	
42	-129.065255	47.995068	2163	2150	13	146.9	623.0	vent	
43	-129.065535	47.995038	2160	2151	9	31.6	397.0	vent	
44	-129.068271	47.995011	2147	2136	11	1353.9	4009.4	vent	

45	-129.064629	47.994775	2152	2149	3	43.0	44.6	mound	
46	-129.063168	47.994631	2149	2141	8	292.0	429.0	vent	
47	-129.069548	47.993950	2161	2154	7	50.0	96.5	vent	
48	-129.066123	47.993588	2147	2139	8	617.1	1874.9	mound	
49	-129.067540	47.992982	2150	2140	10	70.9	157.2	vent	
50	-129.071043	47.990606	2128	2124	4	24.2	122.7	vent	
51	-129.079042	47.990567	2347	2335	12	116.3	64.4	vent	
52	-129.074979	47.990293	2123	2113	10	124.8	541.4	vent	
53	-129.072333	47.989011	2154	2149	5	142.9	141.5	mound	
54	-129.078845	47.988337	2145	2137	8	63.5	229.5	vent	
55	-129.074967	47.987233	2165	2155	10	289.6	1215.5	vent	
56	-129.075142	47.987210	2164	2158	7	83.2	105.8	vent	
57	-129.074766	47.987063	2165	2153	12	117.6	357.6	vent	
58	-129.075066	47.987063	2163	2155	8	45.0	120.7	vent	
59	-129.075307	47.987023	2164	2157	7	37.3	113.3	vent	
60	-129.071730	47.986936	2146	2129	17	89.9	363.2	vent	
61	-129.071801	47.986847	2146	2141	5	67.2	91.5	vent	
62	-129.071895	47.986764	2148	2136	12	60.0	113.7	vent	
63	-129.072062	47.986612	2145	2129	16	239.2	632.6	vent	
64	-129.075127	47.986506	2164	2156	8	57.0	127.2	vent	
65	-129.070926	47.986276	2143	2135	8	84.1	177.7	vent	
66	-129.072740	47.985553	2144	2136	8	205.2	612.0	mound	
67	-129.076632	47.985507	2152	2141	11	44.1	172.3	vent	
68	-129.071738	47.985438	2129	2125	5	66.4	140.6	vent	
69	-129.071167	47.985405	2128	2118	10	85.0	175.4	vent	
70	-129.072813	47.985370	2145	2134	11	402.5	1003.7	mound	
71	-129.071408	47.985328	2132	2126	6	31.3	33.4	vent	
72	-129.072126	47.985172	2153	2142	11	130.6	274.4	vent	
73	-129.072502	47.985114	2136	2128	8	34.8	56.9	vent	
74	-129.073156	47.984880	2166	2153	13	114.6	179.5	vent	
75	-129.073270	47.984724	2147	2130	17	119.5	291.5	vent	
76	-129.073365	47.984472	2149	2143	6	39.3	43.1	vent	
77	-129.073512	47.984419	2150	2145	5	74.2	67.1	vent	
78	-129.072912	47.983282	2262	2250	12	47.2	177.7	vent	
79	-129.074276	47.983174	2158	2152	6	177.3	818.0	vent	
80	-129.075506	47.982933	2153	2134	19	434.7	1499.2	vent	Salty Dawg
81	-129.075615	47.982771	2146	2135	11	412.6	1595.6	vent	Salty Dawg
82	-129.075681	47.982513	2150	2136	14	264.3	681.2	vent	Salty Dawg
83	-129.080239	47.982429	2135	2128	7	74.3	136.6	vent	
84	-129.084752	47.982392	2151	2143	8	22.2	119.1	vent	
85	-129.074795	47.982339	2155	2149	6	26.1	64.7	vent	Salty Dawg
86	-129.079650	47.982330	2126	2115	11	72.9	115.2	vent	
87	-129.080337	47.982320	2137	2121	16	45.2	117.5	vent	
88	-129.075614	47.982253	2201	2196	5	569.4	133.9	vent	
89	-129.079677	47.982250	2131	2125	6	49.3	99.7	vent	
90	-129.076372	47.982233	2158	2139	19	179.4	722.9	vent	Salty Dawg
91	-129.075127	47.982219	2152	2136	16	357.6	1192.0	mound	Salty Dawg
92	-129.072726	47.982199	2106	2097	9	174.7	446.2	vent	
93	-129.078480	47.982171	2134	2117	17	104.5	433.1	vent	
94	-129.079834	47.982072	2145	2132	13	31.3	132.3	vent	

95	-129.079976	47.982064	2131	2121	10	82.8	142.2	vent	
96	-129.076380	47.981943	2161	2157	4	24.4	25.4	vent	
97	-129.076546	47.981940	2160	2154	7	190.5	309.7	mound	Salty Dawg
98	-129.075313	47.981926	2151	2134	17	1981.1	17785.7	mound	Salty Dawg
99	-129.075988	47.981866	2154	2147	7	59.7	101.0	vent	Salty Dawg
100	-129.074563	47.981864	2150	2142	8	84.1	166.8	vent	Salty Dawg
101	-129.076099	47.981849	2156	2151	5	38.3	37.4	vent	
102	-129.076388	47.981727	2163	2160	3	22.4	17.8	vent	Salty Dawg
103	-129.076476	47.981657	2163	2158	5	84.0	109.2	mound	Salty Dawg
104	-129.075283	47.981631	2133	2124	9	66.7	66.2	vent	Salty Dawg
105	-129.081020	47.981336	2132	2125	7	28.3	84.4	vent	
106	-129.075829	47.981298	2161	2152	9	54.2	74.2	vent	Salty Dawg
107	-129.078363	47.981184	2153	2145	8	8.7	20.5	vent	
108	-129.077391	47.980897	2155	2147	8	150.4	297.7	mound	
109	-129.077289	47.980591	2164	2153	11	100.9	157.5	vent	
110	-129.076994	47.980502	2170	2164	6	206.3	113.2	vent	
111	-129.079522	47.980239	2140	2137	3	38.8	28.9	vent	
112	-129.079704	47.980237	2140	2130	10	40.4	75.4	vent	
113	-129.076896	47.980186	2161	2140	21	58.6	1254.3	vent	
114	-129.079801	47.980165	2141	2134	7	26.9	45.3	vent	
115	-129.078881	47.980055	2147	2142	5	136.5	201.6	mound	
116	-129.079378	47.979991	2142	2136	6	175.2	275.8	mound	
117	-129.079075	47.979988	2146	2139	7	198.4	330.8	mound	
118	-129.078597	47.979952	2146	2142	4	160.8	314.7	mound	
119	-129.079057	47.979848	2147	2140	7	36.4	75.6	vent	
120	-129.077269	47.979840	2147	2133	14	410.9	1038.2	vent	
121	-129.077768	47.979833	2166	2160	6	86.4	47.1	vent	
122	-129.078575	47.979770	2149	2143	6	81.1	354.0	vent	
123	-129.076687	47.979750	2172	2166	6	143.4	234.9	vent	
124	-129.077789	47.979740	2166	2160	6	75.3	83.1	vent	
125	-129.077315	47.979451	2150	2145	5	152.8	162.3	vent	
126	-129.078536	47.979390	2169	2163	6	118.3	121.7	mound	
127	-129.081773	47.979367	2142	2131	11	50.5	81.2	vent	
128	-129.077405	47.979330	2153	2147	6	70.8	107.1	vent	
129	-129.078369	47.978882	2140	2129	11	92.6	2767.7	vent	
130	-129.081906	47.978429	2144	2133	11	62.8	127.2	vent	
131	-129.086184	47.978243	2135	2128	7	95.9	308.2	vent	
132	-129.082134	47.977971	2146	2131	15	298.5	920.8	vent	
133	-129.083949	47.977752	2149	2134	15	70.1	280.9	vent	
134	-129.087633	47.977628	2136	2130	6	76.8	114.7	mound	
135	-129.082501	47.977477	2155	2144	11	295.3	782.5	vent	
136	-129.080308	47.976911	2147	2143	4	180.0	239.1	mound	
137	-129.080650	47.976761	2149	2144	5	20.1	50.3	vent	
138	-129.080873	47.976634	2145	2136	9	174.6	503.4	vent	
139	-129.080747	47.976558	2146	2140	6	92.9	162.3	vent	
140	-129.080763	47.976472	2147	2140	7	85.8	146.5	vent	
141	-129.079291	47.976259	2157	2150	7	237.7	647.5	mound	
142	-129.081070	47.976106	2141	2117	24	126.9	890.4	vent	
143	-129.079440	47.976094	2157	2149	8	127.4	182.4	vent	
144	-129.079794	47.976030	2158	2153	5	192.4	169.6	vent	

145	-129.081057	47.976012	2140	2125	15	126.1	758.5	vent	Marias
146	-129.079578	47.976002	2156	2148	8	173.0	479.0	vent	
147	-129.088356	47.975687	2130	2116	14	174.1	749.4	vent	
148	-129.087588	47.975294	2139	2128	11	229.5	681.5	vent	
149	-129.089592	47.974398	2143	2132	11	22.6	48.8	vent	
150	-129.089665	47.974296	2134	2123	11	72.5	146.6	vent	
151	-129.089470	47.974200	2141	2132	9	67.7	844.7	vent	
152	-129.089368	47.974082	2177	2171	6	258.5	527.1	mound	
153	-129.081813	47.973002	2151	2143	8	40.9	127.3	vent	
154	-129.082198	47.972904	2152	2142	10	173.6	213.9	vent	
155	-129.082323	47.972856	2155	2146	9	46.4	107.3	vent	
156	-129.082023	47.972612	2149	2142	7	1236.7	5211.7	mound	
157	-129.089128	47.972529	2146	2136	10	20.7	13.4	vent	
158	-129.082252	47.972364	2156	2142	14	218.0	443.1	vent	
159	-129.089254	47.972077	2142	2136	6	80.4	58.8	vent	
160	-129.088836	47.971403	2120	2114	6	30.6	43.9	vent	
161	-129.089286	47.971217	2124	2114	10	710.8	190.8	vent	
162	-129.086439	47.970764	2170	2165	5	79.7	270.1	vent	
163	-129.082902	47.970688	2168	2164	4	72.9	65.8	vent	
164	-129.086254	47.970680	2158	2152	6	27.0	43.0	vent	
165	-129.089518	47.970641	2143	2134	9	1997.4	3460.7	vent	
166	-129.086492	47.970574	2168	2164	3	180.6	345.7	vent	
167	-129.087818	47.970231	2169	2165	4	149.2	17.9	vent	
168	-129.087880	47.970098	2163	2159	4	36.8	158.0	vent	
169	-129.088088	47.969974	2164	2156	8	160.3	176.6	vent	
170	-129.087200	47.969376	2167	2163	4	37.5	76.3	vent	High Rise
171	-129.088299	47.969269	2165	2160	5	160.8	83.2	vent	
172	-129.086251	47.969169	2151	2146	5	198.1	82.8	vent	High Rise
173	-129.086974	47.969098	2155	2144	11	30.3	75.3	vent	
174	-129.087669	47.969004	2174	2166	8	43.8	91.9	vent	High Rise
175	-129.087598	47.968813	2161	2152	9	263.5	729.9	vent	High Rise
176	-129.087828	47.968804	2172	2167	5	61.6	85.4	vent	High Rise
177	-129.088018	47.968793	2167	2157	10	47.4	242.1	vent	High Rise
178	-129.087067	47.968741	2164	2155	9	306.8	72.5	vent	High Rise
179	-129.087381	47.968733	2125	2116	9	139.3	1123.7	vent	High Rise
180	-129.087581	47.968683	2165	2158	7	25.2	41.5	vent	High Rise
181	-129.087711	47.968679	2168	2158	10	28.8	74.3	vent	High Rise
182	-129.087627	47.968631	2156	2136	20	29.4	1130.8	vent	High Rise
183	-129.087452	47.968416	2154	2127	27	1100.5	3405.5	vent	High Rise
184	-129.087760	47.968323	2166	2153	13	67.7	1287.1	vent	High Rise
185	-129.088291	47.968295	2175	2165	10	121.1	322.2	vent	High Rise
186	-129.087511	47.968283	2154	2141	13	207.6	448.9	vent	High Rise
187	-129.087942	47.968206	2174	2168	6	85.5	289.9	vent	High Rise
188	-129.088317	47.968115	2137	2130	7	531.2	147.0	mound	
189	-129.087471	47.967925	2171	2164	7	270.2	472.5	vent	High Rise
190	-129.088432	47.967837	2171	2166	5	87.7	87.5	vent	High Rise
191	-129.089426	47.967744	2174	2168	6	1423.2	210.2	mound	
192	-129.088486	47.967736	2173	2165	8	18.9	161.3	vent	
193	-129.088802	47.967718	2175	2172	3	139.0	39.1	vent	
194	-129.089876	47.967578	2179	2174	5	24.2	37.3	vent	

195	-129.088964	47.967535	2174	2169	5	73.7	133.0	vent	
196	-129.092447	47.967354	2171	2166	5	7.5	61.1	vent	
197	-129.086904	47.967254	2178	2175	3	30.3	1.7	vent	
198	-129.088827	47.967251	2176	2167	9	132.2	304.1	vent	
199	-129.091535	47.967230	2140	2134	6	30.3	4.0	vent	
200	-129.089672	47.967224	2169	2157	12	66.9	4322.6	vent	
201	-129.089353	47.967216	2177	2165	12	27.7	51.2	vent	
202	-129.089859	47.967159	2180	2167	13	30.9	199.1	vent	
203	-129.091474	47.967150	2178	2175	3	31.5	3.5	vent	
204	-129.088152	47.967110	2235	2224	11	270.9	135.1	vent	High Rise
205	-129.088377	47.966969	2150	2128	22	133.6	1805.8	vent	High Rise
206	-129.088668	47.966897	2157	2142	15	79.3	873.1	vent	High Rise
207	-129.090127	47.966718	2174	2168	6	331.5	96.0	vent	
208	-129.089236	47.966410	2164	2152	12	158.0	1049.0	vent	
209	-129.092643	47.966170	2148	2130	18	56.6	18715.1	vent	
210	-129.087717	47.965952	2166	2153	13	57.5	231.9	vent	High Rise
211	-129.088508	47.965918	2158	2139	19	67.0	3634.2	vent	High Rise
212	-129.087992	47.965772	2163	2154	9	129.7	164.2	vent	High Rise
213	-129.088504	47.965738	2159	2142	17	227.0	653.1	mound	High Rise
214	-129.088255	47.965577	2168	2150	18	703.8	1742.4	vent	High Rise
215	-129.087830	47.965576	2182	2177	5	81.9	179.9	vent	High Rise
216	-129.090572	47.965207	2180	2174	6	84.6	101.4	vent	
217	-129.088722	47.965185	2175	2157	18	603.9	248.3	mound	High Rise
218	-129.088691	47.964698	2158	2153	5	73.2	267.5	mound	High Rise
219	-129.089273	47.964629	2073	2066	7	231.0	506.0	mound	High Rise
220	-129.091053	47.964295	2169	2162	7	40.7	233.7	vent	
221	-129.090618	47.964286	2178	2174	4	53.8	92.4	vent	
222	-129.094902	47.964285	2193	2188	5	350.0	70.7	vent	
223	-129.093800	47.964285	2142	2132	10	174.4	840.9	vent	
224	-129.090624	47.964282	2177	2172	5	63.2	101.7	vent	
225	-129.091122	47.964220	2162	2150	12	20.1	898.2	vent	
226	-129.088824	47.964186	2193	2189	4	54.9	45.1	vent	
227	-129.090716	47.964112	2177	2169	8	390.4	655.3	mound	
228	-129.088587	47.964063	2190	2186	4	451.1	635.4	mound	
229	-129.089027	47.964031	2191	2187	4	29.2	103.8	vent	
230	-129.093888	47.963821	2141	2132	9	293.7	318.2	vent	
231	-129.093037	47.963669	2130	2122	8	180.8	48.6	vent	
232	-129.088812	47.963481	2178	2170	8	21.2	85.3	vent	
233	-129.093984	47.963433	2130	2113	17	260.4	2800.2	vent	
234	-129.098691	47.963016	2076	2066	10	186.4	303.6	vent	
235	-129.095779	47.962975	2138	2128	10	87.2	1123.3	vent	
236	-129.085245	47.962914	2181	2177	4	43.2	39.4	vent	
237	-129.098845	47.962675	2073	2065	8	493.6	1434.7	mound	
238	-129.098753	47.961314	2084	2077	7	39.9	469.5	vent	
239	-129.083019	47.960799	2111	2106	5	192.4	472.8	mound	
240	-129.083244	47.960494	2111	2101	10	1153.9	5494.4	mound	
241	-129.083829	47.959840	2176	2163	13	260.6	857.8	mound	
242	-129.084781	47.959606	2110	2104	6	950.9	372.6	mound	
243	-129.084239	47.959435	2109	2101	8	817.2	2134.2	mound	
244	-129.094541	47.959085	2179	2169	10	53.2	65.7	vent	

245	-129.099856	47.959046	2183	2167	16	17.8	1002.3	vent	
246	-129.084256	47.959026	2112	2101	11	1492.6	4973.0	mound	
247	-129.083961	47.958931	2194	2189	5	126.2	192.8	vent	
248	-129.091788	47.958729	2174	2163	11	42.8	192.2	vent	
249	-129.084100	47.958723	2140	2129	11	246.8	173.6	vent	
250	-129.091803	47.958645	2126	2121	5	68.2	68.5	vent	
251	-129.087089	47.958573	2143	2137	6	49.5	61.0	vent	
252	-129.087448	47.958445	2139	2129	10	17.5	35.7	vent	
253	-129.099175	47.958434	2081	2076	5	58.0	38.3	vent	
254	-129.087770	47.958163	2112	2106	6	9.6	488.3	mound	
255	-129.087685	47.958140	2145	2139	6	40.4	10.5	vent	
256	-129.096973	47.958030	2144	2139	5	17.1	32.4	vent	
257	-129.087625	47.957758	2195	2182	13	546.7	382.7	vent	
258	-129.101500	47.957712	2072	2067	5	293.1	130.3	vent	
259	-129.085161	47.956919	2089	2063	26	6498.3	52535.2	mound	Sweetland
260	-129.097723	47.956478	2137	2133	4	21.7	35.1	vent	
261	-129.103872	47.956422	2069	2062	7	290.0	732.6	vent	
262	-129.097698	47.956340	2138	2128	10	66.3	213.7	vent	
263	-129.097580	47.956338	2136	2129	7	74.7	93.3	vent	
264	-129.097164	47.956308	2136	2128	8	57.3	794.0	vent	
265	-129.098037	47.956277	2141	2135	6	485.3	183.1	mound	
266	-129.094323	47.956192	2182	2172	10	98.3	230.1	vent	
267	-129.094689	47.956161	2171	2165	6	543.2	249.8	mound	
268	-129.098314	47.956148	2134	2128	6	741.4	441.8	vent	
269	-129.092528	47.956111	2191	2183	8	128.2	212.1	vent	
270	-129.097469	47.956110	2136	2130	6	469.8	1115.7	mound	
271	-129.098722	47.956065	2151	2145	6	75.4	171.4	vent	
272	-129.096706	47.955958	2178	2172	6	31.2	128.9	vent	
273	-129.097425	47.955924	2136	2131	5	52.5	59.9	vent	
274	-129.093866	47.955865	2194	2186	8	324.3	632.5	vent	
275	-129.104082	47.955809	2077	2068	9	115.8	296.1	vent	
276	-129.096953	47.955795	2161	2157	4	13.4	24.4	vent	
277	-129.092740	47.955660	2197	2175	22	228.2	540.3	vent	
278	-129.095512	47.955454	2187	2178	9	60.2	186.7	vent	
279	-129.096530	47.955388	2156	2151	5	1835.0	4370.8	mound	
280	-129.094036	47.955339	2197	2185	12	481.3	2738.9	vent	
281	-129.095984	47.955236	2163	2158	5	22.7	409.5	vent	
282	-129.094809	47.955165	2135	2126	9	111.2	465.7	vent	
283	-129.096163	47.955135	2190	2182	8	109.7	658.7	vent	MEF
284	-129.094600	47.955083	2191	2185	6	60.6	197.0	vent	
285	-129.103489	47.955073	2077	2074	3	107.4	101.3	vent	
286	-129.103579	47.954985	2075	2069	6	116.6	256.4	vent	
287	-129.094636	47.954972	2198	2185	13	110.0	311.4	vent	
288	-129.103966	47.954920	2064	2059	5	25.4	44.8	vent	
289	-129.094378	47.954867	2198	2192	6	371.4	801.3	vent	
290	-129.094455	47.954722	2159	2156	3	61.3	29.8	vent	
291	-129.094685	47.954143	2194	2188	6	87.9	174.3	vent	
292	-129.089575	47.954095	2143	2139	4	44.7	39.0	vent	
293	-129.096414	47.954085	2202	2197	5	277.6	81.0	vent	
294	-129.090330	47.953582	2142	2137	5	25.1	188.0	vent	

295	-129.090405	47.953493	2200	2192	8	84.2	126.0	vent	
296	-129.096713	47.953326	2167	2161	6	19.7	30.7	vent	
297	-129.096783	47.952855	2168	2164	4	11.1	10.5	vent	
298	-129.100497	47.952791	2124	2121	3	40.9	35.3	vent	
299	-129.097854	47.952586	2165	2160	5	94.2	153.4	vent	
300	-129.099361	47.952346	2161	2155	6	47.2	155.8	vent	
301	-129.099202	47.952251	2157	2153	3	35.8	41.5	vent	
302	-129.089979	47.952231	2135	2130	5	36.2	79.1	vent	
303	-129.099474	47.952165	2165	2157	8	88.2	254.4	vent	
304	-129.090187	47.952109	2139	2131	8	121.0	749.8	vent	
305	-129.090063	47.952106	2144	2138	6	81.0	84.4	vent	
306	-129.098108	47.951372	2181	2173	8	82.3	177.9	vent	MEF
307	-129.096568	47.950987	2205	2197	8	29.7	84.4	vent	MEF
308	-129.096616	47.950887	2205	2199	6	40.1	91.7	vent	MEF
309	-129.083071	47.950830	2136	2132	4	405.0	55.0	mound	
310	-129.083533	47.950649	2106	2101	5	154.1	477.8	vent	
311	-129.097844	47.950517	2190	2183	7	602.6	2158.6	vent	MEF
312	-129.091689	47.950478	2188	2177	11	167.2	1363.5	vent	
313	-129.087259	47.950421	2106	2102	4	178.1	144.6	vent	
314	-129.086860	47.950365	2113	2106	7	183.9	797.6	vent	
315	-129.086900	47.950226	2107	2101	6	192.9	256.8	vent	
316	-129.097059	47.950181	2194	2178	16	300.3	1432.2	vent	MEF
317	-129.096946	47.949763	2203	2193	10	298.6	780.8	vent	MEF
318	-129.097711	47.949663	2190	2168	22	452.2	914.1	vent	MEF
319	-129.098464	47.949554	2076	2068	8	283.2	79.6	vent	MEF
320	-129.097915	47.949330	2189	2166	23	823.4	3571.9	vent	MEF
321	-129.098686	47.949322	2189	2176	13	116.2	550.8	vent	MEF
322	-129.097073	47.949317	2207	2194	13	131.1	352.5	vent	MEF
323	-129.098492	47.949214	2111	2102	9	566.9	233.5	vent	
324	-129.096868	47.949167	2208	2199	9	475.3	847.1	vent	MEF
325	-129.097186	47.949148	2184	2180	4	87.4	448.1	vent	MEF
326	-129.097358	47.949069	2203	2191	12	196.1	224.2	vent	MEF
327	-129.099226	47.949060	2187	2179	8	60.2	162.2	vent	MEF
328	-129.097603	47.949027	2197	2184	13	255.0	905.3	vent	MEF
329	-129.097100	47.948919	2207	2201	6	71.4	361.0	vent	MEF
330	-129.097283	47.948716	2169	2148	21	222.2	753.2	vent	MEF
331	-129.107854	47.948641	2135	2115	20	78.1	293.9	vent	
332	-129.085628	47.948627	2103	2095	8	59.5	141.9	vent	
333	-129.086164	47.948525	2109	2101	8	46.8	1707.0	vent	
334	-129.107778	47.948401	2076	2070	6	148.2	344.4	vent	
335	-129.098588	47.948038	2143	2134	9	105.6	255.8	vent	MEF
336	-129.097848	47.948022	2205	2197	8	300.8	295.6	vent	MEF
337	-129.097577	47.947927	2206	2191	15	1213.4	3787.5	mound	MEF
338	-129.099576	47.947905	2191	2181	10	55.9	94.8	vent	MEF
339	-129.087320	47.947884	2179	2168	11	45.8	60.3	vent	
340	-129.086866	47.947814	2107	2101	6	86.4	111.9	vent	
341	-129.099180	47.947805	2189	2172	17	1680.3	4220.0	mound	MEF
342	-129.086889	47.947697	2111	2106	5	51.8	1107.5	vent	
343	-129.086333	47.947644	2195	2185	10	47.6	135.6	vent	
344	-129.086652	47.947607	2125	2119	6	339.9	89.3	vent	

345	-129.098378	47.947558	2198	2189	9	435.0	649.1	vent	MEF
346	-129.086090	47.947524	2120	2108	12	97.8	475.8	vent	
347	-129.098813	47.947378	2187	2177	10	288.1	640.2	vent	MEF
348	-129.097989	47.947374	2201	2181	20	116.2	393.8	mound	MEF
349	-129.098332	47.947307	2199	2193	6	58.6	45.4	vent	MEF
350	-129.086372	47.947290	2118	2107	11	36.6	144.6	vent	
351	-129.086515	47.947238	2226	2217	9	104.7	365.9	vent	
352	-129.097779	47.947210	2207	2203	4	49.5	69.2	vent	MEF
353	-129.108375	47.947186	2153	2146	7	236.8	421.5	vent	
354	-129.098395	47.947149	2195	2187	8	452.5	828.3	vent	MEF
355	-129.086418	47.947145	2127	2122	5	40.7	68.9	vent	
356	-129.086509	47.947142	2115	2103	12	39.4	185.7	vent	
357	-129.086266	47.947089	2126	2122	4	25.5	24.1	vent	
358	-129.086700	47.946933	2128	2120	8	224.7	154.3	vent	
359	-129.098275	47.946897	2198	2191	7	330.6	362.0	vent	MEF
360	-129.087530	47.946852	2126	2122	4	36.9	68.2	vent	
361	-129.091938	47.946833	2125	2103	22	49.0	433.4	vent	
362	-129.088243	47.946797	2100	2095	5	64.9	149.0	vent	
363	-129.091848	47.946782	2113	2103	10	49.0	59.5	vent	
364	-129.099768	47.946618	2186	2180	6	320.3	686.6	mound	MEF
365	-129.088738	47.946573	2096	2089	7	27.5	57.0	vent	
366	-129.108728	47.946462	2077	2064	13	1102.9	3836.8	mound	
367	-129.092045	47.946419	2117	2113	4	39.8	61.8	vent	
368	-129.089076	47.946313	2098	2092	7	70.0	142.2	vent	
369	-129.091704	47.946291	2115	2109	6	24.9	46.6	vent	
370	-129.089432	47.946290	2096	2091	5	18.4	21.1	vent	
371	-129.104220	47.946272	2108	2096	12	138.3	746.9	vent	
372	-129.087780	47.946129	2142	2136	6	50.3	638.4	vent	
373	-129.098900	47.946116	2199	2193	6	59.4	85.9	vent	MEF
374	-129.098663	47.946104	2197	2194	3	602.9	1460.8	mound	
375	-129.096743	47.945804	2204	2194	10	113.5	501.0	vent	
376	-129.098639	47.945735	2199	2190	9	269.5	605.0	vent	
377	-129.096762	47.945691	2205	2197	8	99.1	209.6	vent	MEF
378	-129.096828	47.945551	2207	2191	16	231.5	1266.9	vent	
379	-129.098858	47.945520	2199	2191	8	79.2	182.0	vent	
380	-129.098740	47.945339	2194	2182	12	1290.6	2141.0	mound	
381	-129.096817	47.945327	2205	2201	4	108.1	39.4	vent	
382	-129.096896	47.945153	2196	2190	6	158.8	128.2	vent	
383	-129.097256	47.945067	2196	2193	3	104.9	127.1	vent	
384	-129.098596	47.945028	2200	2185	15	234.6	1200.5	vent	
385	-129.098377	47.944921	2210	2195	15	60.2	516.8	vent	
386	-129.099085	47.944843	2193	2187	6	2201.2	7092.6	mound	MEF
387	-129.104738	47.944764	2117	2109	8	22.2	47.4	vent	
388	-129.099441	47.944658	2200	2195	5	70.5	34.5	vent	
389	-129.098721	47.944505	2205	2196	9	63.6	195.9	vent	
390	-129.098733	47.944503	2205	2197	8	107.3	218.2	vent	
391	-129.097673	47.943882	2219	2210	9	152.0	353.2	vent	
392	-129.098699	47.943788	2198	2194	4	246.9	56.4	mound	
393	-129.098416	47.943547	2207	2203	4	41.5	36.1	vent	
394	-129.088983	47.943084	2170	2165	5	572.6	34.5	vent	

395	-129.089209	47.942968	2115	2109	6	29.0	56.0	vent
396	-129.106885	47.942866	2165	2162	3	87.2	34.9	vent
397	-129.106598	47.942752	2110	2101	9	47.6	192.8	vent
398	-129.100849	47.942582	2186	2179	7	126.5	111.4	vent
399	-129.105308	47.942506	2156	2151	5	118.8	79.5	mound
400	-129.105148	47.942499	2159	2158	4	95.0	1.5	vent
401	-129.103507	47.942462	2165	2162	4	38.8	145.5	vent
402	-129.106297	47.942397	2138	2130	8	39.0	9.8	vent
403	-129.107474	47.942346	2188	2174	14	528.1	2855.3	vent
404	-129.104613	47.942320	2135	2131	4	50.0	89.3	vent
405	-129.100546	47.942318	2158	2154	4	65.9	45.0	vent
406	-129.107167	47.942236	2136	2129	7	422.0	1371.9	vent
407	-129.101096	47.942185	2187	2179	8	35.0	6.8	vent
408	-129.101056	47.942074	2185	2181	4	40.4	47.6	vent
409	-129.100457	47.942030	2204	2198	6	35.5	47.3	vent
410	-129.105429	47.942020	2159	2150	9	9.1	62.9	vent
411	-129.100152	47.941874	2232	2229	3	798.4	104.5	mound
412	-129.101314	47.941736	2189	2181	8	63.5	190.8	vent
413	-129.102489	47.941725	2144	2139	5	140.8	53.5	vent
414	-129.100497	47.941722	2210	2204	6	35.4	192.0	vent
415	-129.100221	47.941619	2205	2197	8	71.4	1177.1	mound
416	-129.101141	47.941529	2193	2189	4	79.5	78.8	vent
417	-129.107661	47.941099	2131	2126	5	149.4	313.2	vent
418	-129.100074	47.941007	2168	2161	7	12.1	347.1	vent
419	-129.091875	47.940917	2134	2123	11	2709.3	6800.2	mound
420	-129.092257	47.940663	2132	2122	10	173.3	249.9	vent
421	-129.090593	47.940544	2144	2134	10	301.5	1287.6	vent
422	-129.104993	47.940514	2268	2263	5	283.8	654.0	mound
423	-129.091885	47.940388	2139	2122	17	2257.7	6901.5	mound
424	-129.104776	47.940331	2173	2168	5	336.3	1207.9	mound
425	-129.104588	47.940280	2177	2171	6	37.0	81.1	vent
426	-129.104359	47.940274	2161	2151	10	258.1	363.7	vent
427	-129.091257	47.940269	2136	2128	8	62.3	209.8	vent
428	-129.090797	47.940251	2136	2131	5	49.3	100.3	vent
429	-129.090488	47.940163	2206	2199	7	288.9	22.1	vent
430	-129.088917	47.940106	2155	2151	4	1347.6	503.7	vent
431	-129.103352	47.940032	2170	2165	5	249.6	236.0	mound
432	-129.099740	47.939979	2213	2204	9	38.6	95.7	vent
433	-129.099535	47.939788	2205	2199	6	91.7	189.2	vent
434	-129.099811	47.939463	2203	2195	8	64.4	132.6	vent
435	-129.090310	47.938923	2159	2152	7	1377.7	1108.8	mound
436	-129.100980	47.938916	2232	2229	3	39.3	44.0	vent
437	-129.100579	47.938812	2227	2219	8	95.1	681.1	vent
438	-129.103267	47.938727	2185	2180	5	46.0	73.2	vent
439	-129.102052	47.938542	2228	2222	6	216.1	113.2	vent
440	-129.101308	47.938410	2237	2233	4	86.5	31.1	vent
441	-129.103930	47.938386	2176	2171	5	15.1	29.0	vent
442	-129.101223	47.938322	2222	2211	11	36.7	271.1	vent
443	-129.103977	47.938241	2175	2171	4	20.4	29.5	vent
444	-129.100619	47.938023	2210	2203	7	46.4	149.1	vent

445	-129.093237	47.937887	2110	2104	6	50.3	77.4	vent	
446	-129.101370	47.937649	2129	2123	6	18.8	218.4	vent	
447	-129.102164	47.937403	2207	2201	6	52.2	65.1	vent	
448	-129.091912	47.937398	2133	2126	7	49.7	151.9	vent	
449	-129.100857	47.937283	2221	2213	8	120.6	274.0	vent	
450	-129.101334	47.937141	2239	2233	6	114.3	312.6	vent	
451	-129.101598	47.936754	2231	2211	20	205.3	805.9	vent	
452	-129.101648	47.936525	2232	2214	18	77.6	298.7	vent	
453	-129.103439	47.936330	2224	2219	5	99.2	236.2	vent	
454	-129.102304	47.936223	2232	2223	9	129.5	316.4	vent	
455	-129.102348	47.936070	2153	2147	6	197.5	81.0	vent	
456	-129.101798	47.935528	2236	2226	10	121.8	750.5	vent	
457	-129.103396	47.934465	2222	2210	12	237.7	557.3	vent	Mothra
458	-129.105550	47.934423	2217	2199	18	191.3	1493.5	vent	Mothra
459	-129.105646	47.934150	2230	2226	4	158.2	24.8	vent	
460	-129.105754	47.933960	2213	2200	13	171.4	1108.6	vent	Mothra
461	-129.103610	47.933937	2226	2211	15	184.2	563.4	vent	
462	-129.104660	47.933457	2221	2210	11	801.8	2484.4	vent	
463	-129.110897	47.933313	2230	2220	10	49.9	661.3	vent	
464	-129.106195	47.933221	2206	2199	7	149.1	346.3	vent	Mothra
465	-129.110927	47.933195	2162	2158	4	41.8	94.7	vent	
466	-129.104548	47.932042	2215	2203	12	166.8	598.5	vent	
467	-129.111053	47.930596	2163	2159	4	16.7	36.1	vent	
468	-129.110897	47.930330	2170	2164	6	6.9	20.0	vent	
469	-129.110829	47.930313	2168	2159	9	36.6	5.0	vent	
470	-129.109634	47.927453	2198	2188	10	687.9	784.0	mound	
471	-129.109785	47.926424	2204	2195	9	243.5	420.5	vent	
472	-129.110052	47.926363	2209	2201	8	151.3	284.3	vent	
473	-129.107238	47.925954	2167	2155	12	35.1	200.9	vent	
474	-129.110926	47.925873	2194	2172	22	140.2	538.1	vent	
475	-129.107420	47.925748	2255	2244	11	745.5	1315.0	vent	
476	-129.107929	47.925012	2139	2137	2	47.2	39.4	vent	
477	-129.114928	47.924969	2163	2155	8	332.9	625.1	vent	
478	-129.106977	47.924456	2281	2271	10	311.4	334.9	mound	Mothra
479	-129.108766	47.924223	2268	2257	11	338.8	930.2	vent	Mothra
480	-129.107106	47.924139	2267	2263	4	78.8	73.1	vent	
481	-129.108564	47.923983	2271	2266	5	16.3	29.3	vent	Mothra
482	-129.108729	47.923785	2268	2262	6	234.5	382.2	vent	Mothra
483	-129.116091	47.923606	2149	2143	6	42.5	39.0	vent	
484	-129.115604	47.923598	2140	2137	3	60.2	73.3	vent	
485	-129.109246	47.923342	2209	2201	8	21.5	20.8	vent	
486	-129.109151	47.923301	2283	2269	14	83.4	381.8	mound	Mothra
487	-129.109271	47.923170	2280	2262	18	201.8	483.5	mound	Mothra
488	-129.112354	47.922638	2194	2183	11	218.5	555.1	vent	
489	-129.109187	47.921956	2286	2277	9	51.7	97.6	vent	Mothra
490	-129.109230	47.921841	2286	2282	4	39.5	204.8	vent	Mothra
491	-129.109319	47.921830	2286	2280	5	21.9	47.0	vent	Mothra
492	-129.109182	47.921242	2284	2276	8	236.0	725.6	vent	Mothra
493	-129.109565	47.921134	2284	2270	14	31.6	109.2	vent	Mothra
494	-129.109470	47.921081	2284	2279	5	11.5	12.3	vent	Mothra

495	-129.109584	47.921050	2284	2277	7	24.2	49.9	vent	Mothra
496	-129.109689	47.920964	2284	2269	15	139.5	460.0	vent	Mothra
497	-129.109156	47.920825	2281	2277	4	124.0	70.5	vent	Mothra
498	-129.109377	47.920783	2280	2272	8	96.3	236.1	vent	Mothra
499	-129.109546	47.920750	2278	2273	5	266.8	750.1	mound	Mothra
500	-129.109387	47.920670	2282	2274	8	57.9	89.3	vent	Mothra
501	-129.111483	47.920605	2246	2237	9	382.7	1008.4	vent	
502	-129.109783	47.920576	2282	2276	6	59.7	89.5	vent	Mothra
503	-129.109712	47.920491	2281	2275	6	95.6	132.2	vent	Mothra
504	-129.120560	47.920376	2136	2130	6	49.3	37.8	vent	
505	-129.114440	47.920314	2223	2206	17	142.0	588.6	vent	
506	-129.111668	47.920041	2246	2231	15	95.3	209.9	vent	
507	-129.110625	47.919968	2266	2259	7	185.9	306.7	vent	Mothra
508	-129.110428	47.919906	2280	2276	4	58.3	94.5	vent	Mothra
509	-129.112169	47.918978	2238	2228	10	158.3	684.2	vent	
510	-129.110816	47.918731	2280	2271	9	44.1	100.5	vent	Mothra
511	-129.121738	47.918635	2144	2135	9	29.0	28.1	vent	
512	-129.112473	47.918177	2248	2238	10	55.8	288.5	vent	
513	-129.110869	47.917879	2271	2267	4	40.1	47.5	vent	
514	-129.113835	47.917726	2220	2208	12	780.4	3792.3	mound	
515	-129.122481	47.917485	2148	2138	10	157.5	167.3	vent	
516	-129.111142	47.917463	2270	2265	5	39.4	79.4	vent	
517	-129.115645	47.916285	2235	2224	11	143.2	498.9	vent	
518	-129.115951	47.916107	2230	2213	17	408.3	2529.6	vent	
519	-129.114571	47.916077	2198	2176	22	83.1	374.4	vent	
520	-129.120611	47.915628	2256	2252	4	106.5	29.6	vent	
521	-129.118715	47.915497	2243	2236	7	697.8	1014.7	mound	
522	-129.114708	47.915431	2231	2217	14	141.3	446.0	vent	
523	-129.112793	47.913589	2267	2259	8	253.8	872.1	vent	
524	-129.112831	47.913335	2264	2257	7	121.3	487.6	vent	
525	-129.123391	47.912993	2151	2138	13	156.6	650.1	vent	
526	-129.113678	47.912848	2275	2269	6	597.5	143.8	vent	
527	-129.111969	47.912606	2271	2260	11	112.9	1283.2	vent	
528	-129.120622	47.912298	2230	2206	24	104.0	385.3	vent	
529	-129.120949	47.912106	2226	2219	7	128.6	291.6	vent	
530	-129.114648	47.910696	2243	2238	5	74.1	65.1	vent	
531	-129.121806	47.909613	2240	2231	9	43.2	119.8	vent	
532	-129.121628	47.909563	2242	2231	11	82.1	593.3	vent	
533	-129.121903	47.909521	2246	2229	17	25.3	64.5	vent	
534	-129.121702	47.909373	2253	2247	5	16.3	32.7	vent	
535	-129.121933	47.909336	2250	2245	5	28.9	34.3	vent	
536	-129.120374	47.909080	2249	2227	22	354.9	584.9	vent	
537	-129.122028	47.908575	2259	2251	8	12.3	33.5	vent	
538	-129.122440	47.908470	2255	2235	20	54.2	294.2	vent	
539	-129.123702	47.907365	2224	2215	9	649.5	2057.9	mound	
540	-129.123921	47.907242	2227	2218	9	88.8	137.4	vent	
541	-129.124147	47.907183	2221	2213	8	74.2	66.7	vent	
542	-129.124304	47.907073	2218	2209	9	51.8	55.7	vent	
543	-129.125729	47.906823	2187	2181	6	33.8	640.4	vent	
544	-129.124078	47.906763	2231	2223	8	31.4	51.2	vent	

545	-129.120090	47.906760	2286	2274	12	21.5	55.7	vent
546	-129.124209	47.906737	2227	2219	8	53.7	101.5	vent
547	-129.124060	47.906623	2238	2220	18	38.9	191.6	vent
548	-129.120240	47.906585	2207	2192	15	119.8	373.0	vent
549	-129.120338	47.906414	2202	2196	6	140.1	167.1	vent
550	-129.127565	47.906254	2188	2180	8	289.4	827.4	vent
551	-129.121481	47.905812	2211	2199	12	74.5	145.6	vent
552	-129.118391	47.903060	2271	2265	6	245.4	194.6	vent
553	-129.125087	47.902613	2274	2268	6	60.0	68.7	vent
554	-129.125267	47.902574	2278	2265	13	34.2	212.9	vent
555	-129.125330	47.902500	2297	2293	4	51.2	37.1	vent
556	-129.125163	47.902165	2275	2268	7	93.2	102.4	vent
557	-129.125649	47.901919	2285	2276	9	38.7	243.0	vent
558	-129.128446	47.900994	2316	2311	5	50.0	86.5	vent
559	-129.128872	47.900422	2318	2311	7	470.8	836.0	mound
560	-129.128562	47.900375	2321	2309	12	217.1	428.5	vent
561	-129.128831	47.900367	2320	2305	15	34.6	169.0	vent
562	-129.128677	47.900230	2325	2312	13	65.0	143.8	vent
563	-129.129093	47.900097	2212	2207	5	18.8	34.7	vent
564	-129.118536	47.899444	2231	2223	8	59.1	1000.6	vent
565	-129.127362	47.899382	2296	2285	11	63.4	282.7	vent
566	-129.127448	47.899316	2297	2275	22	45.8	308.7	vent
567	-129.127305	47.898952	2297	2293	4	84.8	151.1	vent
568	-129.127359	47.898835	2323	2317	6	33.8	22.7	vent
569	-129.127174	47.898702	2297	2290	7	64.0	93.0	vent
570	-129.127926	47.898678	2295	2292	3	25.2	27.4	vent
571	-129.128206	47.898575	2299	2293	6	39.7	76.7	vent
572	-129.113377	47.898528	2270	2263	7	247.2	512.9	vent
573	-129.127776	47.898390	2298	2292	6	29.5	26.1	vent
574	-129.128159	47.898006	2282	2274	8	29.9	55.1	vent
575	-129.120755	47.895840	2152	2143	9	86.2	298.3	vent
576	-129.132134	47.895611	2304	2298	6	429.9	697.7	vent
577	-129.124172	47.895545	2315	2300	15	632.7	107.8	vent
578	-129.135870	47.889929	2301	2292	10	62.6	177.2	vent
579	-129.135026	47.889332	2280	2272	8	15.6	2608.2	vent
580	-129.116757	47.885859	2306	2295	11	60.6	59.4	vent
581	-129.131954	47.884486	2334	2327	7	15.9	61.4	vent

APPENDIX F – Sources and calculations for age uncertainties for the ^{226}Ra/Ba dating method

Age uncertainties for hydrothermal samples from the Endeavour Segment that were dated using the ^{226}Ra/Ba method range from ±127 to ±211 years for ages between ~25 and ~5,850 years. The sources of the uncertainties are a combination of analytical uncertainties and the uncertainty associated with determination of the initial ^{226}Ra/Ba value (N_0) used in the decay equation for all dated samples.

Decay equation:

$$t = \frac{\ln {}^{N_0}\!/_{N} \times 1600\,yrs}{\ln 2}$$

Where:

N = ^{226}Ra/Ba of the sample, at the time collected

N_0 = initial ^{226}Ra/Ba of the sample at time of sample formation

1,600 yrs = Half-life of ^{226}Ra

Analytical uncertainties

Barium concentrations (*Ba*), measured by either instrumental neutron activation analysis or fusion inductively coupled plasma mass spectrometry, and ranging from ~0.05 wt. % to 33 wt. % have an uncertainty (δBa) of ~5%, based on repeat measurements of laboratory standard materials with Ba concentrations within the range of the analyzed samples.

Radium-226 activity (^{226}Ra) was measured by gamma spectrometry (see Chapter 4 for details). Uncertainties associated with counting errors ($\delta^{226}Ra$) range from 0.1 to 7%, and average ~1%.

The uncertainty for N (δN) is determined by propagation of the uncertainties associated with measurements of the Ba concentration and ^{226}Ra activity for each sample:

$$\delta N = N\left(\delta {}^{226}Ra/_{^{226}Ra} + \delta Ba/_{Ba}\right)$$

The value N_0 in the decay equation is determined from measurements of N for zero-age (e.g., actively venting) samples. N_0 is taken as the slope of a linear regression through data points for 11 samples:

$$N_0 = S_{xy} \Big/ S_{xx}$$

Where:

$$S_{xy} = \sum (x_i - \bar{x})(y_i - \bar{y})$$

$$S_{xx} = \sum (x_i - \bar{x})^2$$

The uncertainty associated with N_0 is the standard deviation of the slope of the regression line (δN_0):

$$\delta N_0 = \frac{\sqrt{\frac{S_{yy} - (N_0)^2 S_{xx}}{n-2}}}{\sqrt{S_{xx}}}$$

Where:

$$S_{yy} = \sum (y_i - \bar{y})^2$$

n = number of samples

The uncertainties associated with both N and N_0 can then be propagated through the decay equation to determine the uncertainty in the sample age (δt):

$$\delta t = \delta \left[1600\, yrs \Big/ \ln 2 \times \ln \left(N_0 \Big/ N \right) \right] = 1600\, yrs \Big/ \ln 2 \times \delta \ln \left(N_0 \Big/ N \right)$$

$$\delta \ln \left(N_0 \Big/ N \right) = \delta \left(N_0 \Big/ N \right) \Big/ \left(N_0 \Big/ N \right)$$

$$\delta \left(N_0 \Big/ N \right) = \left(N_0 \Big/ N \right) \left(\delta N_0 \Big/ N_0 + \delta N \Big/ N \right)$$

Age uncertainty for the ^{226}Ba/Ra dating method is thus determined using the following equation:

$$\delta t = \frac{1600\, yrs}{\ln 2} \left(\frac{\delta\, {}^{226}Ra}{{}^{226}Ra} + \frac{\delta Ba}{Ba} + \frac{\delta N_0}{N_0} \right)$$